

Development and Experimental Validation of an Impactor for Osseointegrated Transfemoral Implant Stability Assessment

by

Eric Beaudry

A thesis submitted in partial fulfillment of the requirements for the degree of

Master of Science

Department of Mechanical Engineering

University of Alberta

© Eric Beaudry, 2024

Abstract

Osseointegrated transfemoral implants are a promising alternative for individuals who are unable to use a socket prosthesis; it is generally accepted that bone-anchored prostheses can improve patient quality of life. Osseointegration is the long-term process of implant anchorage in bone, caused by the interdigitation of bone at the implant surface; remodelling at the bone-implant interface is responsible for the stability of the implant over time. Osseointegrated dental implants have been studied extensively, and several research and commercial devices have employed vibration analysis to quantify their stability. Such approaches assume the bone-implant interface has an effective stiffness that governs the dynamic response of the bone-implant system. In general, the interface stiffens with progressed osseointegration, and the natural frequencies of the system increase over time. The Osstell and Advanced System for Implant Stability Testing (ASIST) are two devices that leverage this behaviour to monitor osseointegration. The Osstell employs resonance frequency analysis, while the ASIST uses a percussion method in conjunction with an analytical model of the bone-implant system. The ASIST has demonstrated better sensitivity and reliability than the Osstell in a benchtop study, as it accounts for the inertial and geometric properties of the implant itself. The success of the ASIST approach in a variety of applications has made it an attractive option for transfemoral implant stability assessment. To date, a handful of studies have demonstrated the potential of vibrational analysis in transfemoral implant stability assessment, and a parallel investigation established the ability of the ASIST approach to isolate mechanical properties of the bone-implant interface. However, there is currently a need for a novel impactor to increase the sensitivity of the approach. In line with the state of the ASIST approach, four objectives were outlined for this thesis:

1. Develop an impactor for osseointegrated transfemoral implant stability assessment.
2. Integrate the impactor with a mathematical model and the ASIST approach.
3. Enhance the sensitivity of the approach in the full interface stiffness range.
4. Validate the safety, reliability, and sensitivity of the integrated approach.

Four project phases were executed in the development and validation of an impactor for transfemoral implant stability assessment. In the first phase, a benchtop prototype was developed, and a variety of factors were explored for inclusion in a prospective development and evaluation study. Factor exploration was conducted with backing from experimental modal analysis theory and led to a comprehensive framework for the development study. The second phase involved the execution of the study and produced design specifications for impact rod mass, tip geometry, and impact interface stiffness. Tests were conducted on benchtop transfemoral amputation models under three bone-implant interface stiffness conditions. Silicone rubber adhesive, paraffin wax, and superglue simulated low, intermediate, and high stiffness interfaces, respectively. The results indicated that multiple impact rod masses (10; 30 *g*) and impact interface stiffnesses (316 stainless steel; Delrin®) should be included in subsequent phases, as a single optimal configuration was not apparent. Full domain sensitivity was preliminarily demonstrated for a combination of prototype impactor configurations. In the third phase, two handpieces were designed and manufactured with the recommended impact rods and interchangeable impact tips. Sufficient safety and functionality of the 30 *g* impactor was demonstrated, and it was deployed in a parallel clinical study. A design of experiments methodology was synthesized for the last stage of the project, an experimental validation study. Three operators took measurements with both handpieces on various implant configurations under the same interface stiffness conditions as the development study (low; intermediate; high). An objective framework for 1D finite element model matching and

measurement trustworthiness judgements was developed for analysis. The 10 *g* impactor demonstrated superior interface stiffness sensitivity and classification accuracy relative to the 30 *g* impactor.

A novel impactor for osseointegrated transfemoral implant stability assessment was developed and validated in a benchtop study. The selected impactor demonstrated high sensitivity to a wide range of bone-implant interface stiffness conditions and was able to correctly classify all measurements for a simple implant configuration. The enclosed thesis represents a significant achievement in the field of transfemoral implant stability assessment, detailing the first device to implement an electromagnetic impactor, vibration acquisition system, and 1D finite element model in a strong approach to osseointegrated transfemoral implant stability assessment.

Preface

This thesis is the original work of Eric Beaudry. The research project received research ethics approval from the University of Alberta Research Ethics Board, project name “Evaluation of the mechanical properties of the bone-implant interface in lower limb amputees,” No. Pro00091955, Completed April 25, 2022, and project name “An innovative approach for non-invasive evaluation of stability at the implant-bone interface for transfemoral osseointegrated implants,” No. Pro00109990, Currently Active.

This research was supported and funded by the Government of Alberta Major Innovation Fund (Alberta Medical Device Innovation Consortium), NSERC (PI: Hebert), Suncor Energy Inc and the Office of the Assistant Secretary of Defense for Health Affairs through the FY20 Peer Reviewed Orthopaedic Research Program, endorsed by the Department of Defense under Award No. W81XWH-21-1-0857. Opinions, interpretations, conclusions, and recommendations are those of the author and are not necessarily endorsed by the Department of Defense.

This research is part of an ongoing collaborative investigation to develop a vibration-based measurement system for stability assessment of osseointegrated transfemoral implants. The author’s role in publications involved developing experimental models and impactor systems.

Complete list of publications that came out of this research:

The role of E. Beaudry as first author involved developing experimental models, analysis, and results generation in the following conference abstract publications.

E. Beaudry, M. Mohamed, J. Hebert, and L. Westover, “Design of an Impactor for Transfemoral Osseointegrated Implant Stability Assessment,” in *University of Alberta Faculty of Engineering Graduate Research Symposium*, 2023

E. Beaudry, M. Mohamed, J. Hebert, and L. Westover, “Design of an Impactor for Transfemoral Osseointegrated Implant Stability Assessment,” in *Annual Alberta Biomedical Engineering Conference*, 2023

The role of E. Beaudry as second author involved sharing experimental results from various impactors with the first author of the following publication.

M. Mohamed et al., “Evaluation of the transfemoral bone–implant interface properties using vibration analysis,” *Annals of Biomedical Engineering*, Jul. 2024. doi:10.1007/s10439-024-03561-

6

Acknowledgements

I would like to thank and acknowledge:

My supervisor, Dr. Lindsey Westover, for her patience, unwavering support, and invaluable guidance throughout the course of my graduate studies. It was a pleasure to work on this project as a member of her research group.

My co-supervisor, Dr. Jacqueline Hebert, for her dedication, guidance, and feedback over the course of this project.

Dr. Albert Vette for signal processing support and serving as a member of my examination committee.

Dr. Kajsa Duke for design of experiments support and chairing the examination.

Dr. Mostafa Mohamed for endless academic and emotional support, judicious ideas and guidance, and a wonderful friendship.

Dylan Brenneis for his ingenuity, inspiration, and drive on this project.

My family, friends, and lab mates for all the joy, love, support, and enrichment of life in and outside of school over the years.

And lastly, Olivia, whom I would not have survived without. Thank you for all the love, memories, and life.

Table of Contents

| | |
|--|------|
| Abstract | ii |
| Preface..... | v |
| Acknowledgements | vii |
| Table of Contents | viii |
| List of Tables..... | xiii |
| List of Figures | xv |
| Chapter 1 Introduction | 1 |
| 1.1 Background | 1 |
| 1.1.1 Motivation | 1 |
| 1.1.2 Vibration Assessment..... | 2 |
| 1.2 Objectives..... | 4 |
| 1.3 Thesis Outline | 4 |
| Chapter 2 Literature Review | 6 |
| 2.1 Transfemoral Amputation..... | 6 |
| 2.1.1 Anatomy..... | 6 |
| 2.1.2 Prevalence..... | 6 |
| 2.1.3 Prosthetic Attachment..... | 7 |
| 2.2 Osseointegration..... | 11 |
| 2.2.1 History | 11 |
| 2.2.2 Physiology | 12 |
| 2.2.3 Biomechanics..... | 14 |
| 2.3 Implant Stability Assessment | 16 |
| 2.3.1 Overview | 16 |
| 2.3.2 Destructive Methods..... | 17 |

| | |
|---|----|
| 2.3.3 Non-Destructive Methods..... | 18 |
| 2.3.4 Transfemoral Implants..... | 24 |
| Chapter 3 Initial Development and Factor Exploration..... | 31 |
| 3.1 Introduction..... | 31 |
| 3.2 Periotest Handpiece Design..... | 31 |
| 3.2.1 Overview..... | 31 |
| 3.2.2 Documentation..... | 31 |
| 3.2.3 Dissection..... | 35 |
| 3.2.4 ASIST Impact Force..... | 40 |
| 3.3 Impact Model..... | 43 |
| 3.3.1 Two Degree of Freedom Model..... | 43 |
| 3.3.2 1D Finite Element Model..... | 49 |
| 3.3.3 One Degree of Freedom Model..... | 53 |
| 3.4 Benchtop Prototype Synthesis..... | 56 |
| 3.4.1 Components..... | 56 |
| 3.4.2 Magnetic Flux Density Measurements..... | 57 |
| 3.4.3 Modular Prototype..... | 59 |
| 3.5 Initial Benchtop Prototype Testing..... | 61 |
| 3.5.1 Average Velocity..... | 61 |
| 3.5.2 Impact Force..... | 63 |
| 3.6 Recommendations for Development and Evaluation Study..... | 66 |
| 3.6.1 TFA Implant Models..... | 66 |
| 3.6.2 Impact Interface Stiffness..... | 69 |
| 3.6.3 Impact Rod Mass..... | 74 |
| 3.6.4 Actuation Voltage and Impact Tip Geometry..... | 78 |

| | |
|---|-----|
| 3.6.5 Application of Impact Model..... | 81 |
| 3.6.6 Experimental Pilot Testing | 82 |
| 3.7 Conclusion..... | 87 |
| Chapter 4 Evaluation of Benchtop Impactor System..... | 88 |
| 4.1 Introduction | 88 |
| 4.1.1 Background..... | 88 |
| 4.1.2 Modal Finite Element Model..... | 89 |
| 4.1.3 Objectives | 90 |
| 4.2 Materials and Methods | 91 |
| 4.2.1 Overview | 91 |
| 4.2.2 Experimental Setup..... | 93 |
| 4.2.3 Experimental Procedure | 97 |
| 4.3 Results and Discussion..... | 101 |
| 4.3.1 Overview | 101 |
| 4.3.2 Time Domain | 102 |
| 4.3.3 Frequency Domain | 107 |
| 4.3.4 Amplitude Ratio..... | 113 |
| 4.3.5 Mode 1 Power Spectral Density | 117 |
| 4.3.6 Band Power..... | 121 |
| 4.3.7 Final Design Decisions and Amplitude Ratio Intraclass Correlation | 124 |
| 4.3.8 Modal Finite Element Model and Experimental Model Comparison | 128 |
| 4.3.9 Velocity Measurement | 129 |
| 4.3.10 Finite Element Models..... | 131 |
| 4.3.11 Impact Force | 139 |
| 4.4 Conclusion..... | 146 |

| | |
|---|-----|
| Chapter 5 Design of Handheld Impactors..... | 147 |
| 5.1 Introduction..... | 147 |
| 5.2 Component Selection, Evaluation, and Assembly | 147 |
| 5.2.1 Component Selection..... | 147 |
| 5.2.2 Magnetic Flux Density Measurements..... | 149 |
| 5.2.3 Electromagnetic Force Measurements..... | 151 |
| 5.2.4 Handpiece Assemblies..... | 154 |
| 5.3 Clinical and CSA Standards Compliance..... | 157 |
| 5.3.1 Overview | 157 |
| 5.3.2 General Reliability..... | 159 |
| 5.3.3 Impact Force | 160 |
| 5.3.4 Velocity | 163 |
| 5.3.5 Temperature | 163 |
| 5.3.6 Functionality..... | 165 |
| 5.3.7 Conclusion | 171 |
| 5.4 Design of Experiments | 171 |
| 5.4.1 Overview | 171 |
| 5.4.2 Pilot Test..... | 173 |
| 5.4.3 Design..... | 175 |
| 5.5 Conclusion..... | 176 |
| Chapter 6 Experimental Validation of Handheld Impactors | 178 |
| 6.1 Introduction | 178 |
| 6.1.1 Background..... | 178 |
| 6.1.2 Objectives | 178 |
| 6.2 Materials and Methods..... | 179 |

| | |
|--|-----|
| 6.2.1 Overview | 179 |
| 6.2.2 Experimental Setup..... | 180 |
| 6.2.3 Experimental Procedure | 183 |
| 6.3 Results | 186 |
| 6.3.1 Overview | 186 |
| 6.3.2 Matching | 188 |
| 6.4 Discussion | 196 |
| 6.4.1 Overview | 196 |
| 6.4.2 Generalized Linear Mixed Effects Models..... | 198 |
| 6.4.3 Modal Tests..... | 221 |
| 6.5 Conclusion..... | 237 |
| Chapter 7 Conclusion..... | 239 |
| 7.1 Contribution | 239 |
| 7.2 Significance | 239 |
| 7.3 Limitations | 240 |
| 7.4 Future Work..... | 241 |
| References | 243 |

List of Tables

| | |
|--|-----|
| Table 3.1: Benchtop prototype part summary. HF: holding force | 56 |
| Table 3.2: Replica implant with superglue interface experimental model components | 67 |
| Table 3.3: Data acquisition system components | 68 |
| Table 3.4: List of material coupons with associated mechanical properties | 70 |
| Table 3.5: Frequency comparison between initial modal finite element model estimates and experimental setup | 85 |
| Table 3.6: Factors and levels of prospective development and evaluation study | 87 |
| Table 4.1: Modal finite element model frequencies..... | 90 |
| Table 4.2: Factors and levels of development and evaluation experiment. *Delrin® impact tip tested in a subset of runs | 93 |
| Table 4.3: Experimental model and acquisition system components | 96 |
| Table 4.4: Signal processing parameters for development experiment | 101 |
| Table 4.5: Modal frequency extraction cutoffs | 113 |
| Table 4.6: Modal and impact finite element model parameters..... | 132 |
| Table 4.7: Modal and impact finite element model material properties | 133 |
| Table 4.8: Impact finite element model results summary | 137 |
| Table 4.9: All models comparison | 139 |
| Table 5.1: Outsourced components for 10 <i>g</i> and 30 <i>g</i> handpieces..... | 148 |
| Table 5.2: Handpiece angular operating ranges | 159 |
| Table 5.3: Maximum temperatures of various components of 10 <i>g</i> handpiece under continuous operation | 165 |
| Table 5.4: Prospective validation study design..... | 176 |
| Table 6.1: Experimental model and acquisition system components | 182 |
| Table 6.2: Signal processing parameters for benchtop validation experiment | 186 |
| Table 6.3: Handpiece measurement accuracy summary – raw signals | 194 |
| Table 6.4: Handpiece measurement accuracy summary – notch filter | 196 |
| Table 6.5: Fixed effects for gamma regression on data from raw signals | 199 |
| Table 6.6: Interface stiffness estimates for gamma regression on data from raw signals..... | 201 |
| Table 6.7: Classification for binary probit regression on data from raw signals | 203 |

| | |
|--|---------|
| Table 6.8: Fixed effects for binary probit regression on data from raw signals | 204 |
| Table 6.9: Estimated grand mean for binary probit regression on data from raw signals | 205 |
| Table 6.10: Estimated interface means for binary probit regression on data from raw signals .. | 206 |
| Table 6.11: Fixed effects for gamma regression on data from notch filter signals | 209 |
| Table 6.12: Interface stiffness estimates for gamma regression on data from notch filter signals | 211 |
| Table 6.13: Classification for binary probit regression on data from notch filter signals..... | 213 |
| Table 6.14: Fixed effects for binary probit regression on data from notch filter signals..... | 214 |
| Table 6.15: Estimated grand mean for binary probit regression on data from notch filter signals | 215 |
| Table 6.16: Estimated interface means for binary probit regression on data from notch filter signals | 216 |
| Table 6.17: Position test legend | 224 |
| Table 6.18: Transverse noise test legend..... | 227 |
| Table 6.19: Transverse GV connector noise test legend | 228 |
| Table 6.20: Summary plot legend | 230 |
| App. Table D.1: Standards legend | 262 |
| App. Table D.2: Standards summary | 262 |

List of Figures

| | |
|--|----|
| Figure 2.1: OPL implant system components with x-ray image of implantation [3] | 10 |
| Figure 2.2: Physical models used by Cairns [22] | 27 |
| Figure 2.3: Transfemoral axial vibrations elicited by Periotest handpiece [27] | 30 |
| Figure 3.1: Periotest handpiece schematic [15] | 32 |
| Figure 3.2: General schematic of Periotest system [58] | 32 |
| Figure 3.3: Apparatus for assessing percutaneous implant integrity [58] | 33 |
| Figure 3.4: Other apparatus concepts for assessing percutaneous implant integrity [58] | 33 |
| Figure 3.5: Periotest handpiece schematic [59] | 34 |
| Figure 3.6: Periotest patent schematic [60] | 35 |
| Figure 3.7: Subassemblies of dissected Periotest handpiece | 36 |
| Figure 3.8: Periotest impact rod assembly | 36 |
| Figure 3.9: Tip of Periotest impact rod | 37 |
| Figure 3.10: Accelerometer leads exiting Periotest impact rod | 37 |
| Figure 3.11: Linear and rotational motion constraint mechanism of Periotest impact rod | 38 |
| Figure 3.12: Embedded permanent magnet at rear end of Periotest impact rod | 38 |
| Figure 3.13: Solenoid, electromagnet, and connector assembly of Periotest handpiece | 39 |
| Figure 3.14: Configuration of Periotest handpiece coils | 39 |
| Figure 3.15: First ASIST impact force test | 41 |
| Figure 3.16: ASIST ensemble average loading profile (impact load cell) | 41 |
| Figure 3.17: ASIST ensemble average impact acceleration profile (Periotest handpiece) | 42 |
| Figure 3.18: Peak impact force vs. actuation time for various Periotest handpiece configurations | 43 |
| Figure 3.19: ASIST analytical model of bone anchored hearing aid implant/abutment system [16] | 44 |
| Figure 3.20: Two degree of freedom impact vibration model | 45 |
| Figure 3.21: Impact force curves under various mass and stiffness ratio configurations | 48 |
| Figure 3.22: 1D finite element impact vibration model | 50 |
| Figure 3.23: Impact force curves under various mass and stiffness ratio configurations with $d = 225b$ | 52 |

| | |
|---|----|
| Figure 3.24: Impact force curves under various mass and stiffness ratio configurations with $d = 4b$ | 52 |
| Figure 3.25: Impact force curves under various mass and stiffness ratio configurations with $d = b$ | 53 |
| Figure 3.26: One degree of freedom impact model | 54 |
| Figure 3.27: Photo of benchtop prototype components. HF: holding force | 57 |
| Figure 3.28: TD8620 Gauss meter (HFBTE, China) | 57 |
| Figure 3.29: Permanent magnet magnetic flux density measurements..... | 58 |
| Figure 3.30: Magnetic flux density measurements of various magnetic coils..... | 59 |
| Figure 3.31: Magnetic flux density vs. distance from 15 kg HF electromagnet active surface .. | 59 |
| Figure 3.32: Solid model of modular benchtop prototype..... | 60 |
| Figure 3.33: Electromagnet actuation code snippet..... | 61 |
| Figure 3.34: Frame capture of smartphone high-speed video recording | 61 |
| Figure 3.35: Average velocity of 25 kg HF electromagnet paired with neodymium magnets of varying length | 62 |
| Figure 3.36: Average velocity of 1/2 in neodymium magnet paired with electromagnets of varying HF | 62 |
| Figure 3.37: v1 benchtop prototype impact load cell setup | 63 |
| Figure 3.38: v2 benchtop prototype with impact load cell | 64 |
| Figure 3.39: Benchtop prototype impact loading profile comparison to ASIST | 65 |
| Figure 3.40: Impact force vs. actuation voltage for rising and falling trials..... | 65 |
| Figure 3.41: Replica implant transverse acceleration response (silicone interface)..... | 66 |
| Figure 3.42: Sawbones cylinder superglue interface setup..... | 68 |
| Figure 3.43: Data acquisition system schematic..... | 69 |
| Figure 3.44: Impact interface test setup..... | 70 |
| Figure 3.45: Impact force vs. actuation voltage for impact interfaces with varying mechanical properties..... | 71 |
| Figure 3.46: Contact time vs. actuation voltage for impact interfaces with varying mechanical properties (steel and aluminum curves overlapping)..... | 71 |
| Figure 3.47: Superglue interface power spectra for strikes with varying impact interface stiffness – full domain | 73 |

| | |
|--|----|
| Figure 3.48: Superglue interface power spectra for strikes with varying impact interface stiffness – reduced domain | 73 |
| Figure 3.49: Axial strike with GV connector installed | 74 |
| Figure 3.50: Superglue interface axial frequency response – 12 <i>g</i> base rod (nominal mass in legend)..... | 75 |
| Figure 3.51: Superglue interface axial frequency response – 44 <i>g</i> base rod (nominal mass in legend)..... | 75 |
| Figure 3.52: Transverse strike configuration with GV connector installed | 76 |
| Figure 3.53: Superglue interface transverse frequency response (nominal mass in legend) | 77 |
| Figure 3.54: Superglue interface transverse frequency response – reduced domain (nominal mass in legend) | 77 |
| Figure 3.55: Power spectra of superglue interface with GV connector installed. Transverse strikes with 12 <i>g</i> impact rod | 78 |
| Figure 3.56: Flush vs. oblique strike diagram..... | 79 |
| Figure 3.57: Flush vs. oblique strikes in transverse direction on superglue interface setup without GV connector installed | 81 |
| Figure 3.58: Simulated impact curves for $\zeta = 0$ | 82 |
| Figure 3.59: Curing silicone interface setup | 83 |
| Figure 3.60: Time domain responses of silicone interface – ASIST vs. 40 <i>g</i> impact rod..... | 83 |
| Figure 3.61: Frequency domain responses of silicone interface – ASIST vs. 40 <i>g</i> impact rod ... | 84 |
| Figure 3.62: Amplitude normalized frequency domain responses of silicone interface – ASIST vs. 40 <i>g</i> impact rod | 84 |
| Figure 3.63: Repeatability of 10 <i>g</i> impact rod striking silicone interface setup without GV connector installed (axial direction)..... | 86 |
| Figure 3.64: Repeatability of 10 <i>g</i> impact rod striking silicone interface setup with GV connector installed (axial direction) | 86 |
| Figure 4.1: Modal finite element model – silicone mode 1. Left, full system; right, implant..... | 89 |
| Figure 4.2: Modal finite element model – silicone mode 2. Left, full system; right, implant..... | 90 |
| Figure 4.3: Experimental model base components | 93 |
| Figure 4.4: Sawbones femur preparation | 94 |
| Figure 4.5: Development and evaluation experiment setup..... | 97 |

| | |
|--|-----|
| Figure 4.6: Axial strike position without GV connector installed | 98 |
| Figure 4.7: Transverse strike position with GV connector installed | 98 |
| Figure 4.8: Impact tip geometries | 100 |
| Figure 4.9: Time domain signals – silicone; DC; axial; cone; 7.5 V | 103 |
| Figure 4.10: Time domain signals – silicone; GV; axial; cone; 7.5 V | 104 |
| Figure 4.11: Time domain signals – silicone; DC; axial; Delrin®; 7.5 V | 104 |
| Figure 4.12: Time domain signals – wax 1; DC; axial; cone; 7.5 V | 105 |
| Figure 4.13: Time domain signals – wax 2; DC; axial; cone; 7.5 V | 106 |
| Figure 4.14: Time domain signals - superglue; DC; axial; cone; 7.5 V | 107 |
| Figure 4.15: Frequency domain signals – silicone; DC; axial; cone | 108 |
| Figure 4.16: Frequency domain signals – silicone; GV; axial; cone | 108 |
| Figure 4.17: Frequency domain signals – silicone; DC; axial; Delrin® | 109 |
| Figure 4.18: Frequency domain signals – wax 1; DC; axial; cone | 110 |
| Figure 4.19: Frequency domain signals – wax 2; DC; axial; cone | 111 |
| Figure 4.20: Frequency domain signals – superglue; DC; axial; cone | 112 |
| Figure 4.21: Amplitude ratio – silicone; DC; axial | 114 |
| Figure 4.22: Amplitude ratio – silicone; GV; axial | 115 |
| Figure 4.23: Amplitude ratio – wax 1; DC; axial | 116 |
| Figure 4.24: Amplitude ratio – wax 2; DC; axial | 116 |
| Figure 4.25: Amplitude ratio – superglue; DC; axial | 117 |
| Figure 4.26: Mode 1 amplitude – silicone; DC; axial | 118 |
| Figure 4.27: Mode 1 amplitude – silicone; GV; axial | 119 |
| Figure 4.28: Mode 1 amplitude – wax 1; DC; axial | 120 |
| Figure 4.29: Mode 1 amplitude – superglue; DC; axial | 121 |
| Figure 4.30: Band power – silicone; DC; axial | 122 |
| Figure 4.31: Band power – silicone; GV; axial | 122 |
| Figure 4.32: Band power – wax 1; DC; axial | 123 |
| Figure 4.33: Band power – superglue; DC; axial | 124 |
| Figure 4.34: Amplitude ratio ICC vs. actuation voltage across all axial configurations | 126 |
| Figure 4.35: Modal contributions vs. impact rod mass for low condition of 1D finite element model [28] | 128 |

| | |
|--|-----|
| Figure 4.36: Modal finite element and experimental model frequency comparison | 129 |
| Figure 4.37: High-speed camera setup..... | 130 |
| Figure 4.38: High speed camera raw velocity data..... | 131 |
| Figure 4.39: Impact finite element model – silicone interface. Left, 10 <i>g</i> impact rod; right, 30 <i>g</i> impact rod | 134 |
| Figure 4.40: Impact finite element model acceleration measurement location detail for 10 <i>g</i> impact rod simulation. Acceleration recorded from node sets highlighted in red | 134 |
| Figure 4.41: Impact finite element model – frequency domain results | 135 |
| Figure 4.42: Impact finite element model – impact rod loading profiles | 136 |
| Figure 4.43: Impact finite element model – multi-axis superglue interface results..... | 138 |
| Figure 4.44: Load cell setup for impact rods of varying mass..... | 140 |
| Figure 4.45: Load cell setup for ASIST strikes..... | 140 |
| Figure 4.46: Loading profiles for benchtop prototype configurations with conical tip..... | 141 |
| Figure 4.47: Loading profiles for benchtop prototype configurations with Delrin® tip | 142 |
| Figure 4.48: Peak impact force vs. actuation voltage for all benchtop prototype configurations | 143 |
| Figure 4.49: Contact time vs. actuation voltage for all benchtop prototype configurations..... | 144 |
| Figure 4.50: Loading profiles for ASIST strikes..... | 144 |
| Figure 4.51: Impact force and contact time vs. extension (actuation) time for ASIST strikes ... | 145 |
| Figure 5.1: Permanent magnet magnetic flux density measurements..... | 149 |
| Figure 5.2: Magnetic flux density measurements for various magnetic coils | 150 |
| Figure 5.3: Magnetic flux density vs. distance from active surface for various electromagnets | 150 |
| Figure 5.4: Static electromagnetic force measurement setup | 152 |
| Figure 5.5: Repulsive force vs. gap between electromagnet and neodymium magnet – full range | 153 |
| Figure 5.6: Repulsive force vs. gap between electromagnet and neodymium magnet – reduced range..... | 154 |
| Figure 5.7: Assembled Handpieces. Left, 10 <i>g</i> impact rod; right, 30 <i>g</i> impact rod | 155 |
| Figure 5.8: Exploded view of 10 <i>g</i> handpiece assembly..... | 155 |
| Figure 5.9: Exploded view of 10 <i>g</i> impact rod assembly..... | 156 |

| | |
|--|-----|
| Figure 5.10: Dimetric exploded view of 10 <i>g</i> handpiece assembly. Motion limiter and wire reliefs exposed | 157 |
| Figure 5.11: Section view of physical 10 <i>g</i> handpiece..... | 157 |
| Figure 5.12: Loading profiles – T-slot stand impactors | 160 |
| Figure 5.13: Loading profiles – handheld impactors | 161 |
| Figure 5.14: Peak impact force vs. actuation voltage – handheld impactors..... | 162 |
| Figure 5.15: Contact time vs. actuation voltage – handheld impactors | 162 |
| Figure 5.16: Raw velocity profiles – T-slot stand impactors | 163 |
| Figure 5.17: Transient temperature profiles of various components of 10 <i>g</i> handpiece under worst-case normal use | 164 |
| Figure 5.18: Time domain signals – silicone; DC; 12 <i>V</i> ; handheld..... | 166 |
| Figure 5.19: Time domain signals – silicone; GV; 12 <i>V</i> ; handheld..... | 166 |
| Figure 5.20: Frequency domain signals – silicone; DC; handheld | 167 |
| Figure 5.21: Frequency domain signals – silicone; GV; handheld | 168 |
| Figure 5.22: Amplitude ratio – silicone interface; handheld impactors..... | 169 |
| Figure 5.23: Mode 1 amplitude – silicone interface; handheld impactors..... | 169 |
| Figure 5.24: Band power – silicone interface; handheld impactors..... | 170 |
| Figure 5.25: ASIST and Osstell Comparison – Journal of Prosthetic Dentistry [55]. Different installations represent different interface stiffnesses; abutment length shown in legend | 172 |
| Figure 5.26: 1D finite element model GUI..... | 173 |
| Figure 5.27: Full range boxplot of silicone interface stiffness estimates..... | 174 |
| Figure 5.28: Reduced range boxplot of silicone interface stiffness estimates | 174 |
| Figure 6.1: Benchtop validation experiment setup | 183 |
| Figure 6.2: 10 <i>g</i> handpiece. Left, steel tip configuration; right, PEEK tip configuration..... | 183 |
| Figure 6.3: Medial (3:00) strike position on distal screw | 184 |
| Figure 6.4: Participant operating handpiece | 185 |
| Figure 6.5: Matching protocol flow chart. Blue text, sequential step; green text, classification step; orange text, ‘if’ statement with true outcome leading down flow chart and not true outcome leading to next horizontal statement | 188 |
| Figure 6.6: Matching window – silicone; 68.5 <i>mm</i> DC; GV off; 30 <i>g</i> rod; steel tip | 189 |
| Figure 6.7: Matching window – silicone; 68.5 <i>mm</i> DC; GV off; 10 <i>g</i> rod; PEEK tip..... | 190 |

| | |
|---|-----|
| Figure 6.8: Matching window – superglue; 68.5 <i>mm</i> DC; GV off; 30 <i>g</i> rod; steel tip | 191 |
| Figure 6.9: Matching window – superglue; 68.5 <i>mm</i> DC; GV off; 10 <i>g</i> rod; steel tip | 191 |
| Figure 6.10: Matching window – paraffin wax; 68.5 <i>mm</i> DC; GV off; 10 <i>g</i> rod; steel tip | 192 |
| Figure 6.11: Matching window – paraffin wax; 68.5 <i>mm</i> DC; GV on; 10 <i>g</i> rod; steel tip; raw signal | 193 |
| Figure 6.12: Matching window – paraffin wax; 68.5 <i>mm</i> DC; GV on; 10 <i>g</i> rod; steel tip; notch filter | 195 |
| Figure 6.13: Predicted by observed plot for gamma regression on data from raw signals | 198 |
| Figure 6.14: Weighted fixed effects for gamma regression on data from raw signals (thicker line represents greater effect) | 200 |
| Figure 6.15: Interface stiffness estimates for gamma regression on data from raw signals | 201 |
| Figure 6.16: Interface stiffness by impact rod for gamma regression on data from raw signals | 202 |
| Figure 6.17: Interface stiffness and impact rod interaction estimates for gamma regression on data from raw signals | 202 |
| Figure 6.18: Weighted fixed effects for binary probit regression on data from raw signals (thicker line represents greater effect) | 205 |
| Figure 6.19: Match correctness estimates for binary probit regression on data from raw signals | 206 |
| Figure 6.20: Match correctness by impact rod for binary probit regression on data from raw signals | 207 |
| Figure 6.21: Interface stiffness and impact rod interaction estimates for binary probit regression on data from raw signals | 207 |
| Figure 6.22: Predicted by observed plot for gamma regression on data from notch filter signals | 208 |
| Figure 6.23: Weighted fixed effects for gamma regression on data from notch filter signals (thicker line represents greater effect) | 210 |
| Figure 6.24: Interface stiffness estimates for gamma regression on data from notch filter signals | 211 |
| Figure 6.25: Interface stiffness by impact rod for gamma regression on data from notch filter signals | 212 |

| | |
|--|-----|
| Figure 6.26: Interface stiffness and impact rod interaction estimates for gamma regression on data from notch filter signals | 212 |
| Figure 6.27: Weighted fixed effects for binary probit regression on data from notch filter signals (thicker lines represent greater effects) | 215 |
| Figure 6.28: Match correctness estimates for binary probit regression on data from notch filter signals | 216 |
| Figure 6.29: Match correctness by impact rod for binary probit regression on data from notch filter signals | 217 |
| Figure 6.30: Interface stiffness and impact rod interaction estimates for binary probit regression on data from notch filter signals | 217 |
| Figure 6.31: Results summary for raw signals..... | 219 |
| Figure 6.32: Results summary for notch filter signals..... | 220 |
| Figure 6.33: Matching window – paraffin wax; 88.5 <i>mm</i> DC; GV off; 10 <i>g</i> rod; steel tip; notch filter..... | 220 |
| Figure 6.34: Impact hammer used in modal tests | 222 |
| Figure 6.35: Sawbones thigh setup | 223 |
| Figure 6.36: Position 4 modal measurements | 225 |
| Figure 6.37: Signals from accelerometer placed in various positions on implant and composite femur | 226 |
| Figure 6.38: Signals acquired to test presence of transverse noise without GV connector installed | 228 |
| Figure 6.39: Signals acquired to test presence of transverse noise with GV connector installed – bone clamp setup..... | 229 |
| Figure 6.40: Signals acquired to test presence of transverse noise with GV connector installed – Sawbones thigh setup..... | 230 |
| Figure 6.41: Summary plot of modal tests..... | 231 |
| Figure 6.42: Phase analysis setup | 233 |
| Figure 6.43: Phase analysis – 10 <i>g</i> impact rod with steel tip | 234 |
| Figure 6.44: Phase analysis – 10 <i>g</i> impact rod with PEEK tip | 235 |
| Figure 6.45: Phase analysis – 30 <i>g</i> impact rod with steel tip | 236 |
| Figure 6.46: Phase analysis – 30 <i>g</i> impact rod with PEEK tip | 236 |

| | |
|---|-----|
| App. Figure B.1: Impact force of 12 <i>g</i> rod with 5 <i>kg</i> HF electromagnet (neodymium magnet length – actuation time in legend)..... | 254 |
| App. Figure B.2: Impact force of 12 <i>g</i> rod with 15 <i>kg</i> HF electromagnet (neodymium magnet length – actuation time in legend)..... | 255 |
| App. Figure B.3: Impact force of 12 <i>g</i> rod with 25 <i>kg</i> HF electromagnet (neodymium magnet length – actuation time in legend)..... | 255 |
| App. Figure B.4: Impact force of 44 <i>g</i> rod with 5 <i>kg</i> HF electromagnet (neodymium magnet length – actuation time in legend)..... | 256 |
| App. Figure B.5: Impact force of 44 <i>g</i> rod with 15 <i>kg</i> HF electromagnet (neodymium magnet length – actuation time in legend)..... | 256 |
| App. Figure B.6: Impact force of 44 <i>g</i> rod with 25 <i>kg</i> HF electromagnet (neodymium magnet length – actuation time in legend)..... | 257 |
| App. Figure C.1: Power spectrum of superglue interface setup. GV connector struck transversely with 50 <i>g</i> impact rod | 258 |
| App. Figure C.2: Power spectrum of superglue interface setup. GV connector struck transversely with 60 <i>g</i> impact rod | 259 |
| App. Figure C.3: Power spectrum of superglue interface setup. GV connector struck transversely with 70 <i>g</i> impact rod | 259 |
| App. Figure C.4: Power spectrum of superglue interface setup. GV connector struck transversely with 90 <i>g</i> impact rod | 260 |

Chapter 1 Introduction

1.1 Background

1.1.1 Motivation

Transfemoral amputation is the removal of the leg by transection of the femur and distal tissues, with reconstruction of the soft tissues around the bone end [1]. Lower limb amputations commonly result from complications associated with peripheral vascular disease, diabetes, trauma, or bone cancer [2]. In 2005, there were approximately 1.6 million people with amputations in the U.S. (1 in 200), and the population was expected to double by 2050 [3, 4]. Socket fittings have been the standard method of prosthetic attachment to the residual limb [1, 3, 5, 6, 7, 8, 9, 10]; it is estimated that 86% of lower extremity amputation patients have a socket prostheses, with 34-63% having chronic skin problems and associated pain [7, 10]. Despite the prevalence of socket attachments, there are pervasive issues with soft tissue breakdown, residual limb pain, unreliable socket suspension, difficulty donning and doffing, and biomechanical gait deviations [8]. Studies have shown that one-quarter to one-third of persons with transfemoral amputations consider themselves to have poor quality of life [9]. Percutaneous transfemoral implants offer a remedy to many of the shortcomings of socket prostheses [7]. During the implantation procedure, one end of a titanium implant is inserted into the intramedullary canal of the residual femur, and the other end traverses a surgically fashioned stoma, providing a point for prosthetic attachment. The implant becomes integrated with the skeletal system through a process known as osseointegration [11]. Benefits of osseointegrated prostheses have been self-reported by users and supported by functional outcome studies [7, 9, 10]. Studies have reported improved quality of life, prosthesis use, body image, comfort, ease of donning and doffing, and gait biomechanics [8, 9, 10]. The earliest implantation surgeries were performed by Brånemark in 1990 with the Osseointegrated Prosthesis for the Rehabilitation of Amputees (OPRA) system [12]. OPRA implants achieve mechanical stability through screw-fixation [3]. The Integral Leg Prosthesis (ILP) and Osseointegrated Prosthetic Limb (OPL) systems are more modern press-fit implants. A 2018 review of complications in bone-anchored prostheses for extremity amputation reported that implant infection occurred in 2-11% of screw and 0-3% of press-fit transfemoral implants; implant loosening occurred in 6% of screw and 0-3% of press-fit transfemoral implants; and intramedullary device breakage occurred in 0%

of screw and 1% of press-fit transfemoral implants [13]. A more recent study (2024) reported survival rates of screw-fit implants from 72% to 92% and 78% to 99% for press-fit implants [10]. Although rare, major complications and failure of the implant to integrate can be catastrophic, necessitating removal of the implant. Currently, there is no reliable prognostic tool for early detection of implant loosening and failure.

1.1.2 Vibration Assessment

The stability of osseointegrated implants is determined by the biomechanical properties of the bone-implant interface (BII) [14]. Successful post-operative healing is defined by mature bone growth into the bonding region of the implant, which forms the BII [14]. Vibration assessment is premised on the idea that the bone-implant interface stiffens during osseointegration, raising the natural frequencies of the bone-implant system over time [15]. In general, the natural frequencies of a bone-implant system can be extracted in two ways:

1. Performing a sine sweep, where the system is coupled to a shaker that applies an oscillating load across a range of frequencies. In this case, natural frequencies are identified at resonances.
2. Applying a broadband impulse which excites the system into transient free vibration. Frequencies may then be extracted through Fourier transform.

The natural frequencies of a bone-implant system rely on the inertial and geometric properties of the implant as well as the stiffness of the BII. The Advance System for Implant Stability Testing (ASIST) implements a multiple impulse method in conjunction with an analytical model of the bone-implant system [16]. The model accounts for the inertial and geometric properties of the implant [16]. The ASIST matches raw acceleration signals from a modified Periotest (commercially available dental percussion instrument) handpiece to an analytical model through a numerical optimization routine [16]. The ASIST approach has been promisingly applied to natural teeth [17], dental implants [18], and bone-anchored hearing aids [16]. A handful of other research and commercial devices exist for these small systems, such as the Osstell, which utilizes resonance frequency analysis, but there is currently no vibration-based tool for transfemoral implant stability assessment or evaluation of larger orthopaedic implants in general.

The first attempt at a resonant frequency measurement system for osseointegrated transfemoral implants was made in 2005 [19]. The first full investigation of vibration assessment for transfemoral implants was published in 2007 by the same group (Shao et al.) [20]. The results showed a positive linear correlation between dominant natural frequency and BII elastic modulus [20]. In vivo testing with one patient showed an initial decrease in dominant natural frequency after weightbearing followed by increases up to 38 days [20]. From 2011 to 2012, Cairns published a series of papers on the ability of modal analysis to detect osseointegration in transfemoral amputees [21, 22, 23]. In the last publication, natural frequencies and mode shapes of a benchtop transfemoral amputation (TFA) model were found to change in response to insertion torque, boundary condition, and model orientation [23]. The paper demonstrated the potential of modal analysis for use in transfemoral implant stability assessment [23]. In 2022, two papers were published by Lu et al. investigating vibration assessment of transfemoral implants. In the first paper, a vibration related ‘E-index’ was introduced [24]. The second paper showed that E-index increased and eventually plateaued with epoxy resin curing time (simulating rapid osseointegration), evidencing the sensitivity of the approach to increasing interface stiffness [25]. These studies broadly demonstrated the potential of vibration analysis, but none developed a comprehensive approach to isolate the mechanical properties of the bone-implant interface.

In 2022, Mohamed created the first 3D and 1D finite element models of a transfemoral implant system [26]. His work was a part of a larger project, continued here, to extend the ASIST approach to transfemoral implants. The 1D finite element model approximated the behaviour of elongated transfemoral implants better than a traditional analytical model [26]. In 2024, a full investigation was published by Mohamed et al. with experimental validation [27]. An OPL implant was anchored in a Sawbones composite femur with either silicone, paraffin wax, or superglue, simulating low, intermediate, and high interface stiffness conditions respectively [27]. The response of the system to axial strikes by a Periotest handpiece was recorded with a uniaxial accelerometer [27]. The first axial mode was found to be highly sensitive to changes at the bone-implant interface; however, the Periotest handpiece had difficulty exciting the first axial mode in the low interface condition [27]. This caused the low and high conditions to have similar appearances in the frequency domain [27]. Mohamed concluded that the approach would need a revamped impactor to consistently trigger the first axial mode of vibration across all interface stiffness conditions [27].

1.2 Objectives

Following the recommendations of Mohamed [27], the primary objective of this thesis was the development of an impactor for osseointegrated transfemoral implant stability assessment. The impactor should integrate with the approach developed by Mohamed [26, 27, 28] and provide sensitivity in the full interface stiffness range. This means that the impactor should be capable of adequately exciting the first axial mode of vibration of the OPL implant system for a low stiffness interface condition (simulating fibrous tissue formation). It should also be reliable, safe, handheld, and meet all necessary standards for clinical research deployment. Summarizing, the objectives of this thesis were to:

5. Develop an impactor for osseointegrated transfemoral implant stability assessment.
6. Integrate the impactor with the approach developed by Mohamed [28].
7. Enhance the sensitivity of the approach in the full interface stiffness range.
8. Validate the safety, reliability, and sensitivity of the integrated approach.

An evidence base was developed for design decisions made during development, and lastly, the sensitivity and reliability of the impactor was validated in an experimental study with multiple operators.

1.3 Thesis Outline

The background and study objectives of this thesis are presented in Chapter 1. Chapter 2 presents a thorough literature review, where transfemoral amputation is defined and the prevalence of the procedure is detailed; shortcomings of traditional socket-fitting methods are juxtaposed by the benefits of osseointegrated transfemoral reconstruction; and various implant systems are characterized and associated protocols are outlined. The history, physiology, and biomechanics of osseointegration are described in detail before the crux of the review is reached in implant stability assessment. Destructive and non-destructive methods are explored, and the chapter is concluded by a review of vibration approaches to transfemoral implant stability assessment. Chapter 3 details the development process of the initial benchtop prototype impactor and broadly explores the factors influencing impact response and signal composition from a modal analysis perspective. A simple impact model is also developed. The chapter concludes by making recommendations for factors and associated levels that should be tested in a prospective development and evaluation

study. Chapter 4 details the evaluation of the benchtop impactor system, which involves a systematic analysis of design variables. An evidence base is developed for impactor design specifications and initial validation is presented. Chapter 5 takes the recommendations of Chapter 4 and details the design and manufacture of two handheld impactors. Additionally, clinical standards are developed, and a series of tests are outlined that tie into the decision to deploy the 30 *g* impactor in a parallel clinical study. The chapter concludes with the design of the final experiment. Chapter 6 contains the details of the final experimental validation study. Several experimental protocols are detailed, and the results are discussed in the context of device validation. A final recommendation is made between the handpieces and remedies to the major limitations of the study are explored. Significance, limitations, and future work of the project are explored in Chapter 7.

Chapter 2 Literature Review

2.1 Transfemoral Amputation

2.1.1 Anatomy

Transfemoral, or sometimes referred to as above-knee, amputation is the removal of the leg via transection of the femur and surrounding tissues [1]. It may be performed across the distal aspect of the femur (supracondylar), middle section of the femur (diaphyseal), or just below the lesser trochanter (high transfemoral) [29]. In general, preserving femur length improves the success of post-operative prosthetic fitting [29]. The major challenge of transfemoral amputation is the reconstruction of the residual limb to preserve optimal biomechanics and gait [6]. Transecting the femur can give rise to muscle imbalances, as residual flexors and abductors may overpower residual extensors and adductors [6, 29]. Surgeons manipulate tissues to balance muscle groups and position the femur for weight-bearing and ambulation [6]. Transfemoral amputation is a major surgical procedure with significant physical, physiological, and psychological stressors [1]. Interdisciplinary teams are often involved in the process to guide patients through the challenges of surgery and post-operative recovery [1].

2.1.2 Prevalence

Lower limb amputations commonly result from complications associated with peripheral vascular disease, diabetes, trauma, congenital limb defects, or bone cancer [2]. Peripheral arterial disease is the leading cause of all major lower extremity amputations [30]; moreover, complications associated with diabetes are the main reason for lower limb amputations in industrialized nations [2, 31]. Although diabetes is a risk factor for peripheral arterial disease, it can also be a cause of lower extremity amputations without the pathology [30]. In some cases, amputations may progress over time. Approximately 25% of individuals with dysvascular disorders require another amputation within a year of the initial procedure [4]. Furthermore, foot and ankle amputations often advance to higher levels of limb loss or contralateral amputation, and diabetic patients are more likely to experience progression than non-diabetic patients [4]. Although vascular disease is a major cause of amputation, it is a greater risk factor among elderly people; for young persons, trauma and tumor resection have been the primary reasons for amputation [8]. Trauma is

responsible for 8% of lower limb amputations and is the most common cause for people in their second or third decade of life, while cancer accounts for approximately 0.8% of total amputations and is the top cause for individuals 10 to 20 years of age [4]. Global censuses of persons with amputations have been difficult to establish due to inconsistencies in national reporting [3, 4]. However, it is estimated that over 150,000 people undergo amputations secondary to peripheral vascular disease or diabetes each year [4]. In 2005, there were approximately 1.6 million people living with amputations in the U.S. (1 in 200), and the population was expected to double by 2050 [3, 4]. Within the population, approximately 65% had a lower limb amputation [4] and 19% had an amputation at the transfemoral level [5]. According to more recent studies, the population has been estimated at 1.7 million (1 in 190), evidencing predicted increases [8]. In Canada, the average age-adjusted rate of lower limb amputation was estimated to be 22.9 in 100,000 from 2006 to 2012 [2]. Projections of prevalence increases, especially in the U.S., may be attributed to an aging population and high rates of peripheral vascular disease [8, 30]. It is worth noting that overarching amputation trends may not have a one-to-one correlation with specific procedures. In 2004, 31% of all major amputations were performed at the transfemoral level, but there is some evidence that rates of transfemoral amputation are declining [5, 6]. This is undoubtedly because amputation practices have evolved toward limb sparing interventions [6]. At any rate, lower limb amputations are tremendously disabling and expensive, with costs associated with acute and post-acute care exceeding \$4 billion in the U.S. annually [2]. Persons with amputations are also living longer and require prosthetic care throughout their lives [5]. After an amputation, the individual is often fit with a prosthesis to restore mobility.

2.1.3 Prosthetic Attachment

2.1.3.1 Socket Fittings

Transfemoral prosthetic designs have an extensive history, with the first patents awarded in England in 1790 and the first U.S. patent published in 1846 [5]. Socket fittings have been the traditional method of prosthetic attachment to the residual limb [1, 3, 5, 6, 7, 8, 9]. It is widely accepted that there is no universal design for transfemoral socket prostheses; instead, practitioners endeavor to meet the individual needs of their patients and often develop unique approaches to the craft [5]. Among abundant design choices, prosthetists and patients may make decisions related to thigh coverage and support, socket materials and flexibility, and type of suspension system

implemented [5, 6]. The prosthesis should be comfortable and restore mobility, improving quality of life. The ideal socket prosthesis offers full contact and support of the residual limb in weightbearing and can accomplish the swing phase of gait with near conventional biomechanics [5]. The function of the socket itself is to respond to the intermediary soft tissues of the residual limb, facilitating control of the prosthetic limb and transferring force through the lower kinematic chain to the ground [9]. Unfortunately, many prosthetics fall short of this ideal and perceived drawbacks sometimes lead to abandonment of the prosthesis [1, 5, 7]. It is estimated that 86% of lower extremity amputation patients are fitted with socket prostheses, with 34-63% having chronic skin problems and pain associated with the socket [7]. Despite the prevalence of socket attachments, there are pervasive issues with soft tissue breakdown, residual limb pain, unreliable socket suspension, difficulty donning and doffing, and biomechanical gait deviations [8]. Broad discomfort, mobility limitations, and overall dissatisfaction have also been reported [9]. Studies have shown that this culminates in one-quarter to one-third of persons with transfemoral amputations considering themselves to have poor quality of life [9]. In the worst case, an individual may reject their prosthetic limb entirely [1, 5, 7].

2.1.3.2 Osseointegrated Implants

2.1.3.2.1 Overview

One remedy to socket-related problems is the adoption of a percutaneous implant to the residual limb [7]. In this approach, one end of an implant is inserted into the intramedullary canal of the residual femur, while the other end projects through a stoma in the distal limb, providing a port for prosthetic attachment. The implant becomes integrated with the skeletal system through a process known as osseointegration [11]. Although methodological shortcomings have been found in several clinical studies [7, 13] there is an ever-increasing body of evidence demonstrating the benefits of osseointegrated prostheses [3, 7, 8, 9]. Benefits of osseointegrated prostheses have been self-reported by users and supported by functional outcomes [7, 9]. Most users of osseointegrated prostheses were enrolled in a clinical study after years of socket prosthesis use, affording them a direct framework for comparison [7, 9]. Studies have reported improved quality of life, prosthesis use, body image, comfort, ease of donning and doffing, and osseoperception [8, 9]. At 15 years follow up, approximately 64% of patients reported that osseointegration improved their overall situation [10]. Additionally, biomechanical benefits have been proposed such as improved hip

range of motion and walking ability [8, 9]. Intuitively, a bone anchored prosthesis interfacing directly with the skeletal system provides greater loading and kinematic continuity than a socket prosthesis. As a result, it has been shown that osseointegrated prostheses may facilitate bone density increases in patients with local disuse osteoporosis [32]. Of course, bone-anchored prostheses are not without complications and drawbacks. Superficial skin infections at the stoma site have been observed as the most common complication, and deep infections necessitating removal of the implant have been reported less frequently [9, 13]. Major complications include implant infection and loosening and intramedullary device breakage, but these are rare [13]. Minor complications, such as soft tissue irritation and infection, may be common but decreasing rates have been observed with advances in implant design, surgical practice, and rehabilitation protocols [9, 13].

2.1.3.2.2 Systems

Several implant systems have been developed including the Osseointegrated Prosthesis for the Rehabilitation of Amputees (OPRA, Integrum, Sweden), Endo-Exo Femoral Prosthesis (EEFP, ESKA Orthopaedic, Germany), Integral Leg Prosthesis (ILP, Orthodynamics, Germany), Osseointegrated Prosthetic Limb (OPL, Permedica, Italy), Percutaneous Osseointegrated Prosthesis (POP, DJO Global, USA), Compress Device (Zimmer Biomet, USA), and Intraosseous Transcutaneous Amputation Prosthesis (ITAP, Stryker Orthopaedics, USA) [3, 7, 8, 9]. Of the devices, the OPRA, ILP (evolved from EEFP), and OPL (evolved from ILP) systems have been the most extensively evaluated in clinical studies [9]. The earliest implantation surgeries were performed by Brånemark in 1990 with the developing OPRA system, but it wasn't until 1999 that a comprehensive surgical and rehabilitation protocol was implemented [12]. Between 1990 and 2008, 100 patients were treated under the OPRA protocol or preliminary versions [12]. The total treatment time from first surgery to unrestricted prosthesis use was typically 12 to 18 months [12]. One of the conclusions of the study was that implementation of a comprehensive and meticulous surgical and rehabilitation protocol may durastically improve clinical outcomes of bone-anchored prosthesis patients [9, 12]. OPRA implants achieve mechanical stability through screw-fixation, a design that is also popular among smaller osseointegrated implants (e.g., dental implants) [3]. Screw-fixation is generally more mechanically effective than press-fixation, allowing the implants to have the same separation resistance with smaller contact areas [8]. This may be advantageous for short residual femurs (smaller implant lengths are possible) and achieving high primary

stability; however, torsional stability may be limited, and bone resorption may result from stress concentrations around the implant's threads (stress shielding) [8]. The ILP and OPL devices are more modern press-fit implant systems. Primary stability after implantation is achieved through interference with the walls of the intramedullary canal, and porous coatings allow bone ingrowth [3, 8]. Fundamental differences between the implant systems include the implantation process and construction materials. The ILP system requires a two stage implantation process (like the OPRA system), where the implant is first inserted into the femur with a distal plug and the wound is fully closed [3, 8]. In a second procedure, a stoma is created and a dual cone adapter is installed percutaneously [3, 8]. Conversely, the OPL system was designed for single stage implantation and was the first available of its kind [3, 8]. The ILP implant is manufactured from cobalt-chromium-molybdenum alloy and has overlaid 1.5 mm Czech hedgehogs, while the OPL implant is manufactured from titanium alloy with a 0.5 mm plasma-sprayed coating [3, 8]. The implant stem surface treatments form 3D matrices that synthetically model cancellous bone and promote osseointegration [3, 8]. On both implants, surfaces that may come into contact with soft tissues are coated with polished titanium-niobium-oxynitride ceramic to prevent abrasion and infection [3, 8]. OPL system components can be viewed in Figure 2.1.

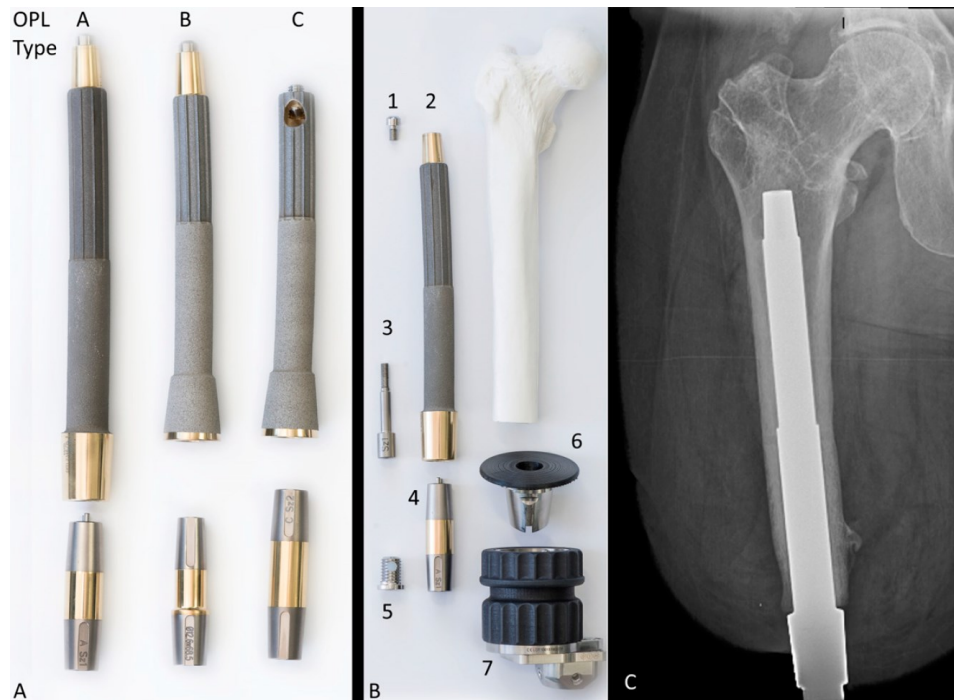


Figure 2.1: OPL implant system components with x-ray image of implantation [3]

The Osseointegration Group of Australia, led by Al Muderis, developed two notable protocols for osseointegrated reconstruction of amputated limbs with the ILP and OPL implant systems: Osseointegration Group of Australia Accelerated Protocol (OGAAP) -1 and -2. Under OGAAAP-1, the time from first surgery to unaided walking was approximately 4.5 months, a significant timeline reduction from the OPRA protocol [33]. The second protocol, OGAAAP-2, built off lessons learned from the first and implemented single-stage osseointegrated reconstruction with the OPL system [34]. OGAAAP-2 dramatically reduced total treatment time again to 3-6 weeks (depending on the prescribed loading protocol) [34]. Osseointegrated prostheses have presented numerous benefits to individuals with transfemoral amputations with the main complications being superficial infections due to the open stoma; major complication rates have remained generally low for all implant systems. In a 2018 review of complications in bone-anchored prostheses for extremity amputation [13], data extracted from 12 cohort studies demonstrated that implant infection occurred in 2-11% of screw and 0-3% of press-fit transfemoral implants; implant loosening occurred in 6% of screw and 0-3% of press-fit transfemoral implants; and intramedullary device breakage occurred in 0% of screw and 1% of press-fit transfemoral implants. A more recent review (2024) reported survival rates of screw-fit implants from 72% to 92% and 78% to 99% for press-fit implants [10]. High survival rates could be further improved by the advent of devices for early detection of implant loosening and failure.

2.2 Osseointegration

2.2.1 History

Prosthetics have been implemented in myriad ways since antiquity, but transcutaneous osseointegration for amputees (TOFA) was first achieved at the tail end of the 20th century [35, 36]. Bothe first investigated titanium as a biocompatible material in 1940; he observed the proclivity of bone to grow in contact with titanium alloy [35]. Maurice Down is credited with the first application of titanium for fracture fixation in 1947, and in 1951, after observing titanium screws tighten in rabbit bone, Leventhal conjectured the aptness of titanium for bone-anchored prostheses [35, 36]. These advances occurred around the 1940s as titanium was first becoming a reasonably available metal [35]. In 1952, Per-Ingvar Brånemark independently observed the same anchorage of titanium screws in rabbit bone and found no evidence of fibrous tissue formation from light microscopy analysis [35, 37]. The titanium oxide layer of the implants would become

fused with ingrown bone to the degree that separation was impossible without fracture [11]. Following canine experiments, Brånemark was the first to apply titanium screw-fixations as long-term dental implants (1965) [35, 36, 37]. In 1977, he coined the term ‘osseointegration,’ originally referring to the growth of bone onto an implant with no interposing fibrous tissue [35, 37, 38]. After the discovery of fibrous tissue at greater microscope magnification levels, the definition was shifted from a histologic to biomechanical perspective; osseointegration became viewed as the process whereby synthetic materials become rigidly and terminally fixed in bone during functional loading [11, 35, 37]. The concept of osseoperception sprang from the work of Haraldson in 1979, where he characterized sensory feedback in patients with osseointegrated dental bridges [11]. The phenomenon continues to be studied and exploited as a serendipitous consequence of osseointegrated prostheses [11]. In the decades since the first human implementation of osseointegration (dental implants), dozens of applications have been investigated, including facial prostheses, bone-anchored hearing aids, finger joint prostheses, thumb amputations, and lower limb amputations [11]. In 1990, Per-Ingvar’s son, Rickard Brånemark, performed the first successful osseointegrated reconstruction surgery for transfemoral amputation [12].

2.2.2 Physiology

2.2.2.1 Osteoconduction

To fully grasp the physiology of osseointegration, it is imperative to have a basic understanding of the backing materials science and metallurgy. To start, metals react with their external environment to develop a passive steady state surface composition; this is known as passivation [35]. Titanium alloys passivate to form stable titanium oxide (TiO_2) on their surface, which persists in vivo [35]. It has been suggested that oxide growth even occurs on titanium implants exposed to biological tissues [11]. The formation of titanium oxide may be catalyzed by proteolytic enzymes, cytokines, superoxide, and hydrogen peroxide excreted by inflammatory cells, especially macrophages [11]. It has also been hypothesized that the titanium oxide layer transitions to a hydrated titanium peroxy matrix, which interfaces with the surrounding bone [11]. This type of matrix formation is unique to titanium among other metals [11]. Titanium does not upregulate or downregulate any cellular process to promote bone growth; rather, it is bioinert, resisting interference with the interdigitation of bone formation [35]. Other materials have demonstrated similar conduciveness to osseointegration, namely Cerosium® (ceramic) and cobalt chromium [35, 38]. For successful

integration, it is necessary for the implant material to be appropriately porous. It has been shown that bone grows fastest into channels between 500 and 1000 μm in diameter, and a 95 μm channel may not experience ingrowth at all [35]. Other studies have suggested that implants with 50 – 400 μm pores and roughened surfaces are most effective at promoting ingrowth, stabilizing the bone-implant interface [38]. It has also been shown that lower-extremity osteons (functional unit of bone) are approximately 246 μm in diameter [35]. Accordingly, inorganic channels that are too small to support an osteon will not experience bone ingrowth, while larger channels take longer to fill [35]. Surface roughness is also an important factor, with suggestions of $\geq 20 \mu\text{m}$ [35] and 4 – 7 μm [38] both being advanced. The latter range was posited as being necessary for proper osteoblast cuboid morphology [38]. Historically, titanium has been the material of choice for osseointegrated implants and has realized immense success in clinical implementation. It is uniquely cooperative with bone, a property that has been touted as ‘osteoconduction.’ It should be noted that although implant porosity, roughness, topography, and surface energy all play a role in the osteoconductive potential of a material, implant shape and design are also important for overall success [38].

2.2.2.2 Interface Evolution

The process of osseointegration involves several tissue evolutions: hematoma, mesenchymal tissue, intramembranous (woven) bone, and lamellar bone [39]. The first stage is the formation of a hematoma, which occurs within one hour of implantation [14, 39]. Bleeding caused by reaming the intramedullary cavity and implant insertion results in red blood cells, platelets, and inflammatory cells adhering to the surface of the implant [14, 39]. These cells cause coagulation and initiate a chemical cascade [14, 39]. Fibroblasts are among the first tertiary response cells to be recruited; their primary function is to build a fibrin matrix [40]. The matrix serves as an osteoconductive (allowing bone growth) and osteoinductive (stimulating osteogenic cells to produce bone) scaffold around the implant [39]. Granulation tissue formation begins within two hours of surgery [39]. Within 24 hours, the fibrin matrix starts to transform into poorly mineralized osteoid tissue, forming a $\sim 0.5 \text{ mm}$ thick layer around the implant [14, 39]. During this process, macrophages stimulate wound vascularization, migration of mesenchymal stem cells, and the clearing of dead tissue [39]. Osteoblasts gradually calcify the osteoid tissue, synthesizing a dense collagen matrix and facilitating the deposition of hydroxyapatite crystals [14, 39, 40]. Non-calcified spaces become occupied with endothelial and mesenchymal stem cells, which encourage

vascularization of the osteoid [39]. Bone fragments created during implantation are incorporated into the forming interface [14, 39]. Osteogenesis (formation of bone) simultaneously occurs at the surfaces of the implant and intact bone [39]. The interposing mineralized osteoid tissue evolves again into woven bone, providing the first hints of secondary stability between the implant and bone [14, 39]. New bone formation begins as soon as 10 days after surgery [39]. The woven bone provides a scaffold for cellular attachment and further bone deposition, eventually remodelling into compact lamellar bone at approximately three months [39, 40]. In the final morphology of the bone-implant interface, osteons encircle and are axially aligned (parallel) with the implant [39]. Osseointegration has reached its last stage when the BII resembles mature bone [14]. The BII can extend up to 1 *mm* from the implant surface and contains mesenchymal stem cells, osteoblasts, osteoclasts, and supporting vasculature, innervation, and lymphatic vessels [39]. However, interface formation is a dynamic process that requires constant maintenance and adaptation to functional loading, which is mediated by osteoblast and osteoclast activity (coupling) [14, 37]. In fact, osseointegration is sometimes divided into three stages: woven bone formation, lamellar bone formation (adaption of bone mass to load), and remodelling (adaption of bone structure to load) [37]. Or in a different view: formation of unmineralized osteoid tissue, formation of mineralized osteoid tissue and woven bone, and remodelling of woven bone into mature bone [14].

2.2.3 Biomechanics

2.2.3.1 Bone-Implant Interface

The stability of osseointegrated implants is determined by the biomechanical properties of the bone-implant interface [14]. Ideal post-operative healing leads to direct and comprehensive contact between lamellar bone and the bonding region of the implant, which presents the highest stability case [14]. As noted in Section 2.1.3.2.2, transfemoral implants may be screw- or press-fixated into the residual femur during implantation. Here, primary, or mechanical, stability is first attained [14, 39]. Primary stability is defined as the stability of the implant immediately after surgery, before healing and the formation of the bone-implant interface [14, 39]. This initial stability primarily owes to the frictional properties of the bone-implant interface without bone ingrowth and is highly dependent on the stresses introduced during surgery [14, 39]. Other factors affecting primary stability include the design and texture of the implant, loading, and quality of surrounding bone [39]. Several studies have suggested the critical role of primary stability in long-term success [14].

Sufficient primary stability must be achieved to limit micromotion, as excessive micromotion has been correlated with implant migration, loosening, and failure [14]. It is hypothesized that low amplitude micromotions stimulate bone remodelling, with motion $\leq 40 - 70 \mu m$ allowing for bone ingrowth [14]. Excessive micromotion ($\geq 150 \mu m$) has been linked to fibrous tissue (0.5 – 2.0 *kPa*) formation (fibroplasia) instead of stiff osseointegrated bone, especially in dental implants [14, 38, 39]. The formation of a fibrous tissue interface can be disastrous, initiating a micromotion feedback loop and potentially preventing osseointegration [14, 38, 39]. Conversely, excessive stresses introduced at implantation may lead to bone fracture or necrosis [14, 38, 39]. Over time, bone growth and remodelling gradually introduce greater stability to bone-implant system. However, the spatial-temporal mechanical properties of the bone-implant interface remain highly heterogenous for several months [14]. Continued osseointegration and mature bone ingrowth ideally lead to continuity and mechanical interlocking between remote layers of bone formed during osteogenesis at the implant surface and intramedullary wall [14]. Ultimately, post-operative healing/osseointegration introduces secondary, or biological, stability as a function time [14, 39]. Temporal secondary stability may be nonlinear, often decreasing in dental and craniofacial implants immediately after implantation [14]. Periodic variability may be observed due to complications (e.g., infection) or general heterogeneity in the healing process. The initial dip has been attributed to osteoclast activity as the interface remodels to form progressively stiffer bone [14]. Secondary stability is required for long-term success of the implant [39]. It should be noted that much of the literature on bone-implant interfaces stems from investigations of dental implants [14, 39]. Dental and craniofacial implants represent systems of far smaller scale and different surrounding bone type (flat or irregular bone) than orthopaedic applications (long bones). Different bone types are associated with variations in cortical, cancellous, and marrow composition; bone mass density; and load tolerance. There is even debate on the degree to which osseointegration occurs for orthopaedic implants, and there is some evidence that fibrous tissue forms at the BII of the implants [14]. However, cementless orthopaedic implants have good clinical outcomes [14]; the potential of osseointegrated transfemoral implants has already been discussed at length in Section 2.1.3.2. At the very least, osteogenesis likely occurs at some distance from the implant surface [14].

2.2.3.2 Titanium Implants

It is worth noting that titanium alloys present several biomechanical advantages compared to other implant material choices. Pure titanium has an ultimate tensile strength of 434 *MPa*, insufficient for adult weightbearing, while titanium alloyed with 6% aluminum and 4% vanadium (Ti6Al4V) has an ultimate tensile strength of 950 *MPa*, improving its fitness for implantation [35]. Furthermore, Ti6Al4V has an elastic modulus of 110 *GPa*, while other common orthopaedic choices, such as 316 stainless steel and cobalt chromium, have elastic moduli of 190 and 230 *GPa*, respectively [35]. Cortical bone is both anisotropic and highly susceptible to variation along human demographic lines, having a Young's modulus ranging from 3 to 20 *GPa* [35]. Implants with a comparatively high Young's modulus can cause stress shielding in cortical bone [14], making materials with more closely matched elastic moduli better options. Accordingly, titanium is a more attractive choice for osseointegrated prostheses than other alloyed metals [35]. Stiffer orthopaedic implants can cause stress concentrations near the implant, leading to bone mineral loss [14]. This is known as stress shielding [14]. The causal mechanism is that stiff materials may 'shield' the surrounding bone from load [39]. Shielded areas are susceptible to bone resorption in accordance with Wolff's law, which states that bone adapts (remodels) to the level of mechanical load it is exposed to [39]. Finally, in comparison to other osteoconductive materials, such as Cerosium® and cobalt chromium, titanium is less brittle and dense, respectively [35].

2.3 Implant Stability Assessment

2.3.1 Overview

A variety of motivations exist to characterize the temporal composition and integrity of the bone-implant interface. Perhaps the earliest motives were to study and acquire fundamental knowledge of the physiological processes of osteointegration itself. To this end, histologic approaches were often employed to observe the composition of the bone-implant interface over time [35]. Later, mechanical approaches were developed to characterize the biomechanical properties of the bone-implant interface [14]. Implant micromotion and bone-implant interface strength/stiffness are often held as indicators of implant stability [14]. In clinical applications, implant stability represents the progress of healing or osseointegration. Clinicians often use prognostic tools to evaluate patient progress and make prescriptive decisions, such as on functional loading. Ideally, clinical

assessment tools should be non-destructive and non-invasive. Radiographic assessment is regularly employed as a non-destructive approach to monitor healing in osseointegrated reconstruction patients. This is the likely default because of precedent in other orthopaedic applications, and the known advantages and risks of the approach have been aptly characterized. Osseointegrated implant stability research usually focuses on the development, refinement, and validation of techniques to measure the degree of fixation of transcutaneous or percutaneous implants in bone. These approaches, whether experimental or clinical, facilitate knowledge and application development within the field of osseointegration. They may also afford protections to osseointegrated reconstruction patients through the early detection of major complications and initiation of preventative measures. Broadly speaking, approaches to implant stability assessment may greatly diverge in their primary motives. The primary goal of devices aimed at clinical deployment is often early detection of implant loosening and failure. This allows for clinical intervention before the occurrence of catastrophic integration failure. Certainly, for clinical applications, stability tests should be non-destructive, lest they are oxymoronic to their primary objective. On the other hand, destructive tests are not restricted by the bounds of patient safety and have immense freedom to investigate the biomechanical properties of the bone-implant interface, usually for knowledge acquisition or validation of non-destructive approaches.

2.3.2 Destructive Methods

Destructive implant stability tests are usually histological or biomechanical in nature. Naturally, histologic examination of the bone-implant interface (histomorphometry) requires tissue sectioning or biopsy, which, in human subjects, is either highly invasive or must be conducted post-mortem; although, animal studies sometimes employ such approaches [14, 15, 41]. Histomorphometry is the gold standard in assessing osseointegration by way of measuring bone-implant contact (BIC) [14, 15, 39, 41]. BIC may be calculated from a dyed specimen of implant and peri-implant bone [41]. Although clinical applications are limited, when histomorphologic analyses are paired with macroscale approaches, an invaluable picture of multi-scale bone-implant interface properties can be realized [14, 15]. Other destructive tests are mechanical in nature, including pull-out, push-out, and reverse torque tests [14]. In typical pull- and push-out tests, a cylindrical implant is anchored in bone (modelled biologically or synthetically) and removed by applying a load parallel to the bone-implant interface [41]. Implant stability has been correlated

with pull-out and push-out maximum force, energy, and shear modulus [14]. These tests are mostly applicable to non-threaded implants [41]. One limitation of this approach is unstable crack propagation at the BII, restraining accurate estimates of effective adhesion energy [14]. Reverse torque tests have helped mitigate this shortcoming, achieving steady state crack propagation [14]. Critical torque is said to be reached at failure of the bone-implant interface; however, there are also more conservative reverse torque approaches that employ a pass/fail framework [15]. In such tests, the aim is to gauge whether a dental implant will withstand a certain torque threshold, approximately $20\text{ N} \cdot \text{cm}$, without failure [15]. Although clinical applications have been proposed, this is almost certainly a destructive test and has not been widely adopted due to its inherent risks. A handful of other mechanical tests have also been investigated, including tensile (load applied perpendicular to the bone-implant interface) and bending tests; however, most applications remain ex-vivo [14, 39, 41].

2.3.3 Non-Destructive Methods

2.3.3.1 Radiographical Assessment

Imaging techniques are commonly used to assess bone quantity and quality changes after implantation [41]. Periapical and panoramic radiography and cone-beam computed tomography (CBCT) are the most common techniques for BII assessment [15]. Osseointegration produces several distinctive features on radiographs, such as the implant appearing radiopaque and lack of radiolucency at the BII [15]. Proximity of the bone to the implant and homogeneity of trabeculation can also be assessed [15]. For dental implants, crestal bone loss is often estimated as a predictor of implant success [15, 41]. However, many radiographic limitations exist. Bone quality and density cannot be quantified with information from conventional periapical and panoramic radiographs [41]. Even demineralization cannot be detected until a 40% reduction in bone mineral density [15, 41]. Standard x-ray and magnetic resonance imaging (MRI) cannot be used to measure bone-implant contact because of artefacts produced by the titanium implant [14, 15]. However, advanced x-ray techniques have been successful in visualizing the bone-implant interface [14]. X-ray micro-CT has enabled 3D-modelling of woven bone formation adjacent to titanium, and such 3D-models have been used in finite element analysis [14]. X-ray diffraction techniques and small-angle x-ray scattering (SAXS) have been employed to observe the preferential alignment of mineral crystals (inorganic constituents of bone) with the implant surface; however, there has not

been an investigation of spatial-temporal osseointegration [14]. X-ray diffraction can be used as an indicator of biological apatite (BAp) c-axis orientation, which may be related to certain bone properties, such as ultrasonic wave velocity, Young's modulus, and microhardness [14]. One of the most promising x-ray techniques is radiostereometric analysis (RSA), a high-resolution 3D-motion analysis method which makes use of metallic markers, such as tantalum beads, to observe extremely small implant movements [14, 42, 43]. The technique involves injecting beads into the bone at implantation and imaging the location of the implant relative to the markers over time [14, 42, 43]. In clinical studies, RSA was able to predict implant removal through excessive migration ($p = 0.009$) [42] and has been used to observe long-term stable fixation in OPRA implants [43]. Briefly, neutron microcomputed tomography is a promising technique that may be used to image the bone-implant interface without artefacts; electron tomography has allowed 3D-visualization of hydroxyapatite crystal orientation at the nanoscale; and two spectroscopic approaches, Fourier-transform infrared spectroscopy (FTIR) and Raman spectroscopy, have been used to study structural changes at the bone-implant interface [14]. Currently, radiographical assessments are mostly qualitative; although, innovations are pushing the field toward more quantitative stability metrics. It is worth noting that many approaches may expose patients to ionizing radiation [15]. Of the common techniques, CBCT has limited radiation compared to CT and panoramic radiography [15].

2.3.3.2 Mechanical Assessment

2.3.3.2.1 Quantitative Ultrasound

Quantitative ultrasound (QUS) is regularly used to evaluate the mechanical properties of bone, especially in osteoporotic patients [14]. Ultrasonic waves are high frequency mechanical waves that can reach the *MHz* range [14]. As such, they do not expose patients to ionizing radiation and have even been used to stimulate osseointegration [14, 15]. There is already a substantial body of evidence for the use of quantitative ultrasound, or guided waves, in evaluating the mechanical properties of the bone-implant interface. To this end, the BII is often treated as a boundary condition to the propagation of ultrasonic waves within osseointegrated implants [15, 44]. Finite element model and experimental studies have been conducted to date [14]. Modelling studies have revealed that the propagation of guided waves around 10 *MHz* is sensitive to changes at the bone-implant interface up to 15 μm from the surface of the implant [14]. Specifically, Vayron et al.

showed radio frequency output amplitude index decreases for increases in bone quantity and quality around dental implants (finite element model) [14]. Experimental studies have also verified results, showing the decrease of echo amplitude as a function of healing time (higher quantity and quality of bone) and differences in ultrasonic velocity between recently formed and mature bone [14]. In a typical setup, a probe transducer is attached to the implant abutment which generates a 10 MHz ultrasonic pulse [15]. The transducer is linked to a receiver which records the output radio frequency signal [15, 44]. The average amplitude of the output signal between 10 and 120 μ s is used as an implant stability index [15, 44]. Ultrasonic evaluation of dental implant osseointegration has been validated in at least one multi-modality study [45]. In the study, quantitative ultrasound was used to evaluate the stability of dental implants in a rabbit model [45]. The radio frequency signal amplitude indicator was found to be significantly correlated with BIC ratio, which was determined through histologic analysis (gold standard) [45]. Furthermore, in a study comparing the abilities of quantitative ultrasound and resonance frequency analysis (RFA) to estimate primary and secondary stability of dental implants in a sheep model, the error in estimating healing time was 10 times lower for QUS [46]. Quantitative ultrasound was more sensitive, accurate, and reliable than resonance frequency analysis as performed by the Osstell device (ISQ index) [46]. This may be because the implant is treated as a conduit for ultrasonic waves reaching the bone-implant interface in QUS, whereas the entire bone-implant system vibrates in RFA [46]. Therefore, quantitative ultrasound may be better at isolating the mechanical properties of the BII within a localized area ($\sim 30 \mu$ m) [46]. Quantitative ultrasound has also demonstrated promise in two transfemoral implant studies [47, 48]; although, it is currently held back by lack of clinical evidence and commercially available devices [15].

2.3.3.2.2 Vibration Approaches

2.3.3.2.2.1 Overview

Vibration assessment has a long tradition within implantology. It is premised on the idea that the bone-implant interface stiffens during healing, raising the natural frequencies of the bone-implant system over time [15]. Anchorage of the implant can be modelled by two springs in series, representing the bone-implant interface and surrounding bone [15]. Naturally, if one layer of springs is softer than the other, then it dominates the response of system [15]. In general, natural frequencies of bone-implant systems can be extracted in two ways:

1. Performing a sine sweep, where the system is coupled to a shaker that applies an oscillating load across a range of frequencies. In this case, natural frequencies are identified at resonances.
2. Applying a broadband impulse which excites the system into transient free vibration. Frequencies may then be extracted through Fourier transform.

It should be noted that damping also plays a role in system response and may have some association with the properties of the bone-implant interface [16]. Considering the cylindrical design of most implants, tests can be conducted in one of three ways. Implant excitation and response can be assessed in the axial (parallel) or transverse (perpendicular) directions relative to the orientation of the bone-implant interface [15]. Feasibly, angular modes of vibration could also be evaluated, where the implant would rotate about its central axis within the BII [49]. This would require an applied torque to the implant. Shear modulus and BIC ratio play significant roles in axial vibration, whereas BII compressive modulus plays the largest role in transverse vibration [15]. It has been suggested that the inducement of shear stresses may give vibration tests more sensitivity [15]. Moreover, angular stiffness has demonstrated greater sensitivity to osseointegration and less sensitivity to extraneous factors, such as implant location and boundary condition in dental implants [49]. In dental implantology, the percussion test is a common practice to evaluate fixation [15, 41]. In such a test, the implant is struck with any crude hammer (e.g., back end of a mouth mirror), and the produced sound is qualitatively evaluated by the clinician [15, 41]. It is said that poorly integrated implants sound low and dull, while well integrated implants have an acute ring [15, 41]. It has been reported that implants with a BIC ratio of only 15% can produce a ‘clear’ sound, evidencing a high degree of error in the approach [15]. Several research and commercial devices have been developed to quantitatively measure the vibration response of bone-implant systems and report their effective stiffnesses through non-dimensional scores. Devices may broadly implement a resonance frequency analysis (sine sweep) or impact (broadband impulse) methodology. For example, the Dental Mobility Checker has built off the standard percussion test by recording the acoustic response of consecutive implant strikes with a small impact hammer [15]. The acoustic signals are processed by fast Fourier transform (FFT), where the peak frequency is taken as an indicator of fixation [15]. Several problems have plagued the device, many of which are shared among all vibration approaches. Briefly, variations in implant mass and geometry mean that there is no absolute scale for quantitative cross-patient implant

stability comparison [15]. Rigid body characteristics greatly influence vibration response; without accounting for them, there is little evidence for the mechanical properties being measured. Other problems with the device include the influence of impact location on repeatability, potential to damage the bone-implant system, and limited input frequency bandwidth [15]. The most popular devices for dental and craniofacial implant stability assessment have tackled these issues in various ways and will be explored in the following sections.

2.3.3.2.2.2 Osstell

Three of the most studied devices include the Osstell, Periotest, and ASIST. The Osstell is the most common device implementing resonance frequency analysis. Current versions of the device mount a magnetic ‘SmartPeg’ to the implant abutment, which is forced by a sine sweep (5 – 15 *kHz*) of electromagnetic waves [15, 41]. Force transfer and response acquisition are achieved without direct contact with the peg, and resonant frequencies are recorded along two orthogonal directions [15, 41]. The highest frequency is then transformed into an Implant Stability Coefficient (ISQ), which accounts for implant geometry through undisclosed constants [15]. The values of the constants are obtained through calibration of the device [15]. Higher ISQ scores represent greater degrees of secondary stability [15, 39]. Numerous factors can influence resonance frequency analysis: bone density, implant location in jaw, abutment length, and implant geometry among others [15]. It is unclear how the ISQ deals with these factors. The Osstell has demonstrated prognostic value in prospective clinical studies [15, 41]; however, temporal changes in ISQ have shown to be dependent on the degree of primary stability [15]. That is, when primary stability is moderate, significant changes in ISQ may not be observed [15]. Considering the limitations, intra-patient longitudinal trends are the most reliable way to interpret results [15]. Although the Osstell is a relatively prolific device in the space of vibration assessment, it has not fared well against other approaches. In an animal study investigating dental implant osseointegration, the error made in estimated healing time was 10 times lower for quantitative ultrasound [46].

2.3.3.2.2.3 Periotest

The Periotest is another iteration of the percussion approach [15]. It was originally developed to assess the damping characteristics (integrity) of the periodontal ligament in natural teeth but has also realized applications in implantology [39, 41, 50, 51, 52, 53]. Its quantitative outcome relies on the contact time of an electromagnetically actuated impact rod with an implant [15, 50]. Here,

contact time is defined as the elapsed time from first contact with the implant to first rebound [15]. The output is a representative integer called the Periotest Value (PTV). Smaller contact times, or PTV scores, are indicative of successful osseointegration, while larger values may indicate loosening or marginal bone loss [15, 50]. The Periotest has realized applications in stability measurement of both dental and craniofacial implants [50]. Again, numerous factors can affect measurement values and repeatability. Implant mass and geometry, surrounding bone density, and jaw position have shown to influence output values [15]. Strike location on the implant, distance from the implant surface, and angle of attack have also been observed to greatly influence repeatability [15, 50]. This necessitates an intra-patient evaluation approach, where the tool is limited to presenting indications of temporal changes for a given implant [15]. The Periotest has demonstrated similar PST variance for implants and natural teeth and reproducible stability assessment in a large, long-term clinical study [51]. However, its prognostic utility is still limited by poor resolution, sensitivity, and intra/inter-rater reliability [50]. At least two devices have built upon the Periotest's electromagnetic actuation mechanism, namely the Implatest and Implomates. The Implatest employs an accelerometer that is supported by a membrane connected to the impact rod, as opposed to the accelerometer being directly integrated (Periotest) [15]. A study of this device indicated that frequency stability and dynamic linearity may be valuable indications of implant stability [54]. That is, frequency response may be noisy for poorly integrated implants and transition to more smooth and harmonic responses with adequate healing [15, 54]. The Implomates is like the Dental Mobility Checker, with a microphone for acoustic signal processing [15, 41]. The main difference is that it utilizes an electromagnetic ram instead of a manual impact hammer [15, 41]. This alteration may help address repeatability and improve safety through enhanced control of striking conditions.

2.3.3.2.2.4 ASIST

The Advanced System for Implant Stability Testing (ASIST) aimed to tackle the shortcomings of the Osstell and Periotest. It is a research device that uses the Periotest handpiece in conjunction with a custom motherboard [16]. The device employs the typical multiple impulse method of implant stability assessment but incorporates an analytical model of the bone-implant system [16]. The model accounts for the inertial and geometrical properties of the implant and incorporates physiologically appropriate viscous damping [16]. Instead of contact duration, the ASIST records raw acceleration responses from the piezoelectric element in the Periotest impact rod [16]. The

acceleration signal is then matched to an analytical model through a numerical optimization routine [16]. The ASIST approach has been applied to natural teeth [17], dental implants [18], and bone-anchored hearing aids [16] with relative success. In a comparative in vitro study of the Osstell and ASIST devices, the ASIST was found to be more sensitive to changes in implant stability and showed less variation in ASIST Stability Coefficient (ASC) due to changes in abutment length than the Osstell's ISQ [55]. The performance of the ASIST has also been evaluated in a longitudinal clinical study of bone-anchored hearing aids [56]. Interestingly, the ASIST was able to detect differences in primary stability between operating surgeons [56]. On average, ASC values decreased up to three months and then increased up to one year after surgery [56]. Additionally, since the ASIST extracts bone-implant interface stiffness from an analytical model, objective inter-patient comparisons were possible [56]. One of the downsides of the ASIST approach is the bottleneck of having to accurately model individual implant geometries, which would have to be done frequently with constantly evolving designs. Overall, the ASIST advances one of the more interesting approaches in the field of vibration assessment, overcoming many of the limitations of other systems.

2.3.4 Transfemoral Implants

2.3.4.1 Digital Image Correlation

Only a handful of studies have investigated mechanical approaches to the stability assessment of osseointegrated transfemoral implants. Most work has been conducted in the realm of vibration assessment, while two studies have investigated quantitative ultrasound, and only one has looked at a digital image correlation (DIC). In the DIC study, a method was developed to evaluate the primary stability and load transfer of transfemoral implants [57]. Five human cadaveric femurs were prepared, and 3D-printed titanium replicas of the Badal X stem (OTN Implants, Netherlands) were press-fit into the bones [57]. The loading protocol was designed to mimic the peak forces of gait; a sinusoidal between 150 and 850 N was applied to each specimen at 1 Hz , providing a moment of 30 $N \cdot m$ at the stem tip level [57]. DIC analysis was performed, providing information on the micromotion of the implant and strain field of the femur [57]. The results showed that it was possible to measure permanent migration and inducible micromotion (translation and rotation) of a press-fit implant by employing digital image correlation [57]. The random error was less than 4.8 μm for translations and 0.03° for rotations [57], which is much less than the scale of

appropriate micromotions for bone ingrowth in dental implants ($\leq 40 - 70 \mu m$) [14]. The approach was largely reliable and presented an interesting method for detection of primary stability; however, applications may be limited due to lack of motion controls and available surfaces for speckle application in a clinical setting.

2.3.4.2 Quantitative Ultrasound

At least two studies have investigated the use of guided waves to assess healing in transfemoral implants. The first study, conducted in 2018, developed both a finite element and synthetic model to evaluate the sensitivity of guided waves to changes at the bone-implant interface [48]. A titanium rod approximating a transfemoral implant was inserted into a Sawbones model 3406-5 femur [48]. Curing epoxy resin was used to simulate rapid osseointegration [48]. Piezoelectric elements were mounted to the percutaneous end of the implant and were used for wave generation and reflected wave sensing [48]. The finite element model, set up identically to the experiment, varied the elastic modulus of the bone-implant interface and showed a 50% decrease in longitudinal wave energy for full osseointegration [48]. The experimental model verified sensitivity of the approach to epoxy curing (wave energy decreases with healing) and showed significant wave energy increases in a pullout test (sensitivity to loosening) [48]. The study presented promising preliminary results for the sensitivity of a guided wave approach. However, limitations include the simplicity of the implant design (cylindrical rod) used in modelling and lack of absolute quantitative scale for clinical evaluation. Another study was conducted in 2019 [47]. A femoral structure was approximated by an aluminum cylinder filled silicone, simulating dense cancellous bone [47]. A custom aluminum implant (novel design) was anchored in the cylinder with two-hour adhesive epoxy to simulate rapid osseointegration [47]. It is not clear whether epoxy was applied between the implant stem and surrogate bone or only between the extramedullary struts and outside surface of the aluminum structure. Finally, piezoelectric elements were mounted to extramedullary struts, and the whole system was covered in plasticine [47]. A developed 'O-Index' based on the power of the difference signal was found to be sensitive to bonding quality between the implant and bone structure [47]. Many of the same limitations existed for this study. The experimental model appeared to be even lower fidelity to any clinical bone-implant system; however, the epoxy curing approach seemed to be an effective way to simulate continuous integration. Much more research is needed within the field to make strong conclusions on the sensitivity and reliability of quantitative ultrasound applied to transfemoral implants.

2.3.4.3 *Vibration Assessment*

A short paper outlining the first attempt at a resonant frequency measurement system for osseointegrated transfemoral implants was published in 2005 [19]. The first full investigation of vibration assessment for transfemoral implants was published in 2007 by the same group (Shao et al.) [20]. A threaded implant system was used in the investigation; although, it was not explicitly identified. Considering the outlined characteristics of the implant and year of publication, it was most likely an OPRA system. Implants were installed in Sawbones femurs with one of three silicone rubbers to simulate different stages of osseointegration [20]. A pendulum steel ball was manually swung at the exposed abutment to excite the system ($< 0.33\text{ N}$) [20]. The strike was administered in the transverse direction, and the acceleration response was also recorded transversely by an accelerometer attached to the abutment with adhesion wax [20]. The results showed a positive linear correlation between dominant natural frequency and elastic modulus of the interface [20]. Natural frequency also tended to decrease with increased abutment length and decreased diameter [20]. In vivo testing with one patient showed an initial decrease in dominant natural frequency after weightbearing followed by increases up to 38 days [20]. In vitro tests realized natural frequencies in the range of $\sim 3000\text{ Hz}$, while the in vivo study showed frequencies around $1200 - 1300\text{ Hz}$ [20]. One limitation of the study appeared to be the narrow range of elastic moduli represented in the physical models, leading to the appearance of low sensitivity (small dominant frequency changes).

From 2011 to 2012, Cairns published a series of papers on the utility of modal analysis in evaluating osseointegration in transfemoral implants. The first conference paper focused on the most effective excitation technique between an impact hammer and electromagnetic shaker and presented preliminary sensitivity findings [21]. It was concluded that a shaker provided superior signal-to-noise ratio, coherence values, and a greater number of modes over the same frequency range [21]. Additionally, changes in natural frequency and mode shape were observed for different interfaces [21]. In a subsequent conference paper, Cairns refined the physical models used in modal analysis [22]. A summary of the models can be viewed in Figure 2.2, extracted from the paper.

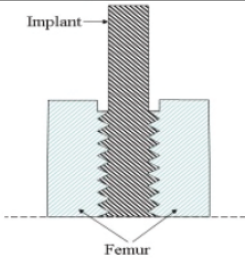
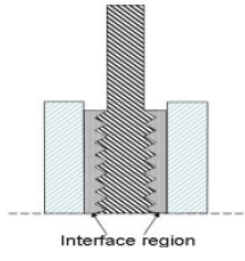
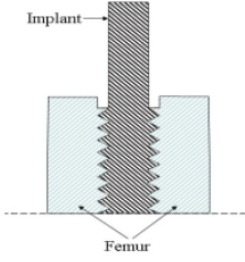
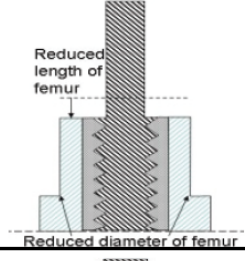
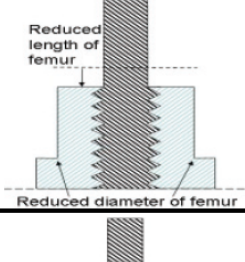
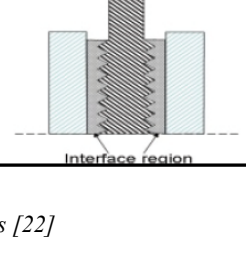
| Stage | Mechanical Characteristics of Physical Model | Schematic of Physical Model |
|-------|---|--|
| 1 | Femur pre-threaded to produce implant insertion torque of 5Nm. No adhesion between implant and femur. Low shear strength at interface |  |
| 2-int | Femur bored out to radius 1.5mm larger than implant. Gap filled with resin. No adhesion between resin and implant. Increase in implant removal torque |  |
| 2-end | Femur pre-threaded to produce implant insertion torque of 20Nm. No adhesion between implant and femur. Increase in implant removal torque |  |
| 3-int | Stage-2-intermediate modified. Femur length reduced by 10mm. Femur diameter reduced over 40mm implant length |  |
| 3-end | Stage-2-end modified. Femur length reduced by 10mm. Femur diameter reduced over 40mm implant length |  |
| 4 | Femur bored out to radius 1.5mm larger than implant. Gap filled with silicone. No adhesion between silicone and implant |  |

Figure 2.2: Physical models used by Cairns [22]

Cairns' work culminated in a full investigation, published in 2012, on the ability of modal analysis to detect osseointegration in transfemoral amputees [23]. Sawbones model 3406 composite femurs were used in combination with custom-machined pure titanium implants (likely modelled after the OPRA system) [23]. Two femurs were prepared such that the implants could be screw-fixed at approximately 0.5 and 4 $N \cdot m$ of torque [23]. These conditions were chosen to represent the extremes of integration [23]. Additionally, two boundary conditions were investigated: freely supported and cantilevered [23]. Femurs were placed on a foam bed for the freely supported condition, and the femoral head was fixed in resin for the cantilevered condition [23]. An electromagnetic shaker positioned transversely relative to the implant abutment performed a sinusoidal sweep from 0.1 – 10 kHz [23]. Force was transferred through a Delrin® stinger and was applied to the abutment through a dynamic force transducer [23]. The maximum recorded force was 4 N [23]. The response of the system was recorded by a single axis piezoelectric accelerometer mounted in 17 positions along the implant and bone with beeswax [23]. The physical model was then rotated 90° to repeat the tests in the orthogonal transverse direction (no axial measurements taken) [23]. Natural frequencies and mode shapes were found to change in response to insertion torque, boundary condition, and model orientation [23]. Natural frequencies ranged from 165 – 4490 Hz [23]. Larger changes in frequency were observed for the second and third bending modes than the first mode between interface conditions [23]. The paper demonstrated the potential of modal analysis to be used in the stability assessment of transfemoral implants.

In 2022, two papers were published by Lu et al. investigating vibration analysis on osseointegrated transfemoral implants. The first paper introduced a novel implant design [24], not unlike that outlined by the same group (Vien et al.) in 2019 [47]. In this paper, a vibration related 'E-index' was introduced [24]. A second paper was then published that elaborated the tested physical models [25]. Sawbones composite femurs were rigidly clamped at three locations to simulate different lengths of residual bone (152; 190; 228 mm) [25]. Custom implants were 3D-printed from ABS plastic, and osseointegration was simulated by curing two-part adhesive epoxy with a setting time of five minutes [25]. An instrumented impact hammer was used to excite the system at a strike point on the implant [25]. The direction of strike application was not clear. Two unidirectional accelerometers recorded responses in the transverse direction [25]. High coherence between the accelerometer signals was observed up to 8000 Hz , which was treated as an upper bound for frequency analysis [25]. E-index was defined as the proportion of power belonging to a certain

frequency range relative to the whole domain [25]. Frequency ranges were defined for each femur length condition based on the distribution of resonant peaks within the cross-spectrum signals [25]. E-index was found to increase and eventually plateau with curing time, evidencing the sensitivity of the approach to increasing interface stiffness [25]. Over time, the signals also became more harmonic, with several prominent peaks growing from an initially flat response [25]. The study implemented an interesting cross-correlation approach with two accelerometers; however, results were only generated for an unconventional implant design. Furthermore, the implant was not constructed from a metal, ceramic, or other biocompatible/osteoconductive material, and the overall fidelity of the physical models was low.

Mohamed created both the first 3D and 1D finite element models of a transfemoral implant system in 2022 [26]. The purpose of the creation of a 1D finite element model was to extend the ASIST approach for dental and craniofacial implant stability testing to larger transfemoral implants [26]. The flexibility of a 1D finite element model was more appropriate for the elongated OPL system than accepting the rigid body assumptions of a traditional analytical model [26]. In 2024, a full investigation was published by Mohamed et al. with experimental validation [27]. An OPL Type A implant was anchored in a Sawbones model SKU 3403 composite femur with either silicone rubber adhesive, paraffin wax, or superglue, simulating low, intermediate, and high interface stiffness conditions respectively [27]. The responses of the system to axial strikes at the distal screw of the dual cone adapter were recorded by a uniaxial accelerometer [27]. Strikes were administered with a Periotest handpiece [27]. The first axial mode was found to be highly sensitive to changes at the bone-implant interface; however, the Periotest handpiece had difficulty exciting the mode in the low condition [27]. As seen in Figure 2.3, this caused the low and high conditions to have similar appearances in the frequency domain [27]. Mohamed concluded that the approach would need a revamped impactor to consistently trigger the first axial mode of vibration across all interface stiffness conditions [27], setting the stage for the work contained within this thesis.

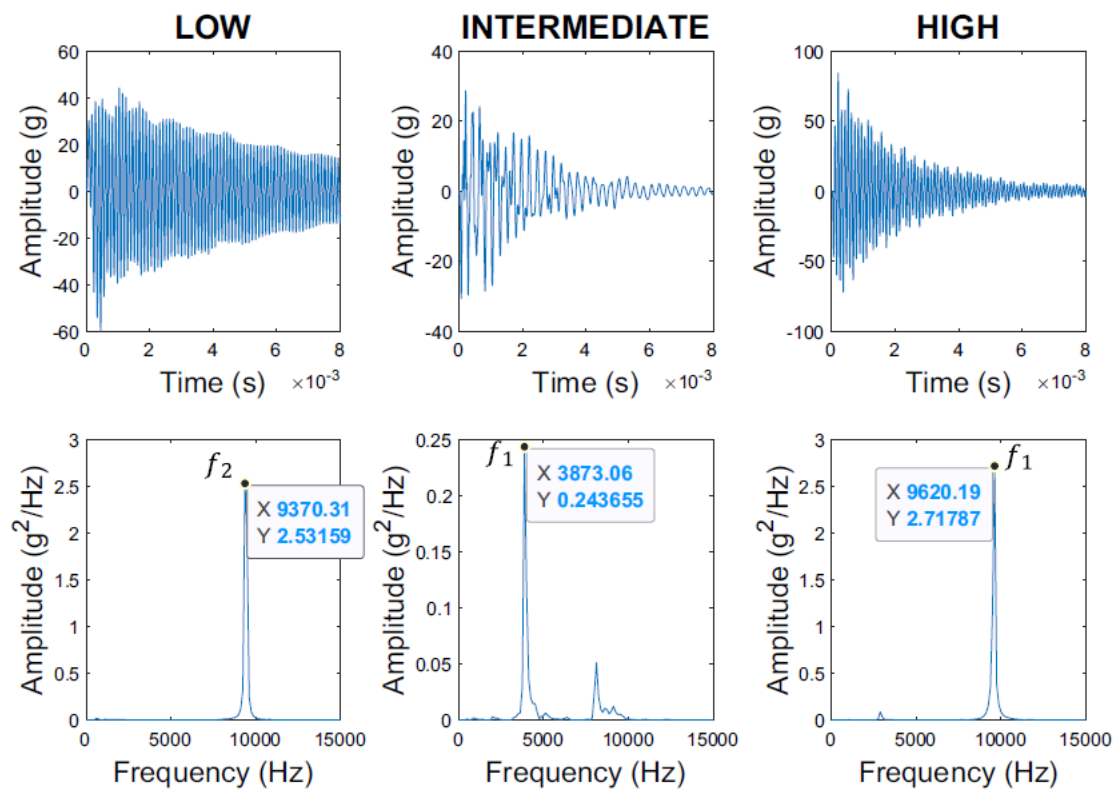


Figure 2.3: Transverse axial vibrations elicited by Periotest handpiece [27]

Chapter 3 Initial Development and Factor Exploration

3.1 Introduction

Various literature sweeps and tests were conducted in the development of a benchtop prototype impactor. These tests helped validate the prototype's function and scope out factors that would be manipulated in the optimization of response signals from transfemoral amputation (TFA) models. First, the build and performance of a Periotest handpiece in conjunction with an ASIST central processing unit was characterized. A modular benchtop prototype was then developed, and each configuration was evaluated, considering the Periotest handpiece as a benchmark. After selection of a high-performing configuration, various tests were conducted to observe the effects of factors such as impact interface stiffness, impact rod mass, and actuation voltage on response signals as well as examine the levels of each factor that would be considered in future development. A simple impact model was developed to aid in factor investigation, providing a theoretical basis for design decisions and observed performance. The model helped delineate a development approach and provided a reference point for all future experimental behaviour. Finally, a list of factors and associated levels was synthesized for further investigation in a follow-up development study.

3.2 Periotest Handpiece Design

3.2.1 Overview

While the Periotest has been used in dozens of studies, there are some misconceptions in the literature about its fundamental mechanisms of operation. Additionally, filed patents put forward several design concepts, the diversity of which may serve to confuse future innovators hoping to improve on current technologies. In this section, some of the patent designs will be highlighted and key design features of the Periotest Classic will be illuminated.

3.2.2 Documentation

In 2018, a description of the Periotest was given in a review of dental implant stability assessment approaches [15]. The impact rod was reported to have a magnetic core propelled at constant velocity by two coils [15]. The review also claimed a ram mass of 8 *g* with an accelerometer mounted to the rear end [15]. The schematic offered by the paper can be viewed in Figure 3.1. This

view of the Periotest Classic was perpetuated from papers in published in 1999 [52] and 1990 [53], which put forth similar schematics.

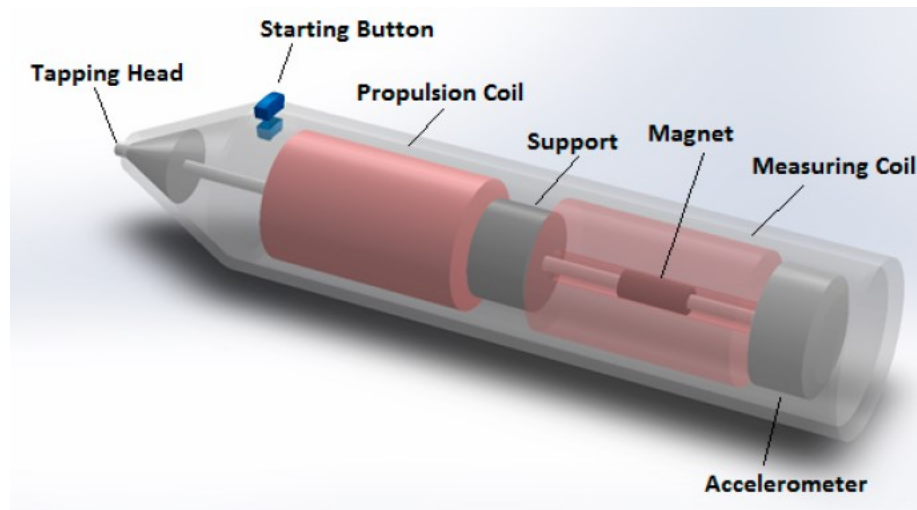


Figure 3.1: Periotest handpiece schematic [15]

In 2008, a patent titled *Apparatus and Method for Assessing Percutaneous Implant Integrity* was published by the World Intellectual Property Organization's International Bureau [58]. This patent broadly outlined the framework from which the ASIST was developed. In developing the ASIST approach, the patent discussed the operation of the Periotest. Figure 3.2 was provided as a general schematic of the Periotest system, which modeled the electromagnet-permanent magnet system as a spring and placed the accelerometer at the rear of the impact rod. The patent suggested that upon impact, the rod briefly maintained contact with a natural tooth (in the specific case of the Periotest) and fed the resulting acceleration signal back to a central processing unit.

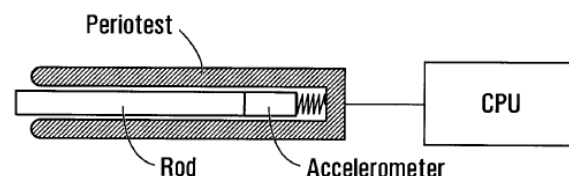


Figure 3.2: General schematic of Periotest system [58]

The patent went on to detail how a similar system in conjunction with a property determiner could operate on osseointegrated implants (dental; maxillofacial; craniofacial). Similarly, a motion detector mounted at the rear of an impact body recorded an impact signal with frequency content from the bone-implant-impact body system. Subsequently, the signal was processed and matched

to a model of the system from which pertinent properties could be extracted. A schematic of the system can be viewed in Figure 3.3.

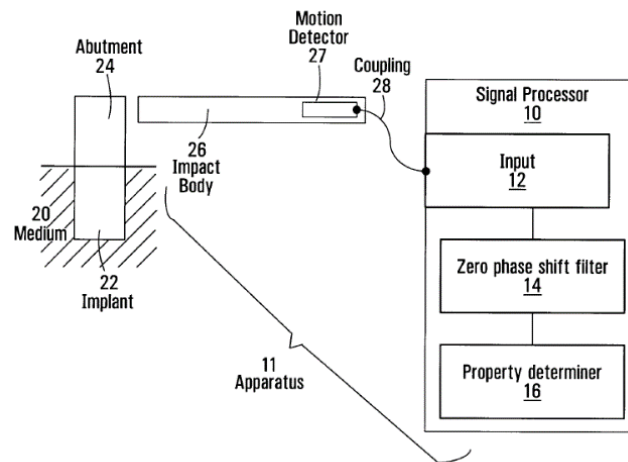


Figure 3.3: Apparatus for assessing percutaneous implant integrity [58]

The patent outlined two other concepts that can be viewed in Figure 3.4. In any case, the apparatus was quite simple with a motion detector mounted at the rear of an impact body. Filtering may have occurred within the body or during signal processing at the central processing unit.

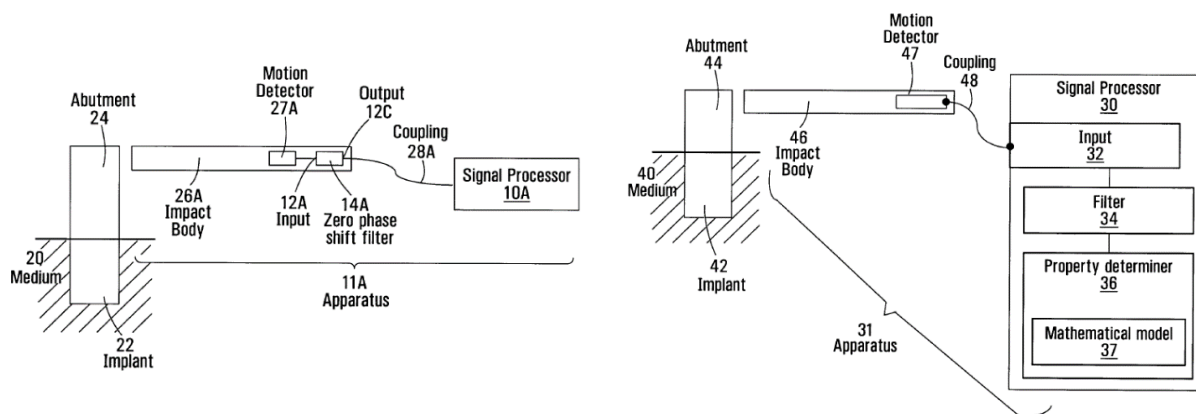


Figure 3.4: Other apparatus concepts for assessing percutaneous implant integrity [58]

In a 1995 thesis by Robertson, *Multiple Impulse Method of Tooth Mobility Assessment*, the Periotest handpiece function and operation characteristics were explored [59]. In particular, the schematic in Figure 3.5 was given, in which a solenoid propulsion coil was pictured enveloping an impact rod. A permanent magnet was pictured at the back of the impact rod, and an accelerometer was set behind the magnet in the middle of a ‘measuring coil.’ Few additional details

were given about the mechanical design of the handpiece. Again, this view seemed to stem from the 1990 paper [53].

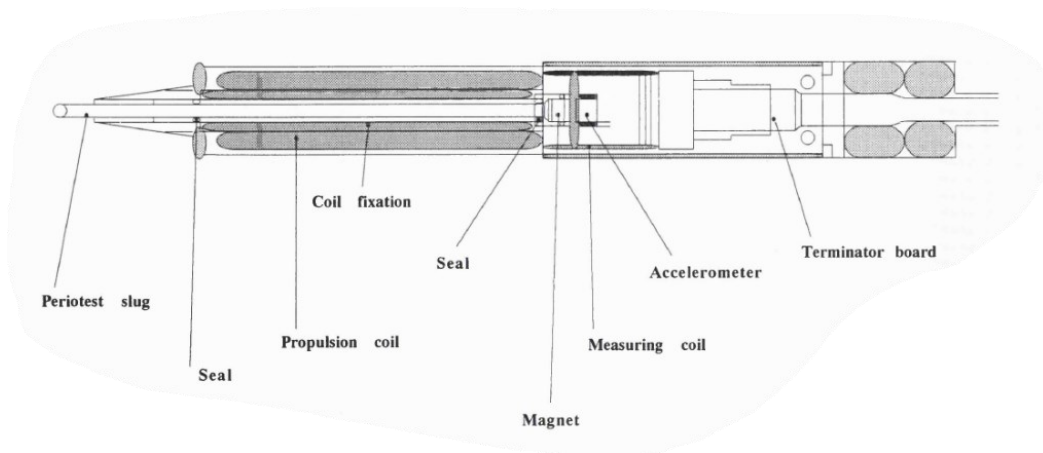


Figure 3.5: Periotest handpiece schematic [59]

In 1987, a patent titled *Dental Percussion Instrument* was published by the United States Patent and Trademark Office. In it appeared the design schematics for the Periotest handpiece (Figure 3.6). As further explored in Section 3.2.3, the schematics largely matched the physical state of the Periotest Classic handpiece, the handpiece used in dozens of studies and the ASIST device [16]. However, the schematics told a different story than some of the versions understood by inventors and researchers that came after 1987. A magnetic propulsion coil (8) was set behind a permanent magnet (7) embedded in the back of an elongated ram (2). The coil and permanent magnet formed a drive for the forward and return motion of the ram. The patent claimed that the ram was supported in a largely friction-free manner by bearings (3) and (4). At the test head (5) of the ram, a piezoelectric element (22) served as an acceleration pickup during impact. The element leads trailed through the ram, exited midspan (28), wrapped around the ram for flexibility and stress relief, maneuvered through the rest of the components, and finally exited the handpiece through a cable (10), which taxied signals and power between the handpiece and central processing unit.

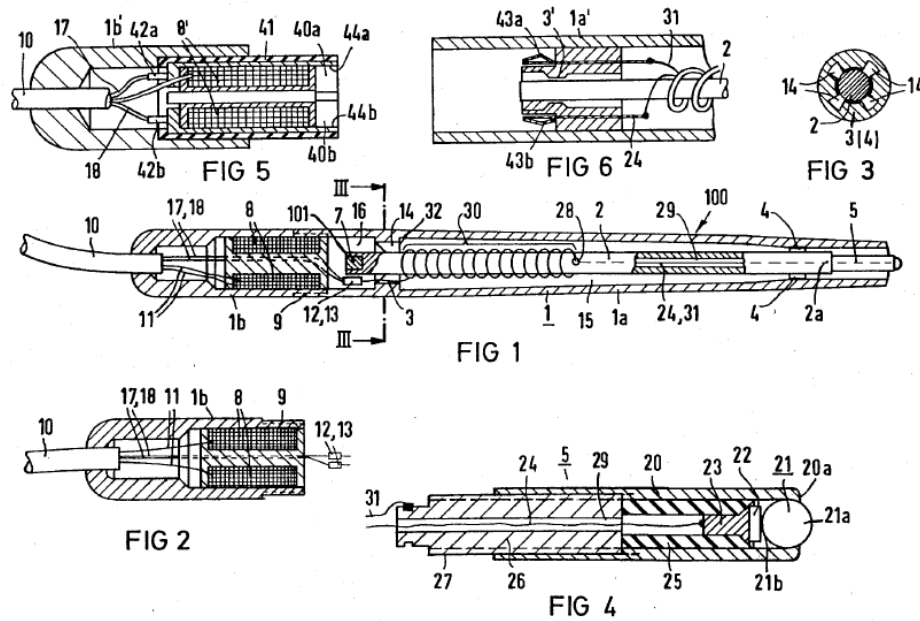


Figure 3.6: Periotest patent schematic [60]

The original patent largely held true to the design of the Periotest Classic, which many papers attempted to vaguely understand and utilize. However, the propulsion mechanism was not always accurately understood, and the process of acceleration acquisition was rarely conceptualized correctly at all. It is important to recognize the configuration of the propulsion system and the nature of acceleration acquisition elements for optimal design of future of impactors. This will be further discussed in Section 3.2.3.

3.2.3 Dissection

A Periotest Classic handpiece was dissected to be sure of the commercially deployed actuation and acquisition systems. As seen in Figure 3.7, the handpiece could be divided into four main subassemblies: the main body; inner carriage; impact rod; and solenoid, electromagnet, and connector assembly.

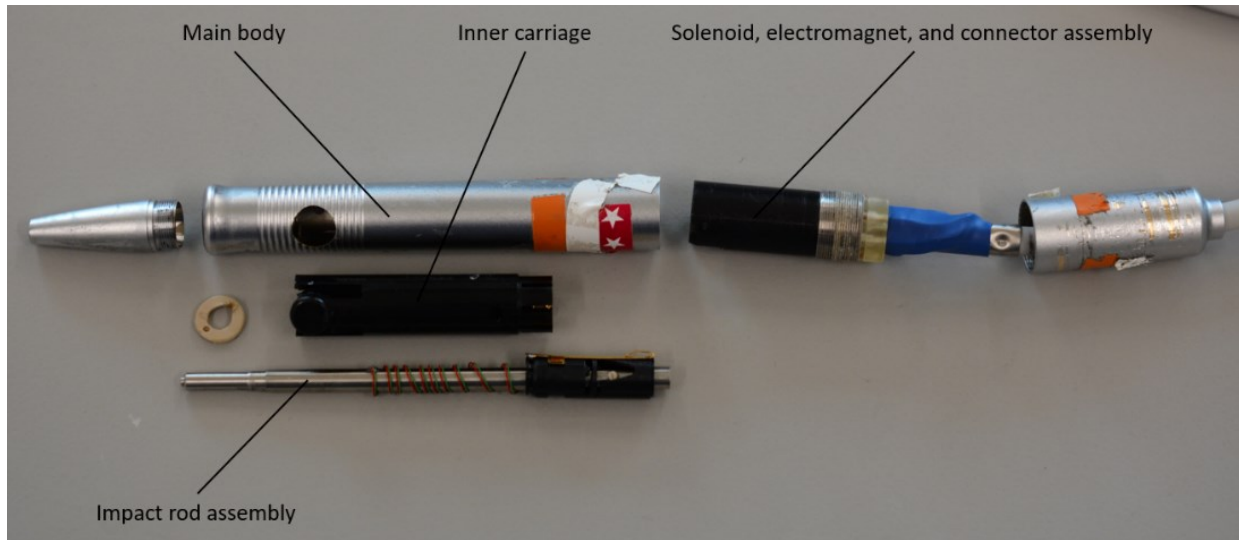


Figure 3.7: Subassemblies of dissected Periotest handpiece

The impact rod was an elongated ram that could be fired by repulsion between a solenoid and embedded permanent magnet. Its mass was approximately 9.4 g [61] (verified in lab). A side view of the rod can be seen in Figure 3.8.

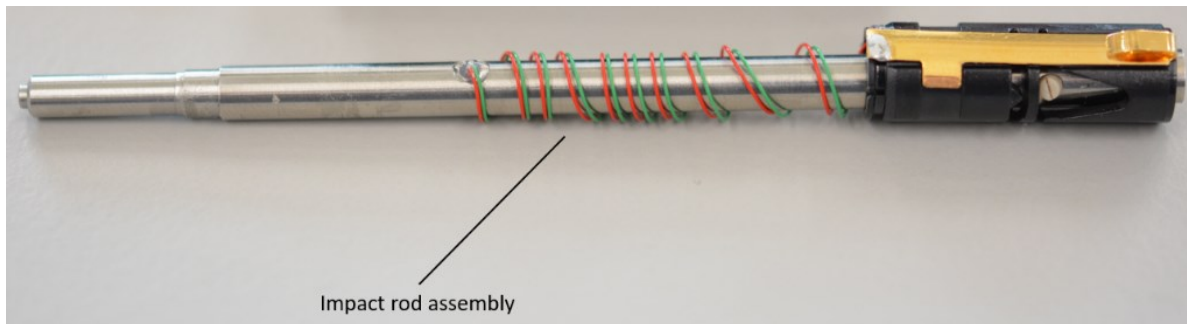


Figure 3.8: Periotest impact rod assembly

A piezoelectric element (accelerometer) sat below a small cylinder that served as the contact point between the impact rod and tooth or implant surface, depending on the application. A closeup view of the tip can be seen in Figure 3.9.

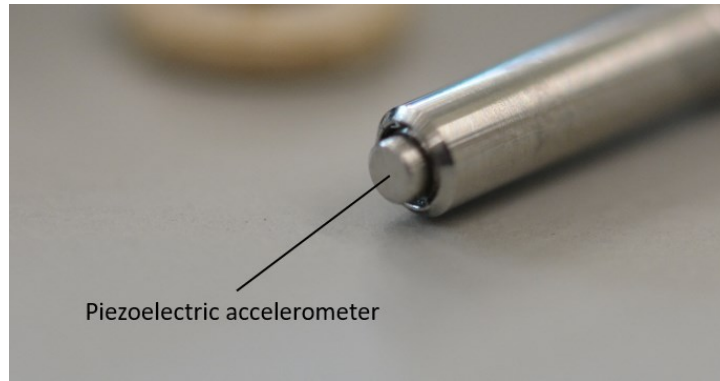


Figure 3.9: Tip of Periotest impact rod

Accelerometer leads trailed through the impact rod and exited mid-span (Figure 3.10). The leads were glued upon exit to provide stress relief and wrapped around the impact rod to provide flexibility to the flight of the rod.

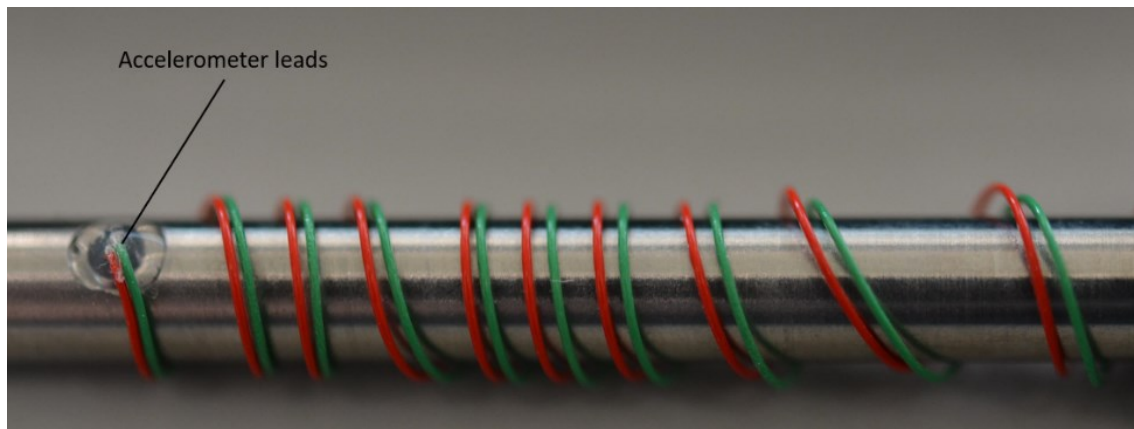


Figure 3.10: Accelerometer leads exiting Periotest impact rod

The impact rod had an inset pin lying in a track that limited linear and rotation motion (Figure 3.11). The linear trace of the rod was measured to be 5 mm.

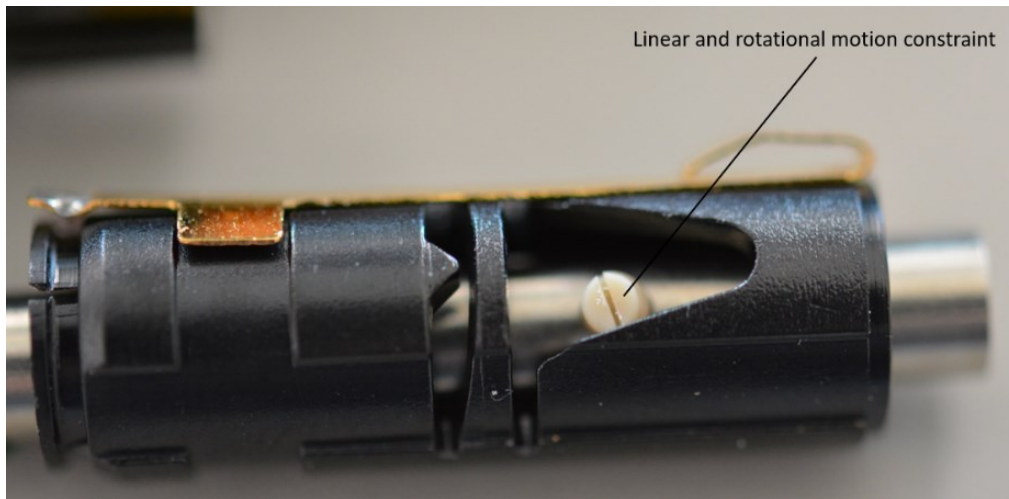


Figure 3.11: Linear and rotational motion constraint mechanism of Periotest impact rod

Finally, the impact rod had an embedded cylindrical permanent magnet at its rear (Figure 3.12). The south end of the magnet faced into the rod.

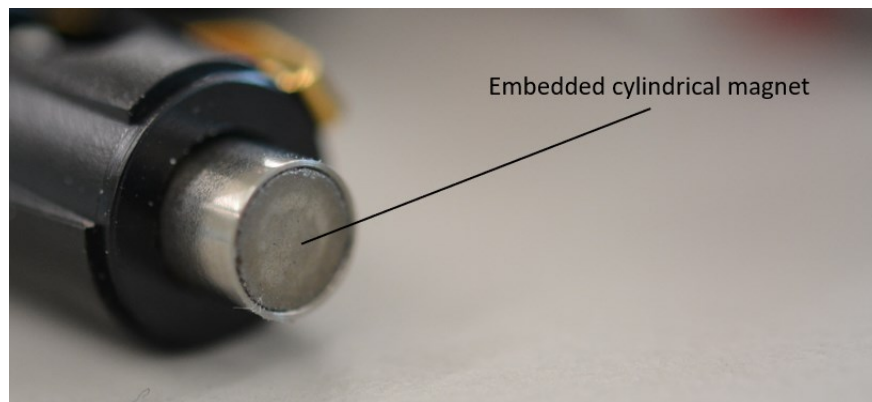


Figure 3.12: Embedded permanent magnet at rear end of Periotest impact rod

Perhaps the most intriguing feature of the commercial handpiece was the presence of a separately powered solenoid and electromagnet positioned behind the impact rod. A view of the subassembly containing the coils and wire connections can be seen in Figure 3.13.

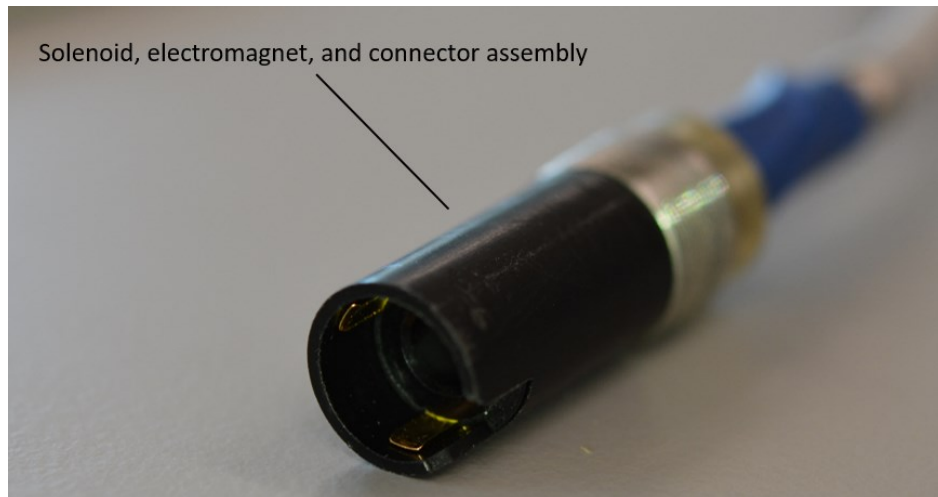


Figure 3.13: Solenoid, electromagnet, and connector assembly of Periotest handpiece

The solenoid sat in front of the electromagnet and actuated the impact rod on a 10 V extension rail (ASIST motherboard), while the electromagnet housed a ferromagnet core and returned the impact rod to its resting position on a 12 V retraction rail (ASIST motherboard). The configuration of the coils can be viewed in Figure 3.14.

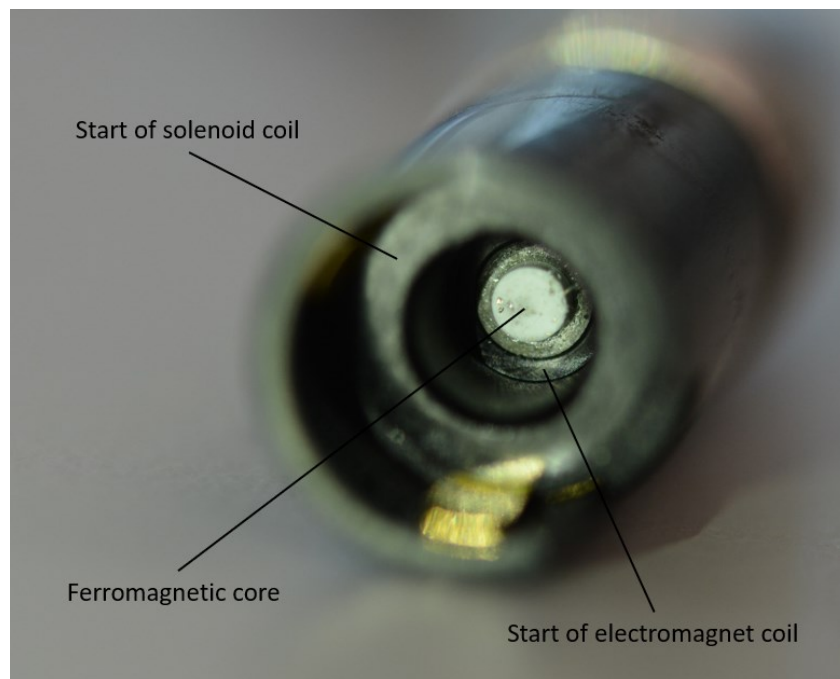


Figure 3.14: Configuration of Periotest handpiece coils

Notably, the Periotest handpiece placed its piezoelectric element near the impact interface. This type of sensor does not require an external power source and has a high frequency response [62].

Placement near the impact interface may help isolate the impact event and prevent noise/leakage from the motion/vibration of the impact rod before or after contact. The use of two coils may serve several purposes. It is feasible that limiting current switching in a single coil prevents overheating and decreased coil performance. While introducing a ferromagnetic core could bolster the magnetic flux density of the solenoid, it could also decrease the repulsive force between the solenoid and permanent magnet. This is because the permanent magnet exerts an attractive influence, or back eddy, on the ferromagnetic core. In repulsion, a permanent magnet may be set close to a solenoid and take advantage of strong and long electromagnetic influence. In attraction, a solenoid coil with a ferromagnetic core (electromagnet) may work synergistically to strongly pull a permanent magnet at a distance.

3.2.4 ASIST Impact Force

The force produced by the Periotest handpiece was tested with a variety of hardware configurations. In a typical configuration, the Periotest handpiece was used with an ASIST central processing unit. The ASIST motherboard has been through multiple versions, with the up-to-date version as of publication applying a 10 *V* extension rail (17 *ms* default) and 12 *V* retraction rail (55 *ms* default) to the handpiece. In the first impact force tests, the Periotest handpiece was mounted in a rigid stand and placed approximately 1 *mm* (valid distance 0.6 – 2.5 *mm* [63]) away from an impact load cell (ICP® Force Sensor Model 208C02, PCB Piezotronics Inc, USA). The load cell was mounted to a 3D-printed stopper compatible with a T-slot bar structure. Finally, the T-slot structure was clamped to a solid base. A setup schematic can be viewed in Figure 3.15.

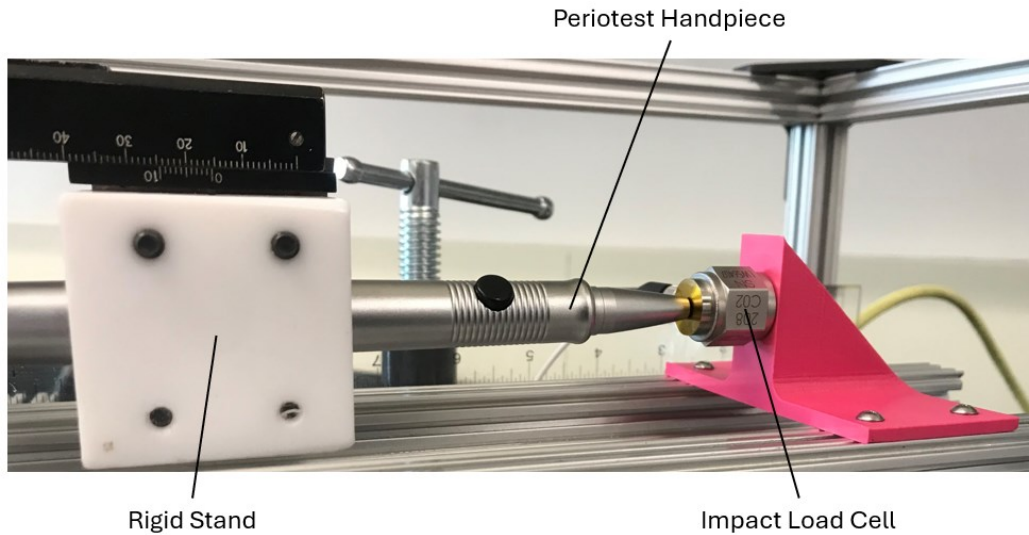


Figure 3.15: First ASIST impact force test

The ASIST device executed 16 strikes in 4 s (4 Hz). Impact force data was recorded at 100 kHz, and the ensemble average of 15 strikes (first strike used for triggering acquisition) was recorded (Figure 3.16). Peak force was measured to be 25.7 N.

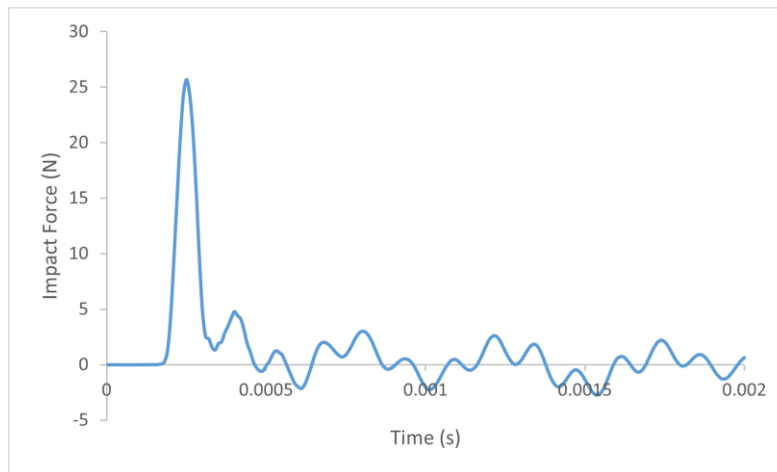


Figure 3.16: ASIST ensemble average loading profile (impact load cell)

Simultaneously, the ASIST unit recorded raw acceleration data from the Periotest handpiece's piezoelectric element. 16 full impact acceleration profiles were recorded, and again, the ensemble average was taken (Figure 3.17). The impact event in Figure 3.17 was not nearly as smooth as in Figure 3.16. The impact load cell likely presented a much more accurate representation of loading, especially with its measurement range of ± 444.8 N. The acceleration recordings, on the other hand, likely experienced clipping below 1 V. This phenomenon was found repeatedly when using

the Periotest handpiece to strike relatively rigid objects and was also verified by oscilloscope measurements. It likely arises from impact accelerations exceeding the dynamic range of the piezoelectric element.

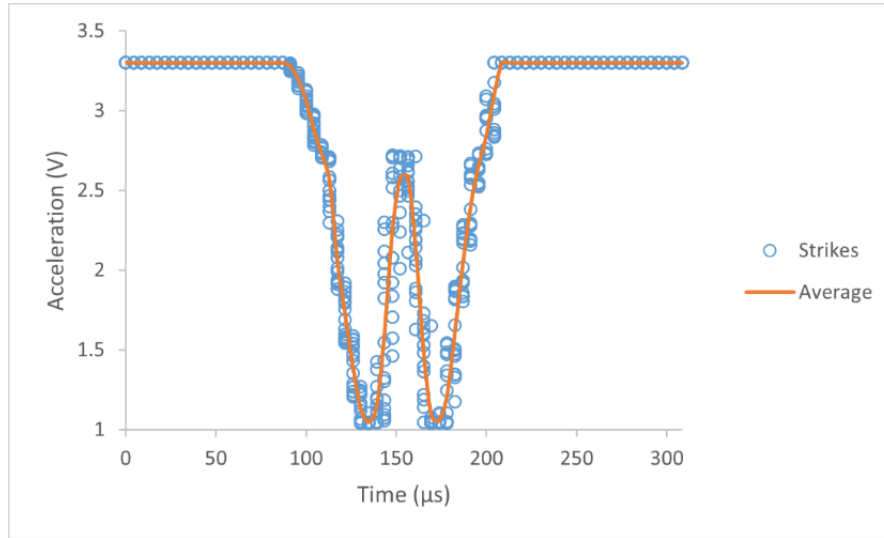


Figure 3.17: ASIST ensemble average impact acceleration profile (Periotest handpiece)

Two versions of the ASIST as well as the original Periotest Classic system were tested with the impact load cell. The ASIST apparatuses were tested along extension (actuation) times (duration of current applied to propulsion solenoid) ranging from 15 – 20 *ms*. The results showed a peak impact force relationship that increased with actuation time and exceeded the original Periotest system for most configurations (Figure 3.18). The Periotest handpiece appeared to perform between 30 – 45 *N* of impact force for various configurations.

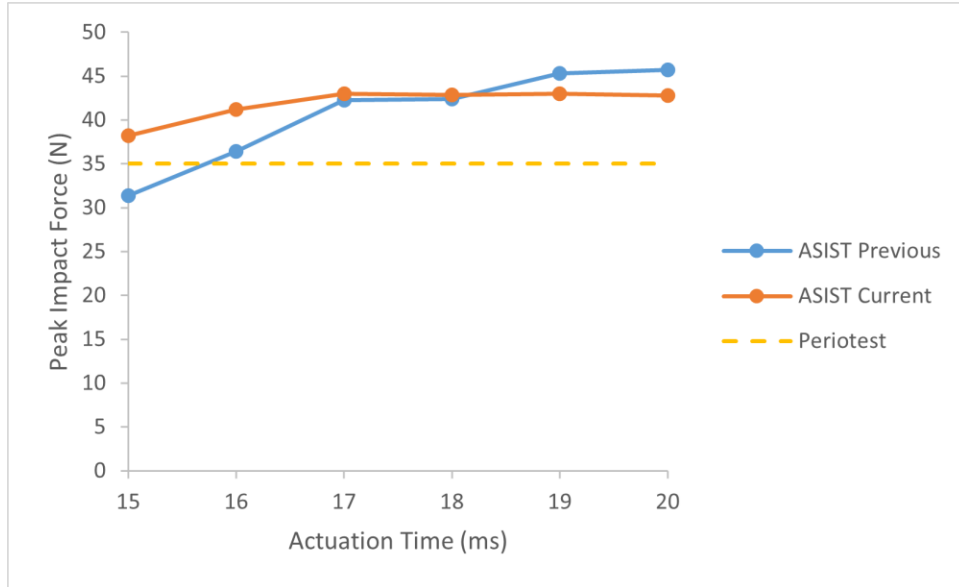


Figure 3.18: Peak impact force vs. actuation time for various Periotest handpiece configurations

When striking preliminary TFA experimental models, very little information could be gleaned from the ASIST. The signals did not have at least two clear modes of vibration, and the clipping phenomenon occurred in most cases. It appeared that, at a minimum, the ASIST was ill-tailored from a transducer standpoint, and it possibly lacked other design characteristics, such as appropriate ram mass to elicit balanced contributions from multiple modes of vibration [15, 64].

3.3 Impact Model

3.3.1 Two Degree of Freedom Model

In ASIST applications, the impact rod is often idealized as a point mass, and the connection between the impact rod and implant system during impact is idealized as a spring or stiffness element (Figure 3.19) [16, 17, 18].

stiffness unit, a is the mass ratio of the implant to impact rod, and b is the stiffness ratio of effective bone-implant interface stiffness to impact stiffness.

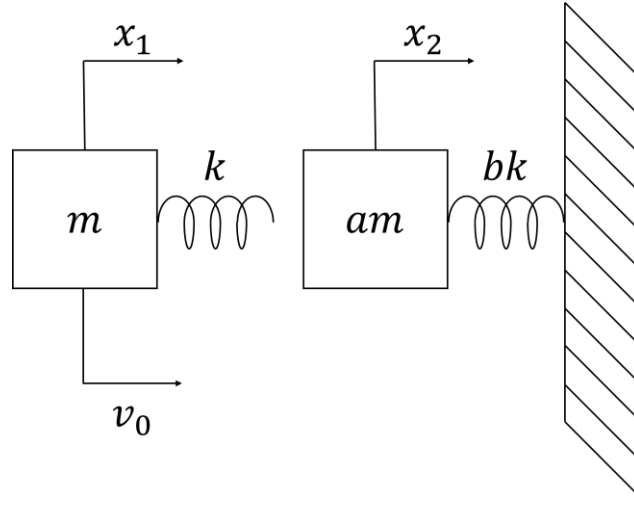


Figure 3.20: Two degree of freedom impact vibration model

Applying Newton's second law to the system, a system of coupled ordinary differential equations can be derived:

$$\begin{aligned} \sum F &= m\ddot{x} \\ -k(x_1 - x_2) &= m\ddot{x}_1 \\ -k(x_2 - x_1) - bkx_2 &= am\ddot{x}_2 \\ \begin{bmatrix} m & 0 \\ 0 & am \end{bmatrix} \begin{Bmatrix} \ddot{x}_1 \\ \ddot{x}_2 \end{Bmatrix} + \begin{bmatrix} k & -k \\ -k & (1+b)k \end{bmatrix} \begin{Bmatrix} x_1 \\ x_2 \end{Bmatrix} &= \begin{Bmatrix} 0 \\ 0 \end{Bmatrix} \end{aligned} \quad 3.1$$

With solution form:

$$\begin{Bmatrix} x_1 \\ x_2 \end{Bmatrix} = \begin{Bmatrix} X_1 \\ X_2 \end{Bmatrix} \sin(pt + \phi) \quad 3.2$$

Where X_1 and X_2 represent the response mode shapes, p represents the natural frequencies of the system, and ϕ represents the phase angles. Inputting the solution form back into Equation 3.1 and simplifying:

$$\begin{bmatrix} k - mp^2 & -k \\ -k & (1+b)k - am^2p^2 \end{bmatrix} \begin{Bmatrix} X_1 \\ X_2 \end{Bmatrix} = \begin{Bmatrix} 0 \\ 0 \end{Bmatrix} \quad 3.3$$

Now taking the determinant to solve for the natural frequencies, p_1 and p_2 :

$$\det \begin{bmatrix} k - mp^2 & -k \\ -k & (1+b)k - am^2p^2 \end{bmatrix} = 0$$

$$am^2p^4 - (1+a+b)kmp^2 + bk^2 = 0$$

$$p_1 = \sqrt{\frac{k(a+b+1 - \sqrt{a^2 + 2a - 2ab + b^2 + 2b + 1})}{2am}} \quad 3.4$$

$$p_2 = \sqrt{\frac{k(a+b+1 + \sqrt{a^2 + 2a - 2ab + b^2 + 2b + 1})}{2am}} \quad 3.5$$

Using the first natural frequency to solve for the first mode shape:

$$[k - mp_1^2 \quad -k] \begin{Bmatrix} X_1 \\ X_2 \end{Bmatrix}_1 = 0$$

$$\begin{Bmatrix} X_1 \\ X_2 \end{Bmatrix}_1 = \begin{Bmatrix} 1 \\ \frac{k - mp_1^2}{k} \end{Bmatrix} \quad 3.6$$

Similarly, for the second natural frequency, the second mode shape can be derived:

$$\begin{Bmatrix} X_1 \\ X_2 \end{Bmatrix}_2 = \begin{Bmatrix} 1 \\ \frac{k - mp_2^2}{k} \end{Bmatrix} \quad 3.7$$

Now combining terms into the final solution form, specifying the initial conditions, and solving for constants A , B , C , and D :

$$\begin{Bmatrix} x_1 \\ x_2 \end{Bmatrix} = \begin{Bmatrix} 1 \\ k - mp_1^2 \end{Bmatrix} \frac{1}{k} [A \sin(p_1 t) + B \cos(p_1 t)] + \begin{Bmatrix} 1 \\ k - mp_2^2 \end{Bmatrix} \frac{1}{k} [C \sin(p_1 t) + D \cos(p_1 t)] \quad 3.8$$

With initial conditions:

$$x_1(0) = 0 \quad 3.9$$

$$x_2(0) = 0 \quad 3.10$$

$$\dot{x}_1(0) = v_0 \quad 3.11$$

$$\dot{x}_2(0) = 0 \quad 3.12$$

Since the displacements of both masses are initially 0, the $\cos(pt)$ terms disappear:

$$B = D = 0$$

Solving for A and C using the initial velocity of the impact rod:

$$v_0 = p_1 A + p_2 C$$

$$0 = \frac{k - mp_1^2}{k} p_1 A + \frac{k - mp_2^2}{k} p_2 C$$

$$A = \frac{v_0 - p_2 C}{p_1} \quad 3.13$$

$$C = \frac{v_0 (mp_1^2 - k)}{mp_2 (p_1^2 - p_2^2)} \quad 3.14$$

Combining all terms into the final displacement solution:

$$\begin{Bmatrix} x_1 \\ x_2 \end{Bmatrix} = \begin{Bmatrix} 1 \\ k - mp_1^2 \end{Bmatrix} \frac{1}{k} A \sin(p_1 t) + \begin{Bmatrix} 1 \\ k - mp_2^2 \end{Bmatrix} \frac{1}{k} C \sin(p_1 t) \quad 3.15$$

Where A and C are given by Equations 3.13 and 3.14 respectively. Lastly, the time domain solution for the impact force, $F(t)$, experienced between the impact rod and implant can be derived, with all variables given above:

$$F(t) = k(x_1(t) - x_2(t)) \quad 3.16$$

Assuming a 10 g impact rod and impact stiffness of $9.8696 * 10^6 \text{ N/m}$, the plots in Figure 3.21 were generated. The impact stiffness was chosen such that a half cycle (contact time) of a one degree of freedom mass-spring system impacting a wall would take $100 \mu\text{s}$. This contact time value corresponded to estimates obtained from experiments and simulations of a 10 g rod impacting a TFA implant system [28].

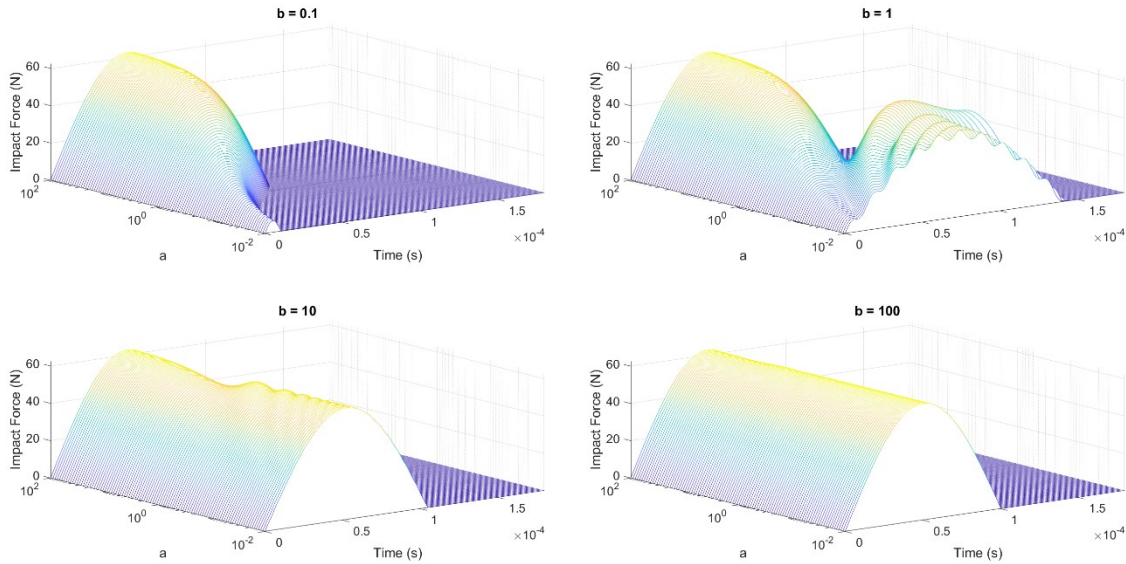


Figure 3.21: Impact force curves under various mass and stiffness ratio configurations

The plots show that beyond certain mass and stiffness ratio thresholds, information regarding both modes of vibration cannot be obtained by recording the impact force between the impact rod and implant alone. For the case where impact stiffness was set close to implant interface stiffness (top right plot) and implant mass was small compared to impact rod mass (roughly 100 times), two modes of vibration were clearly observed. The thought experiment suggests that in this configuration, it may be feasible to glean information pertinent the bone-implant interface by recording impact force or an equivalent signal, such as impact acceleration. This is the approach

utilized by the ASIST for small dental and craniofacial implants. However, in lots of other cases, simulated impact responses contained relatively little information about the system. For the present inputs, a steel impact rod with a mass of 10 *g* would not be appropriate for implants of roughly similar mass or larger or for systems with large bone-implant interface stiffness relative to impact stiffness. For a stiffness ratio of $b = 10$, information became limited, and for a ratio of $b = 100$, there was no information contained in the curves pertaining to multiple modes of vibration for an extremely wide domain of mass ratios. In the cases where the mass ratio was large, stiffness ratio was large, or both were large, the impact event turned into the scenario of a single degree of freedom mass-spring system impacting a wall. Early experimental data suggested that for the Periotest handpiece impacting a TFA implant system, this is the scenario that is encountered. The implant is much larger than the impact rod, and presumably, the effective stiffness of the elongated bone-implant interface is large relative to the impact stiffness. However, fundamental differences in geometry between small implant systems and TFA systems have been shown to play a significant role in impact response [28]. For small implants, the internal stiffness and natural frequency of the implant itself is far greater than the bone-implant system, making the treatment of the implant as a rigid body largely appropriate [28]. For the TFA system, this may not be the case. It has been shown that the internal stiffness of the implant may be comparable to the stiffness of the bone-implant system, making it vital to model the elastic properties of the implant itself [28].

3.3.2 1D Finite Element Model

Considering the revelation of the importance of implant geometry and stiffness for TFA implant systems, the complexity of the two degree of freedom model was increased by modelling the implant as a first order bar element, like the work of Mohamed [28]. In this model, the impact rod was still assumed to be a lumped mass with infinite stiffness; this assumption posits that it experiences negligible deformation compared to the system. Here, x_i was introduced as an axial nodal degree of freedom coordinate. All inertial and stiffness parameters were specified relative to base units m and k . All parameters were identical to those developed in Section 3.3.1, with the addition of a floating parameter, d , which specified the ratio of internal implant stiffness to impact stiffness, k . A schematic of the model can be viewed in Figure 3.22.

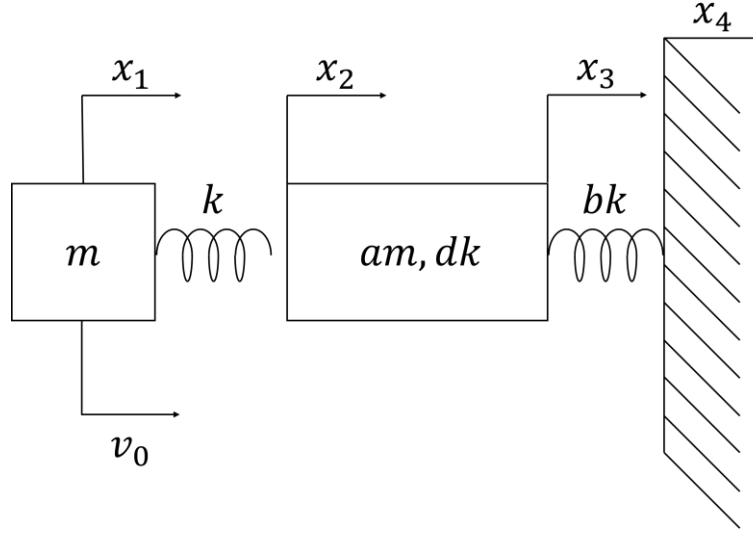


Figure 3.22: 1D finite element impact vibration model

For the first order bar element, the mass (m_b) and stiffness (k_b) matrices can be written as:

$$m_b = \frac{\rho AL}{6} \begin{bmatrix} 2 & 1 \\ 1 & 2 \end{bmatrix} = \frac{am}{6} \begin{bmatrix} 2 & 1 \\ 1 & 2 \end{bmatrix} \quad 3.17$$

$$k_b = \frac{EA}{L} \begin{bmatrix} 1 & -1 \\ -1 & 1 \end{bmatrix} = dk \begin{bmatrix} 1 & -1 \\ -1 & 1 \end{bmatrix} \quad 3.18$$

Where ρ is density, A is area, L is length, and E is elastic modulus. Crudely, these were specified in terms of the ratio to the base mass and impact stiffness of the impact rod. The system can then written in the form:

$$[M]\{\ddot{x}\} + [k]\{x\} = \{0\} \quad 3.19$$

Combining Equations 3.17 and 3.18 with the previously developed system (Equation 3.1), a system of coupled ordinary differential equations arises:

$$\begin{bmatrix} m & 0 & 0 & 0 \\ 0 & \frac{am}{3} & \frac{am}{6} & 0 \\ 0 & \frac{am}{6} & \frac{am}{3} & 0 \\ 0 & 0 & 0 & 0 \end{bmatrix} \begin{Bmatrix} \ddot{x}_1 \\ \ddot{x}_2 \\ \ddot{x}_3 \\ \ddot{x}_4 \end{Bmatrix} + \begin{bmatrix} k & -k & 0 & 0 \\ -k & (d+1)k & -dk & 0 \\ 0 & -dk & (b+d)k & -bk \\ 0 & 0 & -bk & bk \end{bmatrix} \begin{Bmatrix} x_1 \\ x_2 \\ x_3 \\ x_4 \end{Bmatrix} = \begin{Bmatrix} 0 \\ 0 \\ 0 \\ 0 \end{Bmatrix} \quad 3.20$$

Imposing the boundary condition $x_4 = 0$, the system reduces to three degrees of freedom:

$$\begin{bmatrix} m & 0 & 0 \\ 0 & \frac{am}{3} & \frac{am}{6} \\ 0 & \frac{am}{6} & \frac{am}{3} \end{bmatrix} \begin{Bmatrix} \ddot{x}_1 \\ \ddot{x}_2 \\ \ddot{x}_3 \end{Bmatrix} + \begin{bmatrix} k & -k & 0 \\ -k & (d+1)k & -dk \\ 0 & -dk & (b+d)k \end{bmatrix} \begin{Bmatrix} x_1 \\ x_2 \\ x_3 \end{Bmatrix} = \begin{Bmatrix} 0 \\ 0 \\ 0 \end{Bmatrix} \quad 3.21$$

To solve numerically, the system was reduced to a series of coupled first order ordinary differential equations by making the following substitutions:

$$\begin{bmatrix} x_1 \\ x_2 \\ x_3 \\ \dot{x}_1 \\ \dot{x}_2 \\ \dot{x}_3 \end{bmatrix} = \begin{bmatrix} x_{11} \\ x_{21} \\ x_{31} \\ x_{12} \\ x_{22} \\ x_{32} \end{bmatrix} \quad 3.22$$

Resulting in:

$$\begin{bmatrix} 1 & 0 & 0 & 0 & 0 & 0 \\ 0 & 1 & 0 & 0 & 0 & 0 \\ 0 & 0 & 1 & 0 & 0 & 0 \\ 0 & 0 & 0 & m & 0 & 0 \\ 0 & 0 & 0 & 0 & \frac{am}{3} & \frac{am}{6} \\ 0 & 0 & 0 & 0 & \frac{am}{6} & \frac{am}{3} \end{bmatrix} \begin{bmatrix} \dot{x}_{11} \\ \dot{x}_{21} \\ \dot{x}_{31} \\ \dot{x}_{12} \\ \dot{x}_{22} \\ \dot{x}_{32} \end{bmatrix} = \begin{bmatrix} 0 & 0 & 0 & 1 & 0 & 0 \\ 0 & 0 & 0 & 0 & 1 & 0 \\ 0 & 0 & 0 & 0 & 0 & 1 \\ -k & k & 0 & 0 & 0 & 0 \\ k & -(d+1)k & dk & 0 & 0 & 0 \\ 0 & dk & -(b+d)k & 0 & 0 & 0 \end{bmatrix} \begin{bmatrix} x_{11} \\ x_{21} \\ x_{31} \\ x_{12} \\ x_{22} \\ x_{32} \end{bmatrix} \quad 3.23$$

With initial conditions:

$$\begin{bmatrix} x_{110} \\ x_{210} \\ x_{310} \\ x_{120} \\ x_{220} \\ x_{320} \end{bmatrix} = \begin{bmatrix} 0 \\ 0 \\ 0 \\ v_0 \\ 0 \\ 0 \end{bmatrix} \quad 3.24$$

This system was solved in MATLAB using the ode45 function, the impact force was plotted according to Equation 3.16. Three plots were generated with $d = 225b$ (Figure 3.23), $d = 4b$

(Figure 3.24), and $d = b$ (Figure 3.25). Respectively, these ratios were chosen to represent the situations in which the natural frequency of the implant is roughly 15 times, two times, and equal to the natural frequency of the bone-implant system.

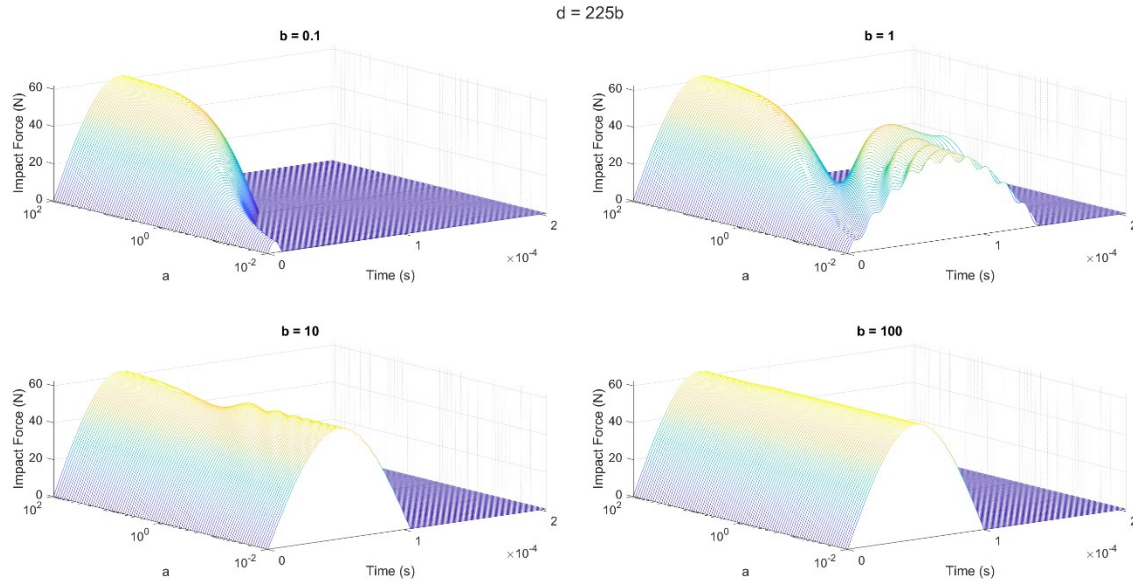


Figure 3.23: Impact force curves under various mass and stiffness ratio configurations with $d = 225b$

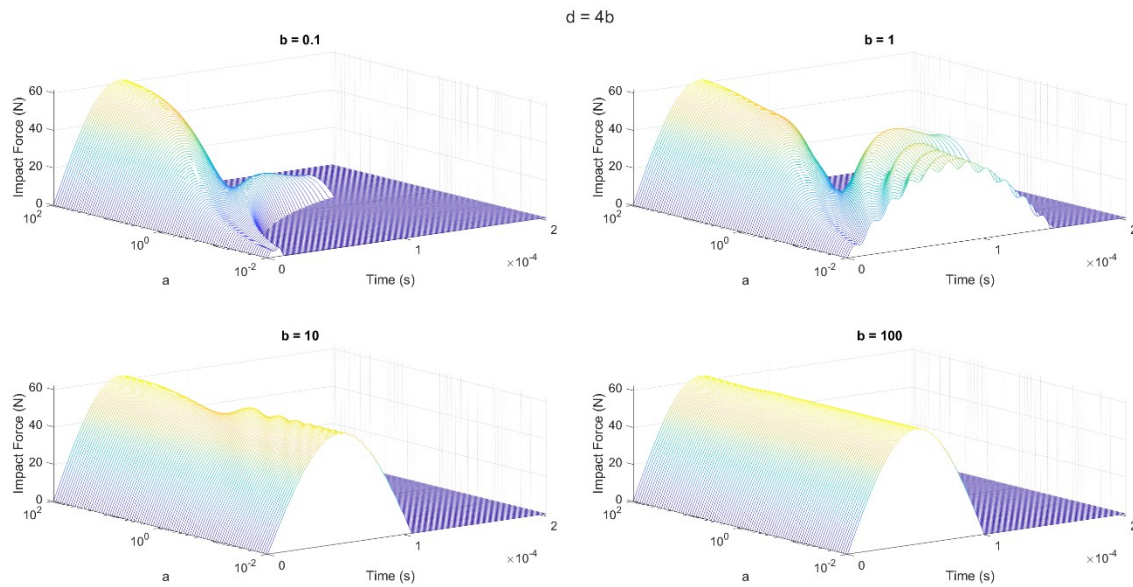


Figure 3.24: Impact force curves under various mass and stiffness ratio configurations with $d = 4b$

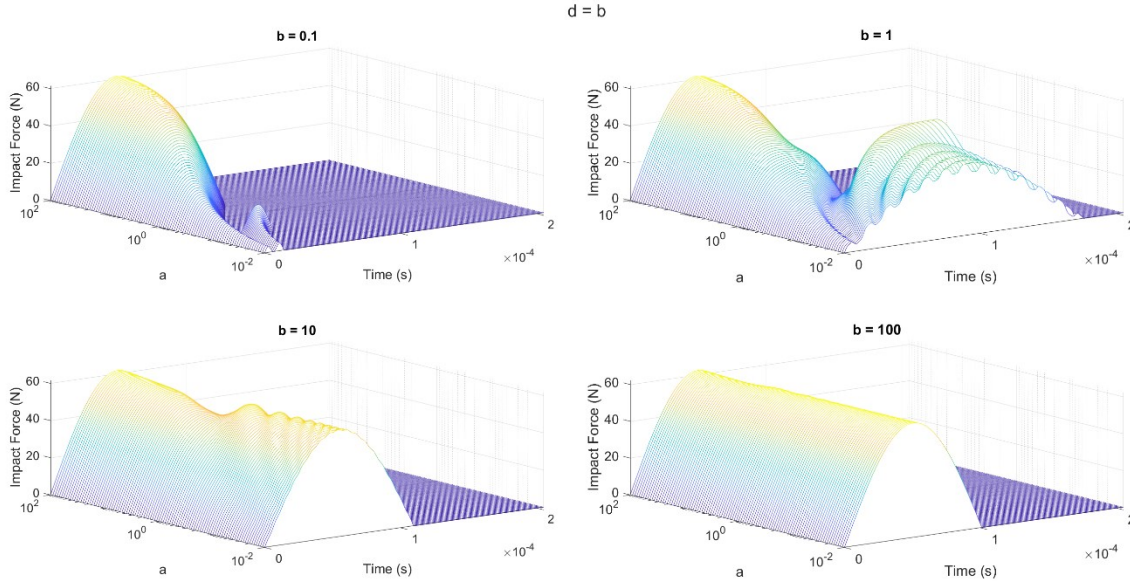


Figure 3.25: Impact force curves under various mass and stiffness ratio configurations with $d = b$

With the system modelled at a slightly higher degree of fidelity, overall similar behaviours to the two degree of freedom model were observed. In all cases, when the mass of the implant and stiffness of the bone-implant interface were high relative to the mass of the impact rod and impact stiffness, little information about the system could be gleaned from monitoring impact force, and the profile started to resemble a strike against a rigid wall. Again, this appears to be the situation encountered with the TFA system when using the Periotest handpiece. All findings considered, the objectives of the project were better met by an approach grounded in experimental modal analysis theory than the ASIST approach used for dental and craniofacial implants.

3.3.3 One Degree of Freedom Model

Considering the early trajectory of the project towards experimental modal analysis, it was appropriate to further idealize the impact event as a half cycle of a forced, damped, single degree of freedom vibration problem, as represented in Figure 3.26. This is a continuous contact dynamic model called a spring-dashpot model [65] and would be appropriate to predict the characteristics of loading profiles produced by simple impactors (impact hammers in experimental modal analysis) on synthetic TFA models. In the diagram, F_0 is any net force acting on the impact rod, x is the displacement of the impact rod once contact is established, v_0 is the velocity at impact, m is the mass of the impact rod, k is the impact stiffness, and c is the impact damping coefficient.

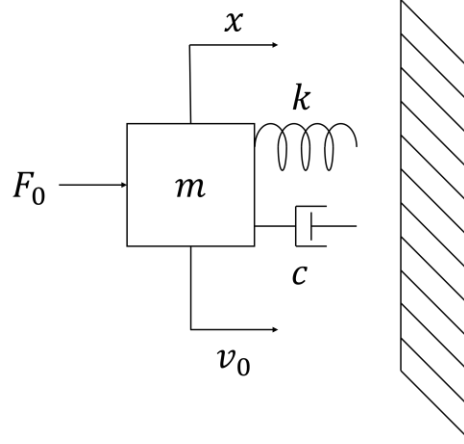


Figure 3.26: One degree of freedom impact model

Applying Newton's second law, an ordinary differential equation of the problem can be derived:

$$\begin{aligned}\sum F &= m\ddot{x} \\ -kx - \dot{x}c + F_0 &= m\ddot{x} \\ m\ddot{x} + c\dot{x} + kx &= F_0\end{aligned}\tag{3.25}$$

The homogeneous solution to this basic problem is given by:

$$x_H = e^{-\zeta pt} \left[\frac{v_0 + \zeta p x_0}{\sqrt{1 - \zeta^2} p} \sin(\sqrt{1 - \zeta^2} pt) + x_0 \cos(\sqrt{1 - \zeta^2} pt) \right]\tag{3.26}$$

Where ζ is the damping ratio, p is the natural frequency of the undamped system, t is time, and x_0 is the initial displacement of the mass. Assuming:

$$x_0 = 0\tag{3.27}$$

$$v_0 \neq 0\tag{3.28}$$

The homogeneous solution simplifies to:

$$x_H = e^{-\zeta pt} \frac{v_0}{\sqrt{1 - \zeta^2} p} \sin(\sqrt{1 - \zeta^2} pt)\tag{3.29}$$

Since the forcing function is a constant, it follows that the particular solution is also a constant:

$$x_p = C$$

Substituting the particular solution back into Equation 3.25 and solving:

$$kC = F_0$$

$$C = \frac{F_0}{k}$$

$$x_p = \frac{F_0}{k} \quad 3.30$$

The total solution is given by the superposition of the homogeneous and particular solutions:

$$x(t) = x_H + x_p \quad 3.31$$

$$x(t) = e^{-\zeta pt} \frac{v_0}{\sqrt{1 - \zeta^2 p}} \sin(\sqrt{1 - \zeta^2 p} t) + \frac{F_0}{k} \quad 3.32$$

Where the undamped natural frequency is given by:

$$p = \sqrt{\frac{k}{m}} \quad 3.33$$

Multiplying the total solution by k and adding the first time derivative of the total solution multiplied by c gives the force exerted on the wall during impact:

$$F(t) = e^{-\zeta pt} v_0 \left(\frac{k}{\sqrt{1 - \zeta^2 p}} \sin(\sqrt{1 - \zeta^2 p} t) + c \cos(\sqrt{1 - \zeta^2 p} t) \right) + F_0 \quad 3.34$$

When impact damping and external forces are neglected, the solution simplifies to:

$$F(t) = \frac{v_0 k}{p} \sin(pt) \quad 3.35$$

The implications of this simplified model will be further explored in Section 3.6.5.

3.4 Benchtop Prototype Synthesis

3.4.1 Components

A modular benchtop prototype system was developed for initial testing and discovery of design specifications for later handheld prototypes. A plethora of components were ordered as well as reused from preceding projects (capstone solenoid) to give a variety of options for configuration testing. A part summary can be viewed in Table 3.1, and a photo of the components can be viewed in Figure 3.27.

Table 3.1: Benchtop prototype part summary. HF: holding force

| Part Description | Manufacturer/Distributor | Part Number |
|--|--------------------------|-------------|
| Capstone Solenoid | Ledex Dormeyer Saia | 195202-231 |
| 5 kg HF Electromagnet | Adafruit Industries | 3873 |
| 15 kg HF Electromagnet | DFRobot | DFR0797 |
| 25 kg HF Electromagnet | Adafruit Industries | 3875 |
| $\emptyset \frac{1}{8} \text{ in} \times \frac{1}{16} \text{ in}$ Neodymium Magnet | McMaster-Carr | 5862K138 |
| $\emptyset \frac{1}{8} \text{ in} \times \frac{1}{8} \text{ in}$ Neodymium Magnet | McMaster-Carr | 5862K101 |
| $\emptyset \frac{1}{8} \text{ in} \times \frac{3}{16} \text{ in}$ Neodymium Magnet | McMaster-Carr | 5862K166 |
| $\emptyset \frac{1}{8} \text{ in} \times \frac{1}{4} \text{ in}$ Neodymium Magnet | McMaster-Carr | 5862K114 |
| $\emptyset \frac{1}{8} \text{ in} \times \frac{1}{2} \text{ in}$ Neodymium Magnet | McMaster-Carr | 5862K125 |
| 5 mm Sleeve Bearing | McMaster-Carr | 6679K32 |
| 8 mm Sleeve Bearing | McMaster-Carr | 6679K12 |

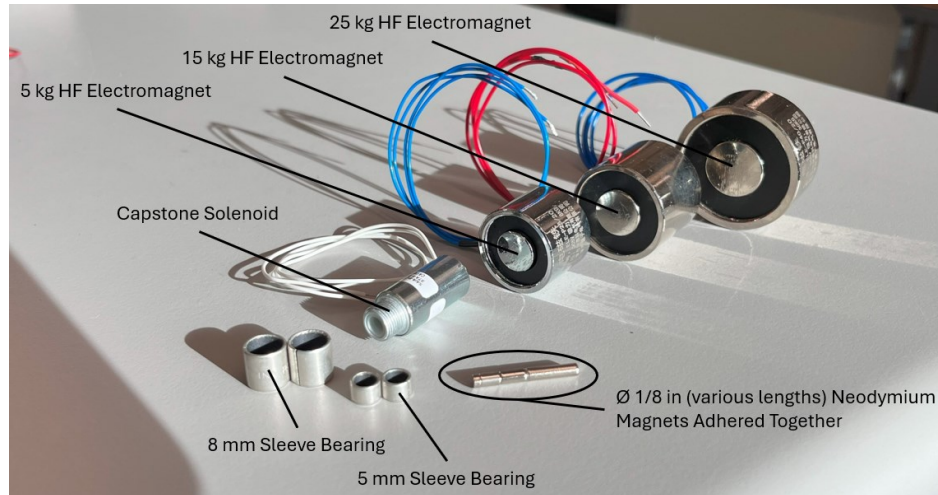


Figure 3.27: Photo of benchtop prototype components. HF: holding force

3.4.2 Magnetic Flux Density Measurements

As a part of initial benchtop prototype evaluation, the magnetic flux density of the solenoid, electromagnets, and neodymium magnets were evaluated with a TD8620 Gauss meter (HFBTE, China) (Figure 3.28).



Figure 3.28: TD8620 Gauss meter (HFBTE, China)

Measurements were taken by holding the wand perpendicular to the surface of the object of measurement and by using the hold function to capture the highest magnetic flux density recording in units of Gauss. Five magnetic flux density measurements were taken and averaged for each component. A plot of magnetic flux density measurements for the neodymium magnets in

comparison to the Periotest handpiece permanent magnet can be viewed in Figure 3.29. Only the $\varnothing 1/8 \text{ in} \times 1/16 \text{ in}$ magnet fell below the Periotest permanent magnet in magnetic flux density.

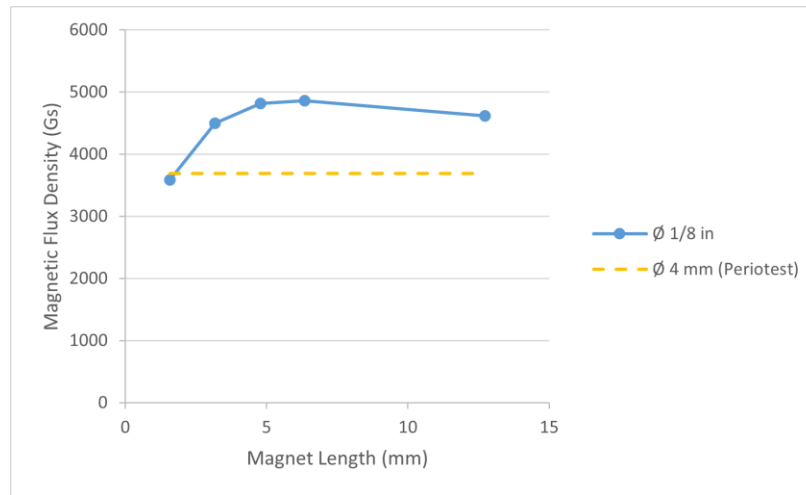


Figure 3.29: Permanent magnet magnetic flux density measurements

Additionally, solenoid and electromagnet performance were tested along various actuation voltage rails (DC voltage supplied to coil). Theoretical estimations of ASIST solenoid and electromagnet magnetic flux density were also plotted according to the calculations and results presented in Appendix A. The results can be viewed in Figure 3.30. All coils experienced relatively linear increases in magnetic flux density with increases in actuation voltage. This was the expected outcome, as magnetic flux density is theoretically proportional to current, which is proportional to voltage according to Ohm's law. However, diminishing returns should eventually be observed as the coil increases in temperature. Fortunately, this point was not reached within the 5 – 10 V operating range. The electromagnets were only rated for 5 V operation, and consequently, became very hot at higher voltages. The electromagnets performed with much higher magnetic flux density than the capstone solenoid and ASIST coils, likely due in part to their large diameters (many turns) and ferromagnetic cores. Consequently, the capstone solenoid was eliminated from prototype consideration. The experimental and theoretical estimates were relatively close for the ASIST solenoid but were farther apart for the electromagnet. This may have been due in part to the fact that it was difficult to position the Gauss meter wand perpendicular to the surface of the electromagnet, as it was set behind the solenoid.

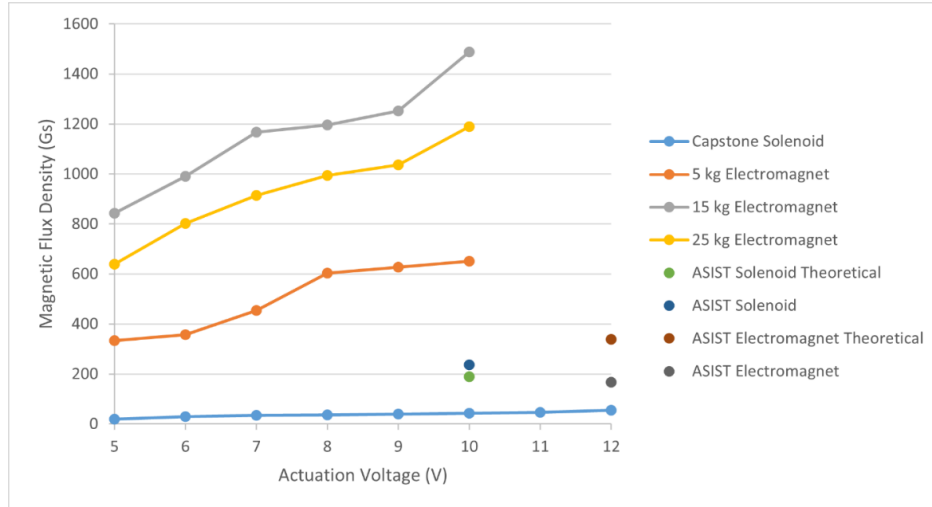


Figure 3.30: Magnetic flux density measurements of various magnetic coils

Magnetic flux density vs. distance was also plotted for the 15 *kg* holding force (HF) electromagnet at three actuation voltages (5; 7.5; 10 V). The plot can be viewed in Figure 3.31. Again, magnetic flux density clearly increased with actuation voltage, but flux appeared to exponentially decay with distance from the electromagnet surface.

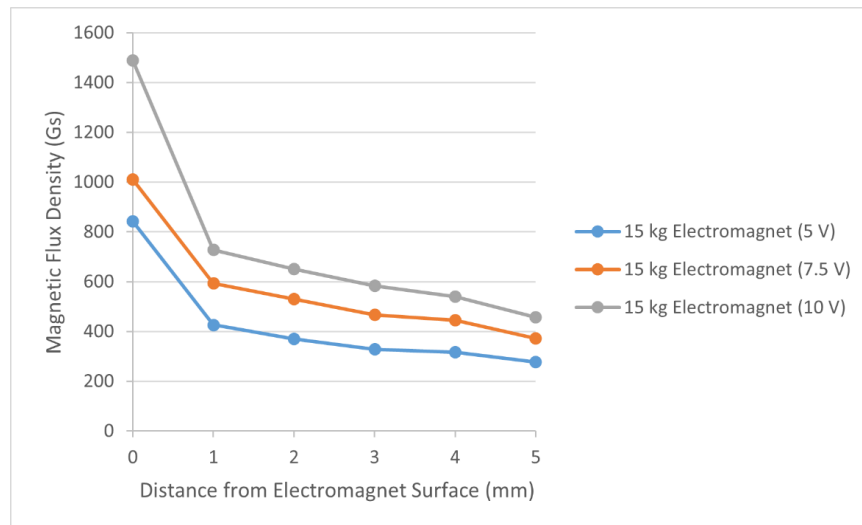


Figure 3.31: Magnetic flux density vs. distance from 15 *kg* HF electromagnet active surface

3.4.3 Modular Prototype

With the performance of various parts characterized in terms of magnetic flux density, other tests could be commenced and practical decisions regarding an optimal configuration of a benchtop prototype could be made. A modular benchtop prototype was designed from T-slot bar. The design

borrowed heavily from the form of the Periotest handpiece. There was an impact rod which would have one of the $\varnothing 1/8$ in neodymium magnets superglued to the rear and a nut screwed to the front as a linear motion limiter. Various 3D-printed supports housed the electromagnets and sleeve bearings and could interface with the T-slot bar structure. A stopper with or without a load cell installed could interface with the structure and limit the forward motion of the impact rod, or the impact rod could be positioned in front of another impact surface, such as a TFA implant system. This prototype allowed for two different sizes of impact rod ($12\text{ g @ } \varnothing 5\text{ mm}$; $44\text{ g @ } \varnothing 8\text{ mm}$), five neodymium magnet lengths, three electromagnet sizes, and a variety of impact scenarios. A solid model graphic can be viewed in Figure 3.32.

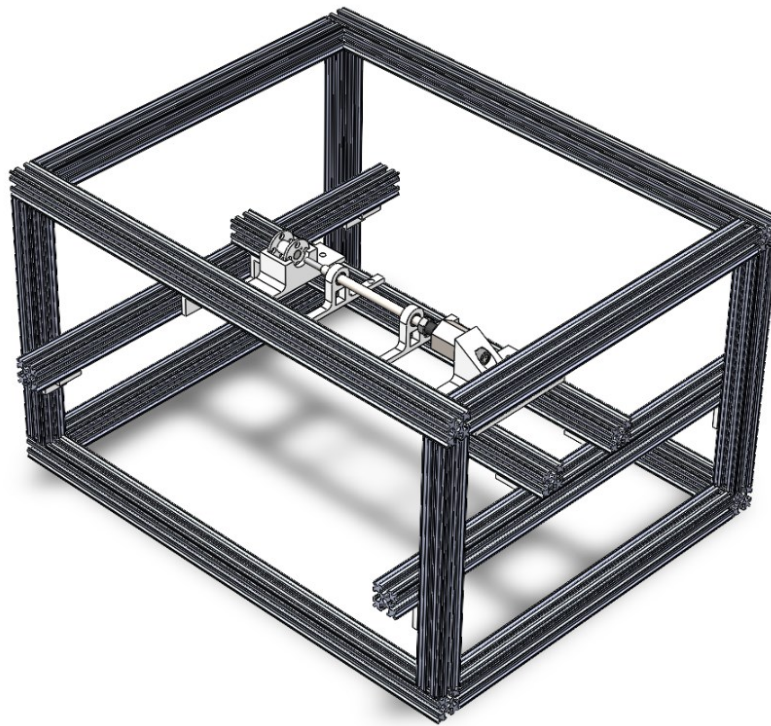


Figure 3.32: Solid model of modular benchtop prototype

An Arduino Uno with Adafruit Motor Shield V2 was used to control the actuation of any electromagnet used in the setup. An actuation code snippet can be viewed in Figure 3.33, which would fire the impact rod 16 times in 4 s (4 Hz). It was found that an actuation time (duration of DC current applied to coil) of 50 ms with a release period of 100 ms and retraction period of 100 ms resulted in smooth impact rod oscillatory motion.

```

void loop() {
  for (int i = 1; i <= 16; i++) {
    myMotor->run(BACKWARD);
    delay(100);
    myMotor->run(FORWARD);
    delay(50);
    myMotor->run(RELEASE);
    delay(100);
  }
  myMotor->run(BACKWARD);
  delay(100);
  myMotor->run(RELEASE);
  exit(0);
}

```

Figure 3.33: Electromagnet actuation code snippet

3.5 Initial Benchtop Prototype Testing

3.5.1 Average Velocity

The average velocities of various prototype configurations were crudely measured with the high-speed video setting of a smartphone camera. The average of velocity of the 12 *g* rod was measured over a 7 *mm* distance, while the average velocity of the 44 *g* rod was measured over a 4 *mm* distance. High-speed video was recorded at 240 *fps* and subsequently analyzed frame by frame. A sample video frame can be viewed in Figure 3.34.

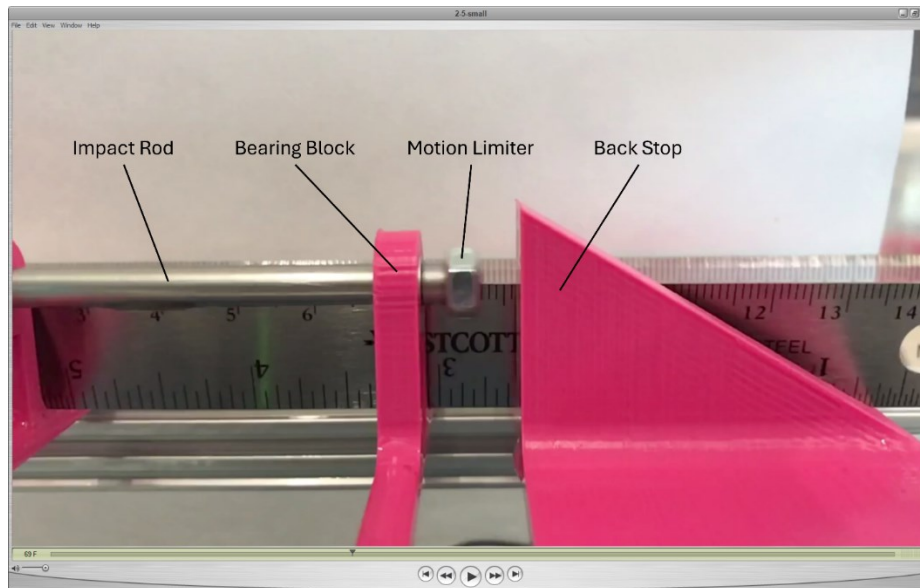


Figure 3.34: Frame capture of smartphone high-speed video recording

Average velocity measurements were taken for each rod and in combinations of the 25 kg HF electromagnet with every neodymium magnet (Figure 3.35) and the $\varnothing 1/8 \text{ in} \times 1/2 \text{ in}$ neodymium magnet with every electromagnet. Lower strength combinations were not plotted if the impact rod failed to fire.

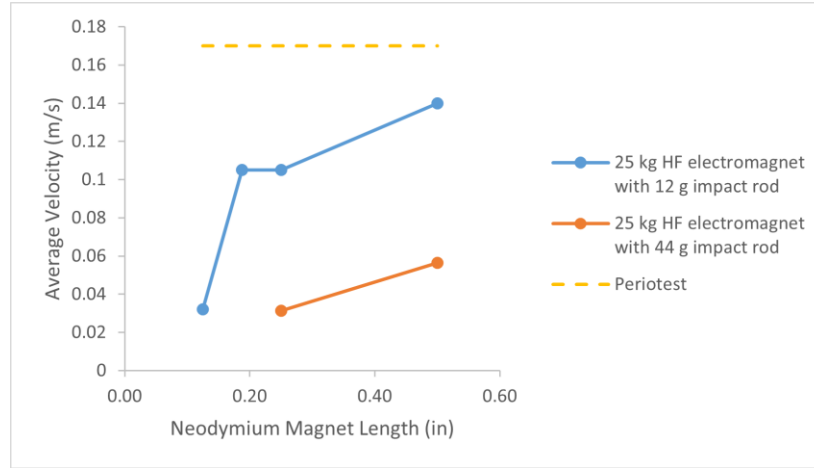


Figure 3.35: Average velocity of 25 kg HF electromagnet paired with neodymium magnets of varying length

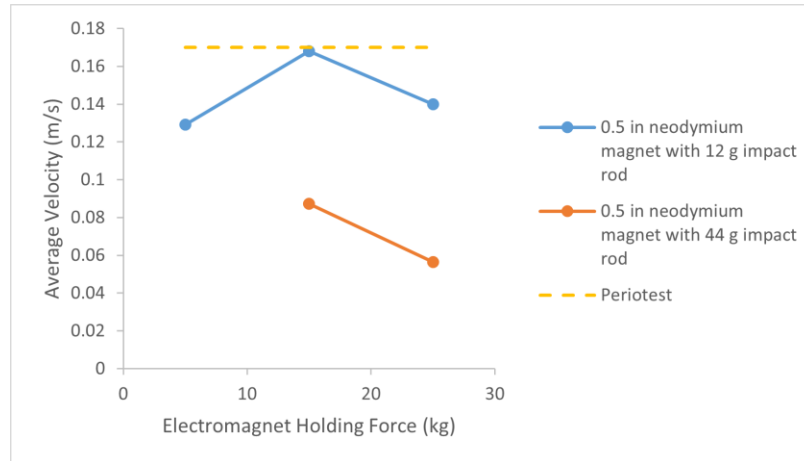


Figure 3.36: Average velocity of $1/2 \text{ in}$ neodymium magnet paired with electromagnets of varying HF

Unsurprisingly, the 12 g impact rod was able to reach a broader range of velocities than the 44 g impact rod. Only the combination of 12 g impact rod, $1/2 \text{ in}$ neodymium magnet, and 15 kg HF electromagnet was able to reach the threshold Periotest handpiece speed of 170 mm/s as measured by Robertson [59]. However, it is worth noting that the average speeds were likely well below the top speeds of the prototype configurations. Although it was surprising that the 25 kg HF electromagnet performed worse than the 15 kg, this agreed with the magnetic flux density

results. It was promising that at least one combination was able to conservatively reach the Periotest threshold.

3.5.2 Impact Force

3.5.2.1 Initial Testing

Impact force was recorded for a variety of prototype configurations. In this set of tests, the configurations consisted of the 15 kg HF electromagnet (discovered to both produce the highest magnetic flux densities and average velocities) in combination with every neodymium magnet and the $\varnothing 1/8 \text{ in} \times 1/2 \text{ in}$ neodymium magnet with every electromagnet. A photo of the setup can be viewed in Figure 3.37.

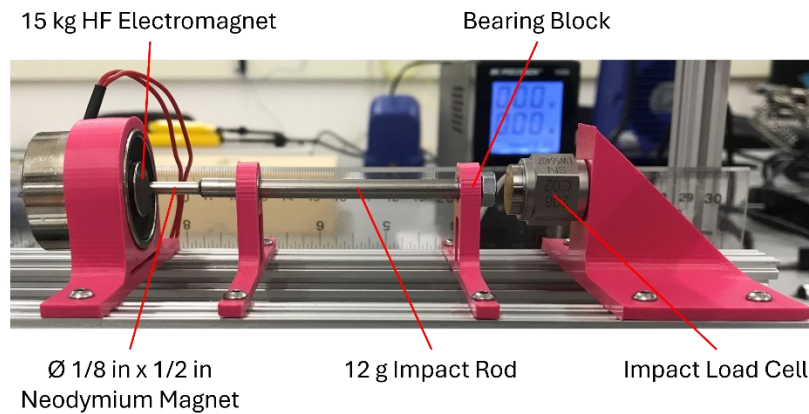


Figure 3.37: v1 benchtop prototype impact load cell setup

Impact force was recorded for each setup at three actuation voltages (5; 7.5; 10 V) and three actuation times (voltage applied for 50; 75; 100 ms). Peak impact force of the ensemble average of 15 strikes was recorded for each intersection of factors. The results for the 12 g rod can be viewed in App. Figure B.1, App. Figure B.2, and App. Figure B.3 in Appendix B, and the results for the 44 g rod can be viewed in App. Figure B.4, App. Figure B.5, and App. Figure B.6, also in Appendix B. Taken together, these plots led to a few key takeaways. To start, the mass of the impact rod played an important role in the peak force and repeatability of a given configuration. In general, the 12 g rod showed a higher degree of clustering for different configurations. Additionally, the 12 g rod could be fired and register an impact force at a greater number of configurations, especially for low magnetic flux density combinations of the neodymium magnets and electromagnets. For large actuation voltages, the 44 g rod lacked the repeatability of the 12 g

rod but often excelled in impact force. In general, increasing actuation time led to small increases in impact force, while increasing actuation voltage led to far greater gains overall. Finally, the 1/2 in length neodymium magnet in combination with the 15 kg HF electromagnet consistently resulted in the highest impact forces and was the only combination for which the 44 g rod could be fired at 5 V. With this configuration knowledge, future testing would primarily be conducted with the 15 kg HF electromagnet and $\varnothing 1/8$ in \times 1/2 in neodymium magnet. Investigating strikes at different actuation times would also be avoided in favor of altering actuation voltage to elicit different strike velocities and impact forces.

3.5.2.2 Refined Testing

The benchtop prototype was reprinted for better axial alignment between the electromagnet and neodymium magnet. The v2 prototype setup can be viewed in Figure 3.38.

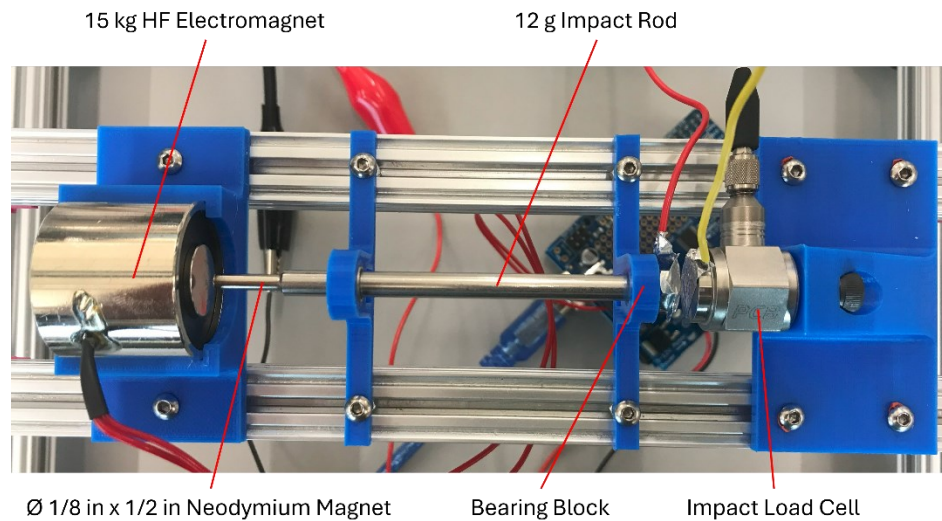


Figure 3.38: v2 benchtop prototype with impact load cell

This setup was further compared to the ASIST in terms of impact loading. It can be seen in Figure 3.39 that the shape of the ASIST loading profile was comparable at two actuation times as well as to the benchtop prototype. The benchtop prototype managed to exceed the peak force of the ASIST at an actuation voltage of 5 V. Similarities in curve shape were unsurprising considering the closeness in impact rod mass. Differences in actuation components and controls largely resulted in differences in peak force rather loading profile shape.

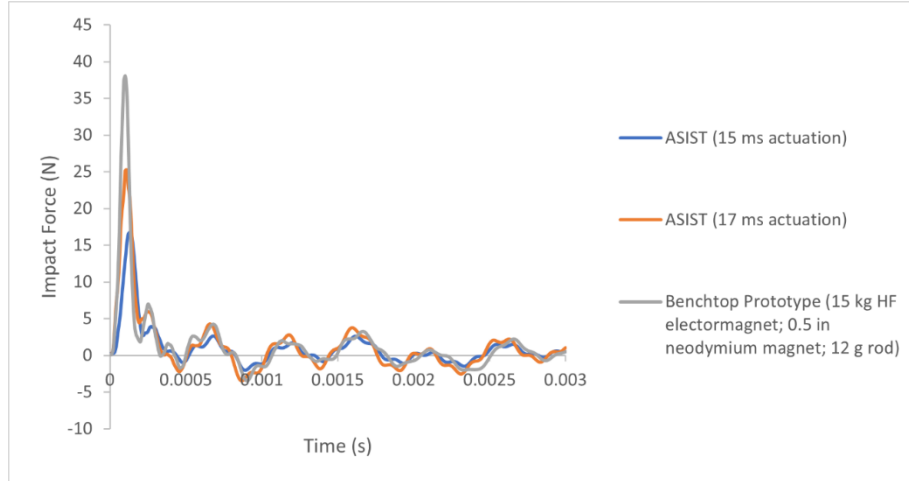


Figure 3.39: Benchtop prototype impact loading profile comparison to ASIST

Further repeatability testing was conducted by investigating hysteresis effects. The peak impact forces of the benchtop setup were recorded at eight actuation voltage (5 – 12 V) for five ascending trials and five descending trials executed in a consecutive, alternating fashion (first trial ascension). The results can be viewed in Figure 3.40.

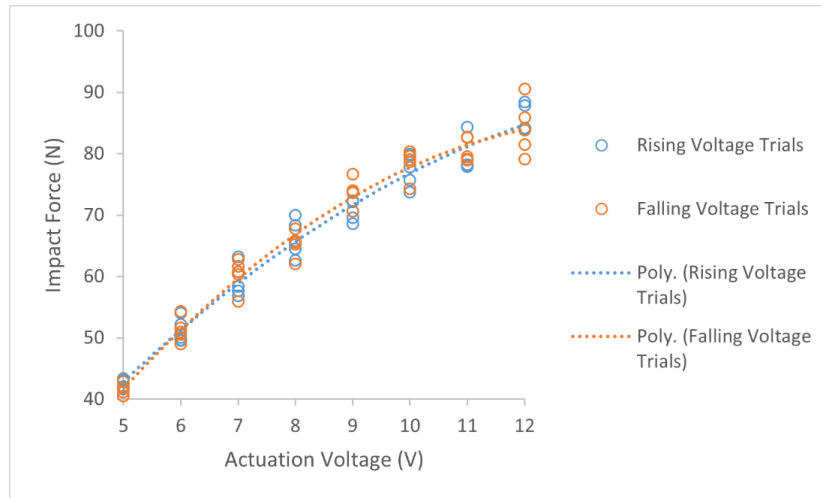


Figure 3.40: Impact force vs. actuation voltage for rising and falling trials

There were no hysteresis effects; however, diminishing returns and increased variability with increased actuation voltage were observed, likely due to electromagnet performance decreases with heat accumulation. Finally, a quick litmus test was performed to see if the benchtop prototype could elicit a substantial acceleration response from a TFA system. A MEMS ADXL1004 accelerometer (Analog Devices, USA) was fixed to the dual cone adapter of a silicone interface setup (see Section 3.6.1 for details). The accelerometer was adhered to the implant with double-

sided tape in the transverse direction. The implant was also struck transversely at the dual cone, and the acceleration response was recorded (Figure 3.41).

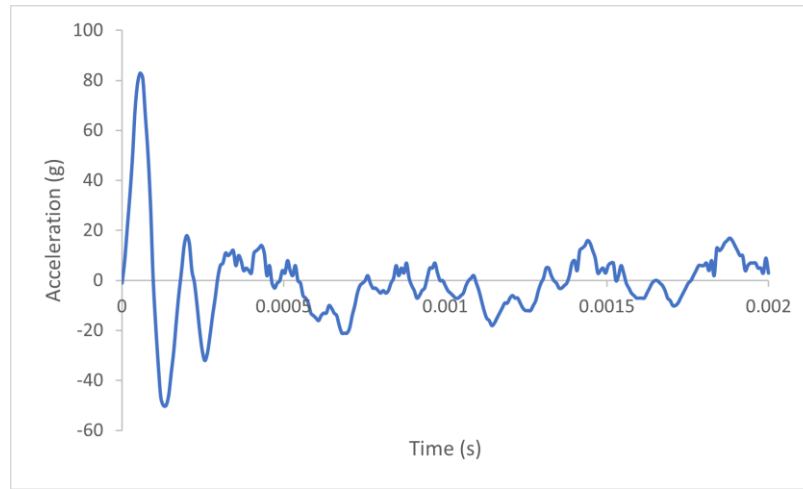


Figure 3.41: Replica implant transverse acceleration response (silicone interface)

The prototype was able to elicit a strong response, with the maximum acceleration exceeding 80 *g*. The prototype was deemed suitable for further investigative testing on TFA implant systems and deployment in an extensive development study.

3.6 Recommendations for Development and Evaluation Study

3.6.1 TFA Implant Models

The first TFA experimental models were produced with Sawbones cylinders (Pacific Research Group, USA) and replica OPL Type A transfemoral implants. This section will focus on the results from a Sawbones cylinder model with superglue interface. A replica OPL implant was anchored in a drilled Sawbones cylinder with Lepage Ultra Gel superglue. The Sawbones cylinder was drilled such that a uniform 0.1 *mm* thick interface would form between the implant and composite bone. The bone-implant system was fixed within a benchtop clamp with a damping liner that minimized the influence of external vibrations and mechanical noise. A detailed list of components and assembly notes can be found in Table 3.2. An annotated picture of the setup can be viewed in Figure 3.42.

Table 3.2: Replica implant with superglue interface experimental model components

| Experimental Model | |
|---------------------------|---|
| <i>Component</i> | <i>Description</i> |
| Sawbones Cylinder | Sawbones 3403-36 straight cylinder (Pacific Research Group, USA). Drilled to allow for uniform interface. |
| Implant Stem | Replica 140 mm OPL Type A implant stem manufactured in-house. |
| Superglue Interface | LePage Ultra Gel superglue (LePage, Canada). Interface 0.1 mm thick. |
| Dual Cone Adapter | 68.5 mm OPL Type A dual cone adapter (Permedica, Italy). |
| Internal Locking Screw | OPL internal locking screw (Permedica, Italy). Tightened to 10 Nm. |
| GV Connector | OPL GV connector (Permedica, Italy). Interfacing component between implant system and prosthetic. |
| Distal Screw | OPL distal screw (Permedica, Italy). Tighten to 2 Nm without GV connector installed or 10 Nm with GV connector installed. |
| Damping Liner | Silicone liner used to provide mechanical isolation to bone-implant system from bone clamp. |
| Bone Clamp | Clamp fixed to table with squeezing force controlled by exposed threaded shaft length (37 mm). |
| Cantilever Brace | Multi-degree-of-freedom adjustable clamp used to lightly brace cantilevered end of Sawbones cylinder. |

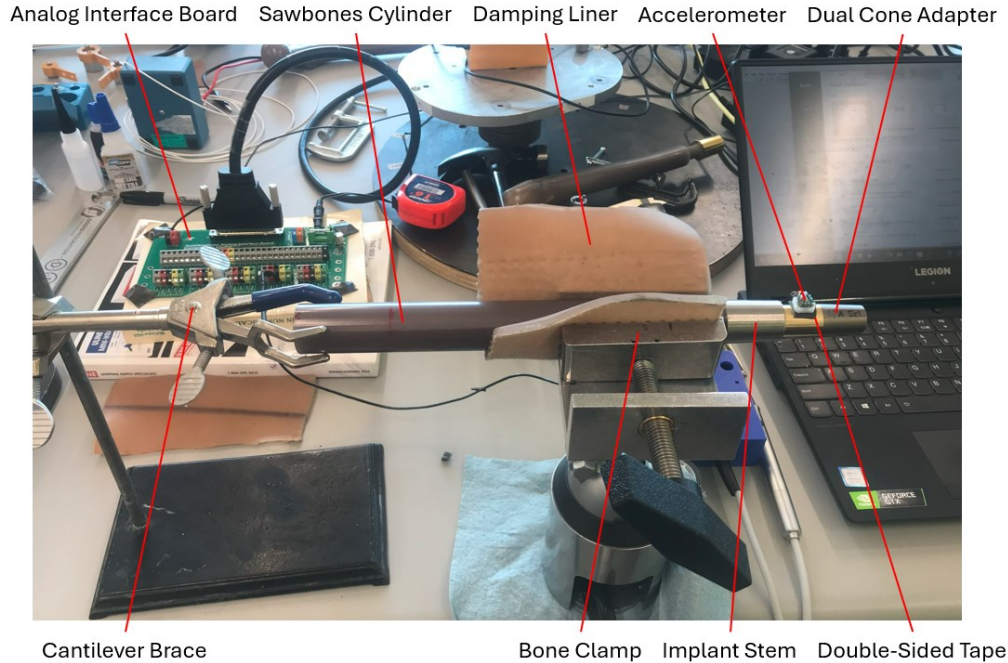


Figure 3.42: Sawbones cylinder superglue interface setup

Vibration data was recorded with a MEMS accelerometer adhered to the implant in variety of locations and orientations with double-sided tape. Data was recorded via an acquisition system with components detailed in Table 3.3 and layout visualized in Figure 3.43.

Table 3.3: Data acquisition system components

Acquisition System

| Component | Description |
|-----------------------------|--|
| Accelerometer | Analog Devices ADXL1004 MEMS Accelerometer (Analog Devices, USA). |
| Accelerometer Raft | 3D-printed support for accelerometer protection. |
| Double-Sided Tape | Double-sided gorilla tape for adhesion between accelerometer and implant. |
| Analog Interface Board | Interface board for analog signals, DC power, and signal grounds. Designed in-house. |
| Analog-to-Digital Converter | National Instruments NI-9205 DAQ (National Instruments, USA). |
| Host PC | Host PC for signal processing through LabVIEW GUI (National Instruments, USA). |

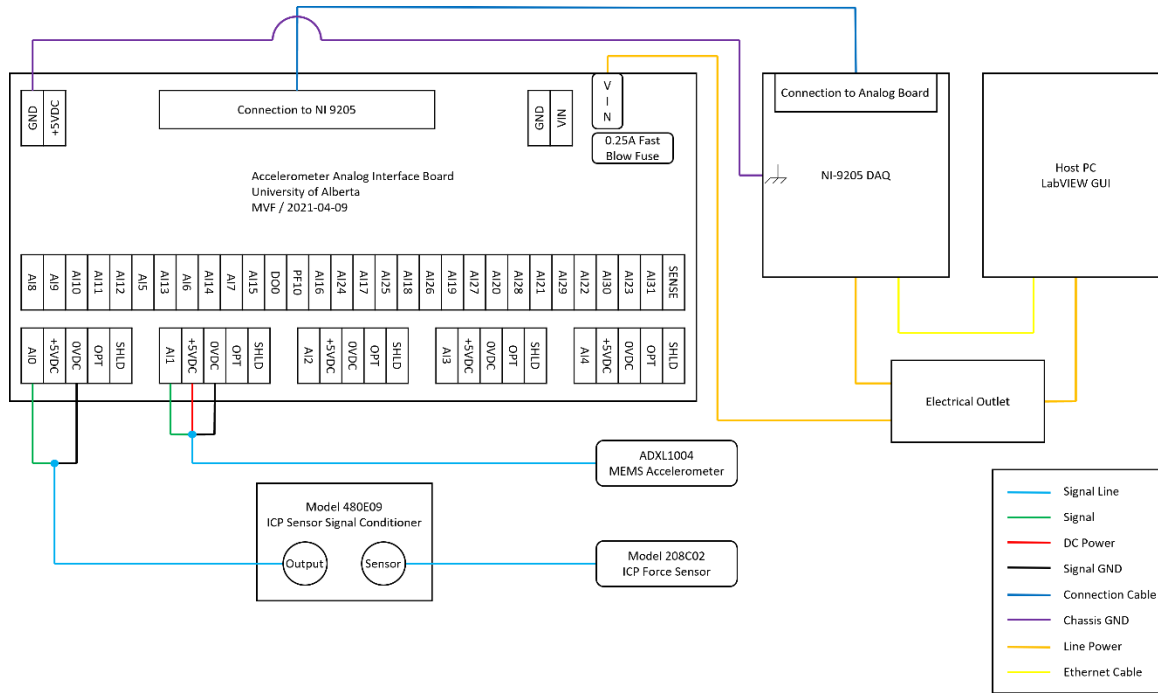


Figure 3.43: Data acquisition system schematic

3.6.2 Impact Interface Stiffness

3.6.2.1 Load Cell Data

In experimental modal analysis practice, one of the primary ways to optimize input frequency bandwidth is by the selection of an appropriate impact tip [64]. Input force frequency spectrum content is governed by the time pulse (contact time) applied to the system [64]. In accordance with Equations 3.33 and 3.35, there are fundamentally two ways that the contact time of the impact problem can be altered:

1. Decrease the stiffness of the impact interface.
2. Increase the mass of the impact rod.

In general, the harder the tip, the wider the frequency spectrum, and the softer the tip, the narrower the frequency spectrum [64]. Tips generally range from soft rubber, air capsules, plastic, to metal [64]. The effective stiffness of a uniform beam with constant area is directly related to its elastic modulus by Equation 3.36.

$$k_{eff} = \frac{EA}{L} \quad 3.36$$

Here, preliminary testing was conducted to determine the types of materials that could be suitable as impact interface substitutes. Five materials were selected, representing a wide range of elastic moduli. The materials, as well as their elastic moduli and effective axial stiffness of a 5 mm coupon, are listed in Table 3.4.

Table 3.4: List of material coupons with associated mechanical properties

| Material Coupon | Modulus of Elasticity (GPa) | Diameter (mm) | Length (mm) | Effective Stiffness (N/mm) |
|------------------------|------------------------------------|----------------------|--------------------|-----------------------------------|
| Neoprene Rubber | 0.00614 | 6.35 | 5.00 | 38.8898 |
| Silicone Rubber | 0.0167 | 6.35 | 5.00 | 105.775 |
| Delrin® Acetal Resin | 3.30 | 6.35 | 5.00 | 20901.7 |
| Aluminum | 68.9 | 5.00 | 5.00 | 270570 |
| Low-Carbon Steel | 200 | 5.00 | 5.00 | 785398 |

The material coupons were superglued to the end of the 12 g impact rod and were first used to strike the impact load cell. The setup with a sample material coupon can be viewed in Figure 3.44.

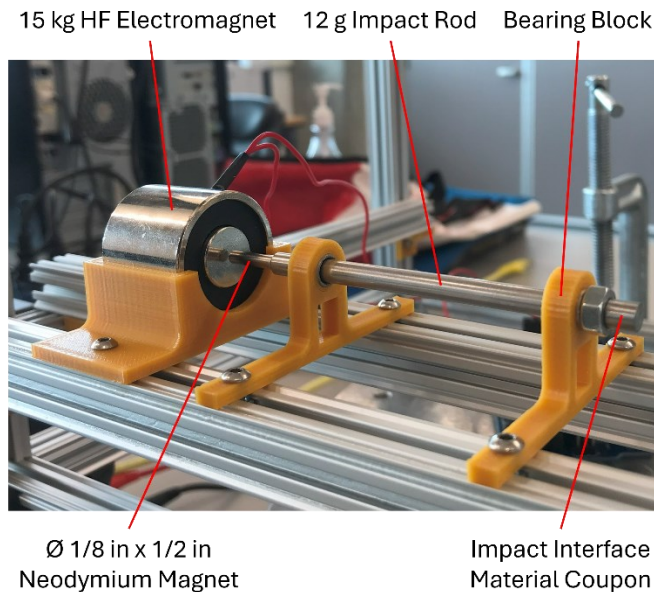


Figure 3.44: Impact interface test setup

The ensemble average of 15 strikes was taken and peak impact force was extracted. Additionally, contact times, or the widths of the loading profiles, were obtained. A plot of peak impact forces can be viewed in Figure 3.45, and a plot of the contact times can be viewed in Figure 3.46.

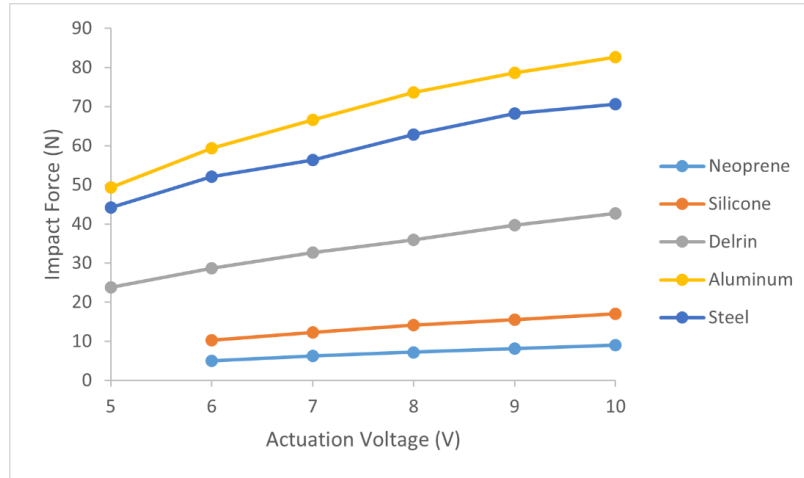


Figure 3.45: Impact force vs. actuation voltage for impact interfaces with varying mechanical properties

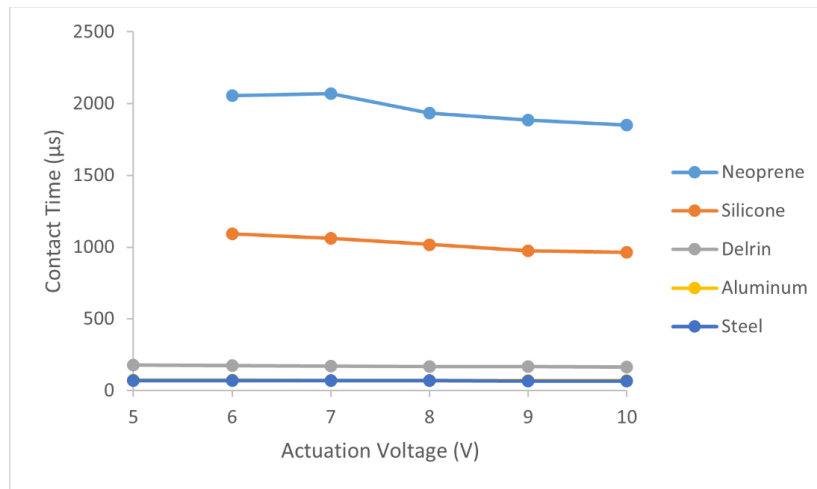


Figure 3.46: Contact time vs. actuation voltage for impact interfaces with varying mechanical properties (steel and aluminum curves overlapping)

Rubber coupons provided significantly longer contact times than the other interfaces, but any gain came at the cost of impact force. In general, contact time had an inverse relationship with impact force, and the materials followed this relationship in a predictable way: the least elastic materials had the longest contact times and lowest impact forces, while the most elastic materials had short contact times and large impact forces. Steel and aluminum had nearly indistinguishable contact times at all voltages ($\sim 70 \mu s$) and slightly different impact forces. Considering similarities in

contact time and relative stiffness, these materials would likely perform similarly in any future study. Differences between the impact force curves in Figure 3.45 may be attributed to variability in the position of the impact rod relative to the load cell (gap between the impact face of the rod in its retracted position and the load cell), temperature of the electromagnet (decreased performance with continuous use above rated voltage), or even the relationship between impact velocity and total mass (steel typically 2.5 times denser than aluminum). Delrin® had an average contact time across voltages of $170\ \mu\text{s}$, with a slight decrease with increased voltage, and silicone and neoprene rubber reached contact times in excess of $1\ \text{ms}$, with noticeable decreases with increased voltage. The decreases may have been indicative of some non-linearity in material properties or the system at large. Any effect would appear to be less significant, if at all, for the metal and Delrin® interfaces. It is also worth noting that the damping properties of the rubber materials were likely to play a more significant role than in other interfaces and contribute to contact times in accordance with Equation 3.34 (increases in damping ratio resulted in increases to the period of the system).

3.6.2.2 Accelerometer Data

Each material was tested on the first replica implant superglue setup. Strikes were administered and recorded in the transverse direction without the GV connector installed. Time domain responses were recorded as the ensemble average of 15 strikes. The associated power spectra were also recorded. A sample power spectrum at $10\ \text{V}$ actuation can be viewed in Figure 3.47, with a reduced domain view of the same plot in Figure 3.48. It should be noted that this was the only actuation voltage for which the silicone rubber impact interface could trigger the accelerometer. Even then, the material coupon had to be reduced to $1\ \text{mm}$ thickness for triggering.

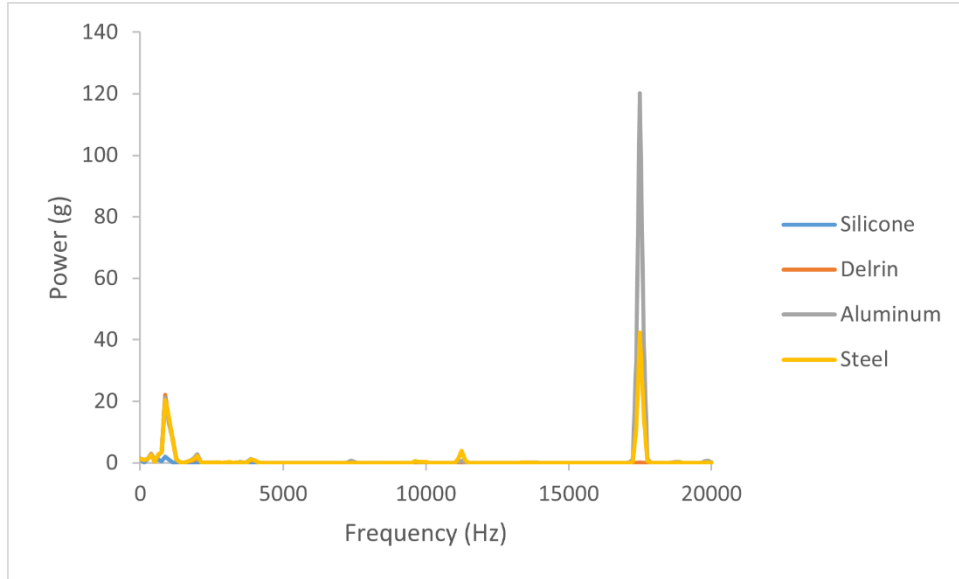


Figure 3.47: Superglue interface power spectra for strikes with varying impact interface stiffness – full domain

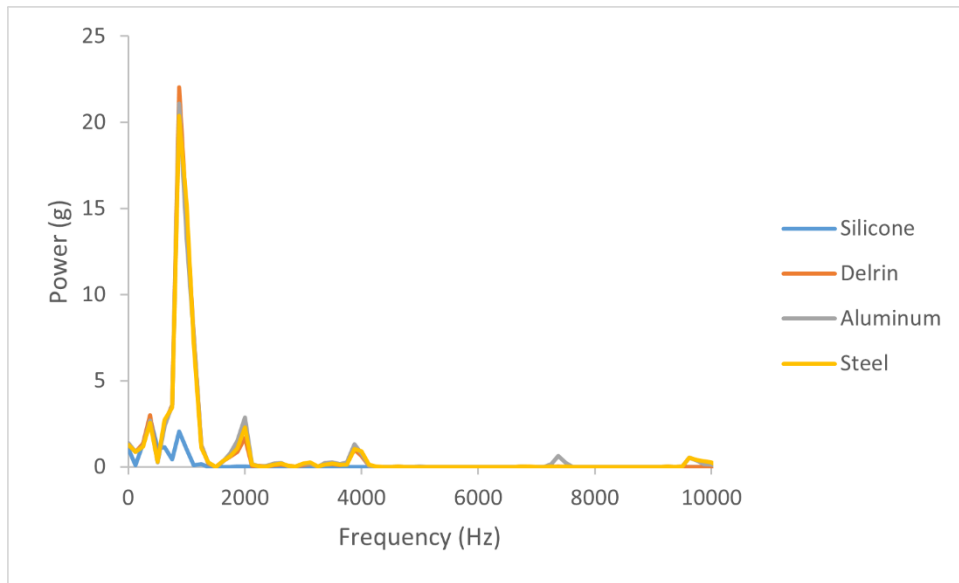


Figure 3.48: Superglue interface power spectra for strikes with varying impact interface stiffness – reduced domain

Steel and aluminum provided the highest powers and widest excitation bandwidths among the interfaces. Two dominant frequencies were elicited at 875 Hz and 17500 Hz. The Delrin® and silicone interfaces completely attenuated the latter frequency. Steel, aluminum, and Delrin® all had similar contributions to the former frequency, while silicone lowered the frequency to a level indistinguishable from mechanical noise within the system. With these results, it was concluded that two levels of impact interface stiffness, particularly those belonging to the families of a stiff

thermoplastic ($\sim 3 \text{ GPa}$) and metal ($69 - 200 \text{ GPa}$) would be appropriate for further investigation.

3.6.3 Impact Rod Mass

3.6.3.1 Axial Signals

Equations 3.33 and 3.35 suggested that impact rod mass was an important way to alter contact time, and therefore, frequency excitation of an impact event [64]. In accordance, additional masses were crudely hung from the baseline impact rods (nominally 10 and 40 g ; formally 12 and 44 g) with double-sided tape, and the rods were used to impact the superglue interface setup in the axial and transverse directions with the GV connector installed. A picture of an axial configuration can be viewed in Figure 3.49.

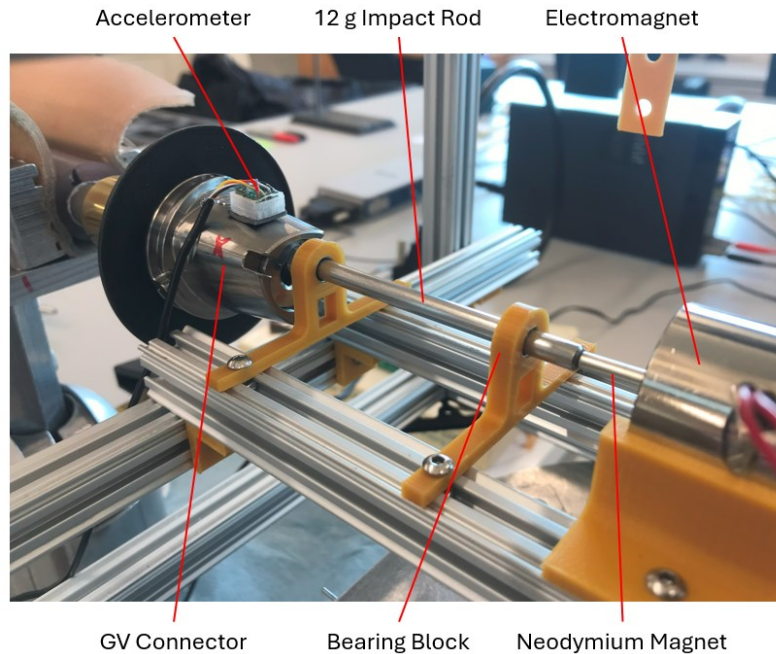


Figure 3.49: Axial strike with GV connector installed

Results plots can be viewed in Figure 3.50 (12 g base rod) and Figure 3.51 (44 g base rod) for axial strikes.

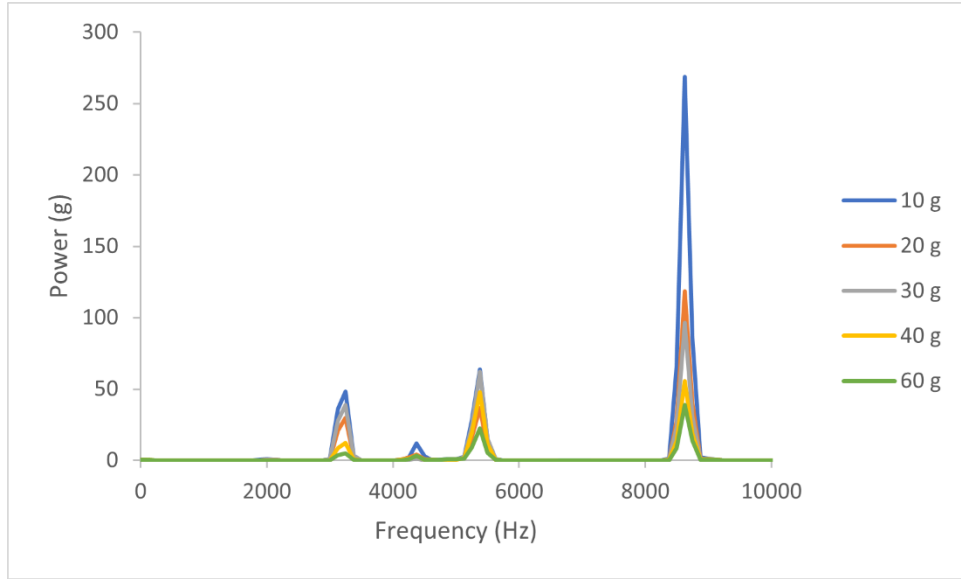


Figure 3.50: Superglue interface axial frequency response – 12 g base rod (nominal mass in legend)

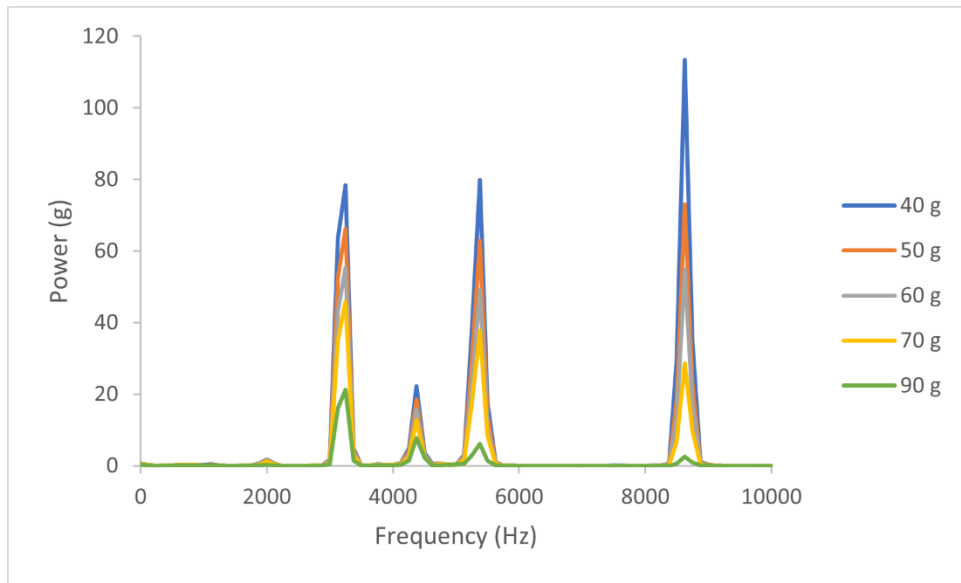


Figure 3.51: Superglue interface axial frequency response – 44 g base rod (nominal mass in legend)

Together, the plots suggested that mass could be effectively used to alter signal composition. The dominant natural frequency was 8625 Hz for small rods (approximate 10 – 40 g), and the composition shifted left and greatly attenuated higher frequencies for large rods (50 – 90 g). However, there was also a clear signal power trade off for large rods in that they likely could not be actuated to the same impact velocities as smaller rods and resulted in diminished power for each frequency bin (beyond a certain mass threshold). Up to some threshold, however, increased mass could likely contribute to power gains in low frequency bins.

3.6.3.2 Transverse Signals

The same approach was tested in the transverse direction without the GV connector installed. A picture of a transverse configuration can be viewed in Figure 3.52.

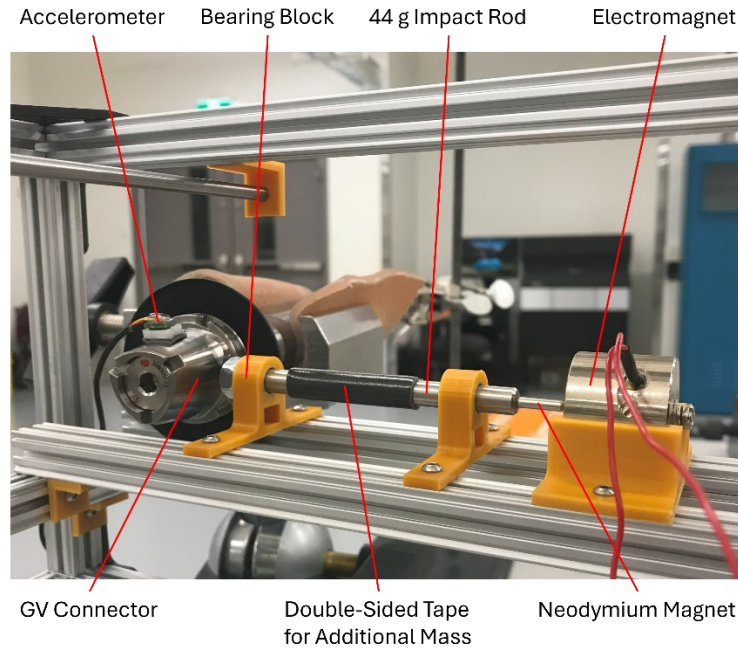


Figure 3.52: Transverse strike configuration with GV connector installed

The results for heavy rods tested in the transverse orientation without the GV connector installed can be viewed in Figure 3.53 (full domain) and Figure 3.54 (reduced domain).

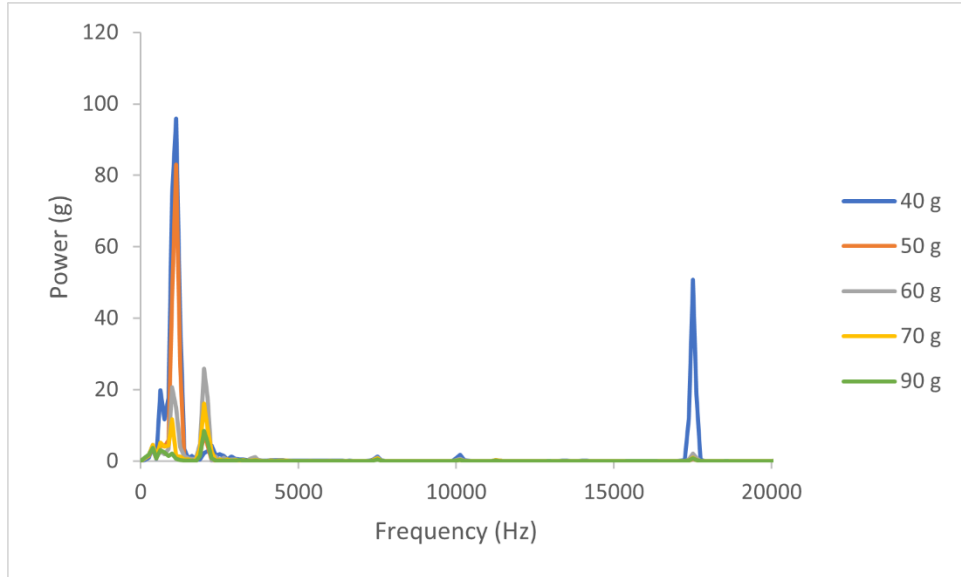


Figure 3.53: Superglue interface transverse frequency response (nominal mass in legend)

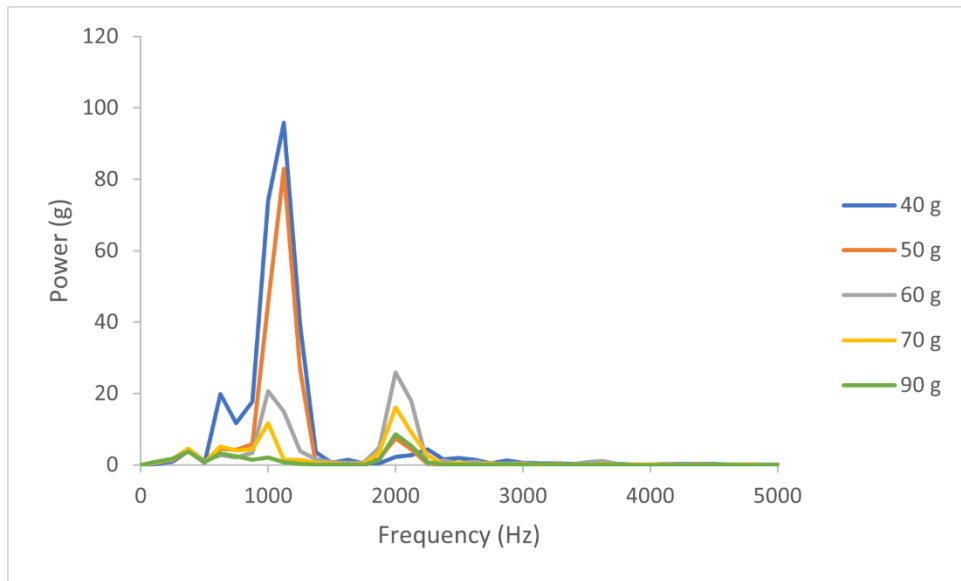


Figure 3.54: Superglue interface transverse frequency response – reduced domain (nominal mass in legend)

Here, similar patterns to the axial results were observed: heavier impact rods resulted in the attenuation of high frequency components but also in the reduction of signal power and quality. Beyond 50 *g* of impact rod mass, there was a precipitous power drop off at 1125 *Hz*. After testing a variety of axial and transverse configurations with and without the GV connector installed, it was determined that the limiting, or noisiest, configuration was the transverse orientation with the GV connector installed. The responses of the 50, 60, 70, and 90 *g* rods are represented in App. Figure C.1, App. Figure C.2, App. Figure C.3, and App. Figure C.4, respectively (Appendix C). In

these ascending mass plots, significant noise began to show up in the transition from 60 to 70 *g*, placing the upper limit on impact rod mass at 60 *g*. From 10 to 60 *g*, and in a variety of configurations, axial and transverse signal composition could be altered while mitigating detrimental decay in signal power and meaningful influence of mechanical noise.

3.6.4 Actuation Voltage and Impact Tip Geometry

3.6.4.1 Actuation Voltage

In addition to interface stiffness and rod mass, a few practical influencing factors were considered. Actuation voltage was already known to influence impact rod velocity and force; however, according to Equation 3.35, changing the parameter would have little bearing on contact time and signal composition. A limited batch of signals were collected to prove this concept. The 12 *g* impact rod was used to strike the superglue setup in the transverse direction with the GV connector installed. Signals were recorded for actuation voltages of 5, 7.5, and 10 *V*, and the power spectra were plotted in Figure 3.55.

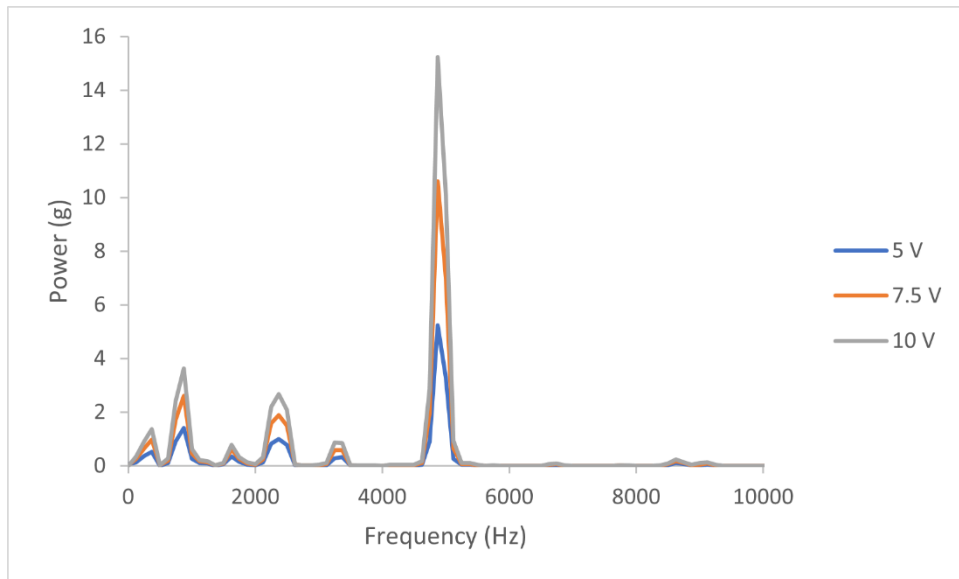


*Figure 3.55: Power spectra of superglue interface with GV connector installed. Transverse strikes with 12 *g* impact rod*

Actuation voltage, directly related to impact velocity, had a bearing primarily on signal band power rather than composition. Raising actuation voltage was concluded to be the simplest way to improve signal power and quality without altering relative frequency contributions.

3.6.4.2 Impact Interface Geometry

Shortcomings of the ASIST included its susceptibility to the influence of angle of attack and operator experience level [15, 50]. These concerns would matter less to the modal analysis based approach to TFA systems, because most of the information obtained in a signal would belong to the transient free vibration of the implant after the impact rod separates from the system. It is largely contact time that dictates response composition, and as seen in Section 3.6.2, many magnitude orders of interface stiffness difference were needed to meaningfully change impact contact time and signal composition. However, it is still desirable to optimize the repeatability of the response signals, especially among different operators. The angle of attack of the device was certainly a factor that could influence impact location and stiffness. For a flat impact interface, as in the Periotest handpiece and benchtop prototypes, any minute angular divergence from the impact rod running perpendicular to the implant strike surface would result in a different impact interface distribution and center of pressure location. For example, in the case of a $\varnothing 5\text{ mm}$ impact rod, an infinitesimal angular rotation would result in a 2.5 mm center of pressure shift. Likewise, for a $\varnothing 8\text{ mm}$ impact rod, it would be 4 mm . This concept is demonstrated in Figure 3.56.

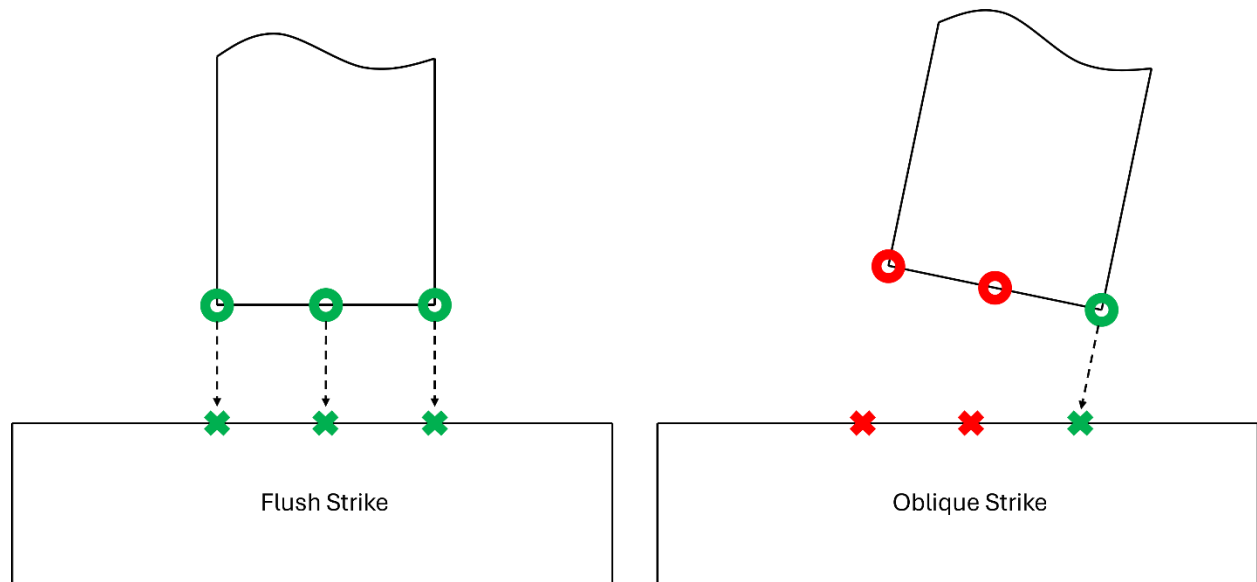


Figure 3.56: Flush vs. oblique strike diagram

For the application, it was hypothesized that a central/collinear and direct impact event would create more reliable conditions than eccentric and oblique contact [65]. Additionally, the reliance

of impact interface stiffness on impact tip geometry was demonstrated. The displacement, δ , of a bar under a distributed axial force, $F(x)$, is given by:

$$\delta = \int_0^L \frac{F(x)}{EA(x)} dx \quad 3.37$$

Where x is the axial coordinate of the bar, L is total length, E is elastic modulus, and $A(x)$ is the area of the bar at a given point along its axis. Now, let Δ be the axial deformation for a unit axial force:

$$\Delta = \int_0^L \frac{1}{EA(x)} dx \quad 3.38$$

Using a flexibility approach, the effective stiffness, k_{eff} , of the bar can be calculated as the inverse of Δ :

$$k_{eff} = \frac{1}{\Delta} = \frac{1}{\int_0^L \frac{1}{EA(x)} dx} \quad 3.39$$

Equation 3.39 shows that k_{eff} has a direct relationship with $A(x)$; moreover, if $A(x)$ is a constant, the relationship turns into Equation 3.36. This implies that changing the area of impact, which would occur in the flush vs. oblique strike of a flat impact interface, would change impact stiffness and potentially elicited signal compositions. This concept was verified with a quick series of tests with the superglue setup without the GV connector installed and in the transverse direction. In these tests, the 44 g impact rod was aligned ‘flush’ with the dual cone adapter, meaning the contacting surfaces of the impact rod and implant were aligned as close as possible to parallel, or ‘oblique,’ meaning the impact rod was arbitrarily skewed from the flush position. The results can be viewed in Figure 3.57.

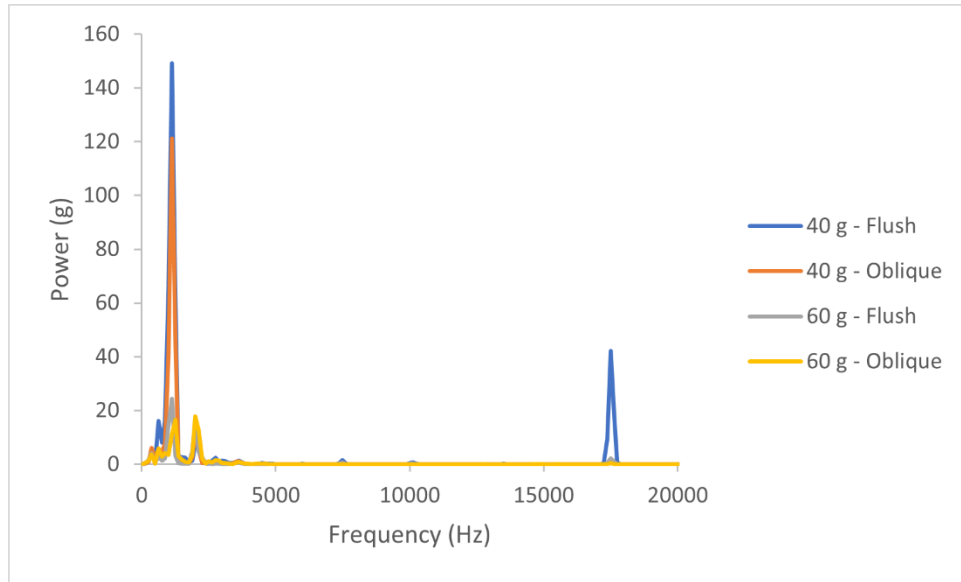


Figure 3.57: Flush vs. oblique strikes in transverse direction on superglue interface setup without GV connector installed

Some compositional changes were observed, especially for the 44 *g* impact rod, where the flush strike had a uniquely high amplitude at 17500 *Hz*, which was in line with the expected result. For the ideal flush case, the impact interface stiffness was expected to be higher than for an oblique strike, meaning higher frequency signal components would be amplified. This was verified. For future experiments, it was hypothesized that altering tip geometry could provide an avenue to control impact interface stiffness and strike reliability. A flat interface was hypothesized to vary greatly in impact interface stiffness and deliver the lowest level of reliability due to wandering center of pressure. Conical and hemispherical tips were hypothesized to improve reliability, but it was unclear whether one would provide an advantage, whether quantitative or anecdotal, over the other. For instance, a hemispherical tip with a large radius may provide an advantage over a point contact (conical tip) in terms of resistance to variability in strike angle of attack, whereas a conical tip may provide an advantage for operator strike positioning.

3.6.5 Application of Impact Model

Equations 3.34 and 3.35 were used to model the loading profiles of impact rods ranging from 10 to 60 *g* in mass for two impact stiffnesses. The stiffnesses were selected such that the first level would result in a contact time of 200 μ s for a 10 *g* rod in an undamped impact, and the second level would result in a contact time of 100 μ s for the same set of conditions. The impact velocity

was set to 200 mm/s for all rods. Impact profiles and associated power spectral density estimates for an undamped impact can be viewed in Figure 3.58.

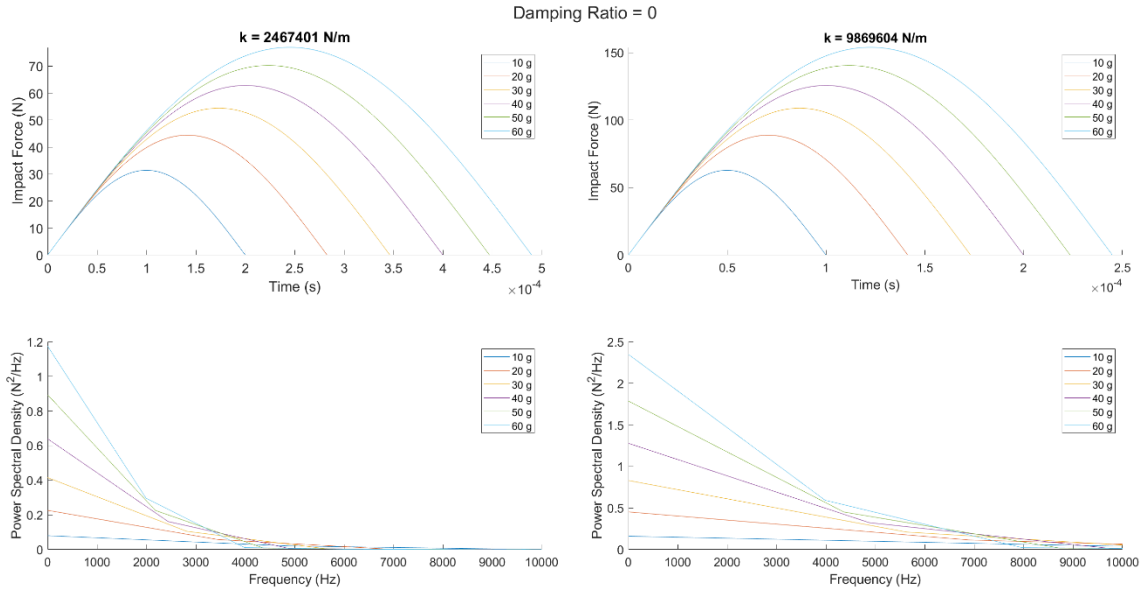


Figure 3.58: Simulated impact curves for $\zeta = 0$

Mass was observed to increase contact time as well as peak impact force, and contact time was doubled when mass was quadrupled. Increasing contact time cut down the frequency excitation bandwidth, and increasing peak force raised power spectral density levels, especially at low frequencies. Moving from the higher stiffness level to the lower, the frequency excitation bandwidth was significantly reduced, and frequencies in the range of $8 - 10 \text{ kHz}$ were likely to be completely attenuated. Within the simulated domain, it appeared likely that signals with a broad range of characteristics would be possible to generate on experimental apparatuses.

3.6.6 Experimental Pilot Testing

With factors and levels of interest explored in the previous tests, a final set of confirmation tests were conducted with the first high-fidelity setup. The setup consisted of a 160 mm OPL Type A implant stem anchored in a Sawbones composite femur with silicone adhesive. Once installed, the setup was allowed to cure for 72 hours (Figure 3.59). Further details can be found in Section 0.

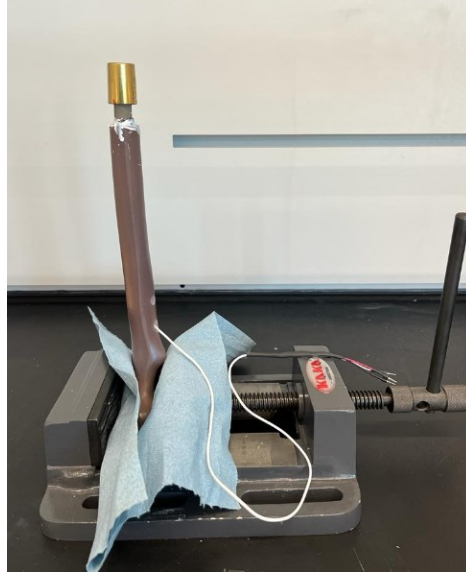


Figure 3.59: Curing silicone interface setup

The implant was secured in the bone clamp and struck in the axial direction with both the ASIST and 40 g impact rod. Time domain responses can be viewed in Figure 3.60, and frequency domain responses can be viewed in Figure 3.61 with normalized responses in Figure 3.62.

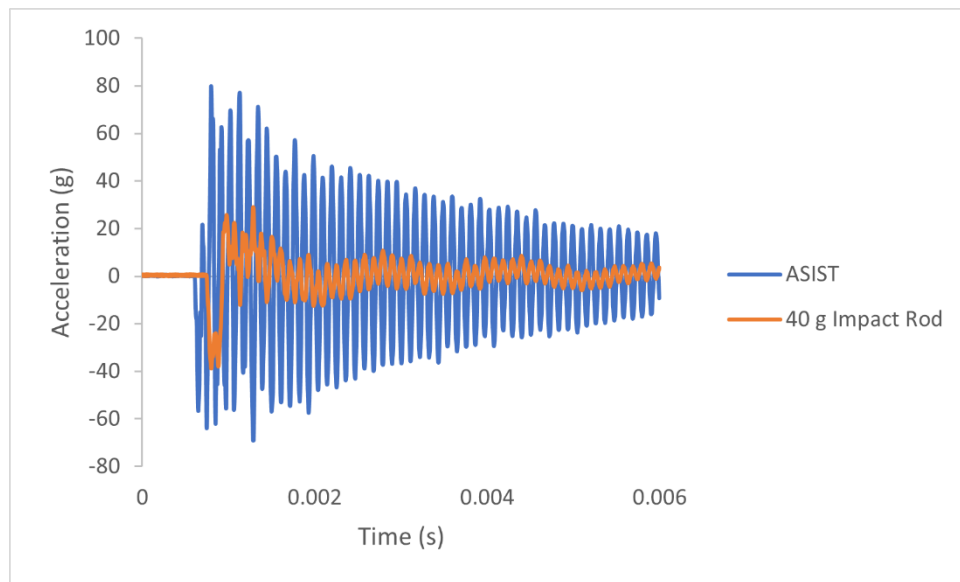


Figure 3.60: Time domain responses of silicone interface – ASIST vs. 40 g impact rod

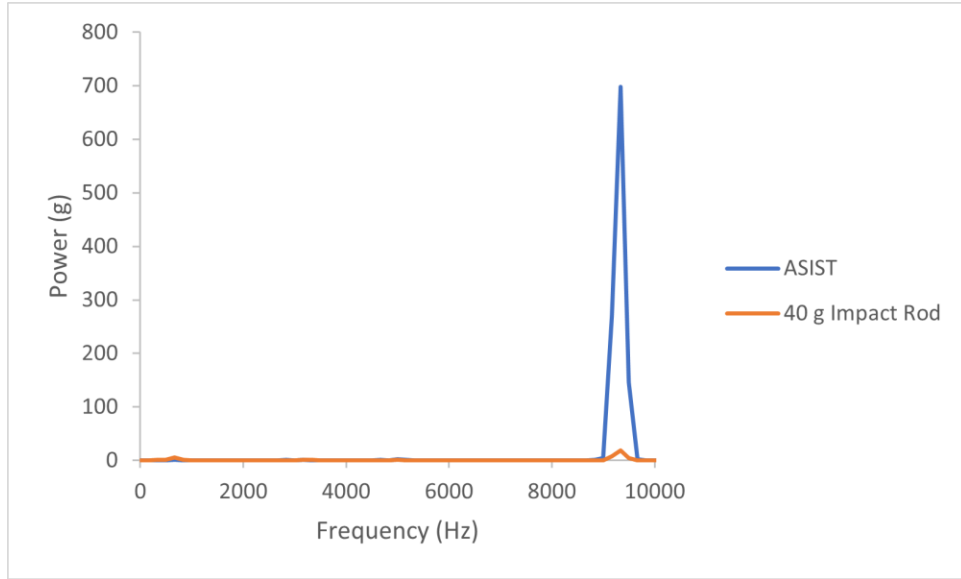


Figure 3.61: Frequency domain responses of silicone interface – ASIST vs. 40 g impact rod

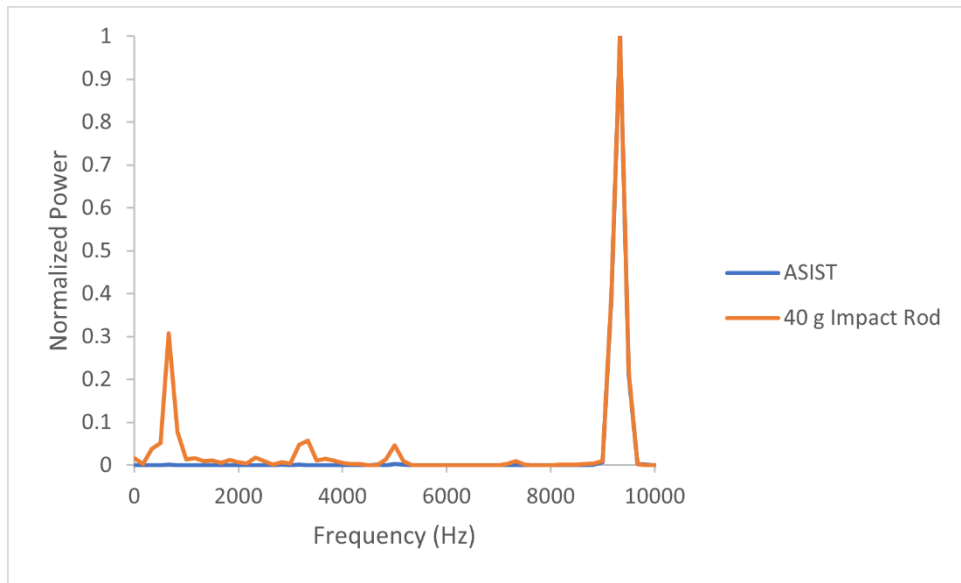


Figure 3.62: Amplitude normalized frequency domain responses of silicone interface – ASIST vs. 40 g impact rod

Although the heavier rod significantly lowered the power level of the 9333 Hz frequency, it also exposed a low lying 666 Hz frequency that was undetectable under ASIST excitation. A modal finite element model developed by Mohamed [28] and further explored in Section 4.1.2 showed in first estimates that a silicone interface should have two dominant axial frequencies. Like the impact model developed in Section 3.3.2, the frequencies would belong to the shearing of the implant relative to the bone, primarily owing to the stiffness of the bone-implant interface, and the vibration of implant itself, owing to its internal stiffness. For the silicone setup, the first axial mode

was relative shearing, making it the primary focus for obtaining information about the BII, while the second mode could be described as axial compression and expansion of the implant itself. A frequency comparison of results obtained from the finite element model and experimental setup can be viewed in Table 3.5.

Table 3.5: Frequency comparison between initial modal finite element model estimates and experimental setup

| Mode | Simulation | ASIST | | 40 g Impact Rod | |
|-------------|---------------------------|---------------------------|-------------------------------|---------------------------|-------------------------------|
| | <i>Frequency (Hz)</i> | <i>Frequency (Hz)</i> | <i>Percent Difference</i> | <i>Frequency (Hz)</i> | <i>Percent Difference</i> |
| 1 | 491 | N/A | N/A | 666 | 30% |
| 2 | 9711 | 9333 | 4% | 9333 | 4% |

The results showed reasonable matching between the finite element model and experimental setup. Notably, only the 40 g impact rod allowed for comparison between the first mode frequencies, verifying the use of heavier rods within the domain of interest. Finally, repeatability tests were conducted with the 10 g impact rod to get a sense of the robustness of the system. The 10 g impact rod was repeatedly removed then repositioned in front of the implant in the axial direction. 10 trials were executed without, then with, the GV connector installed. The results can be viewed in Figure 3.63 and Figure 3.64 respectively.

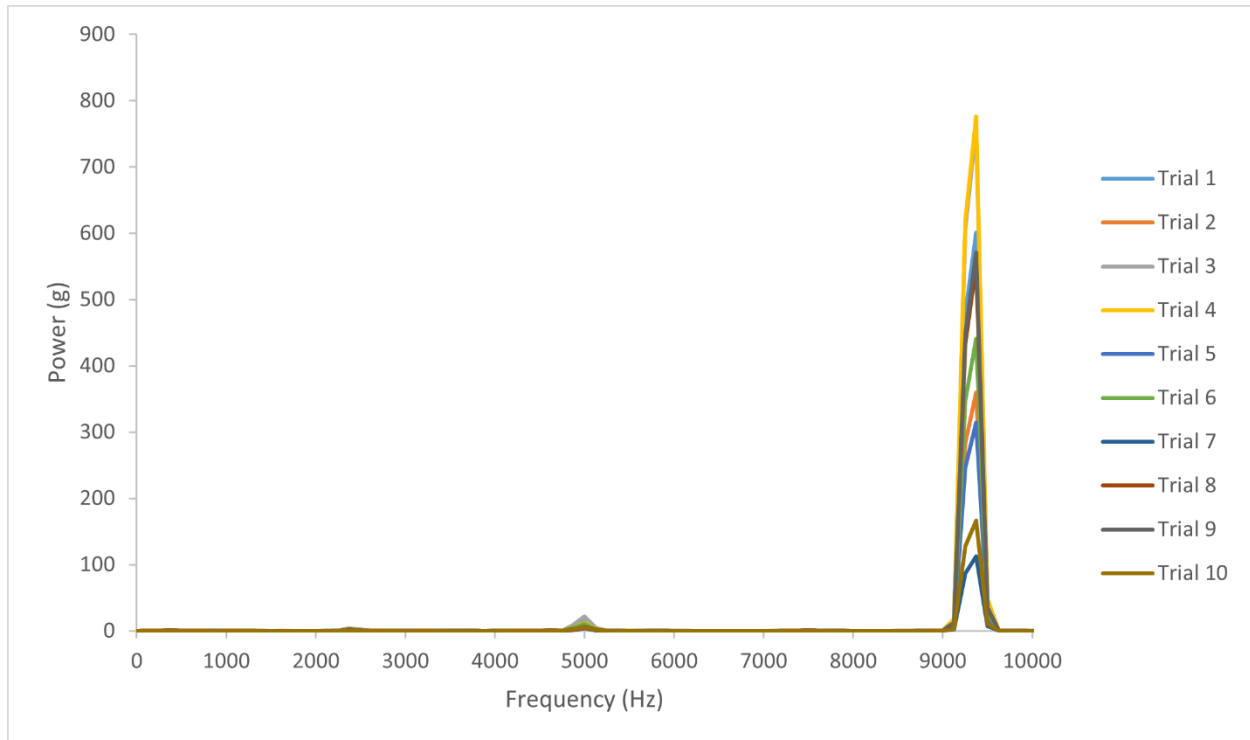


Figure 3.63: Repeatability of 10 g impact rod striking silicone interface setup without GV connector installed (axial direction)

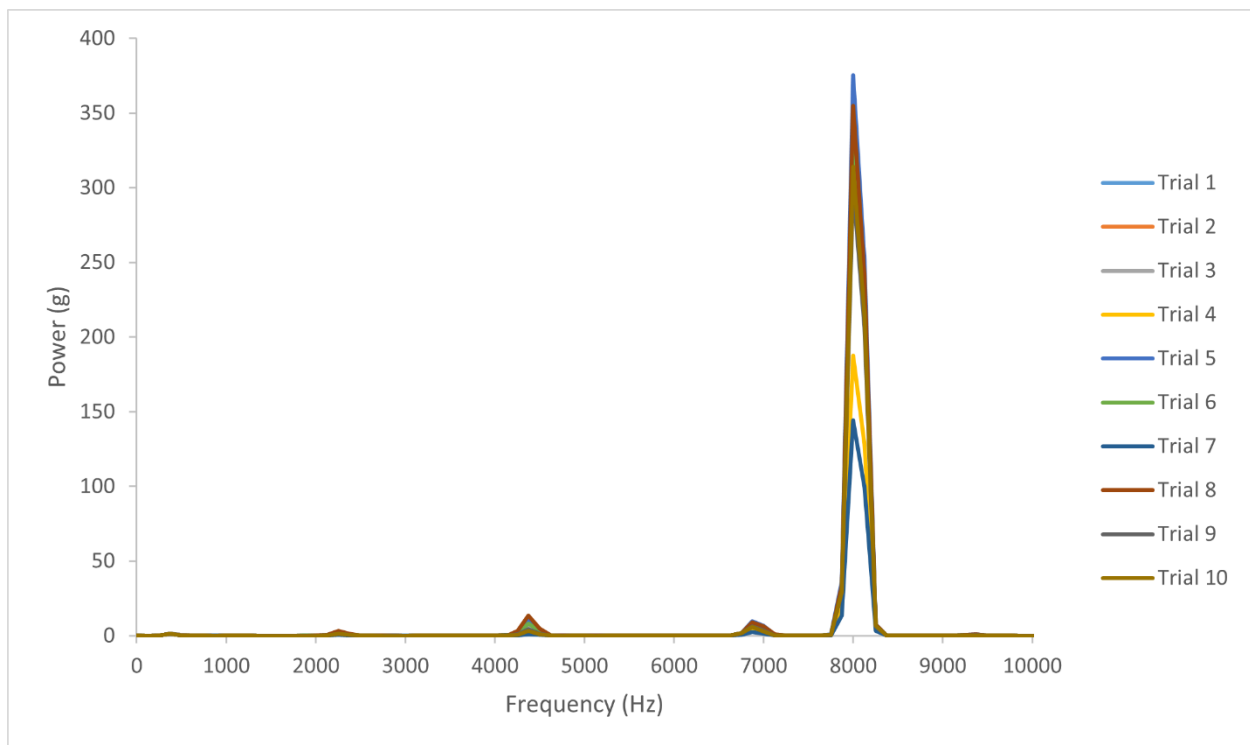


Figure 3.64: Repeatability of 10 g impact rod striking silicone interface setup with GV connector installed (axial direction)

The results showed varying levels of power being expressed in the system but extremely similar and characterizable frequencies or modes. The addition of the GV connector was observed to measurably decrease the second mode of compressive implant vibration, as it primarily added mass to the system.

3.7 Conclusion

A benchtop prototype impactor capable of repeatable excitation of a surrogate bone-implant system was synthesized. Several factors were investigated for relevance to a prospective development study. Impact rod mass, impact interface stiffness, and tip geometry were found to affect signal composition within a given implant configuration. Actuation voltage was observed to influence signal power without significant changes to composition. Dominant frequencies varied between axial and transverse configurations, with axial configurations generally displaying more harmonic behaviour. Finally, the added mass of the GV connector discretely shifted dominant frequencies within a given setup and contaminated transverse signals with significant noise. The main objective for the development study would be to identify an impactor configuration with the ability to reliably excite modes of interest across a range of interface stiffness conditions. Briefly, three interface conditions would be represented by silicone rubber adhesive, paraffin wax, and superglue. Further explanation to these selections will be given in Chapter 4. A summary of the prospective factors for investigation can be found in Table 3.6.

Table 3.6: Factors and levels of prospective development and evaluation study

| Factor | Levels | | | | | |
|--------------------------------|----------|----|--------------|------------|-----------|----|
| BII Interface Stiffness | Silicone | | Paraffin Wax | | Superglue | |
| GV Connector | Off | | | On | | |
| Accelerometer Orientation | Axial | | | Transverse | | |
| Impact Rod Mass (<i>g</i>) | 10 | 20 | 30 | 40 | 50 | 60 |
| Impact Interface Stiffness | Delrin® | | | Steel | | |
| Impact Tip Geometry | Flat | | Hemisphere | | Cone | |
| Actuation Voltage (<i>V</i>) | 5 | | 7.5 | | 10 | |

Chapter 4 Evaluation of Benchtop Impactor System

4.1 Introduction

4.1.1 Background

The potential of modal analysis to provide information about the mechanical properties of the bone-implant interface in transfemoral implants has been demonstrated by several seminal studies [20, 23, 27]. Mohamed et al. demonstrated the sensitivity of a percussion test across a range of interface stiffness conditions but recommended the development of a new impactor to improve resolution in the low range [27]. In his tests, low, intermediate, and high interface stiffness conditions were simulated by silicone rubber adhesive, paraffin wax, and superglue, respectively [27]. Silicone interfaces had previously been tested by Shao [20] and Cairns [22] for transfemoral implants, the latter study citing the ability of silicone to simulate fibrous tissue formation. Sensitivity in the this ‘low’ condition would therefore be imperative for early detection of implant loosening and failure. Mohamed found the elastic modulus of silicone to be approximately 0.45 MPa after conducting tensile testing [28]. Cured epoxy resin has been used in a variety of studies to simulate a fully integrated transfemoral implant interface [22, 24, 25, 47, 48]; there is also precedent in studies of bone-anchored hearing aids [16, 55]. However, there was concern that the only available implant could be irreparably damaged by epoxy, so an alternative was desirable. Westover also used superglue [16] and Krazy Glue [55] to simulate interfaces in benchtop investigations of bone-anchored hearing aids. Superglue would represent a lower stiffness case than epoxy [16, 55], but would likely provide an adequate juxtaposition to silicone, which was verified by Mohamed [27]. The elastic modulus of superglue is approximately 1.23 GPa [66]; Mohamed specified a value of 1000 MPa in finite element modelling [27]. The implementation of paraffin wax was a completely novel approach. It was selected as a relatively low risk material with an intermediate elastic modulus ($\sim 55.7\text{ MPa}$ [67]), which was specified as 40 MPa by Mohamed [27]. A novel installation approach also had to be synthesized, which is detailed in Section 0. A variety of factors stemming from modal analysis theory were explored in Chapter 3 and informed the design of the experiment.

4.1.2 Modal Finite Element Model

A modal finite element model (FEM) was developed by Mohamed [28] and laid an exceptional framework for the current experiment and future impact finite element models. Details of finite element model setups can be found in Section 4.3.10.1. The model incorporated an OPL Type A implant system and three different interface stiffness conditions (silicone; paraffin wax; superglue). Simulations demonstrated that the OPL implant system experiences two dominant modes of axial vibration, which would both be detectable by a uniaxial accelerometer. As demonstrated in Figure 4.1, the first mode was characterized by relative shearing between the implant and cortical bone. Increasing the stiffness of the bone-implant interface, modelled as a thin material layer between the implant and bone, caused the first mode to drastically increase in frequency. This would become the primary mode of interest, as it demonstrated high sensitivity to stiffness changes at the bone-implant interface.

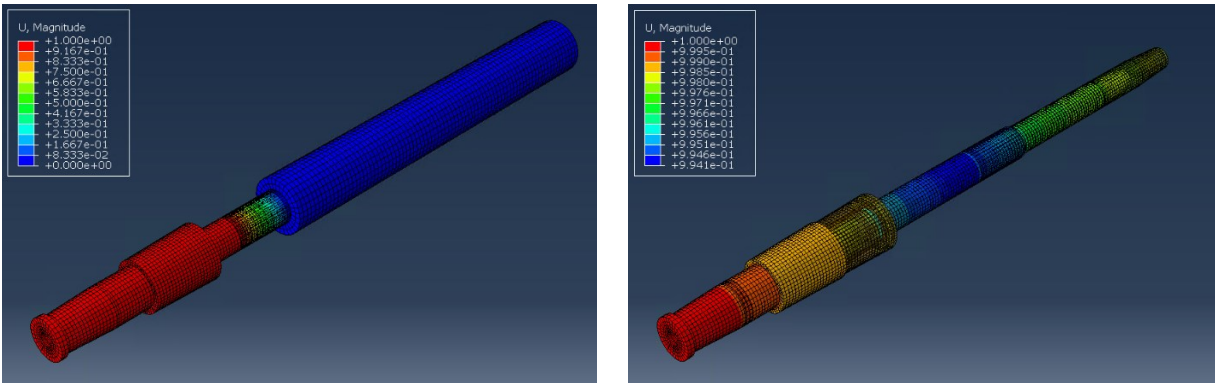


Figure 4.1: Modal finite element model – silicone mode 1. Left, full system; right, implant

The second mode was characterized by compression and expansion of the implant itself. The stiffness of the BII had limited bearing on the frequency of this mode, which remained relatively stable for different interfaces. This indicated that the behaviour of the second mode was primarily governed by the internal stiffness of the implant. The shape of the second mode can be viewed in Figure 4.2.

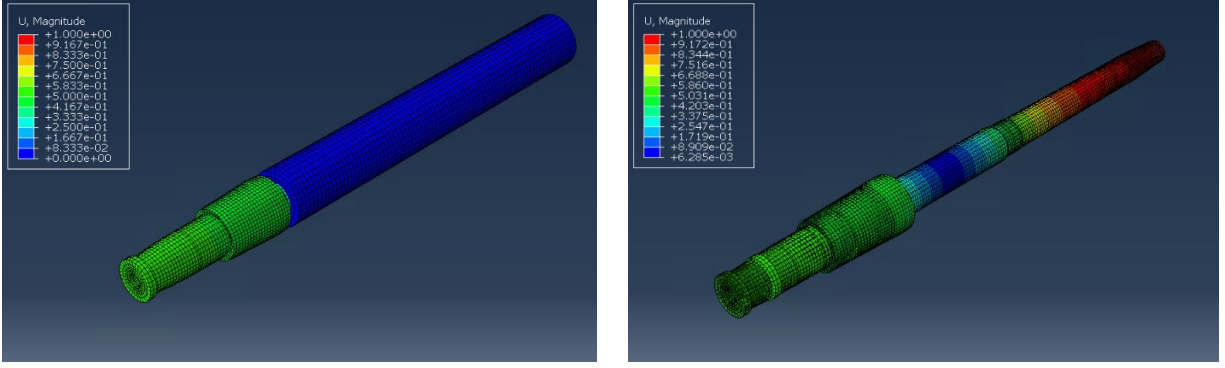


Figure 4.2: Modal finite element model – silicone mode 2. Left, full system; right, implant

As the stiffness of the BII increased, the first mode frequency approached the second mode frequency. When they began to overlap for the superglue interface simulation, the first mode continued to be observable at the dual cone adapter, but the second mode transitioned to isolated axial motion at the proximal end of the implant stem. This meant that the second mode would cease to be measurable with an accelerometer placed at the distal dual cone adapter. A summary of the observed frequencies can be viewed in Table 4.1.

Table 4.1: Modal finite element model frequencies

| Interface (Young's modulus in <i>MPa</i>) | Modal FEM Frequencies (<i>Hz</i>) | |
|--|-------------------------------------|---------------|
| | <i>Mode 1</i> | <i>Mode 2</i> |
| Silicone (0.45) | 663.48 | 9381.4 |
| Wax (40) | 5447.6 | 9667.6 |
| Superglue (1000) | 9770.1 | 11135 |

4.1.3 Objectives

The objectives of the present study were to evaluate a series of impactor and implant factors over a range of actuation voltages and interface stiffness conditions. For the impactor, the optimal ram mass should be able to excite the first axial mode across the full range of interface stiffness conditions, and the optimal impact tip would provide the highest degree of reliability among the tested geometries. Testing across three actuation voltages would allow for observation of impactor performance at different power levels, potentially distinguishing optimal actuation conditions. For

the optimal impactor configuration, the sensitivity of the percussion approach would also be validated in a wide range of BII stiffness scenarios, and the performance of the impactor would be evaluated for different implant configurations (with/without the GV connector installed). Strike orientation was included in the experimental procedure but was eliminated from analysis as knowledge of the system evolved (axial vibrations were generally easier to characterize). To mitigate risk within the approach, a soft Delrin® tip was added in a subset of runs to provide extremely narrow frequency input to the system. Ultimately, the objectives of the experiment were two-fold:

1. Collect experimental data to inform design decisions on optimal impactor mass, tip geometry, and impact interface stiffness.
2. Validate the sensitivity of the approach by detecting the first axial mode across all interface stiffness conditions.

4.2 Materials and Methods

4.2.1 Overview

The experiment tested a wide array of factors and levels to systematically explore the design space of potential impactors as well as provide validation to 1D and 3D finite element models developed in parallel study [28]. Bone-implant interface stiffness was included as a factor with three levels to model the complete range of expected healing or failure conditions that could foreseeably occur in the clinic. The levels would approximate a failure or fibrous tissue formation condition (silicone) [22, 27], intermediate healing condition (paraffin wax) [27], and a fully healed or stiff interface condition (superglue) [27]. These levels would set a wide and ambitious operating range for handpiece development to cover. The GV connector represented a more massive, complex, damped, and noisy implant configuration; although, one that was more relevant to clinical realities, as patients would not often remove their GV connector post-operation. The device would also prospectively be used for excitation of a variety of implant configurations, especially because implant designs regularly change and evolve. Consequently, the optimal device should be able to operate universally. At this stage in the project, accelerometer orientation was still an important risk mitigating factor to consider in development. Questions remained about the best way to model the TFA implant systems: whether transverse modelling with literary backing for smaller implant

systems or an innovative axial modeling approach would be ideal. As such, the factor was included in the experimental design. Impact rod mass would be the primary factor of interest and would incorporate a large design space. At 10 *g*, the impactor was likely to perform similarly to the ASIST and represent the low end of highly tunable masses in terms of speed and impact force, whereas the 60 *g* impactor would represent the high end of massive rods, hypothetically significantly cutting down frequency excitation bandwidth and pushing limits of electromagnet actuation potential. Impact tips represented a way to alter strike conditions to enhance the repeatability of future impactors. Although impact conditions outside of ram mass, such as strike angle, have plagued the ASIST [15, 50], relatively little is known about how minute manipulations of strike angle, position, and impact stiffness affect the reliability of vibration approaches for stability assessment of TFA implant systems. A variety of impact tip geometries were implemented, and a soft impact interface stiffness material (Delrin®) was tested in a subset of runs. Conical and hemispherical tips were hypothesized to provide greater reliability than a flat tip. It was realized that although a wide range of rod masses were to be tested, a uniquely cropped frequency domain could be accessed through implementation of a magnitude orders softer interface than 316 stainless steel. The Delrin® tip was implemented as the most practical material for this endeavor, limiting extreme damping effects while maintaining a significantly reduced Young's modulus. It was tested for the paraffin wax and superglue interface setups and for the 10, 30, and 50 *g* impact rods, all other factors constant. Finally, a range of actuation voltages were tested to generate design curves. Actuation voltage was not expected to significantly affect signal composition (primary response variable) but was included to help fine tune the impactors and showcase their performance at varying levels of a common covariate (impact velocity). All factor and levels of the development and evaluation experiment can be viewed in Table 4.2.

Table 4.2: Factors and levels of development and evaluation experiment. *Delrin® impact tip tested in a subset of runs

| Factor | Levels | | | | | |
|--------------------------------|----------|------------|--------------|------------|-----------|----|
| BII Interface Stiffness | Silicone | | Paraffin Wax | | Superglue | |
| GV Connector | Off | | | On | | |
| Accelerometer Orientation | Axial | | | Transverse | | |
| Impact Rod Mass (<i>g</i>) | 10 | 20 | 30 | 40 | 50 | 60 |
| Impact Tip | Flat | Hemisphere | | Cone | Delrin®* | |
| Actuation Voltage (<i>V</i>) | 5 | | 7.5 | | 10 | |

4.2.2 Experimental Setup

The foundation of the experimental setup was a synthetic model of a TFA implant system. The model consisted of a Sawbones composite femur, OPL Type A implant stem, and adhesive interface for anchorage between the components. Base components can be viewed in Figure 4.3.

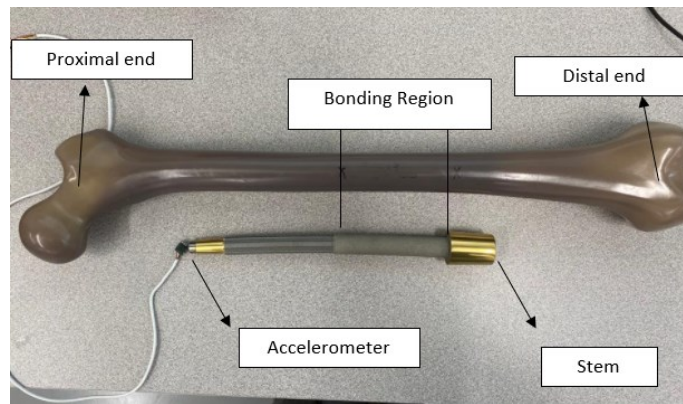


Figure 4.3: Experimental model base components

The composite femur was cut 150 mm from its distal end to mimic a transfemoral amputation. From the cut face, a $\varnothing 15$ mm hole was drilled to a depth of 170 mm to expand the intramedullary cavity, making space for the implant stem and interface. Schematics of the bone preparation process can be viewed in Figure 4.4.

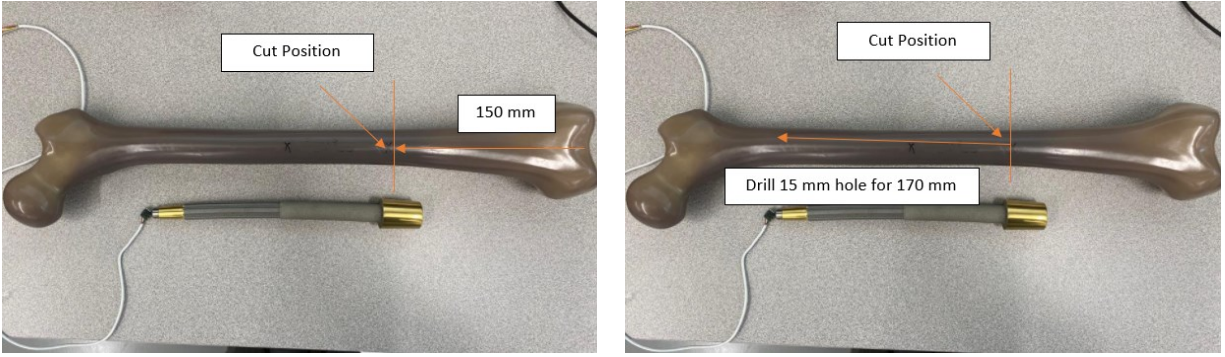


Figure 4.4: Sawbones femur preparation

With a femur prepared, an implant was then anchored in the composite bone in one of two ways. For the silicone and superglue interfaces, the adhesives were thickly coated on to the entire bonding region of the implant before insertion into the intramedullary cavity. The bone-implant systems were allowed to cure upright for at least 72 hours. Double-sided tape was used as a stopper to create an approximate 16 mm gap between the start of the bonding region and cut face of the composite femur. Excess adhesive was removed before extensive curing, and after the curing period, any remnants on the exposed bonding region and around the cut-face were carefully removed. For the paraffin wax interface setup, granular paraffin wax was melted into a homogenous liquid on a hot plate at approximately 250°C . The implant and bone were placed in a temperature chamber at 65°C and allowed to reach equilibrium for approximately 20 min. After the elapsed time, the components were removed, and the femur was mounted distal end up in a clamp. Molten wax was poured over the implant before insertion into the bone with a piece of supporting cardboard (double-sided tape failed to adhere to the hot implant) to create the $\sim 16\text{ mm}$ gap. Extra molten wax was slowly dripped into the interface gap between the implant and bone with an eyedropper until wax began to spill over the cut face. The temperature of the bone and implant was deliberately set close to the melting point of paraffin wax to ensure solidification would occur soon after administering the wax. This would allow the wax to penetrate down the interface as much as possible before partially solidifying and forming a plug, allowing more wax to fill higher areas of the bonding region. In this state, the system was allowed cool for 24 hours. Excess wax was then removed from the exposed bonding region and cut face as well as from a small proximal hole in the composite femur. The synthetic TFA models were then fixed in a bone clamp with a silicone rubber liner under a controlled squeeze force. This would closely mimic a fully fixed boundary condition as characterized by Mohamed in the development of experimental

and finite element models [28]. A comprehensive summary of experimental model and data acquisition system components with relevant set up notes can be found in Table 4.3, and a picture of the full setup can be viewed in Figure 4.5.

Table 4.3: Experimental model and acquisition system components

| Experimental Model | |
|-----------------------------|--|
| <i>Component</i> | <i>Description</i> |
| Composite Femur | Sawbones SKU 3403 composite femur (Pacific Research Group, USA). Drilled to allow for 0.1 mm uniform interface between composite bone and implant. |
| Implant Stem | OPL Type A implant stem (Permedica, Italy). \varnothing 14 mm \times 160 mm. |
| Silicone Interface | DOWSIL 7091 silicone rubber adhesive (DOW, USA). |
| Paraffin Wax Interface | Raw paraffin wax. Melted and solidified to form interface. |
| Superglue Interface | LePage Ultra Gel superglue (LePage, Canada). |
| Dual Cone Adapter | OPL Type A dual cone adapter (Permedica, Italy). 68.5 mm length. |
| Internal Locking Screw | OPL internal locking screw (Permedica, Italy). Tighten to 10 Nm. |
| GV Connector | OPL GV connector (Permedica, Italy). |
| Distal Screw | OPL distal screw (Permedica, Italy). Tighten to 2 Nm without GV connector installed or 10 Nm with GV connector installed. |
| Damping Liner | Silicone rubber liner for mechanical isolation. |
| Bone Clamp | Fully fixed clamp with squeezing force controlled by exposed threaded shaft length (37 mm). |
| Acquisition System | |
| <i>Component</i> | <i>Description</i> |
| Accelerometer | Analog Devices ADXL1004 MEMS Accelerometer (Analog Devices, USA). |
| Accelerometer Raft | 3D-printed support for accelerometer protection. |
| Double-Sided Tape | Double-sided gorilla tape for adhesion between accelerometer and implant. |
| Analog Interface Board | Interface board for analog signals, DC power, and signal grounds (designed in-house). |
| Analog-to-Digital Converter | National Instruments NI-9205 DAQ (National Instruments, USA). |
| Host PC | Host PC for signal processing through LabVIEW GUI (National Instruments, USA). |

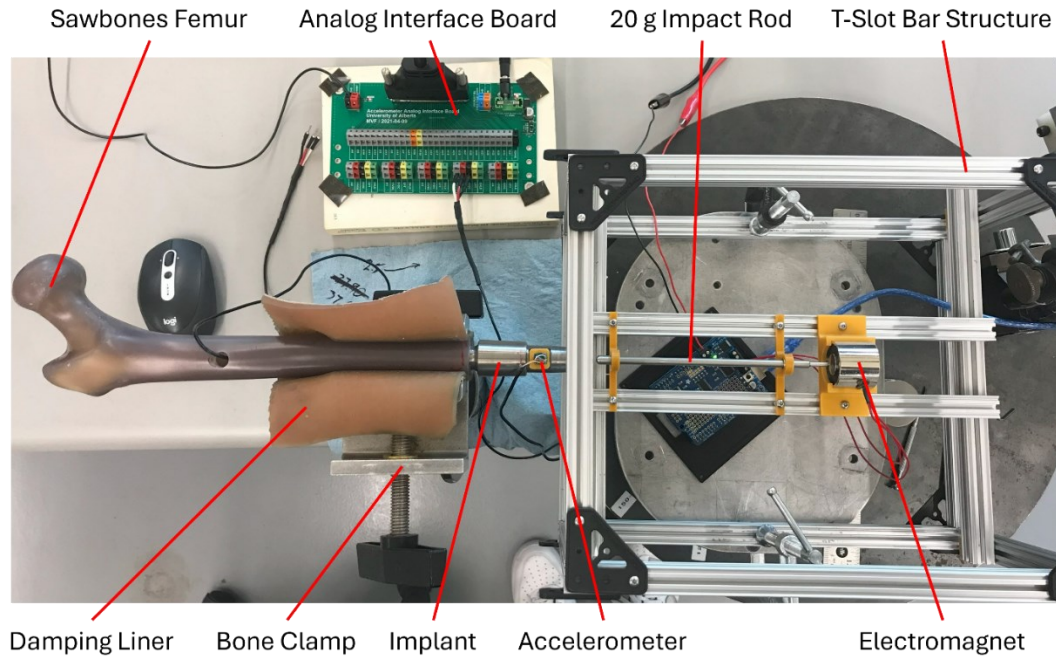


Figure 4.5: Development and evaluation experiment setup

4.2.3 Experimental Procedure

Experimental runs were completed by assembling an implant configuration followed by testing multiple impactor configurations. Once an implant configuration was assembled, a uniaxial MEMS accelerometer was adhered to the dual cone adapter or GV connector in the axial or transverse direction. This was done by adhering a piece of double-sided tape to the none tapered region of the dual cone adapter or approximate middle of the top, flat portion of the GV connector, then firmly pressing the 3D-printed support raft of the accelerometer into the exposed side of the tape. The use of double-sided tape to adhesively mount an accelerometer is a common and reliable practice [68]. An axial configuration without the GV connector installed can be viewed in Figure 4.6, while a transverse configuration with the GV connector installed can be viewed in Figure 4.7.

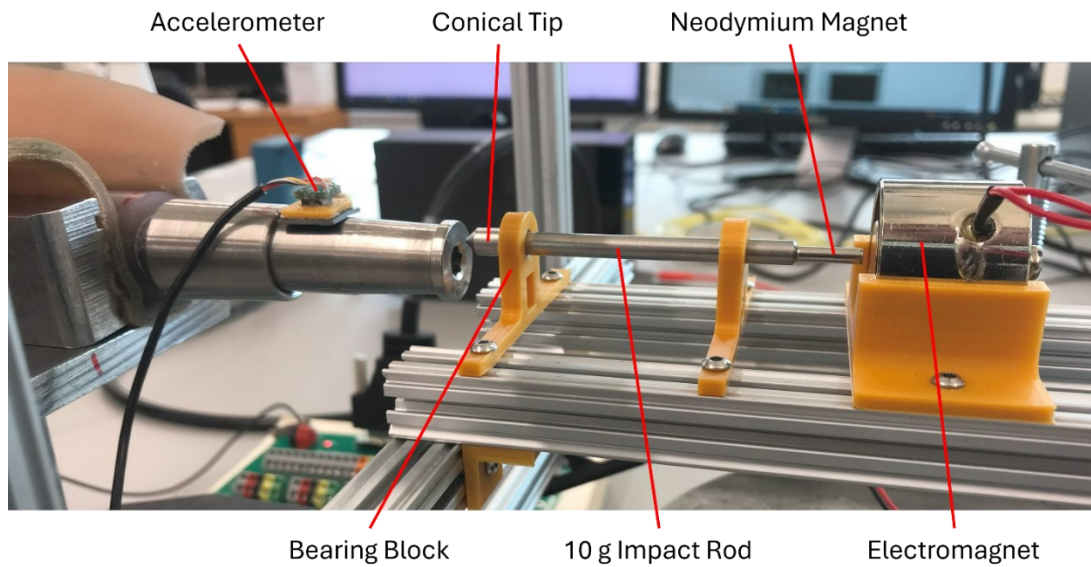


Figure 4.6: Axial strike position without GV connector installed

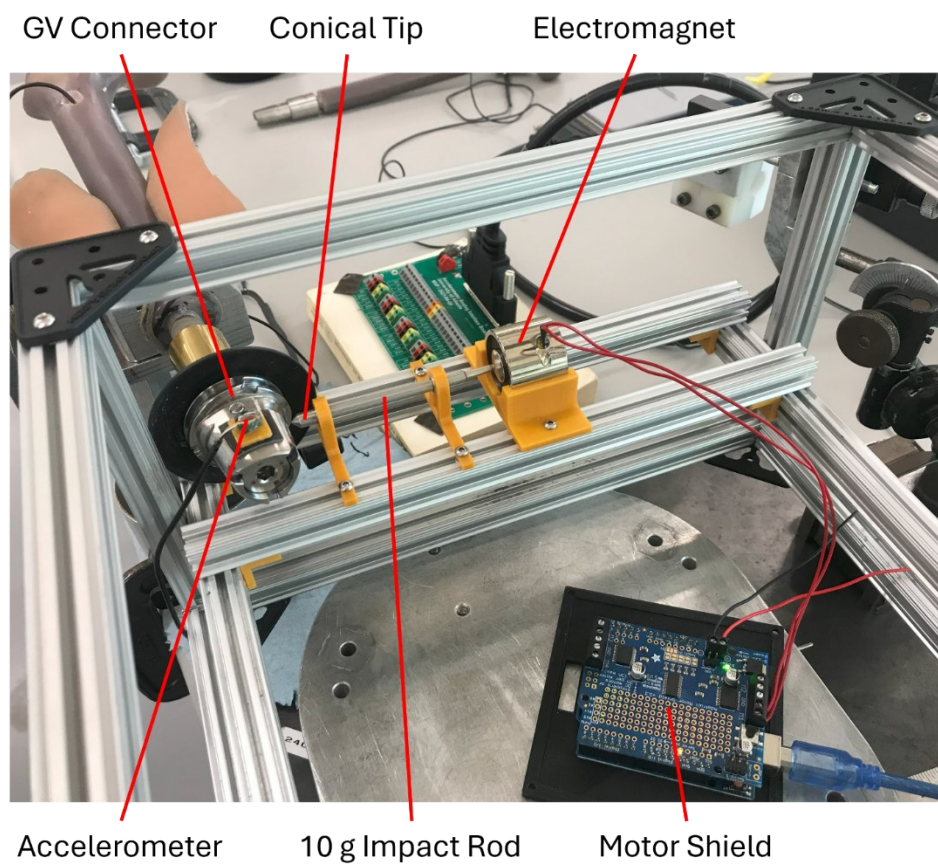


Figure 4.7: Transverse strike position with GV connector installed

Impactor configurations were constructed by selecting one of six different impact rods differentiated by mass and adhering a $\varnothing 1/8 \text{ in} \times 1/2 \text{ in}$ neodymium magnet to the rear end with superglue. One of three different tip geometries (Figure 4.8) was selected and installed on the impact rod by threading to the front end. For the Delrin® runs, the flat impact tip was installed and a $\varnothing 1/4 \text{ in} \times 1 \text{ mm}$ Delrin® coupon was superglued to the front flat face. After the impact rod was assembled, the ram would be positioned within sleeve bearings mounted to the T-slot bar structure, and the 15 kg HF electromagnet would be positioned at its rear. The distance between the neodymium magnet and electromagnet was calibrated for each configuration by running 5 V of direct current through the electromagnet, closing the distance such that the neodymium magnet was attracted to the ferromagnetic core of the electromagnet, and then slowly moving the neodymium magnet away, extending the gap until the impact rod was repelled from the electromagnet. This procedure was completed to ensure that the impact rod would fire starting at the transition from attraction to repulsion and travel through a strong region of repulsive magnetic interaction. The front bearing block location relative to the electromagnet would lock in this position and limit the back stroke of the impact rod. The front stroke would be limited by any impact surface. Once all factors of a run were configured, the operator would position the impact tip $2.5 \pm 0.5 \text{ mm}$ from the impact surface. Some leeway in strike position was afforded to provide controlled variability between measurements and mimic distance variability that future handheld configurations would be susceptible to. Occasionally, for heavier impact rods and lower actuation voltages, there was difficulty in ram actuation or accelerometer triggering. In these cases, the impact rod would be moved incrementally closer to the impact surface until a signal could be acquired, or if all attempts failed, the runs would be skipped, and the experiment would be continued at a higher actuation voltage. Except for the Delrin® level of impact tip and any runs that could not physically be completed, a full factorial design of experiments framework was implemented. It should be noted that the paraffin wax interface was installed and tested twice, with the second installation having a fractional factorial execution. Delrin® runs were only conducted for the second paraffin wax and superglue interface setups and for the 10, 30, and 50 g impact rods, all other factors having full implementation. For a given intersection of factors, five measurements were completed by positioning the impact rod at the $2.5 \pm 0.5 \text{ mm}$ distance, activating the data acquisition system, actuating the impact rod, allowing the system to record 15 strikes (first strike trigger), then removing the impact rod and repeating.

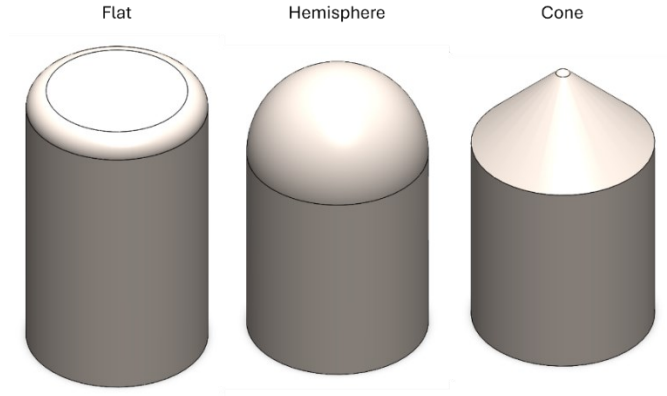


Figure 4.8: Impact tip geometries

Accelerometer signals were recorded at a sampling frequency of 250 kHz , which was magnitude orders above the most conservative Nyquist frequency estimate. The Nyquist frequency was assumed to be twice the accelerometer bandwidth ($24\text{ kHz} * 2 = 48\text{ kHz}$), which was also well above the largest anticipated implant frequencies. After completion of the experiment, the accelerometer signals were digitally processed by applying a lowpass Butterworth filter with cutoff frequency of 24 kHz . The ensemble average of time domain signals belonging to the same measurement (batch of strikes) was taken before applying an exponential window and Periodogram transform. The exponential window was applied over the entire time record of the ensemble average in accordance with Equation 4.1:

$$w_e(t) = e^{-\frac{t}{\tau}} \quad 4.1$$

Where t is time and τ is the time constant, both in seconds. An exponential window is a common selection for impact vibration testing and helps limit spectral leakage [64, 69]. The time constant was chosen to be one quarter the time record length, which followed a common suggestion to create an exponential function that decays to approximately two percent by the end of the time record [69]. The transform resulted in frequency domain data for all runs. A signal processing summary can be viewed in Table 4.4.

Table 4.4: Signal processing parameters for development experiment

| Signal Processing | | |
|-------------------|------------------------|-------------------|
| | Parameter | Value |
| Samples | Frequency (kHz) | 250 |
| | Length | 2501 |
| Strikes | Recorded | 15 |
| | Ensemble Average | Time Domain |
| Filter | Design | Butterworth (IIR) |
| | Order | 4 |
| | Cutoff Frequency (kHz) | 24 |
| | Type | Lowpass |
| | Phase Shift | Zero |
| Transform | Type | Periodogram |
| | Window | Exponential |
| | Time Length (s) | 0.01 |
| | Time Constant (s) | 0.0025 |

4.3 Results and Discussion

4.3.1 Overview

Signals were visualized in both the time and frequency domains. Once accelerometer signals were transformed to the frequency domain, a variety of parameters were extracted to make design decisions on impact rod mass, impact tip geometry and stiffness, and appropriate actuation approaches. Amplitude ratio, first mode amplitude, band power, and intraclass correlation coefficients were plotted across various factor interactions. Amplitude ratio represented signal

composition by taking the second dominant mode frequency spectrum amplitude and dividing it by the first. Modes were established as the dominant frequencies in predefined regions and were referenced against results from finite elements models created in a parallel study [28]. First mode amplitude was defined as the power spectral density value of the first mode frequency; it represented the primary mode of interest, having high sensitivity to changes at the bone-implant interface. Band power was included as a signal quality metric, with greater band power indicating a well actuated vibration. Intraclass correlation was primarily used to characterize the reliability of different impact tip geometries. It should be noted that only axial signals were analyzed. Throughout the process of data acquisition, the incoming data and continued modelling suggested that executing the vibration approach in the axial direction would yield less temperamental results. Signals collected in the axial direction were generally more harmonic and less susceptible to the ill effects of damping and noise presented by the GV connector. Finally, an impact finite element was developed, and impact force measurements were taken for further validation and preliminary safety testing.

4.3.2 Time Domain

Signals were first visualized in the time domain. For the silicone interface setup, the primary concern was the ability of an impactor to adequately excite or reveal the first mode frequency. This was the imperative goal of the experiment, as properly classifying a failure or fibrous tissue condition would be the critical function of any novel impactor. The ASIST had difficulty exciting this first mode frequency, which would result in misclassification of the setup as a high stiffness interface condition. It was hypothesized that heavier rods would elicit a more significant presence of this mode and give the impact vibration modelling approach sensitivity in the low stiffness range. Figure 4.9 shows the time domain signals for the silicone setup without the GV connector installed. In this case, it was qualitatively apparent that the 10 *g* impactor signal primarily consisted of one high frequency mode, like the ASIST response. At the jump to 20 *g*, an immediate change was apparent, with a low frequency mode visually entering the signal. From 20 – 60 *g*, the mode was evident to varying degrees, but heavier rods generally seemed to present larger contributions.

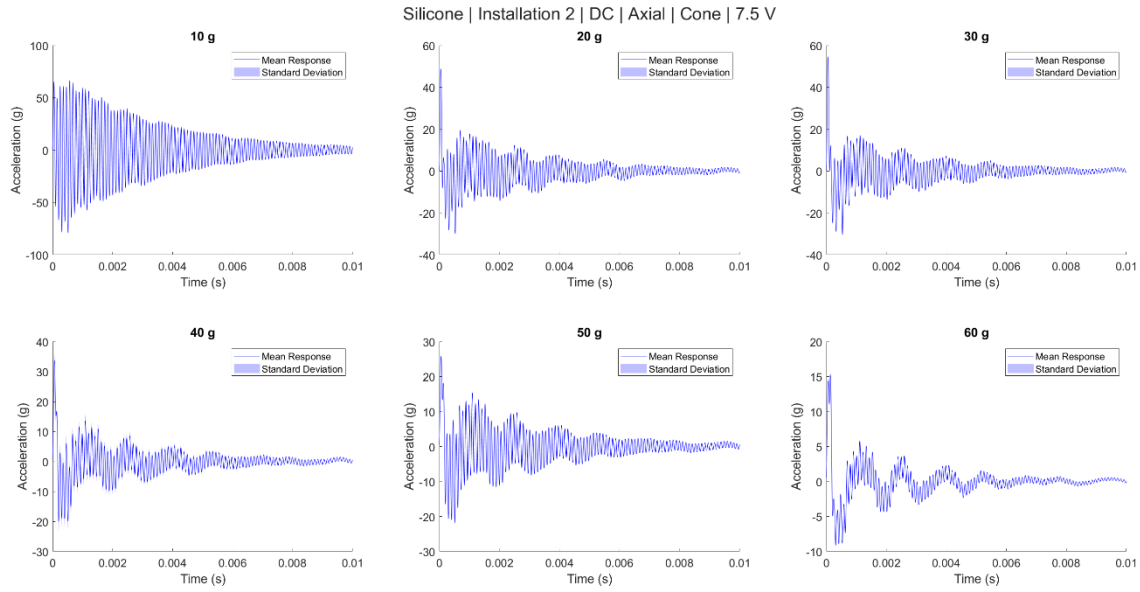


Figure 4.9: Time domain signals – silicone; DC; axial; cone; 7.5 V

Signals with the GV connector installed generally displayed similar behaviour to signals without. The jump in first mode contribution from 10 *g* to 20 *g* was not as apparent but was still visualized to some extent. The first mode was more visible at greater impact rod masses; however, all signals appeared to contain a high degree of damping and potential noise, which made visualization more difficult. A sample of silicone setup signals without the GV connector installed can be viewed in Figure 4.10.

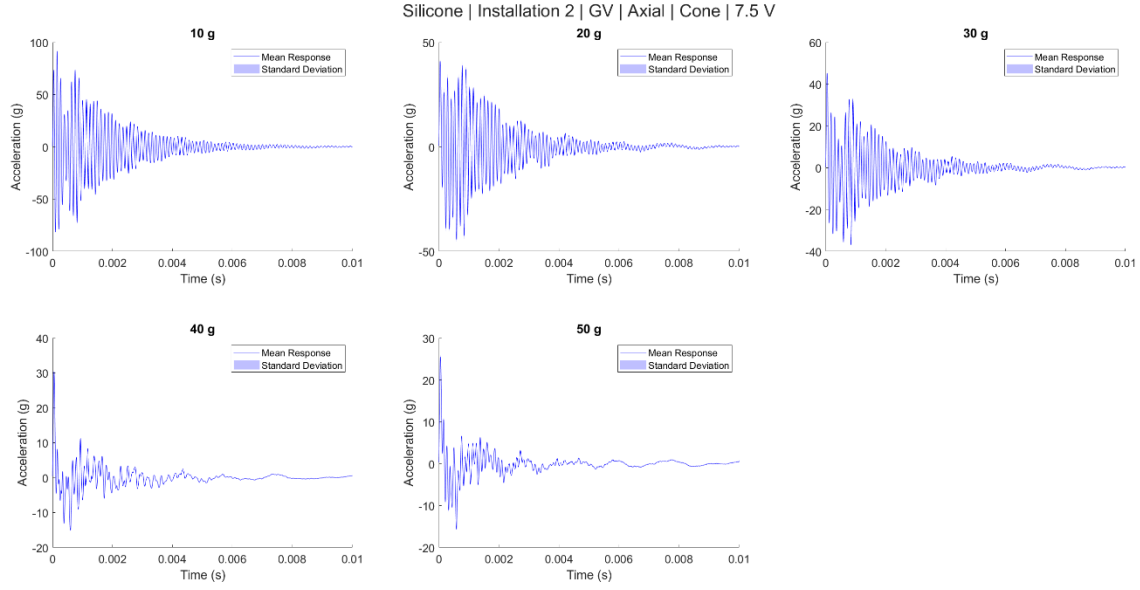


Figure 4.10: Time domain signals – silicone; GV; axial; cone; 7.5 V

Additionally, a Delrin® impact interface was tested on the silicone interface setup in a subset of impact rod masses. The Delrin® interface greatly enhanced the visual contribution of the first mode, even for the 10 g impact rod, as seen in Figure 4.11.

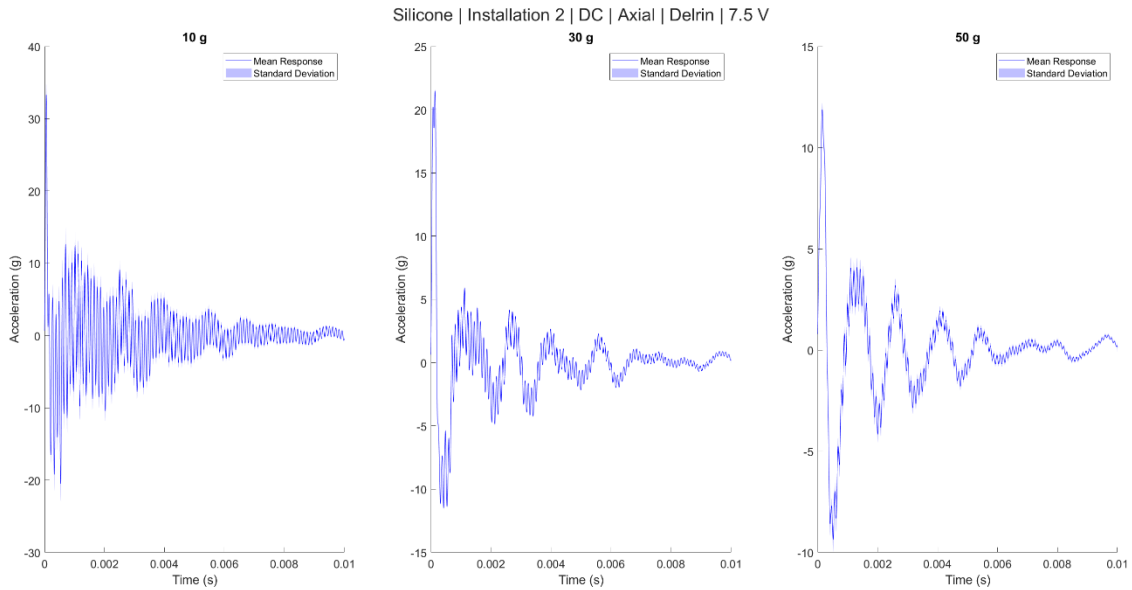


Figure 4.11: Time domain signals – silicone; DC; axial; Delrin®; 7.5 V

Paraffin wax interface signals often contained a combination of intermediate and high frequency components. Two installations were performed to verify the results considering the novelty of the

approach. Like the silicone interface, a distinct difference in signal composition was observed in the jump from 10 *g* to 20 *g*. At 10 *g*, a higher frequency component could be seen at the start of the transient vibration. From 20 *g*, the signals generally lacked significant contribution from high frequency sources. Between the two installations, the behaviours of the systems were relatively similar in the time domain. Sample results for installation 1 can be viewed in Figure 4.12, and results for installation 2 can be viewed in Figure 4.13.

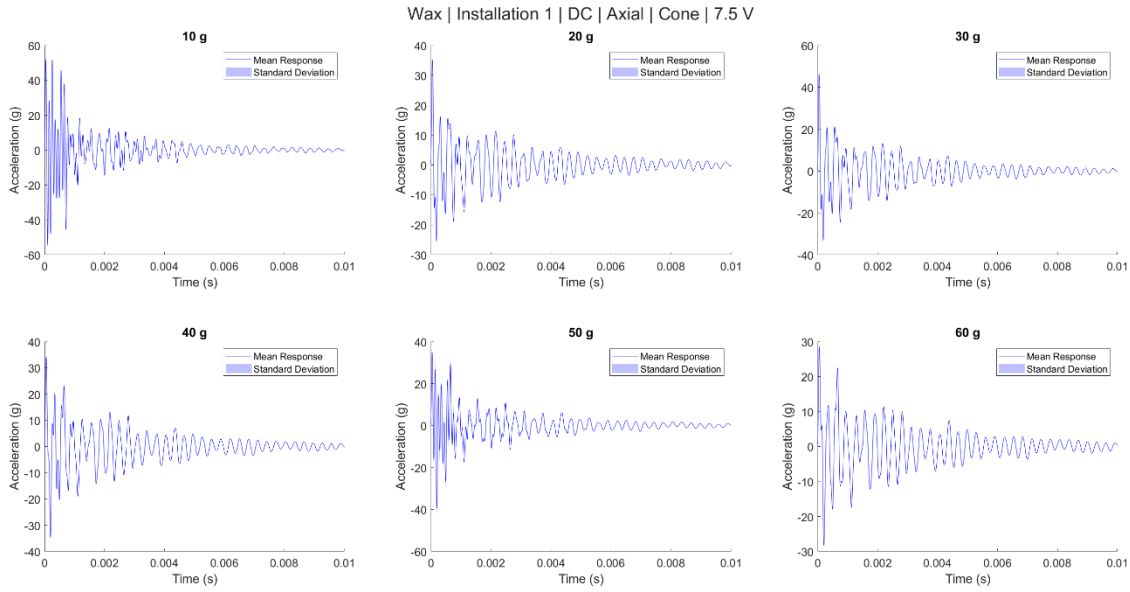


Figure 4.12: Time domain signals – wax 1; DC; axial; cone; 7.5 V

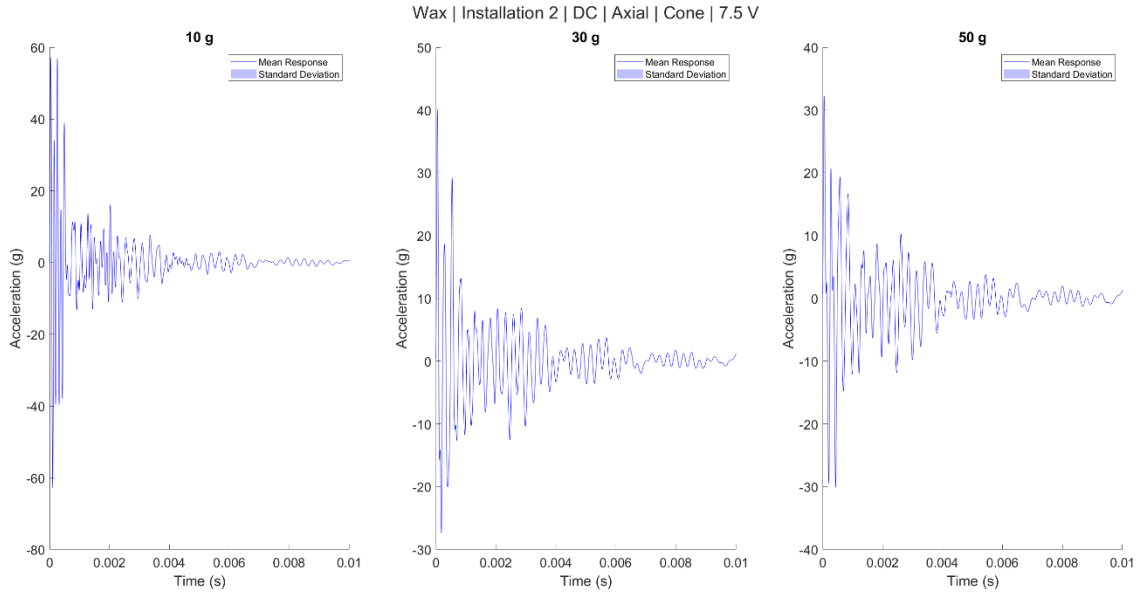


Figure 4.13: Time domain signals – wax 2; DC; axial; cone; 7.5 V

Finally, superglue displayed similar behaviours to the preceding interfaces. The 10 g impactor generally produced homogenous signals with a single high frequency component. In the time domain, signals produced by the 10 g impactor on the silicone and superglue interfaces looked extraordinarily similar. Once 20 g was reached, like the other interfaces, a distinct drop in high frequency contributions relative to other signal constituents was seen. After the drop, signals appeared to be dominated by an intermediate frequency and bared a striking resemblance to intermediate compositions. Sample superglue interface time domain signals can be viewed in Figure 4.14.

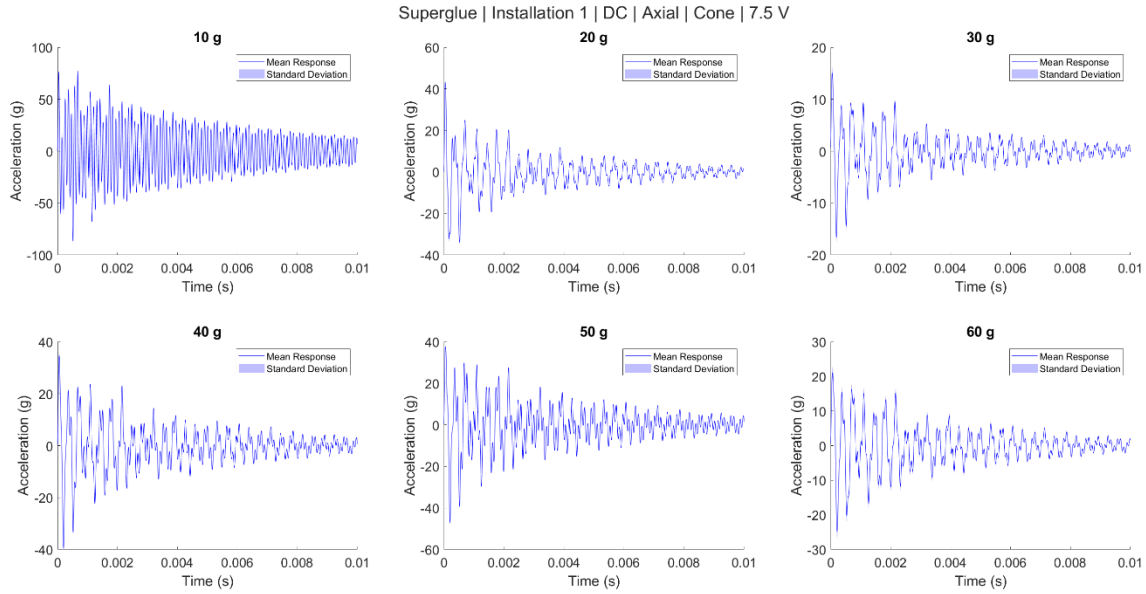


Figure 4.14: Time domain signals - superglue; DC; axial; cone; 7.5 V

4.3.3 Frequency Domain

Ensemble average time domain signals were taken into the frequency domain through a periodogram transform. Here, preliminary time domain observations were verified. For the silicone setup, low frequency contributions were generally boosted by heavier impact rods. It was also observed that increasing actuation voltage generally served to enhance all contributions uniformly, preserving gross signal composition. The results without the GV connector installed can be viewed in Figure 4.15.

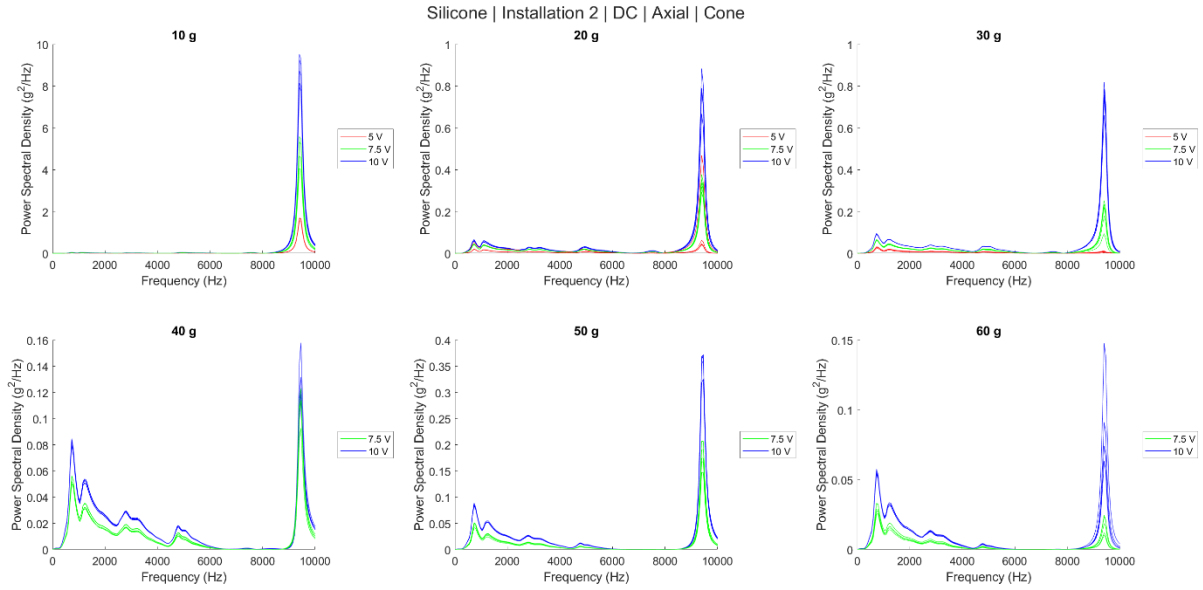


Figure 4.15: Frequency domain signals – silicone; DC; axial; cone

With the GV connector installed (Figure 4.16), it was more difficult to adequately visualize low frequency components. It wasn't until 40 g that low frequency contributions became apparent in the signals. Several noisy peaks distributed throughout the mid-range were also observed.

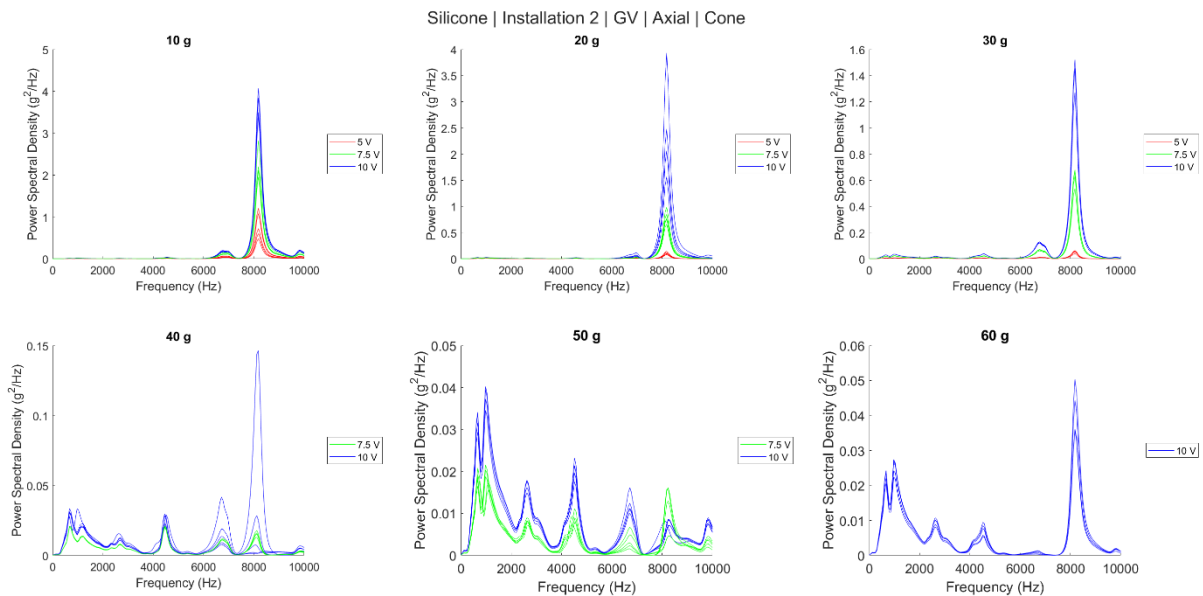


Figure 4.16: Frequency domain signals – silicone; GV; axial; cone

Deploying the Delrin® interface, low frequency components were immediately apparent for the 10 g impactor through to the 50 g impactor. The same actuation voltage patterns were seen as for

a stainless steel interface, and heavier rods appeared to work synergistically with the soft impact interface to strongly shift signal composition towards the low frequency domain. Delrin® frequency domain signals extracted from the silicone interface setup can be viewed in Figure 4.17.

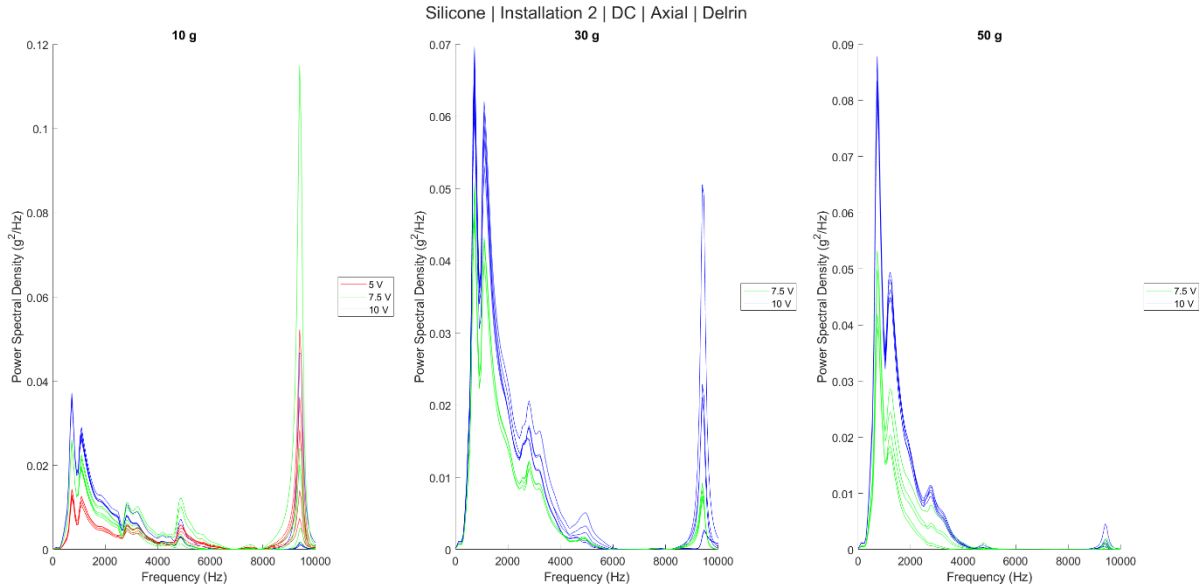


Figure 4.17: Frequency domain signals – silicone; DC; axial; Delrin®

The first wax interface setup generally showed a single dominant, mid-range frequency for impactors 20 *g* or greater in mass. At 10 *g*, the signals generally had a more balanced composition with a dominant high frequency component and another constituent in the mid-range. The signals also contained some noise adjacent to the presumed second mode. These results were extremely promising for validating the experimental modelling of an intermediate stiffness interface condition, showing the expected high frequency and mid-range composition. Additionally, the dominance of the mid-range frequency would lend sensitivity to future mathematical model matching.

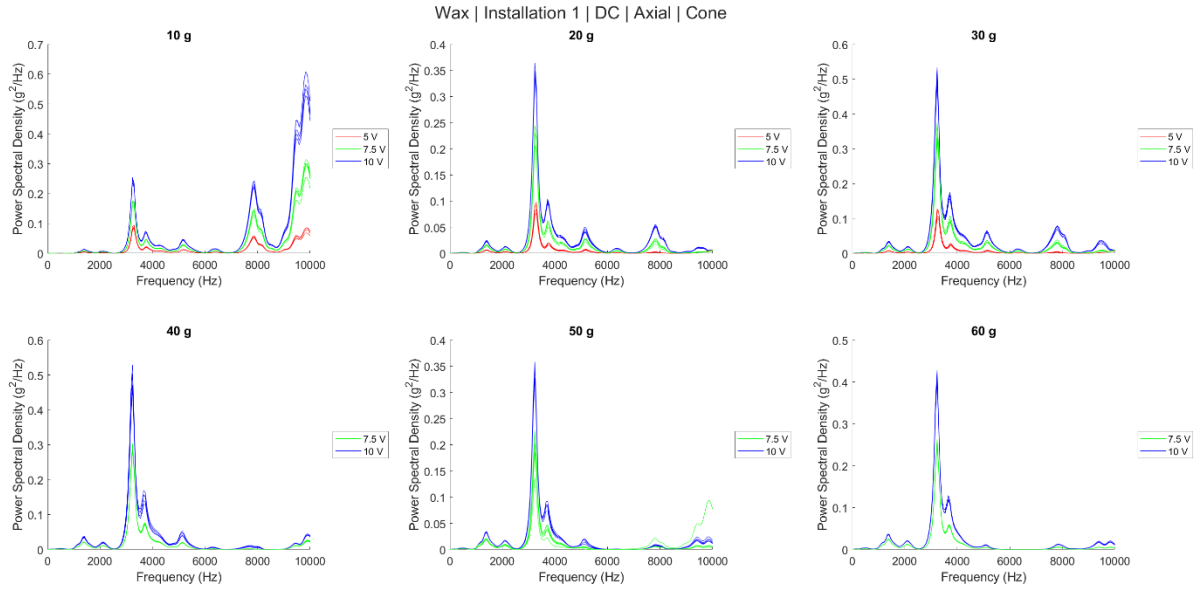


Figure 4.18: Frequency domain signals – wax 1; DC; axial; cone

The second installation generally displayed similar behaviour; however, there were a few notable differences. To start, the 10 *g* impactor signals showed much greater noise in the high range; although, a peak could still be distinguished. In the mid-range, the dominant peak was shifted higher than the previous installation. It should be noted that the installation process was refined over time, and later installations likely had improved interface coverage. Enhanced coverage could have resulted in higher levels of effective interface stiffness, matching the observed behaviour (increase in first mode frequency). Paraffin wax signals from the second installation and for a subset of impact rod masses can be viewed in Figure 4.19.

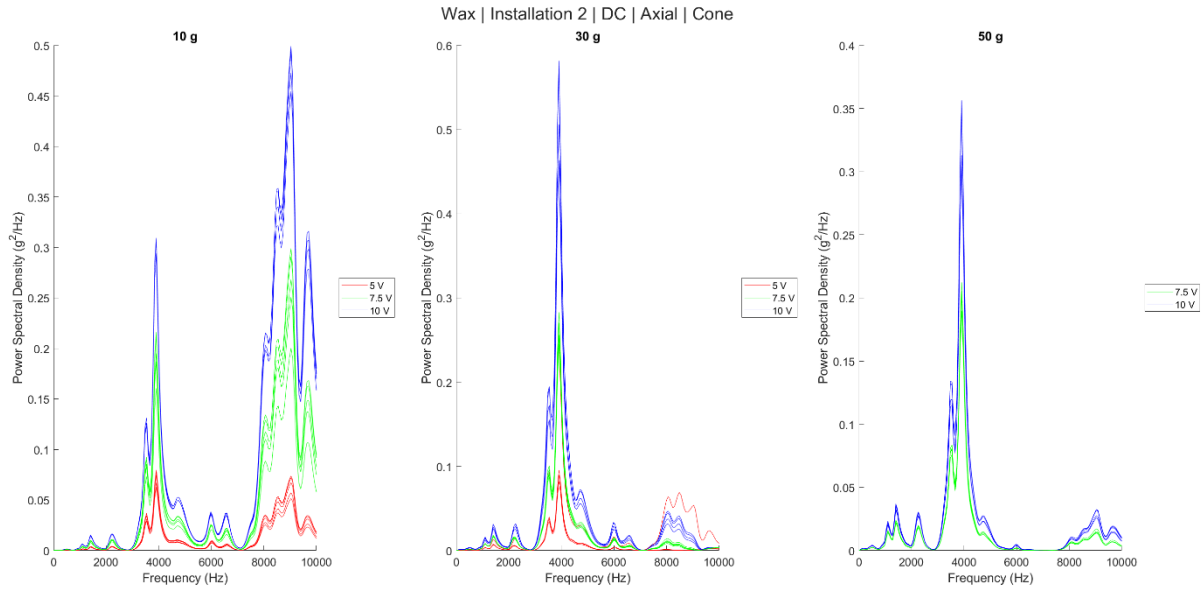


Figure 4.19: Frequency domain signals – wax 2; DC; axial; cone

Common patterns were again observed for the superglue interface setup. Signal composition shifted towards a dominant frequency occurring in the first half of the frequency domain ($< 5000 \text{ Hz}$) for the 20 g impact rod, with a few outliers occurring at an actuation voltage of 5 V . Beyond 10 g , the signals resembled an intermediate interface setup, with a dominant frequency occurring in the mid-range. This presented a troubling obstacle for impact rod selection: rods that amplified first mode frequencies for low stiffness interfaces also revealed noise in high stiffness interface conditions. Revealing mid-range noise within a high stiffness condition could easily result in an intermediate stiffness misclassification.

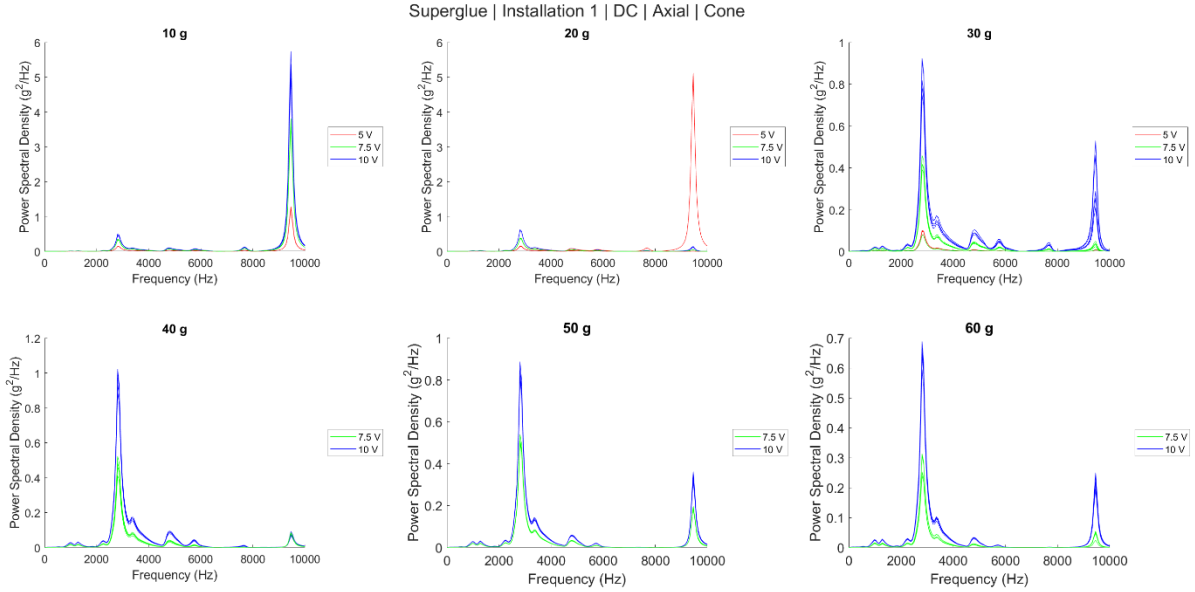


Figure 4.20: Frequency domain signals – superglue; DC; axial; cone

With the frequency domain curves plotted, modes predicted by the modal finite element model were tracked across various factor interactions. Regions were defined according to Table 4.5 to track the same dominant modes across factors, even if they were not the tallest or second tallest peak in the full domain. For example, the first mode for the silicone setup without the GV connector installed was defined as the largest peak below 1000 *Hz*. This presented an opportunity to track the behaviour of the same mode across various impactor configurations. The regions were defined by taking a holistic view of the frequency domain data in conjunction with the known modal finite element frequencies. Again, for the silicone setup, although a dominant frequency was not always apparent below 1000 *Hz*, in a handful of configurations, power in the region dominated the signals, which lent credence to defining the region. Regions were defined for each interface and implant configuration to objectively track the dominant modes across other factors, especially impact rod mass and actuation voltage. Considering noise was a significant issue for the superglue setup, a first and second mode region were still defined. The low mode region was not presumed to be the first axial mode of the system, characterized by relative shearing between the implant and bone. Instead, it was tracked as an indication of how the impactors could influence and amplify noise within the system. The second axial mode was assumed to be the true, single detectable axial mode of the system (the superglue setup was not expected to have an observable second axial mode). Also considering that noise was likely to present the system as an intermediate

interface condition, the first region was defined the same way for superglue as for paraffin wax. For each region, the frequency and amplitude of the dominant mode was extracted. Parabolic interpolation was employed to improve the resolution of peak frequency extraction [70].

Table 4.5: Modal frequency extraction cutoffs

| GV | Interface | Mode 1 Upper Frequency Cutoff (Hz) | Mode 2 Lower Frequency Cutoff (Hz) |
|-----|--------------|------------------------------------|------------------------------------|
| Off | Silicone | 1000 | 9000 |
| | Paraffin Wax | 5000 | 9000 |
| | Superglue | 5000 | 9000 |
| On | Silicone | 800 | 8000 |
| | Paraffin Wax | 5000 | 8000 |
| | Superglue | 5000 | 8000 |

4.3.4 Amplitude Ratio

Amplitude ratio was defined as second mode power spectral density divided by the first. It provided a signal composition metric to aid in impact rod selection. Amplitude ratio was plotted against actuation voltage for each impact tip, interface, and other cascading factors. A first order polynomial was fit to each scatter to visualize changes over actuation voltage. Theoretically, the slope of the curves should be relatively flat, and the height should represent the ability of an impactor to shift signal composition towards the high frequency domain. The y-scale of the amplitude ratio figures were plotted logarithmically to aid in visualization. In general, the 10 g impact rod data fit the highest curves, representing exceptional ability to excite a wide frequency domain. For silicone, the 10 g curve generally resided above an amplitude ratio of 10^2 , while the shift to 20 g represented a dip to the vicinity of 10^1 . Some 30 g data points fell below 10^0 (signal equally composed of both modes), and heavier rods generally continued to lower amplitude ratio. The Delrin® impact tip worked to drastically lower amplitude ratio, with the 10 g curve descending below an amplitude ratio of 10^0 for some actuation voltages. Curves tended to increase with actuation voltage (higher speeds caused compositional shifts toward higher frequencies), and

there tended to be less uniform behaviour for the flat and Delrin® impact tips. Amplitude ratio curves for the silicone setup without the GV connector installed can be viewed in Figure 4.21.

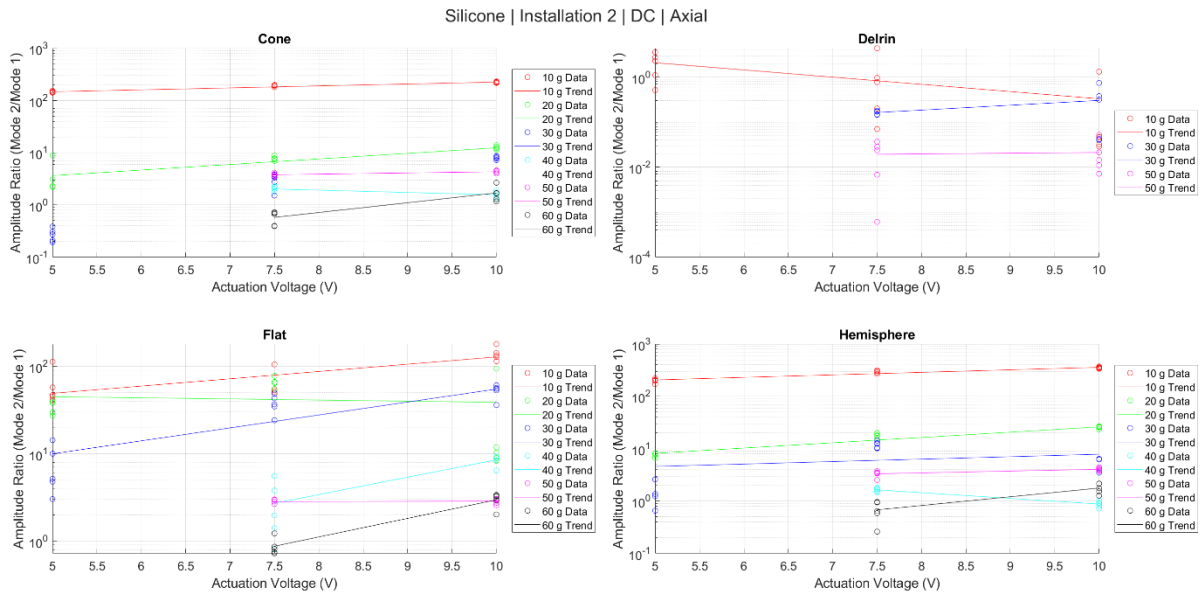


Figure 4.21: Amplitude ratio – silicone; DC; axial

Similar patterns were observed for silicone signals with the GV connector installed; however, it was more difficult for heavy impactors to lower amplitude ratio levels. Additionally, it was more difficult to trigger a response from the system at all. The 30 g impact rod generally owned the lowest curve to elicit responses at all actuation voltages, and the 60 g rod was only able to elicit responses at 10 V. Curves for the silicone setup with the GV connector installed can be viewed in Figure 4.22.

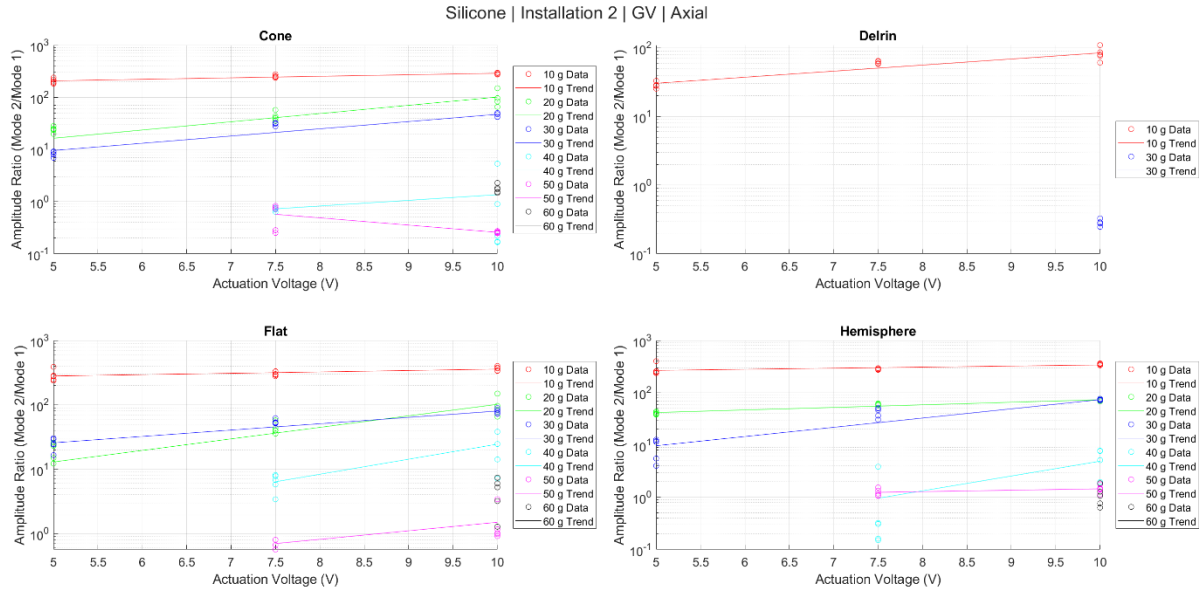


Figure 4.22: Amplitude ratio – silicone; GV; axial

For the first paraffin wax interface, again, the 10 *g* impact rod resulted in the highest amplitude ratio, hovering around 10^0 . The other impact rods were mostly clustered between 10^{-2} and 10^{-1} . In this case, actuation with the 10 *g* impactor resulted in more balanced signals than the other impact rods. The conical and hemispherical tips continued to display more uniformity and similarity than the flat tip. Amplitude ratio curves for the first wax installation without the GV connector installed can be viewed in Figure 4.23.

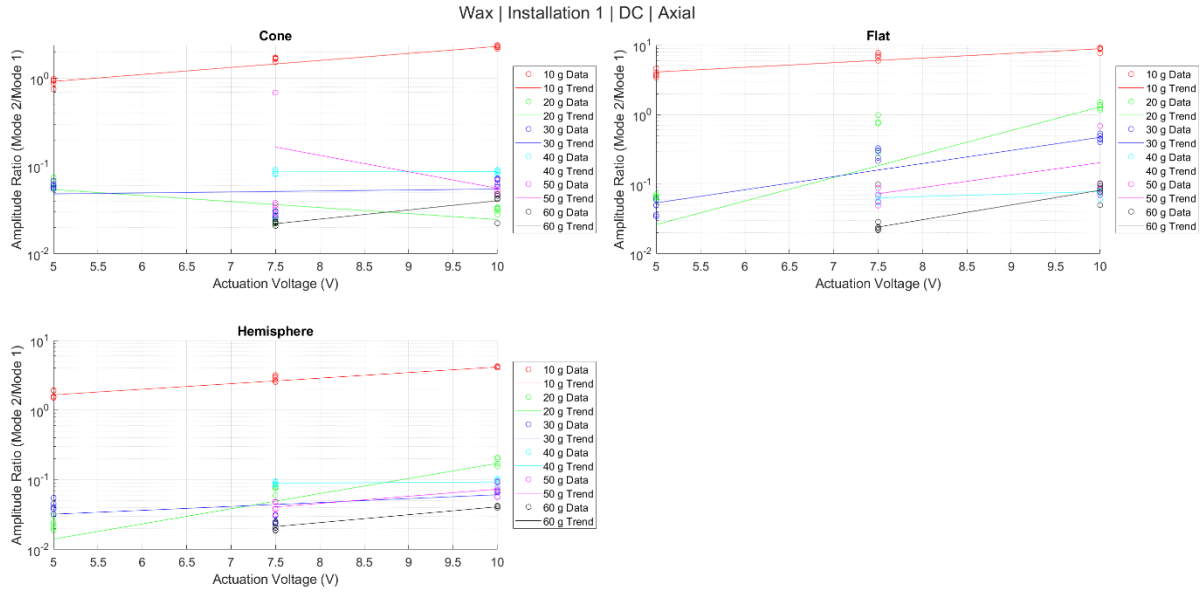


Figure 4.23: Amplitude ratio – wax 1; DC; axial

The second wax installation did not display significantly divergent amplitude ratio behaviour: the 10 g impactor largely produced balanced signals, and there was a distinct drop for heavier impactors. The second wax installation curves can be viewed in Figure 4.24.

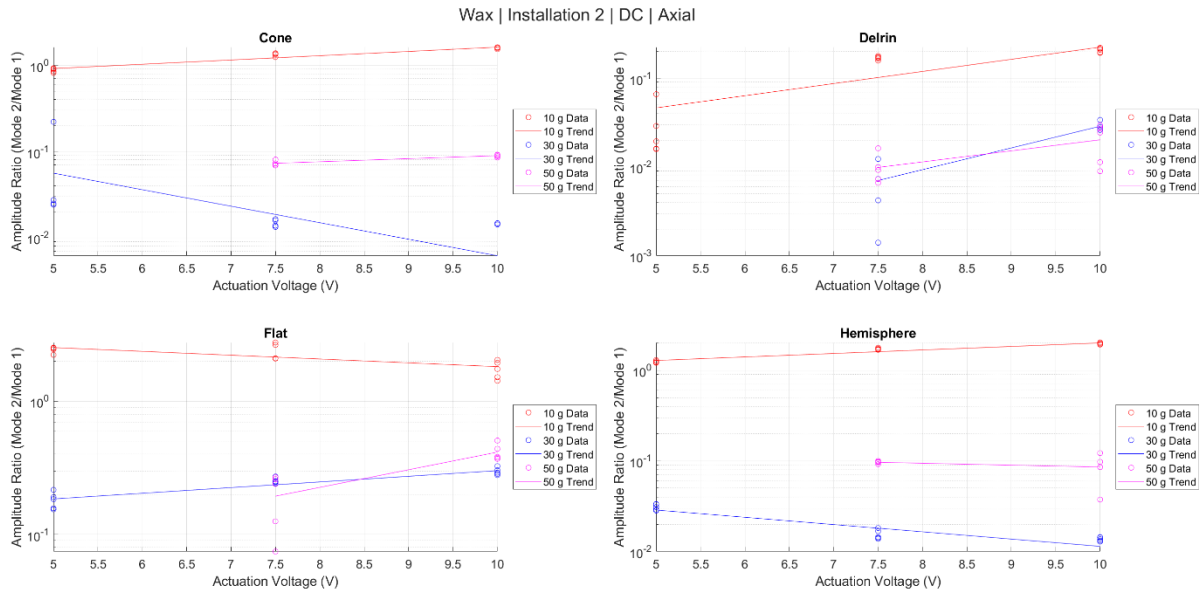


Figure 4.24: Amplitude ratio – wax 2; DC; axial

For the superglue interface setup, the 10 g impactor produced uniquely large amplitude ratios. The other rods skewed the amplitude ratios towards mid-range noise (as defined through the peak

identification process) for the conical and hemispherical impact tips. The flat impact tip generally resulted in higher amplitude ratios than the other geometries. This was in line with predictions (Section 3.6.4.2), as flush strikes with a flat impact interface were expected to have higher impact stiffnesses than conical or hemispherical geometries, shifting power spectral density to higher frequencies.

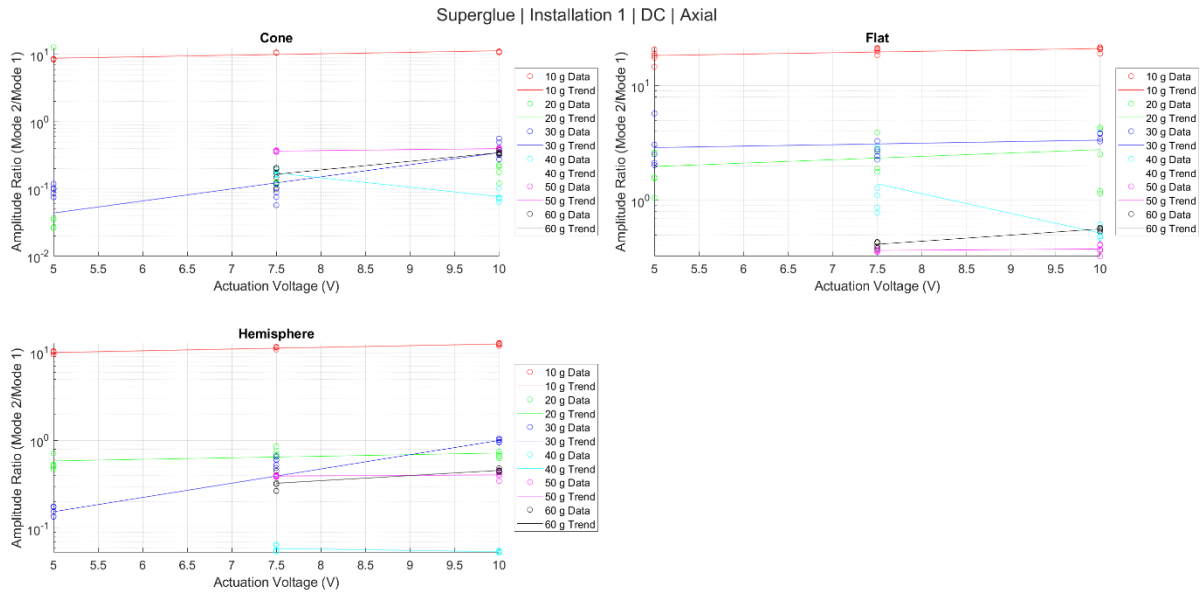


Figure 4.25: Amplitude ratio – superglue; DC; axial

4.3.5 Mode 1 Power Spectral Density

Mode 1 power spectral density in g^2/Hz was used to further evaluate the ability of impactors to strongly excite first mode frequency across all interface stiffness conditions. First mode amplitude was plotted against actuation voltage for various factor interactions; a linear y-scale was most appropriate for visualization. For the silicone interface, the 10 g impactor generally resulted in the lowest first mode frequency amplitudes. Amplitudes were generally raised with increased mass until a mass of 30 g was reached. At this point, the mass curves tended to fall but stayed above the 10 g baseline. This phenomenon raised two interesting design considerations: larger impact rods were generally better at exciting lower frequencies but produced them with diminishing, and eventually negative, power returns. The drop in power spectral density for the latter half of the mass range may be attributed to slow impact velocities. When actuated under the same conditions as lighter rods, heavier rods accelerate slower according to Newton's second law,

resulting in sluggish impact speeds. Beyond a certain threshold, the benefits of increasing mass to first mode frequency amplification are outweighed by the consequence of weaker actuation. It is also possible that beyond a certain point, extremely large masses could cut down the excitation domain so much as to eliminate first mode coverage; however, this is an unlikely scenario considering the small first mode frequency value of the silicone setup. Mode 1 amplitude curves for the silicone setup without the GV connector installed can be viewed in Figure 4.26.

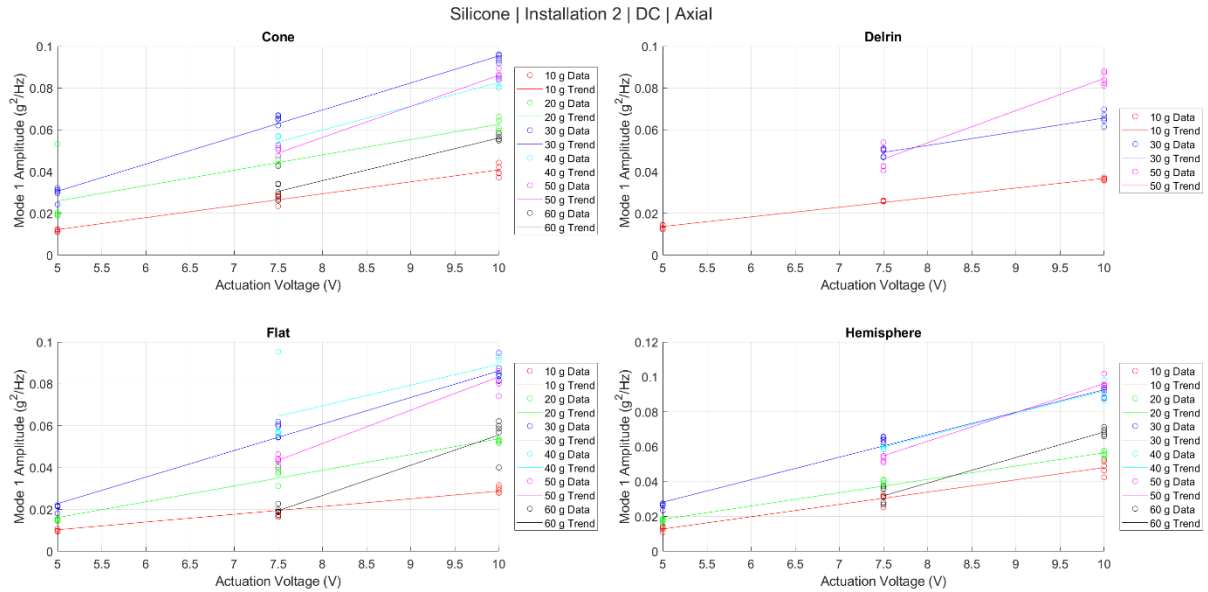


Figure 4.26: Mode 1 amplitude – silicone; DC; axial

Results were slightly altered by the addition of the GV connector (Figure 4.27). Once installed, heavier impact rods often provided a mode 1 power spectral density benefit beyond 30 *g*. However, for the conical tip, the benefit was marginal, if present at all, especially considering the loss of low voltage actuation potential. For the hemispherical tip, only the 40 *g* impactor exceeded the 30 *g* curve, and for the flat tip, the 40 *g* impactor held the highest curve, followed by 50 *g*, then 30 *g*.

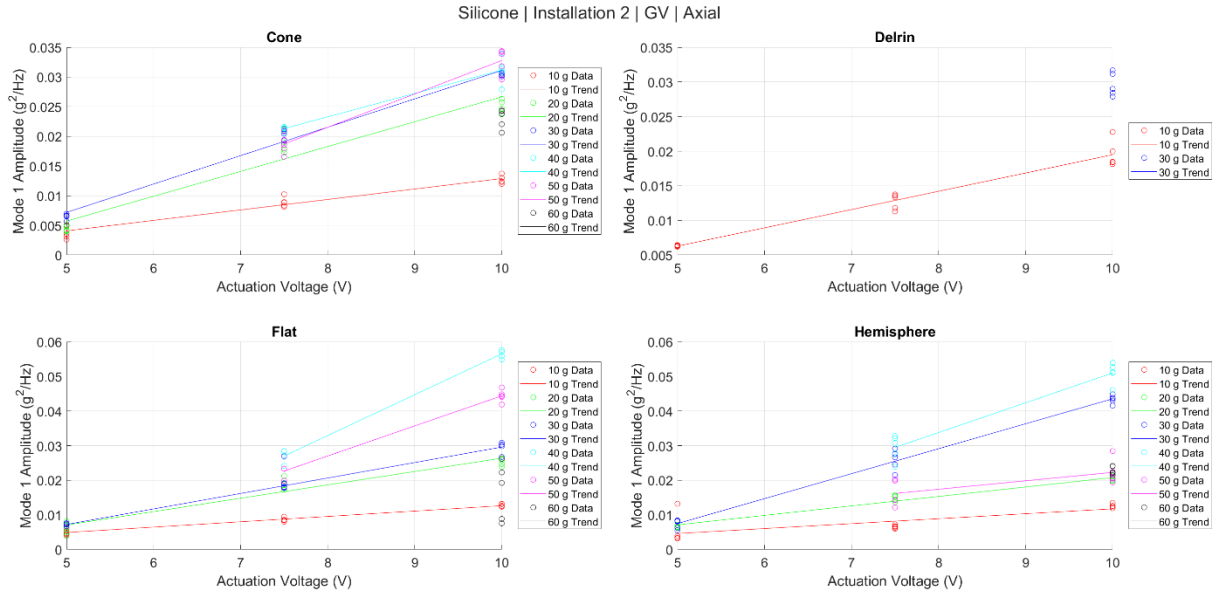


Figure 4.27: Mode 1 amplitude – silicone; GV; axial

Both wax interface installations shared similar properties, with the 30 g impact rod maximizing mode 1 amplitude in most cases. The mode 1 amplitude curves for the first paraffin wax setup can be viewed in Figure 4.28. For the silicone and wax interface conditions, the 30 g impact rod appeared to optimize the response variable (mode 1 amplitude). Also considering the amplitude ratio results, the impactor was effective at both balancing signal compositions and adding power to modes of interest under the same actuation conditions as other impact rods.

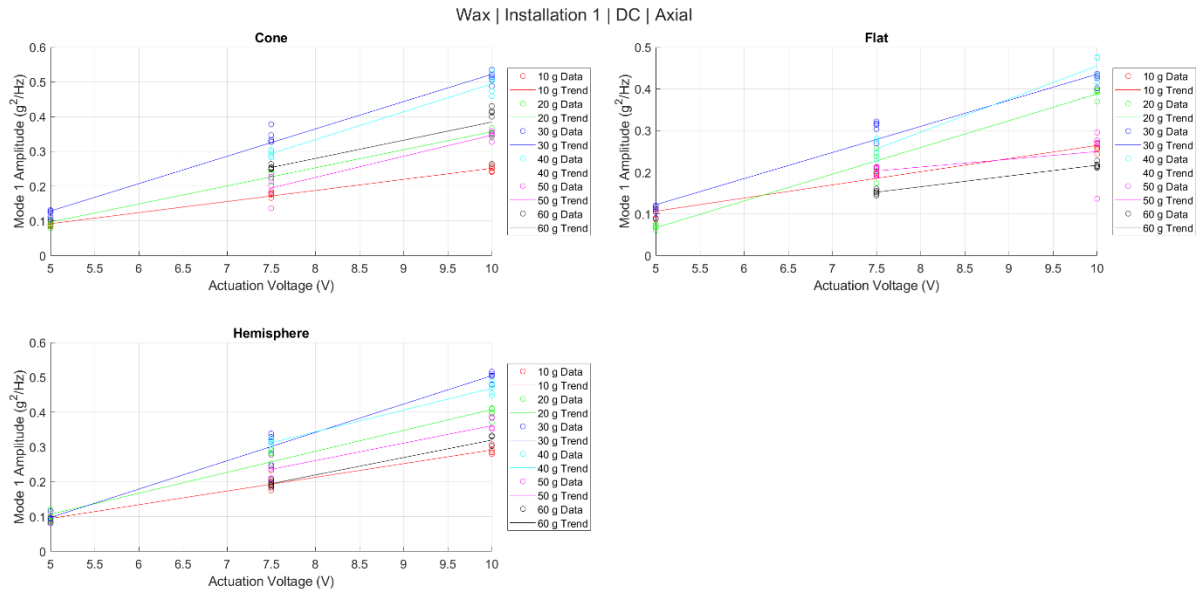


Figure 4.28: Mode 1 amplitude – wax 1; DC; axial

Finally, results were mixed for the superglue interface. The 30 *g* impactor continued to elevate first mode frequency, but perhaps not to the same extent as previous setups. For the superglue setup, first mode frequency represented mid-range noise within the system, with amplification being an undesirable outcome. In this case, heavier rods generally continued to amplify first mode amplitude, and the amplitude ratio results indicated that they also attenuated the second mode of the system (actual sensitive first mode). The benefits the 30 *g* rod carried to the silicone and wax setups were detrimental to the superglue setup.

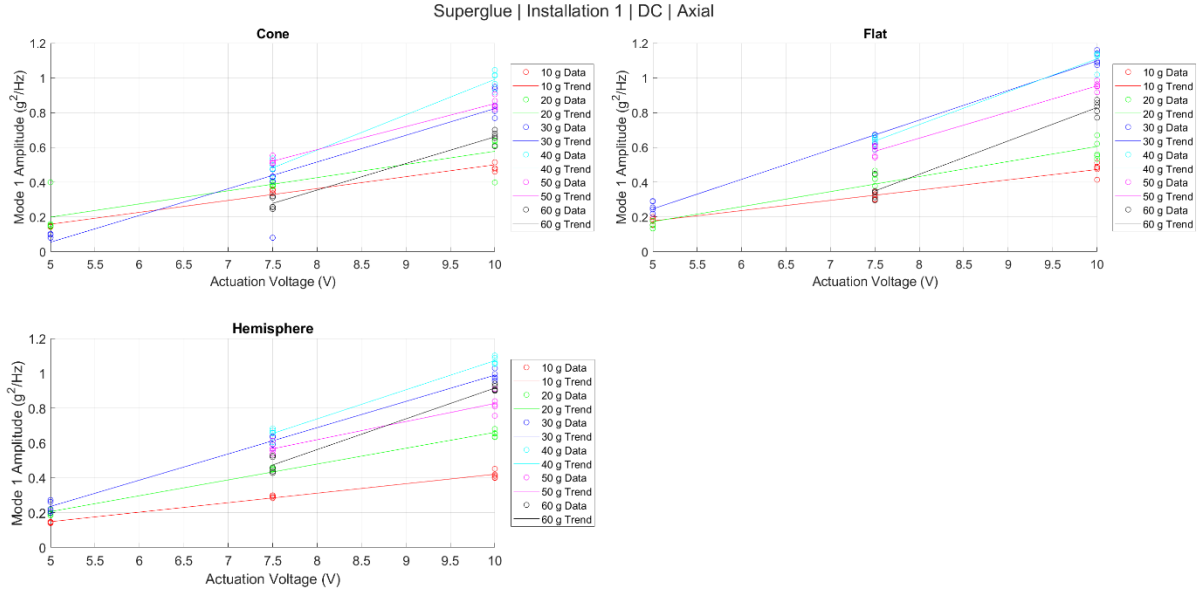


Figure 4.29: Mode 1 amplitude – superglue; DC; axial

4.3.6 Band Power

Band power was taken as the power integrated over the power spectral plots for $0 \text{ kHz} \leq f \leq 24 \text{ kHz}$, with the upper bound representing the bandwidth of the accelerometer. It was taken as a signal quality metric; like mode 1 amplitude, high band power would represent a well actuated signal. For the silicone setup without the GV connector installed (Figure 4.30), the 10 g impactor generally resulted in the largest band power estimates across actuation voltages.

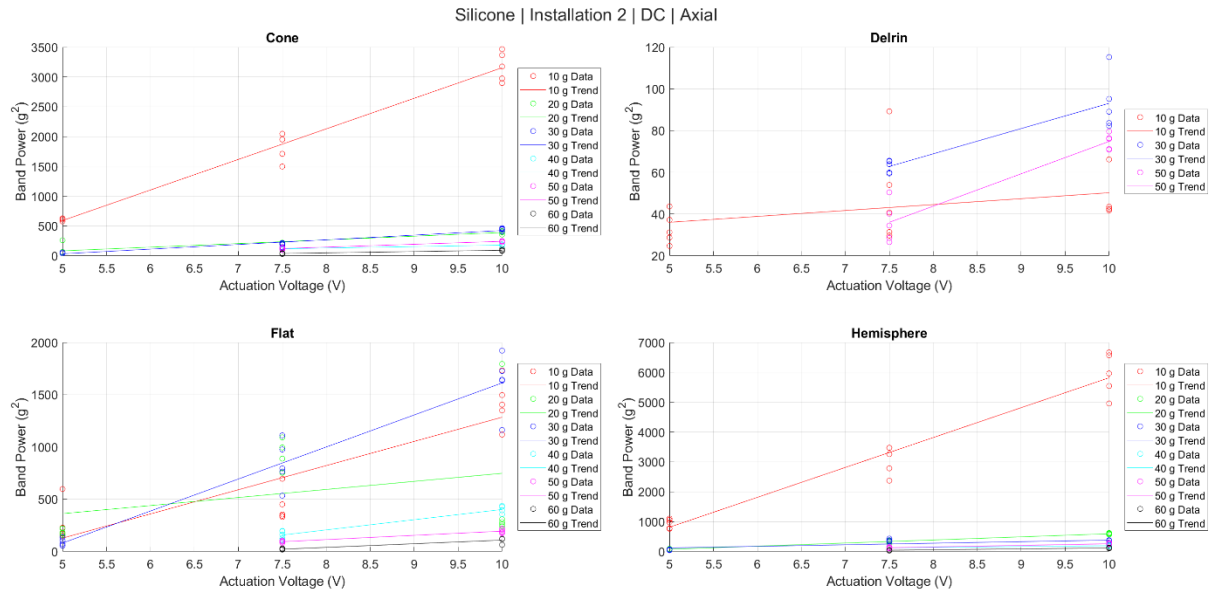


Figure 4.30: Band power – silicone; DC; axial

With the GV connector installed (Figure 4.31), there was much less separation in band power between different impactors; however, the 10 *g* impactor still resulted in the largest band power estimates. The 20 *g* and 30 *g* impactors generally crossed over as the second highest band power curves.

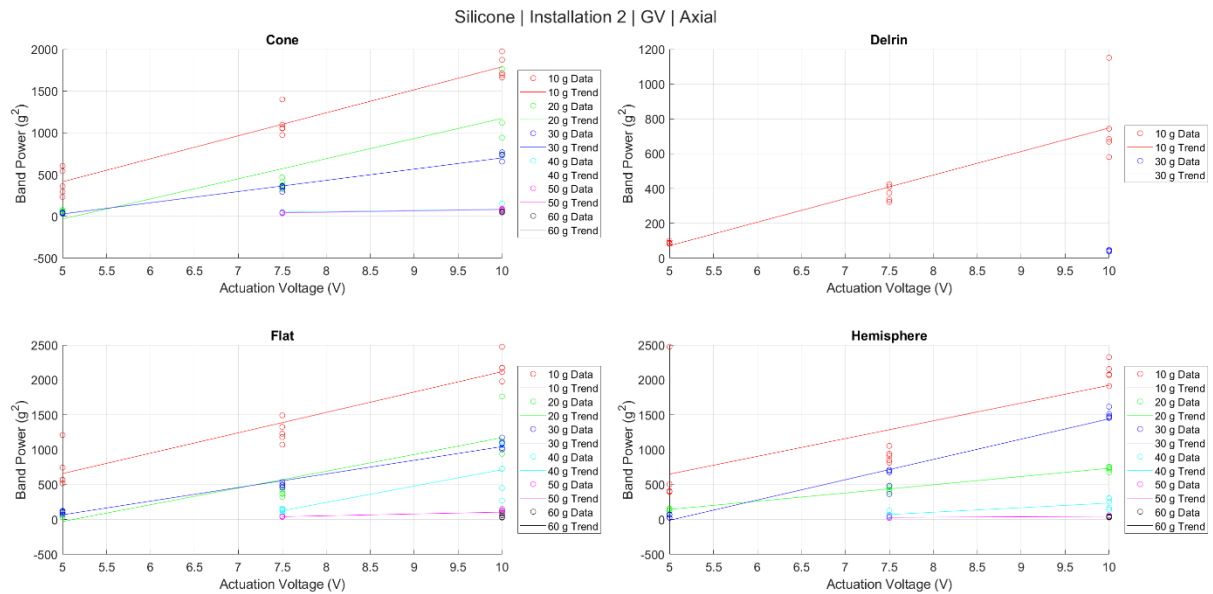


Figure 4.31: Band power – silicone; GV; axial

Also like the mode 1 amplitude curves, the silicone and wax interfaces largely shared similar band power characteristics. For the paraffin wax interface setup without the GV connector installed (Figure 4.32), the 10 *g* impactor resulted in the largest band power estimates, followed by either the 20 *g* or 30 *g* curves.

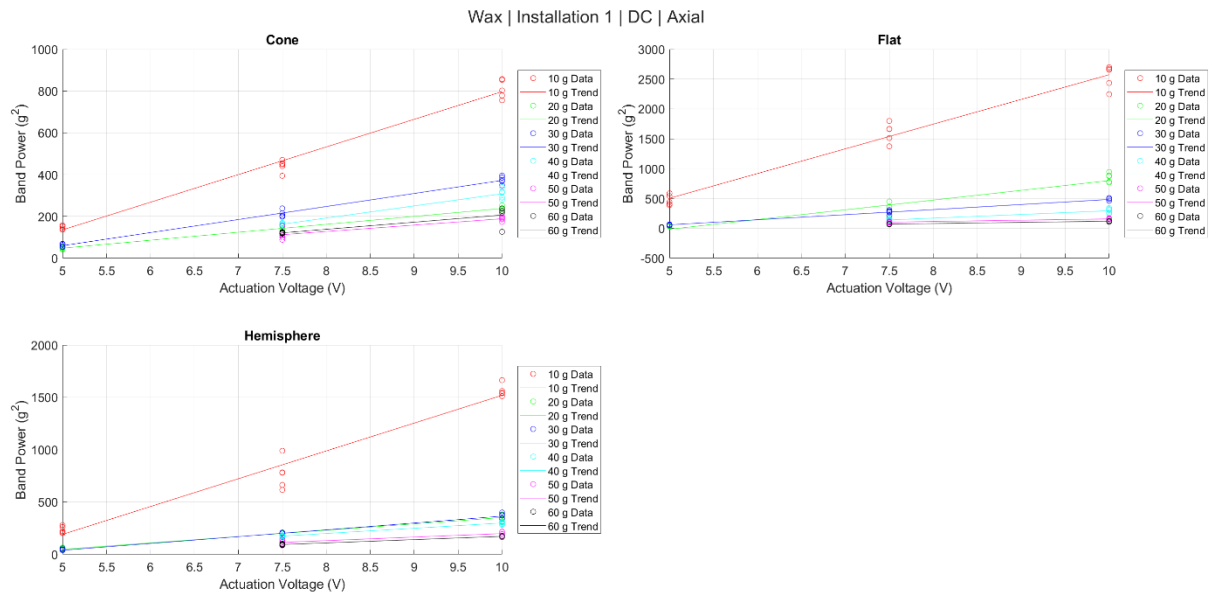


Figure 4.32: Band power – wax 1; DC; axial

The superglue setup had similar band power curve distributions to the other interfaces. The 10 *g* impactor would again provide superior band power, with the 20 *g* and 30 *g* impact rods being the next obvious choices for enhanced signal quality among the heavier rods.

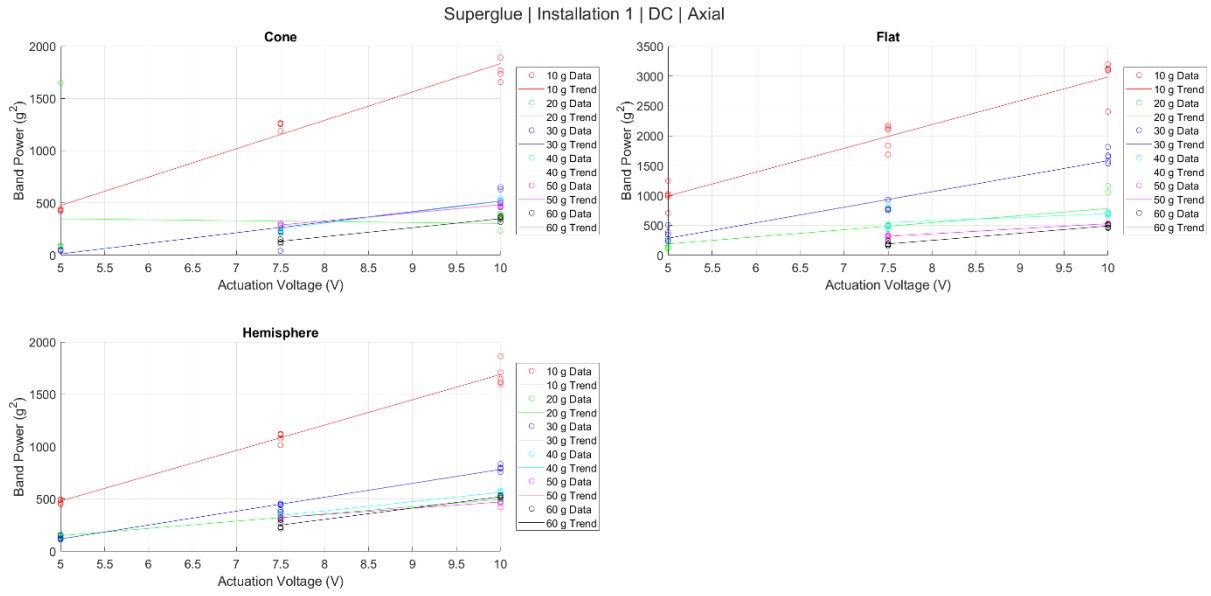


Figure 4.33: Band power – superglue; DC; axial

4.3.7 Final Design Decisions and Amplitude Ratio Intraclass Correlation

With impact rod performance evaluated across a plethora of response variables, the last step was to evaluate the reliability of the impact tip geometries and make final design decisions. Intraclass correlation coefficients were calculated for amplitude ratio measurements according to the case 3 model, ICC(A,1) designation as defined by McGraw et al. [71, 72], using open source code [73]. This is a two-way mixed effects model that indicates the absolute agreement of measurements made under fixed levels of the column factor [71]. Coefficients were calculated under the column factors of interface stiffness and GV connector presence. Five repeated measures for each object of measurement represented random effects within the model. Amplitude ratio was chosen as the response variable of interest because it was a convenient representation of signal composition. An ideally reliable impactor would elicit identically composed signals for a given object of measurement. ICC curves were plotted for each impact tip geometry and impact rod mass across actuation voltages. The curves in Figure 4.34 represent all measurements taken within this development and evaluation study. Before making a tip selection, it was necessary to narrow down which impact rods would be considered for further development. From amplitude ratio, mode 1 amplitude, and band power analysis, it was apparent that no single impactor configuration would be optimal in all interface stiffness conditions. It was immediately apparent that the conical and hemispherical geometries shared more uniform results than the flat and Delrin® impact tips.

However, Delrin® demonstrated utility in drastically reducing frequency excitation bandwidth. Even when combined with the 10 *g* impactor, the Delrin® tip consistently allowed visualization of the first axial mode for the silicone interface setup. It was also noted that there were distinct differences in response characteristics between the 10 *g* impactor and the rest of the impact rods. The 10 *g* impactor had excellent band power and was the only impactor that mitigated mid-range noise for the superglue interface condition. Furthermore, it offered more balanced signal compositions in the paraffin wax case than other impactors. The major downside of the 10 *g* impactor was its inadequacy in exciting the first axial mode of the silicone interface condition. Under the condition, the other impactors provided better amplitude ratios and the 30 *g* impact rod generally maximized the power spectral density amplitude of the first mode frequency. With this knowledge, it was apparent that further experimentation was needed, and a multi-impact approach was synthesized for development. It was hypothesized that a light impact rod with interchangeable tips of varying impact stiffness would be able to cover a large frequency excitation domain. The 10 *g* impact rod was selected to operate with 316 stainless steel and Delrin®, or an equivalent material (PEEK), impact tips. However, the promise of heavier impact rods was not thrown away entirely. It was decided that designing two handheld impactors in parallel would mitigate risk within the approach, with the other handpiece having a 30 *g* impact rod and identical interchangeable tips. The handpieces would have to go through further development and experimentation before a thorough operating procedure for making trust/distrust decisions between the signals generated by each impact tip could be outlined. In any case, the two impact rods masses were known, and final decisions on impact tip geometry could be made. The conical and hemispherical tips proved more uniform and similar than the flat tip across the various response variables. This qualitative observation also aligned with theoretical assumptions outlined in Section 3.6.4.2. It was apparent from Figure 4.34 that the conical impact tip provided extremely high amplitude ratio ICC values for both the 10 *g* and 30 *g* rods across all actuation voltages. Additionally, the tip was anecdotally easier to aim and position on the distal screw than other geometries, which could boost the reliability of future handheld impactors. Two handheld impactors would be developed, differentiated by impact rod mass (10; 30 *g*), and each handpiece would fit with interchangeable, conical impact tips of differing impact stiffness (316 stainless steel; PEEK).

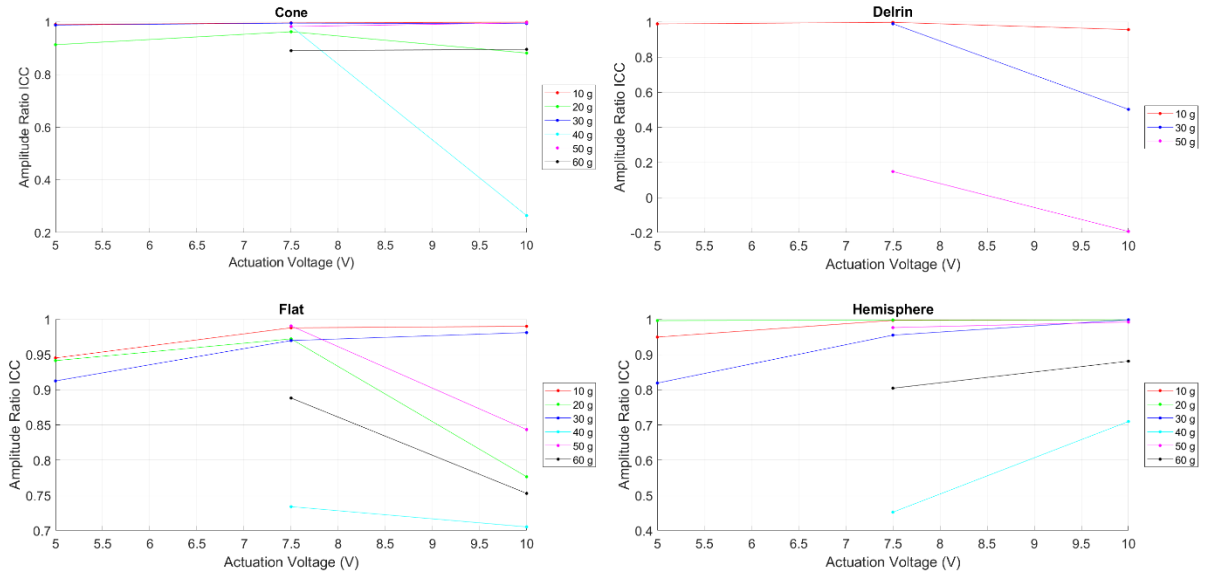


Figure 4.34: Amplitude ratio ICC vs. actuation voltage across all axial configurations

The design choices were further validated by a parametric study conducted by Mohamed on a 1D finite element model of the bone-implant system under a low interface condition [28]. The study demonstrated the effects of varying impact rod parameters (mass; impact stiffness; velocity) on the modal response of the system. Changing impact speed did not influence signal composition; instead, amplitude ratio was preserved across a range of initial velocity conditions [28]. Increasing velocity served to linearly raise the contribution of each mode, generally adding power to the overall response [28]. Changing impact stiffness primarily affected the contribution of the second mode, with lower stiffnesses reducing its amplitude [28]. Manipulating the stiffness did not significantly change the contribution of the first mode in any case [28]. Varying impact rod mass presented the most intriguing behaviour. As seen in Figure 4.35, contact time increased with mass, which was the intuitive and expected behaviour from the simple impact model (Section 3.3.3). Naturally, increasing contact time, or the width of the impulse applied to the bone-implant system, leads to a narrowed frequency input; however, if velocity is held constant, the impulse applied to the system increases with mass. In other words, increasing the mass while holding velocity constant imparts greater energy to the system. In the parametric study, this phenomenon was encountered. Since the first mode was in a low frequency bin because of the low interface condition, the impulse magnitude governed the first mode response and resulted in increased contribution with increased mass [28]. For the second mode, the increased contact time and

impulse resulted in competing behaviours: the frequency was either attenuated by the increased contact time or raised by the increased impulse [28]. Ultimately, this coupling manifested in a sharp peak when amplitude ratio (mode 1 amplitude/mode 2 amplitude) was plotted against impact rod mass (Figure 4.35). Interestingly, the peak occurred at approximately 30 *g*. The parametric study served to precisely demonstrate the effects of impact mass, stiffness, and velocity on the response of the bone-implant system. For velocity, this development study generally demonstrated similar behaviour to the model. Velocity appeared to be one of the least contributing factors to signal composition, instead transmitting power to all modes comprising a signal. Impact stiffness had straightforward effects in both the development study and 1D model; its effects on signal composition are generally a large focus of excitation optimization within the field of experimental modal analysis [64, 74]. It is well known that softer tips result in longer contact times and generally serve to attenuate higher frequencies components. This was observed in both the development experiment and parametric study. Lastly, the effects of impact rod mass were less obvious in both cases. In the development study, the high frequency attenuating effects of increased mass were observed, but diminishing returns appeared to be caused by slower impact velocities. The results from the parametric study indicated that if velocities were constant, a ~30 *g* impact rod would be the most favourable for a high amplitude ratio because larger rams also caused a larger impulse, boosting the contribution of the second mode. In this study, larger rods were observed to further reduce amplitude ratio (mode 2/mode 1), and mode 1 amplitude also fell beyond 30 *g*. From a theoretical and experimental standpoint, the 30 *g* impact rod appeared to present a practical mass optimization point in addition to the 10 *g* rod.

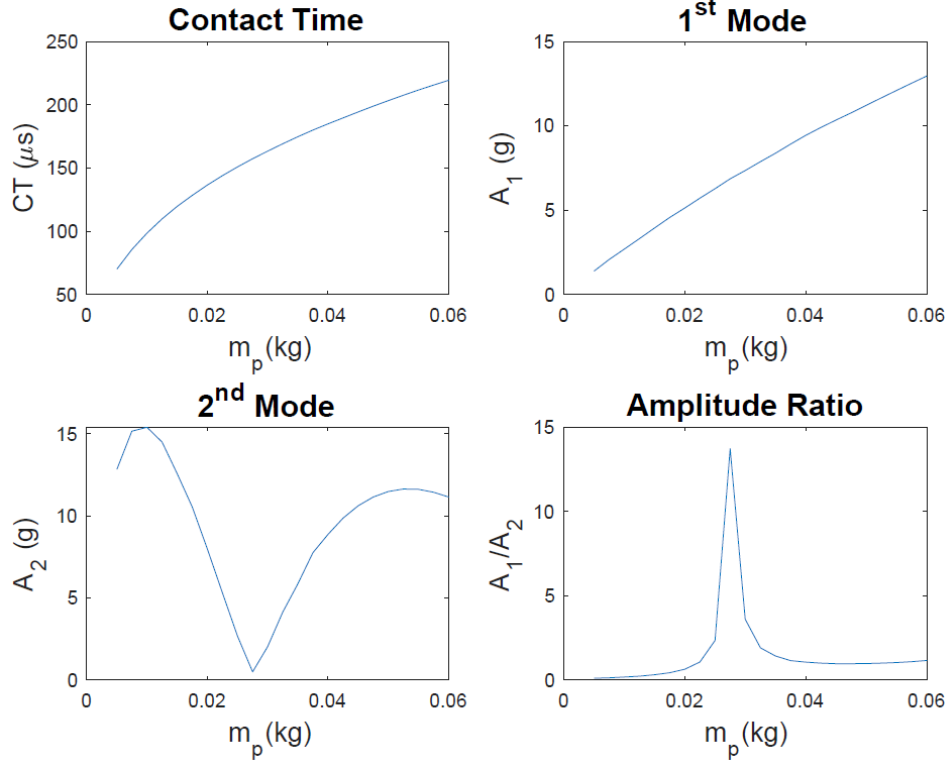


Figure 4.35: Modal contributions vs. impact rod mass for low condition of 1D finite element model [28]

4.3.8 Modal Finite Element Model and Experimental Model Comparison

To compare the modal finite element and experimental models, dominant frequencies were extracted and averaged for every measurement taken on setups without the GV connector installed (not present in modal finite element model). This meant that both modes could be compared for each interface in the entire design space of the experiment. For the superglue setup, the colloquial first mode would represent mid-range noise within the system. To help visualize the results of the analysis approaches, the extracted frequencies from both models were plotted in the frequency domain (Figure 4.36). It should be noted that the peaks only graphically represented the extracted frequencies, and the associated amplitudes had no particular significance. The modal finite element model results showed the desired or ideal outcome for the experiment. Here, the low frequency peak (red) grew towards the intermediate frequency peak (green) as the interface stiffened. In the final healing stages, the green peak should move towards its own second mode, which remained relatively constant for low and intermediate stiffness interfaces. As the interface reached the high stiffness condition (superglue), the first axial mode grew to usurp any second mode and dominated the frequency response of the system. In this final stage, the blue peak (first mode) resided among

the second modes of softer interface stiffness conditions. The experimental results grossly showed similar system behaviour to the modal finite element results. In the experimental plot, the silicone and paraffin wax curves were remarkably similar to the modal finite element plot. Discrepancies in the intermediate condition could be due to overestimating the Young's modulus of paraffin wax in the simulation or inadequate bonding region coverage in the physical model. In any case, demonstrating the sensitivity of the approach to an intermediate stiffness condition was the larger goal and was observed. The superglue contained at least one peak in the expected position; however, the other observed peak was not predicted by the modal finite element model. The extra peak was attributed to mid-range noise and fell amongst the first mode frequencies of the paraffin wax installations. In the frequency domain, it is easy to see how the presence of this noise could throw off the sensitivity of the vibration approach. Additional modelling would be conducted to deduce and potentially mitigate the source of the noise.

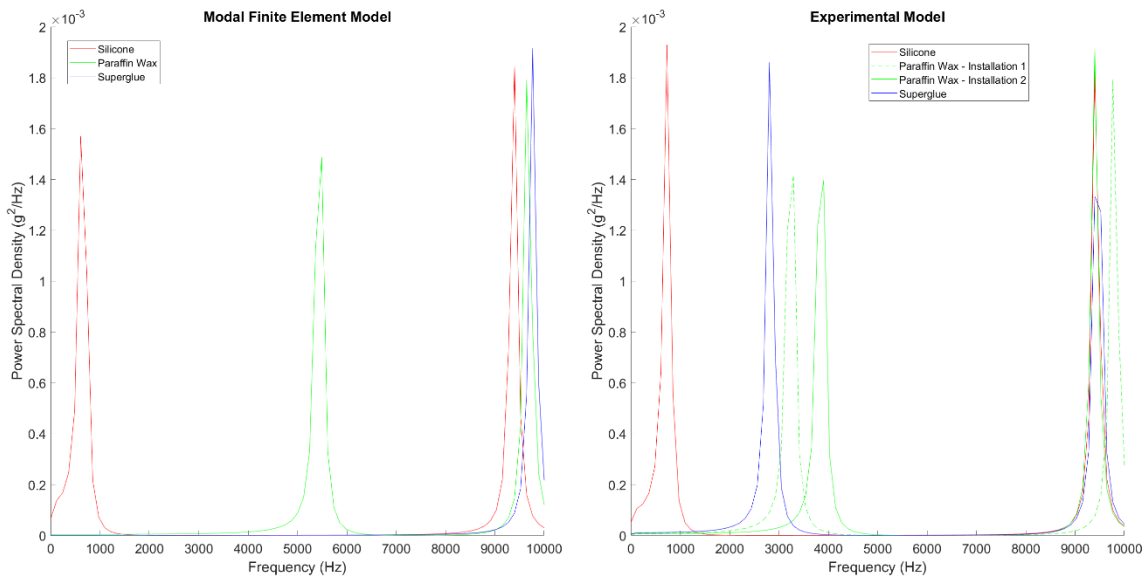


Figure 4.36: Modal finite element and experimental model frequency comparison

4.3.9 Velocity Measurement

4.3.9.1 Setup

Impact rod velocity measurements were taken to aid in the execution of high-fidelity impact finite element model simulations. The setup involved the same T-slot bar structure used in the main procedure of the experiment, with a plain white background to contrast a piece of tape adhered

mid-length to the impact rods. A high-power light was set up adjacent to a Fastec IL5 high speed camera (Fastec Imaging, USA), which recorded a 10 kHz . Impact rods were recorded in regular operation at three actuation voltages, previously specified. A photo of the setup can be viewed in Figure 4.37.

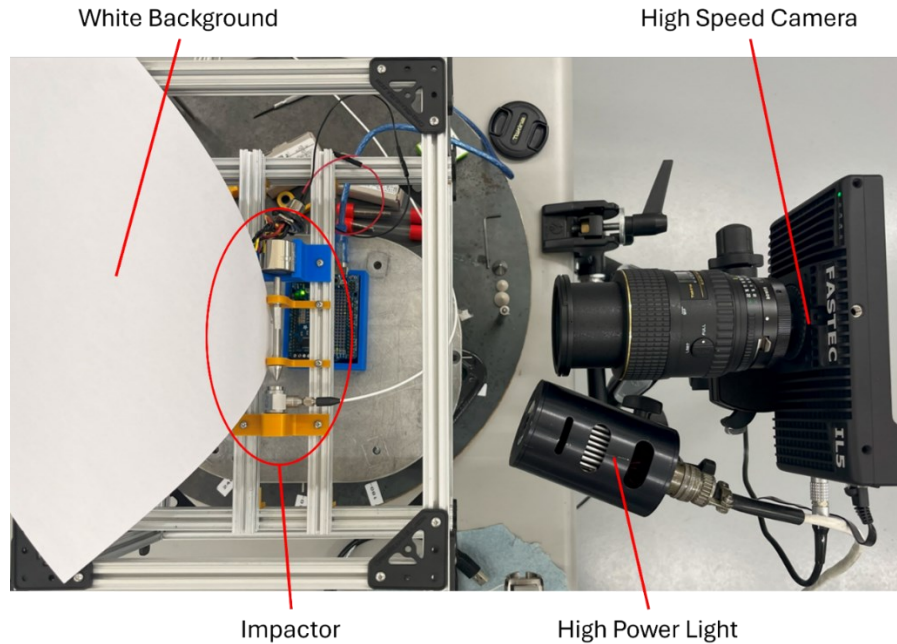


Figure 4.37: High-speed camera setup

4.3.9.2 Results

High speed camera recordings were digitally processed to obtain position data for the impact rods. The position data was then numerically differentiated to plot raw impact rod velocity vs. time (Figure 4.38). The velocity profiles occurred after an extended inert period within the raw signals. Oscillations occurred at the impact events with the front stop used in the test or bearing block back stop. The top speeds for the 10 g and 30 g impactors were recorded at the intermediate actuation voltage of 7.5 V . They were used as inputs to the impact finite element models discussed further in Section 4.3.10.

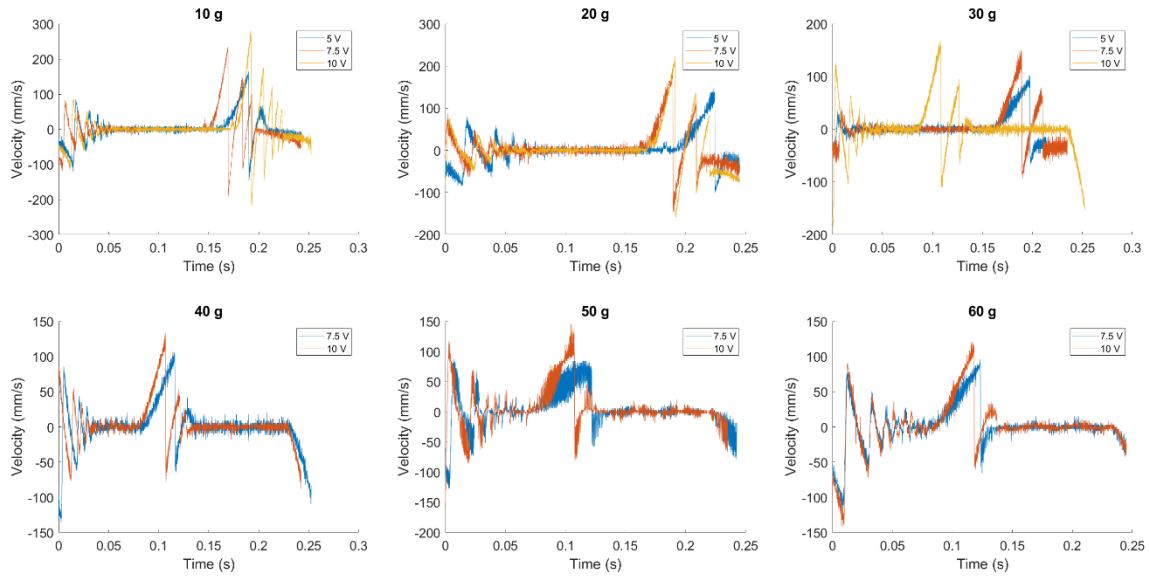


Figure 4.38: High speed camera raw velocity data

4.3.10 Finite Element Models

4.3.10.1 Setup

Modal and impact finite models were developed by Mohamed [28]. The modal model used a Lancsoz solver with hexahedral elements, while the impact model used an implicit solver with hexahedral elements. The maximum velocities of the 10 *g* and 30 *g* impact rods at an actuation voltage of 7.5 *V* were used as initial condition inputs to the impact model. Full scale solid models of the impact rods were used in the simulations; however, all impact interfaces were modelled as flat, cross-sectional planes of the impact rods. The impact rods were positioned to strike the distal screw at the 12:00 position, as they were in the main procedure of the experiment and were initially placed five time steps away from contact with the implant. The contact stiffness was found through trial and error, matching the impact force profile of the 10 *g* impact rod striking the intermediate (paraffin wax) interface to a contact time of approximately 100 μs (experimentally observed for the ASIST and 10 *g* impact rod). A general setup summary of both finite element models can be viewed in Table 4.6.

Table 4.6: Modal and impact finite element model parameters

| Parameter | Modal Model | Impact Model | |
|------------------------------|------------------------------------|------------------------|----------|
| | | 10 g Rod | 30 g Rod |
| Solver | Lancsoz | Implicit | |
| Element Type | Hexahedral | Hexahedral | |
| Boundary Condition | Fully fixed | Fully fixed | |
| Damping | N/A | Stiffness proportional | |
| Initial Velocity (mm/s) | N/A | 230 | 150 |
| Contact Stiffness (N/mm) | N/A | 600 | |
| Time Step (μs) | N/A | 4 | |
| Samples | Natural frequencies up to 24 kHz | 2001 | |

Material properties were set to the common or measured properties of each material. The properties of silicone [28], paraffin wax [28, 67], superglue [28, 66], short fiber epoxy [28, 75], titanium [28, 76], and 316 stainless steel [76, 77] are listed in Table 4.7. Additionally, first and second mode damping ratios were set by specifying Rayleigh proportional damping constants α and β as defined by Equation 4.2, where c is viscous damping, m is mass, and k is stiffness.

$$[c] = \alpha[m] + \beta[k] \quad 4.2$$

Diagonalizing the relationship using the mass normalized modal matrix, ϕ , Equation 4.3 can be derived, which gives the damping ratio, ζ_i , for each mode, i :

$$\begin{aligned}
 [\phi]^T [c] [\phi] &= \alpha [\phi]^T [m] [\phi] + \beta [\phi]^T [k] [\phi] \\
 [2\zeta\omega] &= \alpha [I] + \beta [\omega^2] \\
 \zeta_i &= \frac{\alpha}{2\omega_i} + \frac{\beta\omega_i}{2}
 \end{aligned} \quad 4.3$$

For simplicity, α was set to zero, which equivalently set up the model to have stiffness proportional damping. It follows that β is given by Equation 4.4:

$$\beta = \frac{2\zeta_i}{\omega_i} = \frac{\zeta_i}{\pi f_i} \quad 4.4$$

Using the natural frequencies extracted from the modal model and specifying $\zeta_2 = 1\%$, the stiffness proportional damping constant, β , was calculated for each interface condition. Every material within the bone-implant system was set to the same damping ratio, while the impact rod was left undamped. Damping constants for each material can be viewed in Table 4.7.

Table 4.7: Modal and impact finite element model material properties

| Part | Material | Density (tonne/mm ³) | Young's Modulus (MPa) | Poisson's Ratio | Damping (s/rad) |
|---------------------------|---------------------------|-------------------------------------|-----------------------------|--------------------|--------------------|
| BII | Silicone | 1.24E-09 | 0.45 | 0.30 | 3.39E-07 |
| | Paraffin Wax | 1.24E-09 | 40 | 0.30 | 3.29E-07 |
| | Superglue | 1.24E-09 | 1000 | 0.30 | 2.86E-07 |
| Cortical Shaft | Short Fiber Epoxy | 1.90E-09 | 16000 | 0.30 | BII Value |
| Implant Stem | Titanium | 4.40E-09 | 100000 | 0.31 | BII Value |
| Dual Cone Adapter | | | | | |
| Internal Locking Screw | | | | | |
| Distal Screw | | | | | |
| 10 g Impact Rod | 316 Stainless Steel | 8.00E-09 | 193000 | 0.30 | 0.00E+00 |
| 30 g Impact Rod | | | | | |

Each impact model consisted of one of three interfaces and one of two impact rods, for a total of six simulations. Impact acceleration plots for each impact rod striking the intermediate interface setup can be viewed in Figure 4.39.

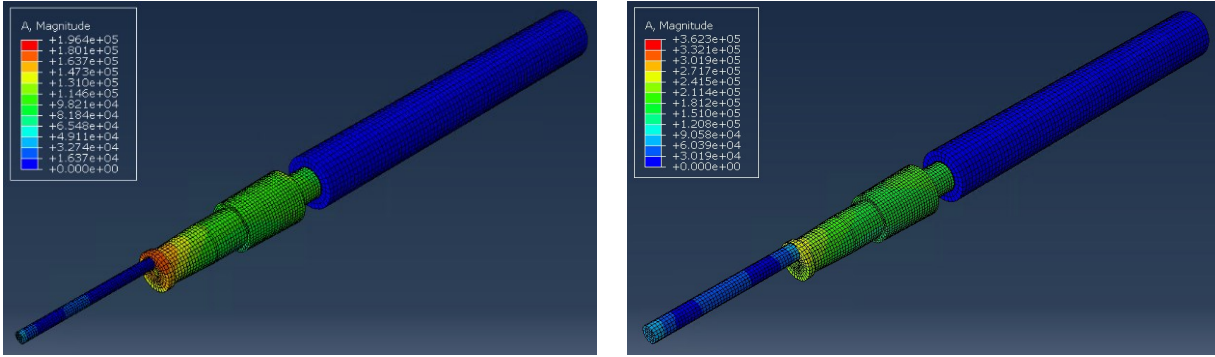


Figure 4.39: Impact finite element model – silicone interface. Left, 10 g impact rod; right, 30 g impact rod

For all simulations, the average axial acceleration of the entire impact rod node set as well as a node set defined to mimic the size and location of the experimental accelerometer were extracted. Sample node sets are visualized in Figure 4.40.

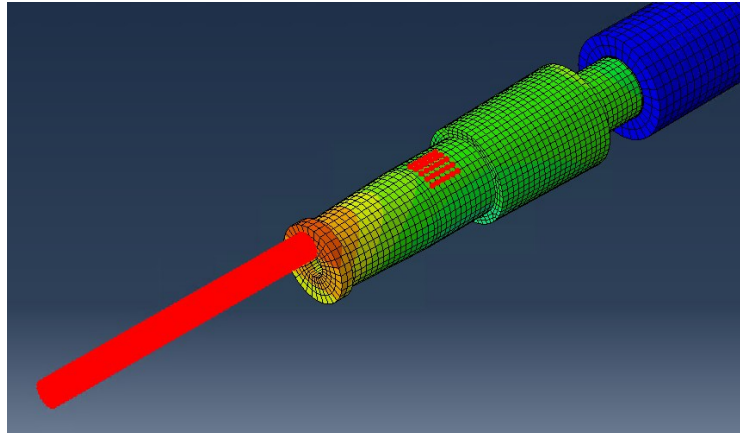


Figure 4.40: Impact finite element model acceleration measurement location detail for 10 g impact rod simulation. Acceleration recorded from node sets highlighted in red

4.3.10.2 Impact Model Results

Frequencies extracted from the impact model displayed similar overall tendencies to the modal and experimental models. Frequencies were distributed similarly to the modal model, with the first axial mode spanning nearly the entire 10 kHz domain. Like the experimental model, the 30 g impact rod attenuated high frequency components and amplified the first mode for all interface conditions compared to the 10 g impactor. The silicone setup was less sensitive overall to actuation than the other interface conditions, and the wax setup had the highest first mode power spectral density in all cases. Interestingly, the superglue simulations contained an unexpected frequency in the latter half of the mid-range domain. No other setups contained this mode. The frequency domain signals of each simulation are compared in Figure 4.41.

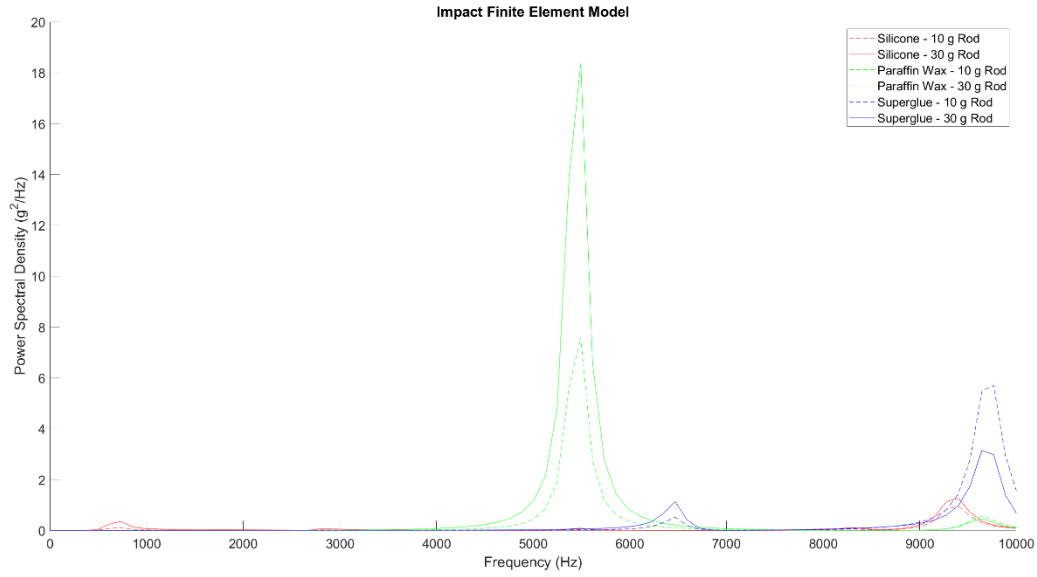


Figure 4.41: Impact finite element model – frequency domain results

Additionally, impact profiles were plotted in Figure 4.42 by multiplying the average acceleration response of the impact rod node sets by the mass of the impact rods. A rectangular window was used crop the profiles once the curves crossed the x-axis, which is a common modal analysis practice [64]. The 10 *g* impact rods had an impact force of approximately 65 *N* and contact time of approximately 100 μ s. The 30 *g* impactors generally hovered around 100 *N* of impact force and ~ 120 μ s of contact time. All results aligned with theoretical expectations outlined in Section 3.6.5.

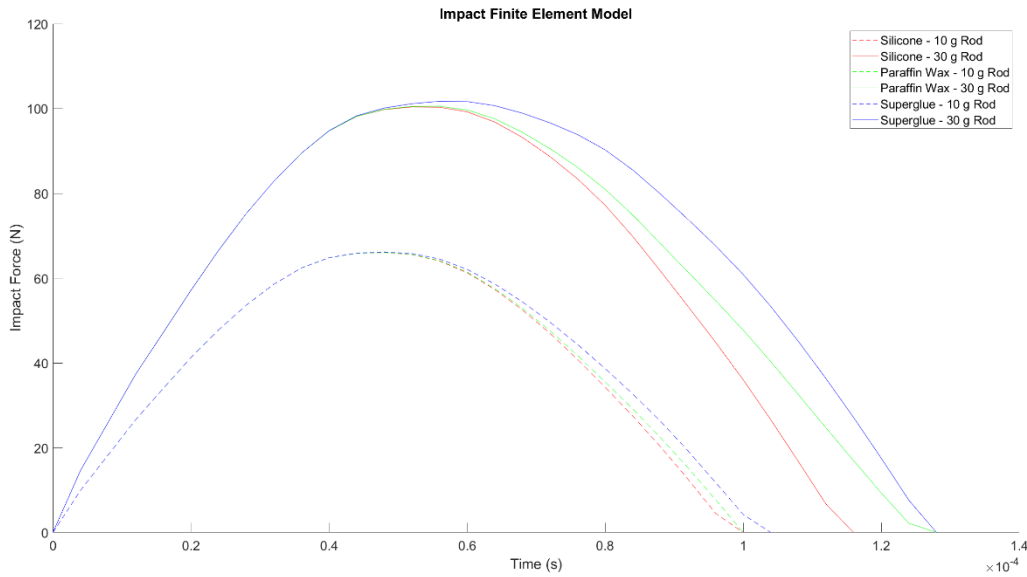


Figure 4.42: Impact finite element model – impact rod loading profiles

All results are summarized and compared in Table 4.8. In general, the frequencies extracted from the impact models showed a high degree of matching to the modal model. They also matched well to the experimental model in the low and high cases and displayed the same intermediate stiffness first mode behaviour; although, the frequencies did not match as closely. The 30 g impact rod significantly decreased amplitude ratios; however, like the experimental model, it had difficulty balancing the low condition to a ratio less than 10^0 for a steel impact interface. Surprisingly, the superglue interface signals contained a frequency at 6469.73 Hz of unknown origin. However, this was interesting considering the experimental setup also contained mid-range noise.

Table 4.8: Impact finite element model results summary

| 10 g Impact Rod | | | | | | |
|---|---|--------------------|--------------------|------------------------------------|------------------------------------|------------------|
| <i>Interface (Young's Modulus in MPa)</i> | <i>Contact Time (μs)</i> | <i>Freq 1 (Hz)</i> | <i>Freq 2 (Hz)</i> | <i>Amp 1 (g^2/Hz)</i> | <i>Amp 2 (g^2/Hz)</i> | <i>Amp Ratio</i> |
| Silicone (0.45) | 100 | 732.42 | 9399.41 | 0.12 | 0.96 | 8.12 |
| Paraffin Wax (40) | 100 | 5493.16 | 9643.55 | 7.57 | 0.57 | 0.08 |
| Superglue (1000) | 104 | 6469.73 | 9765.62 | 0.52 | 5.71 | 10.88 |
| 30 g Impact Rod | | | | | | |
| <i>Interface (Young's Modulus in MPa)</i> | <i>Contact Time (μs)</i> | <i>Freq 1 (Hz)</i> | <i>Freq 2 (Hz)</i> | <i>Amp 1 (g^2/Hz)</i> | <i>Amp 2 (g^2/Hz)</i> | <i>Amp Ratio</i> |
| Silicone (0.45) | 116 | 732.42 | 9399.41 | 0.36 | 1.27 | 3.53 |
| Paraffin Wax (40) | 128 | 5493.16 | 9643.55 | 18.36 | 0.47 | 0.03 |
| Superglue (1000) | 128 | 6469.73 | 9643.55 | 1.13 | 3.15 | 2.78 |

To help elucidate the source of mid-range noise within the superglue simulations, the transverse x and y average acceleration profiles of the accelerometer node set were extracted. Acceleration frequency domain profiles were plotted in Figure 4.43, with z representing the original axial direction. The x or horizontal, medial-lateral direction contained no frequency information; the y or vertical, anterior-posterior direction only contained the same 6469.73 Hz frequency as the axial direction, at less power for both impact rods; and the z or axial direction contained the same frequency information as previously described. This revelation suggested that measurements taken from a high stiffness interface condition could be sensitive to leakage from transverse or out-of-plane modes of vibration. It is intuitive that out-of-plane motion would occur in the y -direction, as the 12:00 distal screw impact location would create a torque in this plane.

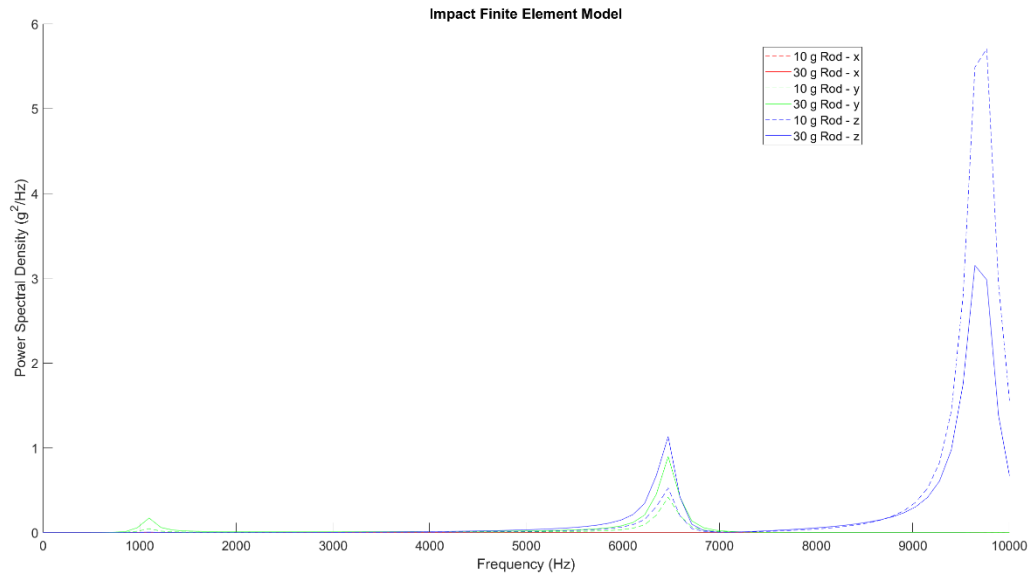


Figure 4.43: Impact finite element model – multi-axis superglue interface results

4.3.10.3 Summary

A comparison of all models used in the development and evaluation study can be viewed in Table 4.9. All models showed reasonably good matching and similar first mode frequency growth behaviour. It should be noted that the superglue interface second mode predicted by the modal finite element would not be detectable experimentally or by the nodal accelerations extracted from the impact finite element model due to its shape. Sensitivity of the stability measurement approach was limited for the experimental model because of mid-range noise in the superglue setup. The impact finite element model helped reveal that transverse or out-of-plane modes could be a source of noise for high stiffness interface conditions.

Table 4.9: All models comparison

| Interface (Young's Modulus in <i>MPa</i>) | Modal FEM Frequencies (<i>Hz</i>) | | Impact FEM Frequencies (<i>Hz</i>) | | Experimental Model Frequencies (<i>Hz</i>) | |
|--|-------------------------------------|---------------|--------------------------------------|---------------|--|---------------|
| | <i>Mode 1</i> | <i>Mode 2</i> | <i>Mode 1</i> | <i>Mode 2</i> | <i>Mode 1</i> | <i>Mode 2</i> |
| Silicone (0.45) | 663.48 | 9381.4 | 732.42 | 9399.41 | 744.74 | 9421.21 |
| Wax - Installation 1 (40) | 5447.6 | 9667.6 | 5493.16 | 9643.55 | 3245.80 | 9790.66 |
| Wax - Installation 2 (40) | | | | | 3854.80 | 9394.37 |
| Superglue (1000) | 9770.1 | 11135 | 6469.73 | 9704.59 | 2828.72 | 9458.35 |

4.3.11 Impact Force

4.3.11.1 Setup

Impactor loading profiles were recorded with an impact load cell (ICP® Force Sensor Model 208C02, PCB Piezotronics Inc, USA). The load cell was mounted directly to the T-slot bar structure with a 3D-printed support. All impact rod configurations were used to strike the load cell at the same distances and actuation voltages as the main procedure of the development experiment. A photo of an impactor configuration setup can be viewed in Figure 4.44.

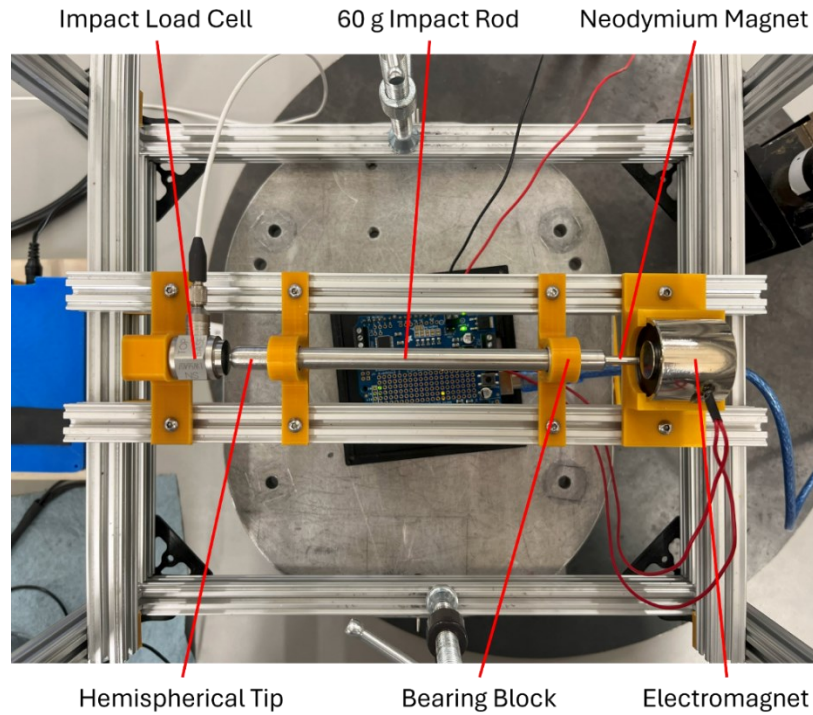


Figure 4.44: Load cell setup for impact rods of varying mass

Additionally, Periotest handpiece (ASIST motherboard) loading profiles were recorded for a range of actuation times. The handpiece was mounted within a freestanding clamp and was positioned approximately 1 mm from the surface of the load cell. The setup can be viewed in Figure 4.45.

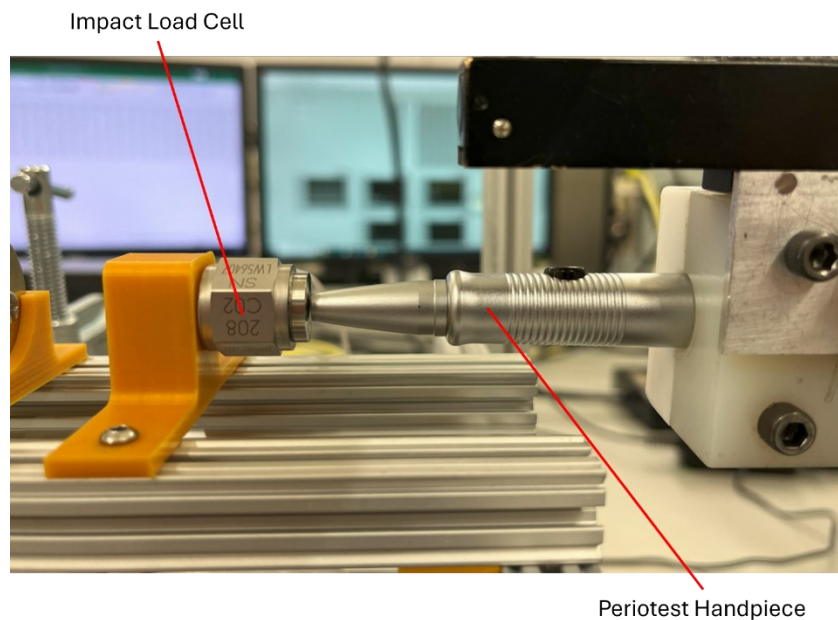


Figure 4.45: Load cell setup for ASIST strikes

All impactors, including the Periotest handpiece, struck the impact load cell 16 times in ~ 4 s. The first strike was used as a transducer trigger, while the remaining strikes were plotted as ensemble average time and frequency domain signals.

4.3.11.2 Results

Conical tip loading profiles with frequency domain transformations for the various impact rod masses can be viewed in Figure 4.46. A rectangular window was used crop the profile once the curve either crossed the x-axis or reached a local minimum (first occurrence). In general, lighter impact rods had shorter contact times and larger peak forces. Increasing actuation voltage led to increases in peak force and some decreases in contact time. At 5 V of DC actuation, the 10 g impact rod had a contact time of approximately 100 μ s. At 10 V, the same impactor had the largest recorded impact force of approximately 50 N. In the frequency domain, small impactors, especially the 10 g impact rod, extended their frequency excitation bandwidth beyond 10 kHz. Larger rods appeared to cut down the domain, with the 60 g rod appearing to significantly, if not completely, attenuate frequencies at 10 kHz.

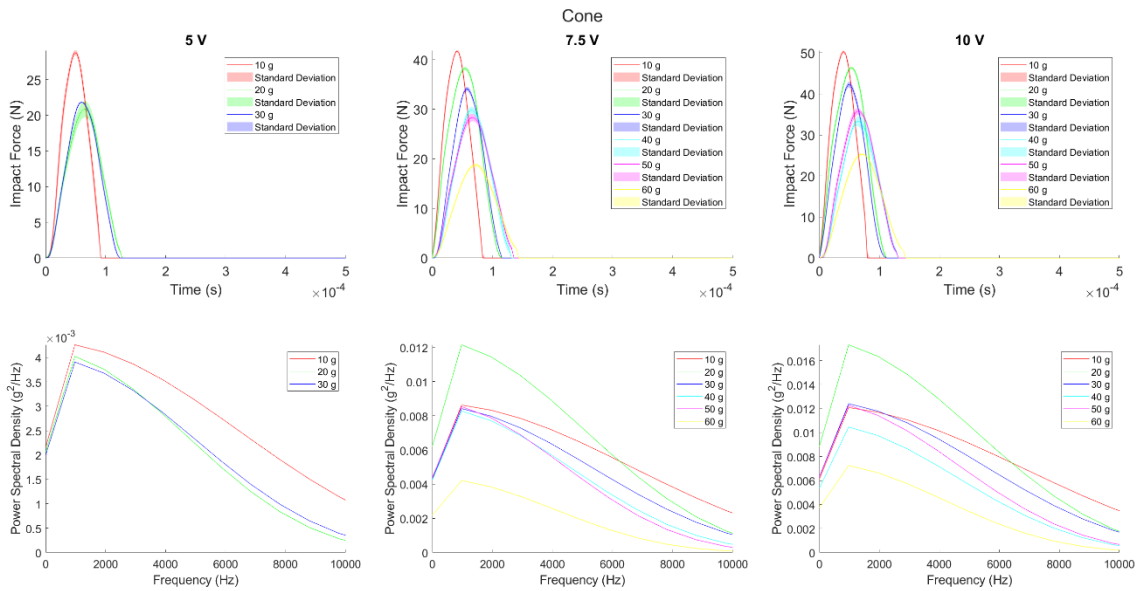


Figure 4.46: Loading profiles for benchtop prototype configurations with conical tip

Delrin® tip signals (Figure 4.47) were windowed in the same manner and exaggerated the effects associated with increased impact rod mass. They lowered peak impact force, extended contact time, and cut down frequency excitation bandwidth. All 10 g signals were well above 100 μ s in

contact time, and 30 *g* signals even extended beyond 200 μs . In the frequency domain, some impactors appeared to completely attenuate frequencies beyond 6 *kHz*, a drastic reduction from the steel tip impactor configurations.

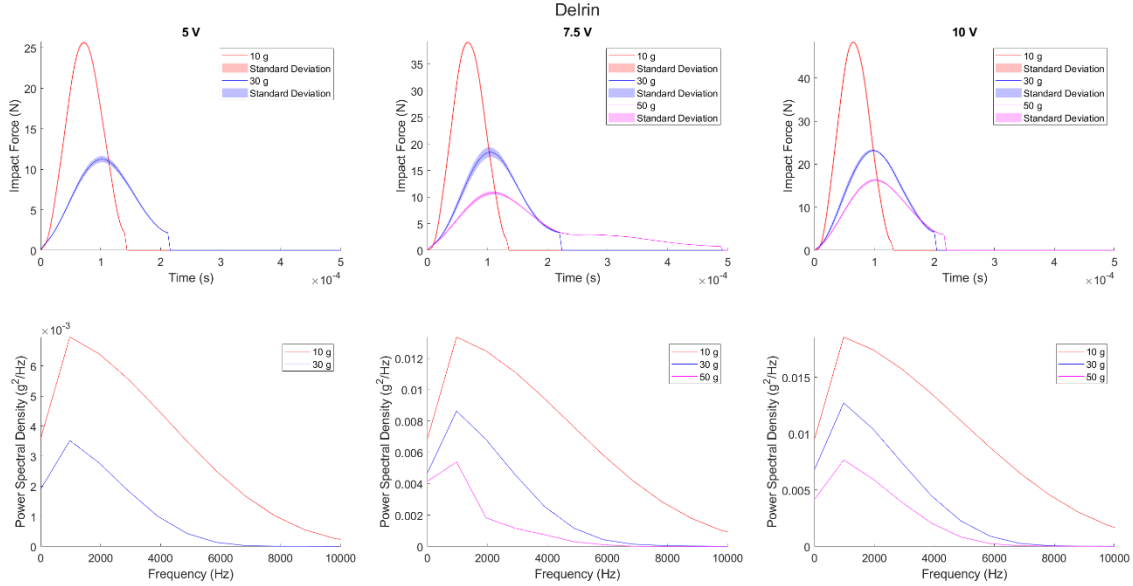


Figure 4.47: Loading profiles for benchtop prototype configurations with Delrin® tip

Plotting peak impact force vs. actuation voltage for the impactor configurations (Figure 4.48), the same general patterns were observed. The 10 *g* impactor generally covered a span of 30 – 50 *N*, and the 30 *g* impactor generally ranged from 20 – 45 *N*. Larger impactors generally resulted in lower impact forces, and increases in actuation voltage resulted in increases in impact force.

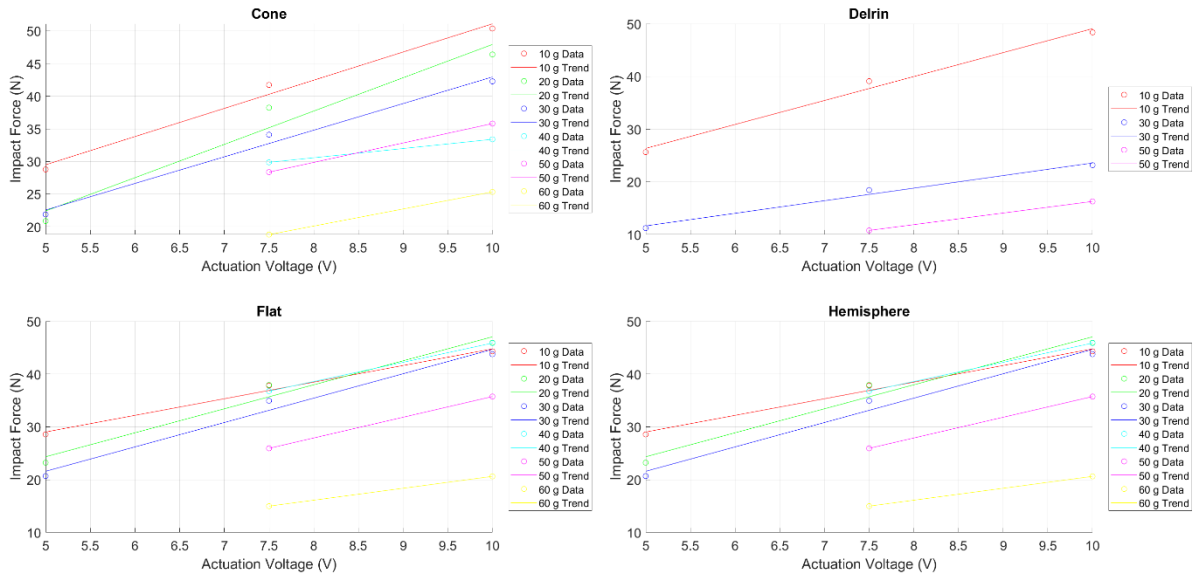


Figure 4.48: Peak impact force vs. actuation voltage for all benchtop prototype configurations

Extracting and plotting contact time (Figure 4.49), with few exceptions, larger impactors displayed longer contact times and increases in actuation voltage generally resulted in decreases in contact time. At 5 V of actuation, the 10 g impact rod hovered around a contact time of 100 μs , except for the Delrin® tip, where contact was extended to nearly 150 μs . Similarly, the contact time of the 30 g rod at 5 V went from approximately 120 μs to over 200 μs with the installation of the Delrin® tip.

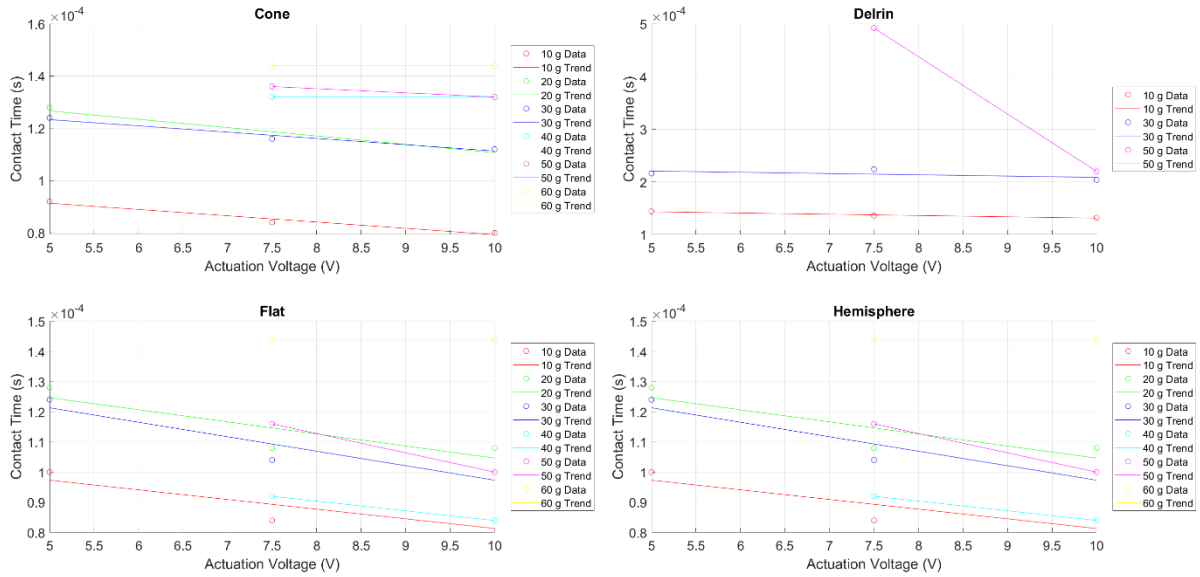


Figure 4.49: Contact time vs. actuation voltage for all benchtop prototype configurations

Loading profiles for the Periotest handpiece (ASIST motherboard) were plotted in the time and frequency domains (Figure 4.50). Here, actuation time was altered to affect impact loading. Longer actuation times resulted in a wide range of peak impact forces and little consequence to contact time. Impact loading profiles resulted in frequency excitation bandwidths that extended well beyond 10 kHz.

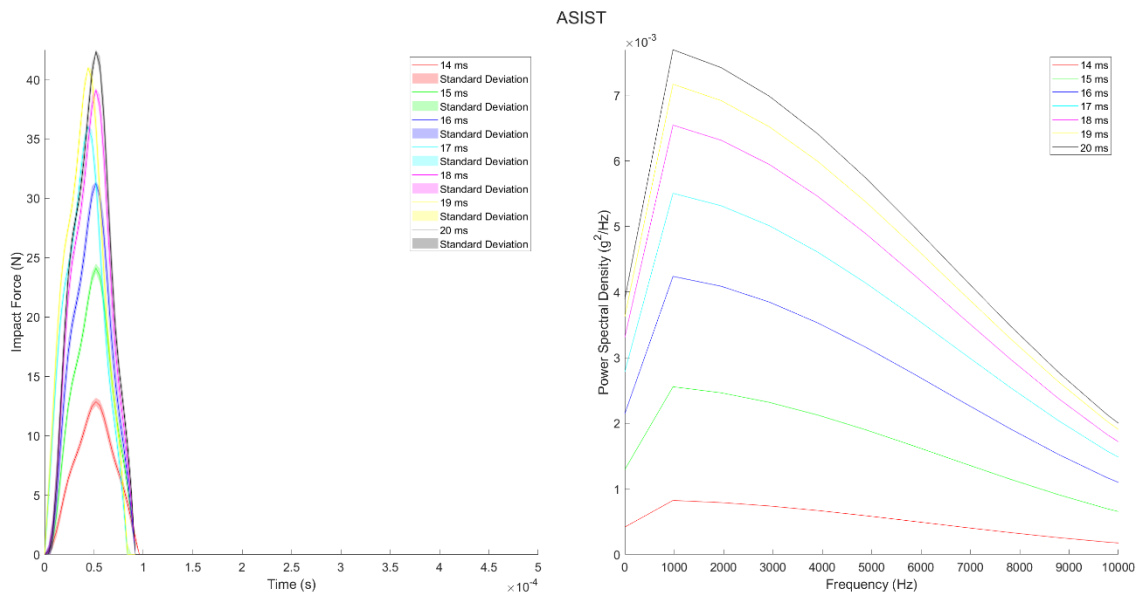


Figure 4.50: Loading profiles for ASIST strikes

Peak impact forces and contact times were extracted and plotted against extension (actuation) time in Figure 4.51. Increases in actuation time resulted in diminishing returns to peak impact force; though, the Periotest handpiece was able to cover a large range of forces (10 – 45 N). Contact time did not show any notable pattern of change and ranged from 84 – 95 μ s.

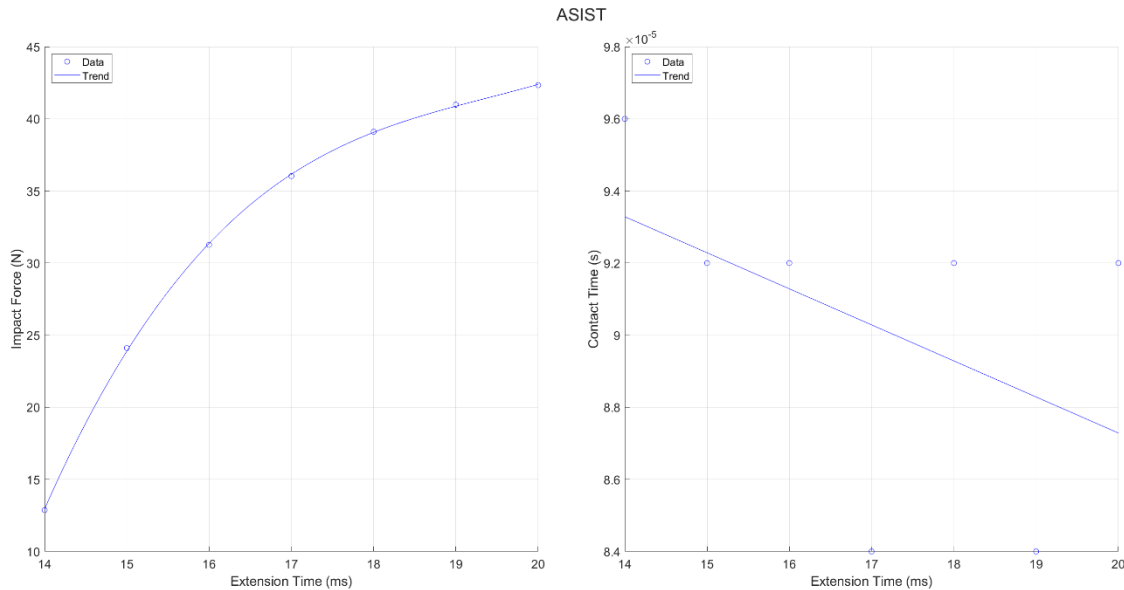


Figure 4.51: Impact force and contact time vs. extension (actuation) time for ASIST strikes

4.3.11.3 Summary

The 10 g impact rod showed comparable loading and contact time to the Periotest handpiece. This made sense considering the similarities in mass and speed of the devices. The ASIST was able to cover a larger range of impact forces with adjustment to only extension time. This would suggest finer tuning of the hardware components and actuation mechanism. The 30 g impact rod generally extended contact time by 20 – 25% compared to the 10 g rod when a steel tip was used and up to ~50% when a Delrin® tip was used. Experimental contact times largely matched those observed in the impact finite element model (Section 4.3.10.2); though, peak impact force patterns were not well matched. Within the finite element model, the 30 g impact rod resulted in larger impact forces than the 10 g rod, while the opposite was true for the experimental results. Fortunately, impact force magnitude had more of a bearing on signal band power than composition. Finally, considering the observed ranges of peak impact force, benchtop prototype configurations appeared preliminarily safe for a clinical setting. The ranges were similar to those observed for the

ASIST and fell within the maximum initial static load prescribed by the post-operative clinical protocol (50 *N*).

4.4 Conclusion

The experiment ultimately met both objectives of the study. First, and simple enough to interpret, the first axial mode was detected across all interface stiffness conditions. This verified that the percussion approach would be appropriate to track osseointegration from the worst case scenario of fibrous tissue formation (potential implant loosening and failure), through intermediate healing stages, and finally in lamellar bone formation or a high stiffness interface condition. The remaining question would be how to accomplish this in a compact, clinically deployable device. This question was at least partially answered by experimental data. A 30 *g* impact rod was able to maximally excite the first axial mode in the low interface condition; however, the same rod introduced mid-range noise to high interface condition signals. On the other hand, a 10 *g* rod provided a wide frequency input range and optimally excited high condition signals. Like the Periotest, it was not able to detect the first axial mode in the low stiffness range. A Delrin® tip provided an effective way to cut down frequency input without altering ram mass, and a conical tip proved reliable among the other tested geometries. With these findings, another study would be conducted to formulate an objective measurement and model matching protocol for transfemoral implant stability assessment. Two handpieces would be produced with different ram masses (10 *g*; 30 *g*) and interchangeable 316 stainless steel and PEEK (Delrin® surrogate) impact tips.

Chapter 5 Design of Handheld Impactors

5.1 Introduction

This chapter outlines the design, manufacture, and safety testing of two handheld impactors. Impactor ram mass, tip geometry, and impact interface stiffness were previously specified in Chapter 4. Components were selected and their performance was evaluated for implementation in the handpieces. The full assemblies were solid modelled before manufacture and preliminary testing. A rigorous safety testing protocol was developed with the aim of adherence leading to clinical deployment of at least one of the handpieces. Finally, after thorough characterization of the handpieces, a final experiment was designed for benchtop validation of the impactors.

5.2 Component Selection, Evaluation, and Assembly

5.2.1 Component Selection

With the largely successful execution of the development study, minimal design changes were needed to produce handheld impactors. However, some outsourced components were upgraded for enhanced performance, ergonomics, and safety in clinical deployment. A list of the selected components for the handheld impactors can be found in Table 5.1. To start, the steel bearings were switched to all-polymer plain bearings from igus motion plastics. The switch to a non-ferromagnetic bearing was made to ensure ease of installation and as little magnetic interaction in impact rod actuation as possible. Additionally, the new bearings had several attractive features, including low wear against different shaft materials, low coefficients of friction in dry operation, vibration-dampening (vibration should be localized to the free motion of the implant), good resistance to chemicals, and low humidity absorption [78]. Additionally, the bearings were designed for press-fit and had a typical application area of ‘cleanroom.’ Of paramount importance was finding a low-friction, dry-running sleeve bearing. The specified bearings would allow for swift and smooth impact rod flight. Low wear, chemical resistance (possible contact with isopropyl alcohol), low humidity absorption, and lack of need for lubrication were all desirable characteristics for clinical deployment. Confirmation for bearing selection was also given by the cleanroom application area, which would presumably have a handful of similar standards to the clinic. Finally, vibration dampening was a bonus given that it was desirable to limit mechanical

noise leakage into bone-implant systems from outside sources. The electromagnet was reselected to have a minimum holding force of 15 *kg* (same as magnet used in Chapter 4) and maximum diameter of 1 *in* for handpiece compactness. Additionally, a maximum operating DC voltage of 12 *V* was specified. An electromagnet from Eclipse Magnetics was selected and neodymium magnets from the same manufacturer were also sourced. For the neodymium magnets, a minimum holding force of 1 *lb* (same as $\varnothing 1/8 \text{ in} \times 1/2 \text{ in}$ neodymium magnet used in Chapter 4) and maximum diameters of 4 *mm* for the 10 *g* impactor and 7 *mm* for the 30 *g* impactor were specified. The minimum diameters were specified to allow for 0.5 *mm* wall thickness once the neodymium magnets were embedded in the impact rods. For both the electromagnet and neodymium magnets, magnets that maximally exceeded the minimum holding force specifications were selected. This was because tuning the speed and impact force of the impactors down would be much easier than pushing past any performance limits of the parts. The selected electromagnet slightly exceeded the 15 *kg* HF minimum at 150 *N*; the 10 *g* impactor neodymium magnet exceeded the 1 *lb* HF minimum at 0.9 *kg*; and the 30 *g* impactor neodymium magnet exceeded at 2 *kg*. Finally, other functional components were selected, including a tactile switch with LED indicator, connector assembly, cable, and thermistor for temperature monitoring.

Table 5.1: Outsourced components for 10 *g* and 30 *g* handpieces

| Part Description | Manufacturer/Distributor | Part Number |
|---|--------------------------|-------------------|
| 5 <i>mm</i> sleeve bearing | igus | JSM-0507-05 |
| 8 <i>mm</i> sleeve bearing | igus | JSM-0810-03 |
| $\varnothing 4 \text{ mm} \times 4 \text{ mm}$ neodymium magnet | Eclipse Magnetics | N803 |
| $\varnothing 6 \text{ mm} \times 6 \text{ mm}$ neodymium magnet | Eclipse Magnetics | N824 |
| 150 <i>N</i> HF electromagnet | Eclipse Magnetics | M52172/12VDC |
| Tactile switch | E-Switch | TL1220R1BBBB-HALO |
| NTC thermistor | Tewa Temperature Sensors | TT7-12KC4-2 |
| M12 connector | TE Connectivity | T4132012081-000 |
| M12 cable | TE Connectivity | T4161420008-003 |

5.2.2 Magnetic Flux Density Measurements

Once components were received, magnetic flux density measurements were taken, adhering to the same procedure outlined in Section 3.4.2. The measurements were plotted with the magnetic flux density data from previous tests. Figure 5.1 plots magnetic flux density for various permanent magnets. The $\varnothing 4\text{ mm}$ magnet fell below expectations of magnetic strength, while the $\varnothing 6\text{ mm}$ magnet narrowly exceeded all other permanent magnets in the arsenal.

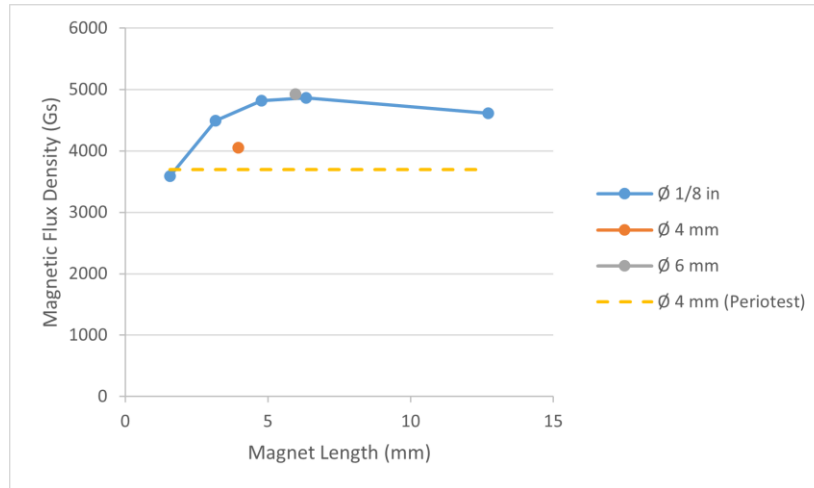


Figure 5.1: Permanent magnet magnetic flux density measurements

The 150 N HF electromagnet did not outperform the 15 kg HF electromagnet at any actuation voltage; however, it exceeded all other electromagnets in magnetic flux density when compared at their rated operating voltages. That is, in Figure 5.2, every electromagnet curve was operating above rated voltage if the actuation voltage was greater than 5 V, except for the 150 N HF electromagnet, for which the entire curve was legitimate (rated voltage 12 V). The magnetic flux density of the 150 N electromagnet at 12 V exceeded the 5 kg and 25 kg HF electromagnets at 5 V. This performance was reasonable and somewhat expected, as the high magnetic flux density of the 15 kg HF electromagnet seemed to be anomalous among comparable parts.

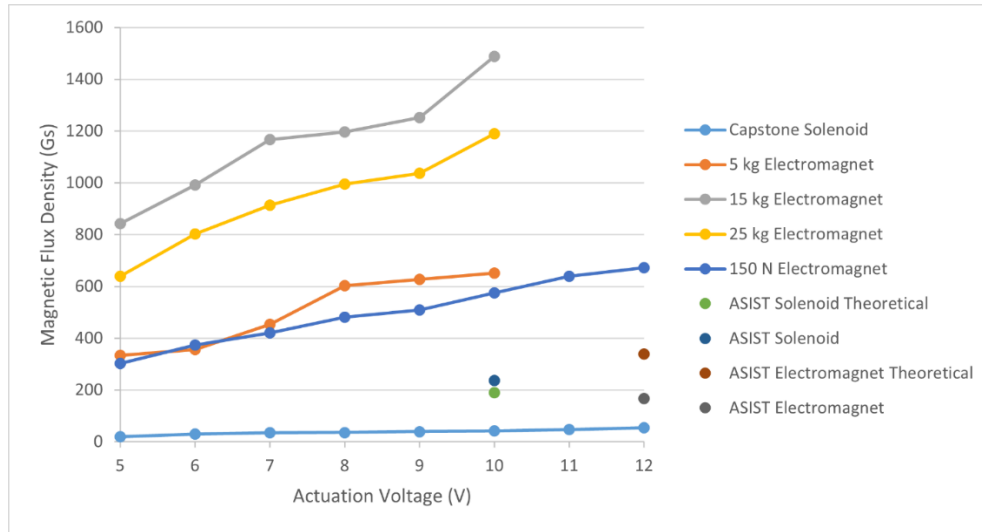


Figure 5.2: Magnetic flux density measurements for various magnetic coils

Looking at magnetic flux density vs. distance from the electromagnet surface (Figure 5.3), the 150 N HF electromagnet curve had a similar shape to the 15 kg HF electromagnet curves. Additionally, when both magnets were powered at their rated operating voltages, the 150 N electromagnet did not fall far below the 15 kg electromagnet when compared to shifts in performance made by the 15 kg HF electromagnet operating above its rated voltage.

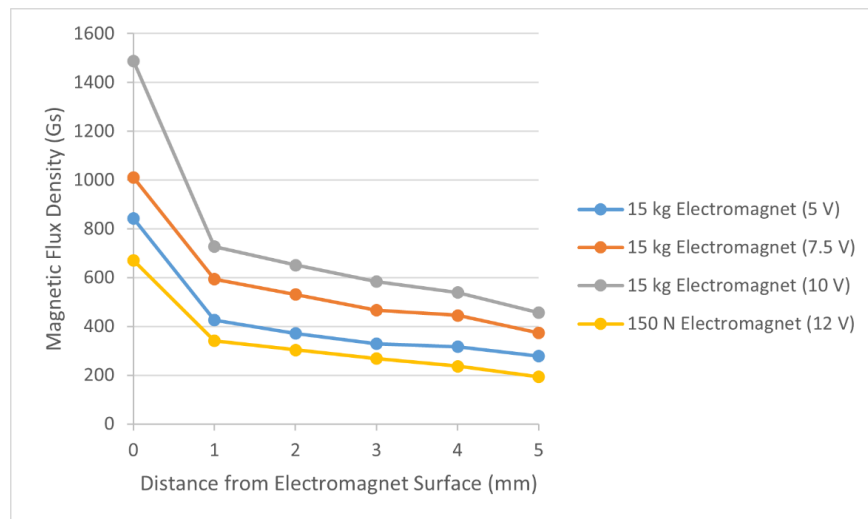


Figure 5.3: Magnetic flux density vs. distance from active surface for various electromagnets

Considering the fickle nature of magnetic performance, the sourced neodymium and electromagnets seemed to reasonably meet magnetic flux density requirements. That is, they did

not disastrously underperform as a first litmus test in the design and manufacture process. Further testing would provide insight to more relevant performance and safety benchmarks.

5.2.3 Electromagnetic Force Measurements

In the original benchtop T-slot bar setup, the distance between the neodymium magnet in the impact rod's back position and the electromagnet's active surface was set by energizing the electromagnet with constant DC voltage such that repulsion between the magnets would occur; sliding the electromagnet away from the neodymium magnet starting from a zone of attraction; and stopping once the impact rod was actuated away from the electromagnet. This inflection point was treated as the optimal distance to set the neodymium magnet and electromagnet apart. However, once the first handheld prototypes were created, impact rod flight became more difficult to actuate. To improve reliability, a test was devised to find the optimal magnet gap in the impact rod's back position. As pictured in Figure 5.4, the electromagnet and impact rods with embedded neodymium magnets were fixed in a Bose ElectroForce 3200 test machine (Bose Corporation, USA). The static force generated between the magnets was recorded for various actuation conditions and multiple magnet gaps. For the 10 *g* impact rod, measurements were taken for the electromagnet pulling, off, and pushing at 12 *V*. For the 30 *g* impact rod, measurements were recorded for the electromagnet pulling, off, and pushing at both 12 *V* and 15 *V*. The 30 *g* impactor experienced more reliability issues prior to the test, so a greater variety of conditions were tested.

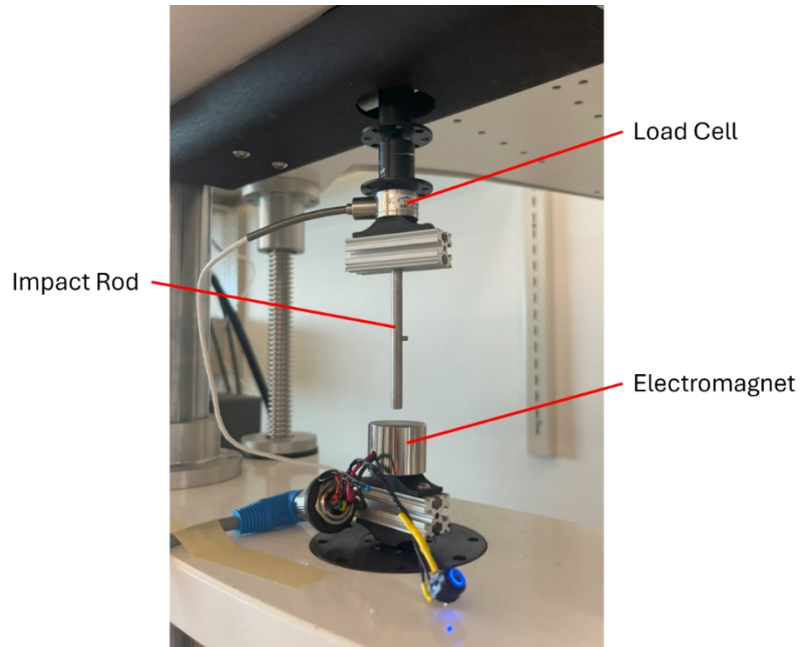


Figure 5.4: Static electromagnetic force measurement setup

A full range of repulsive force measurements can be viewed in Figure 5.5, while a reduced range can be viewed in Figure 5.6. In any actuation scenario, the attractive force between the electromagnet and neodymium magnet was much greater for the 30 *g* impactor at short distances. At short distances, the attractive force between the ferromagnetic core of the electromagnet and neodymium magnet was greater than any repulsive forces (if the electromagnet was actuated to push). This was likely a greater problem for the 30 *g* impactor because the $\varnothing 6\text{ mm}$ magnet had a higher rated holding force and observed magnetic flux density than the $\varnothing 4\text{ mm}$ magnet.

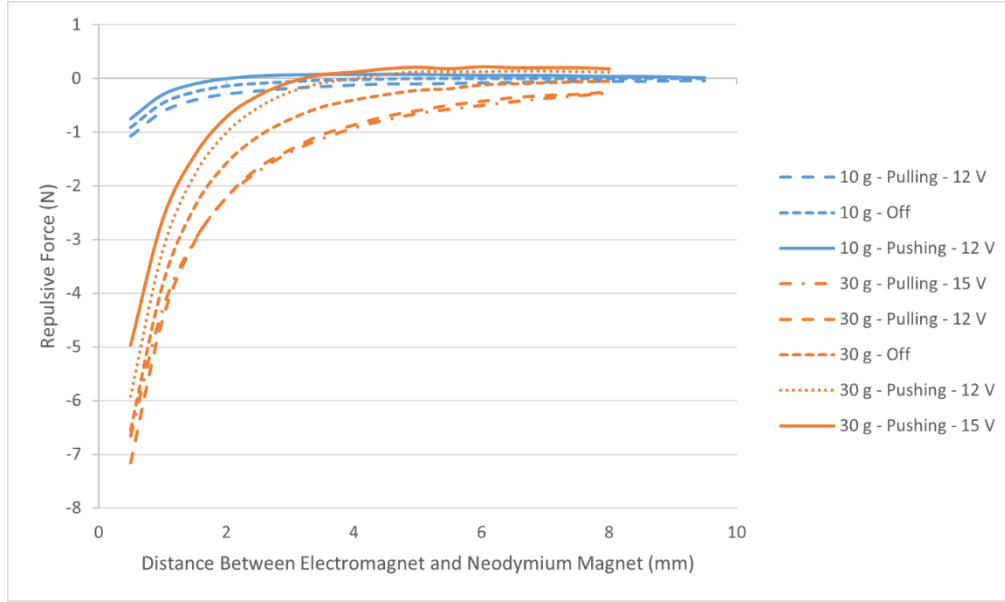


Figure 5.5: Repulsive force vs. gap between electromagnet and neodymium magnet – full range

In the reduced domain, repulsive force was close to being maximized at a gap of ~ 3 mm for the 10 g impactor (12 V) and ~ 5 mm for the 30 g impactor (12; 15 V). It was desirable to set the gap distance just before the true maximum to allow the neodymium magnet (impact rod) to be accelerated through a highly repulsive portion of the curve. When the electromagnet was off, the repulsive force was generally negative, and when the electromagnet was pulling, all attractive effects worked synergistically to strongly withdraw the impact rod.

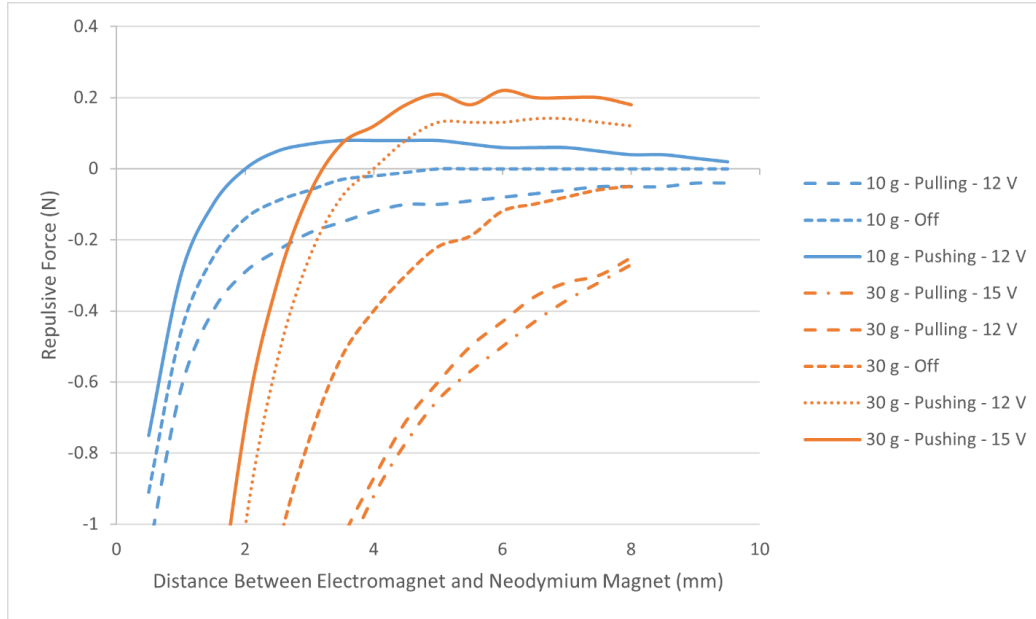


Figure 5.6: Repulsive force vs. gap between electromagnet and neodymium magnet – reduced range

The gap distance was set to 3 mm and 5 mm for the 10 g and 30 g handheld impactors, respectively. After the revisions, impact rod actuation was significantly improved, and the handpieces achieved an acceptable level of preliminary reliability.

5.2.4 Handpiece Assemblies

With parts sourced and optimal magnet gaps determined, two handpiece assemblies were created for each impact rod. The designs were highly compact and ergonomic, making them easy hold and operate with one hand. A side-by-side comparison of the assembled handpieces can be viewed in Figure 5.7.

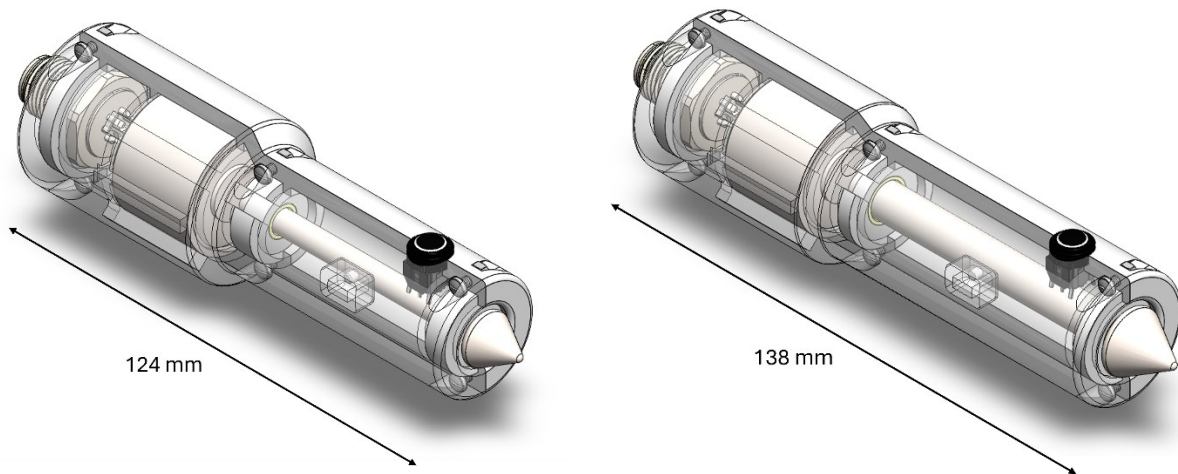


Figure 5.7: Assembled Handpieces. Left, 10 g impact rod; right, 30 g impact rod

Figure 5.8 and Figure 5.9 show an exploded view of the 10 g impactor assembly and 10 g impact rod subassembly, respectively. The main body of the handpieces were 3D-printed and had a clam-shell design, making them easy to assemble, disassemble, and service on-the-fly. Bearings were press-fit into bearing blocks, which were held by reliefs in the clam-shell walls.

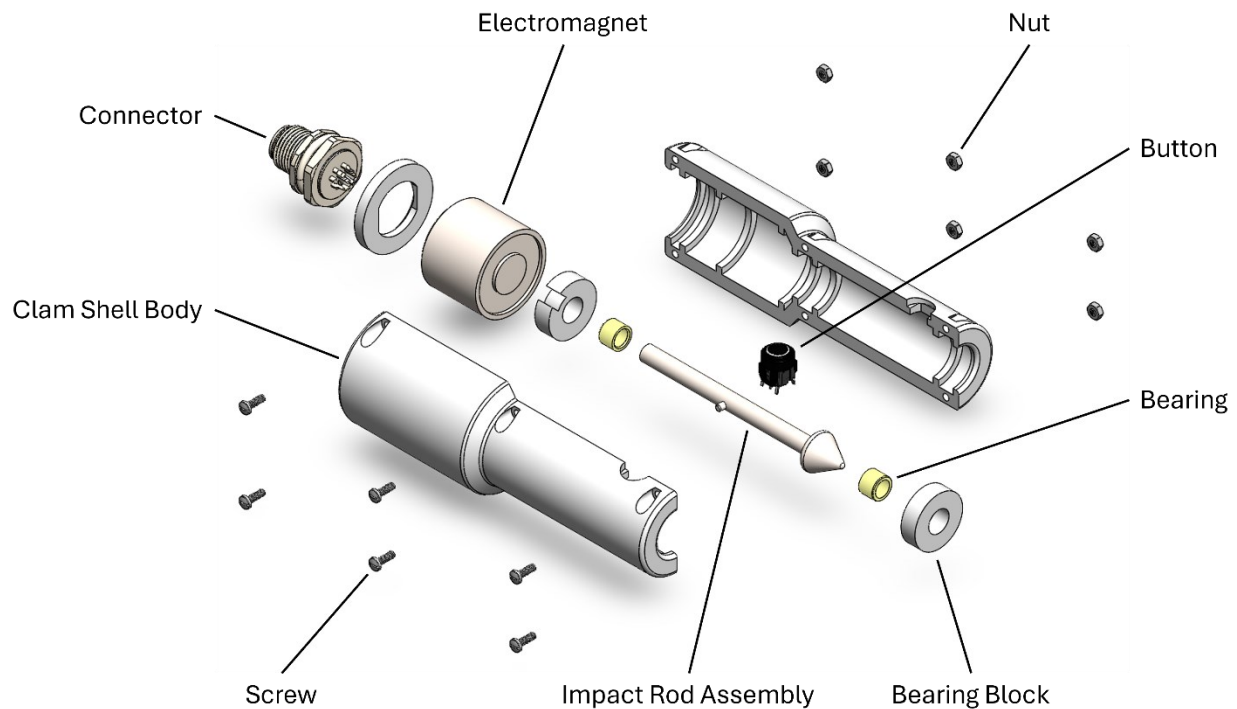


Figure 5.8: Exploded view of 10 g handpiece assembly

The impact rods were machined from medical grade 316 stainless steel. The neodymium magnet was embedded into the rear of the impact rod with epoxy resin, and a motion limiting pin was set

into the side. A set screw was partially secured in the front of the impact rod with Loctite Threadlocker Red, and the free end was left exposed to interface with either a stainless steel or PEEK conical impact tip.

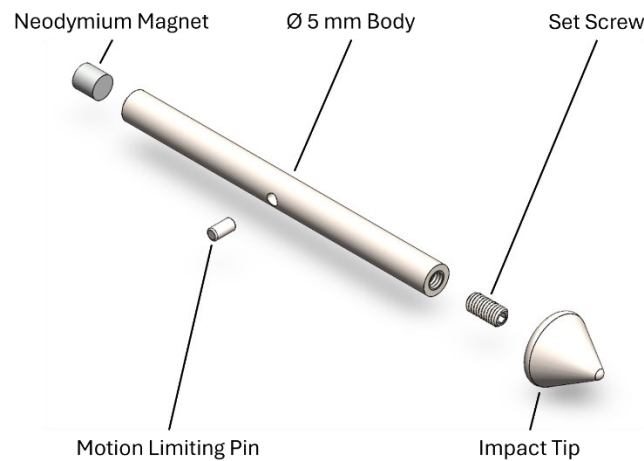


Figure 5.9: Exploded view of 10 g impact rod assembly

One side of the clamshell body contained additional reliefs for wiring associated with the tactile switch, electromagnet, and thermistor. An extrusion was also added as a linear and rotational motion constraint, allowing the impact rod a 3 mm linear travel lane. A connector at the rear of each handpiece would allow for quick and pain-free access to each power and signal line. A dimetric view of the reliefs can be seen in Figure 5.10.

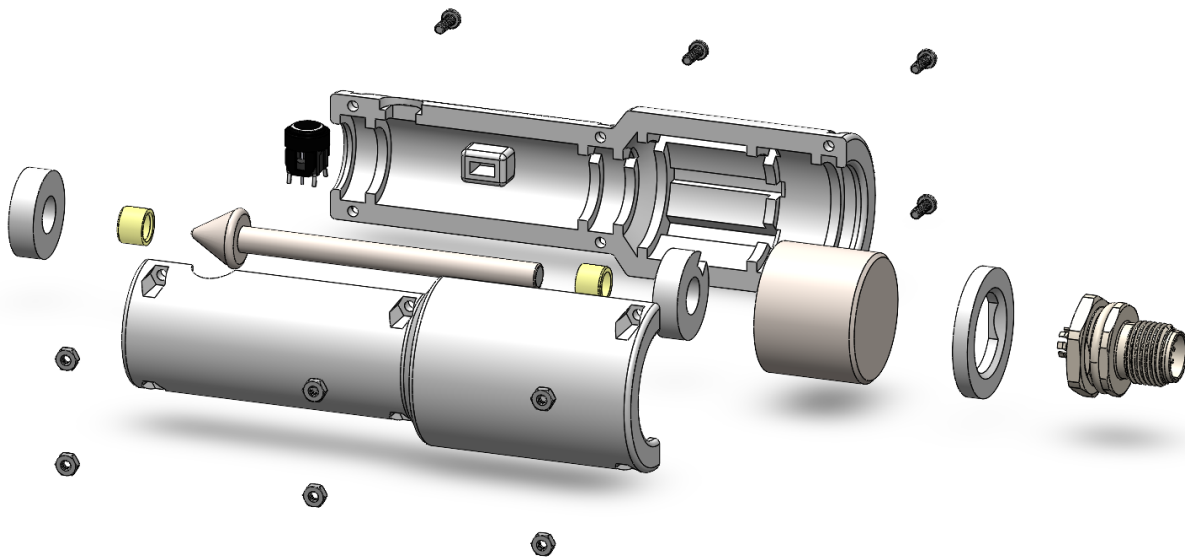


Figure 5.10: Dimetric exploded view of 10 g handpiece assembly. Motion limiter and wire reliefs exposed

The final handpiece assemblies snugly fit all required components; were handheld and ergonomic; and could easily be assembled, disassembled, and serviced in the event of disrepair or failure. A cross-sectional view of the physical 10 g handpiece can be seen in Figure 5.11.



Figure 5.11: Section view of physical 10 g handpiece

5.3 Clinical and CSA Standards Compliance

5.3.1 Overview

One of the primary goals of development was rapid deployment of at least one of the handpieces in a parallel clinical study. This would greatly help advance research, development, and validation as well as present a potential benefit to future patients. However, rigorous testing would have to be conducted to ensure value was safely delivered on these fronts. For the handpiece to be

responsibly deployed, the answer to both of the following questions would have to be ‘yes’ when scrutinized by the research team:

1. Is the prototype safe?
2. Does the prototype make the hypothesis testable?

Answering ‘no’ or insufficient evidence to answer either of the questions would negate the possibility of present deployment. To help answer these questions, a master table of standards with their minimum adherence levels was developed in Appendix D. The standards consisted of self-prescribed clinical standards based on excerpts from the post-operative protocol; research integrity standards, also developed by the research team; and selected CSA standards. Given clinical pressures and time limitations, the table did not contain an exhaustive list of CSA standards, but it did contain a variety of highly relevant selections from CAN/CSA-C22.2 No. 60601-1:14 (Medical electrical equipment – Part 1: General requirements for basic safety and essential performance) [79]. Certain standards were not included with the understanding that the device was going to be deployed in a controlled research environment, under the operation of its developers and supervision of the clinical team. For example, hazards labels were not considered, as test personnel would already be knowledgeable of the inner workings of the device and potential hazards. Furthermore, standards were coded according to their importance in being met, including non-negotiable comprehensive adherence and acceptable adherence/risk with acknowledgment of need for future development. The latter was specified if the standard would not explicitly help answer either of the above questions but was still relevant in some broad stroke to research and development. If the minimum adherence level to a standard was not met, it would result in an automatic no-go for clinical deployment. With an early version of the system already deployed to the clinic with the Periotest handpiece (ASIST controller) as an impactor, any new impactor would have to outperform the Periotest handpiece in some capacity to answer ‘yes’ to the second question. To this end, standards were generated that would weigh the benefit of deploying a new impactor compared to continued use of the current system. Largely, the standards were consolidated to balance the need for timely device deployment and data capture with responsible research execution. Moreover, they would aid the research team in answering the above questions beyond a reasonable doubt and help guide future development. It should be noted that this chapter and Appendix D were intended to only list and discuss standards pertaining exclusively to the

handpieces or consequences of the handpieces interacting with the system at large. A handful of other standards were explored related to electrical systems and general safety investigated through finite element model simulations. Because they were undertaken by other team members and for sake of brevity, they will not be discussed here.

5.3.2 General Reliability

General reliability was of high interest in the early days of prototype development. The electromagnetic force test outlined in Section 5.2.3 helped set the prototype up for consistent firing. However, firing angle could add a significant gravitational force to impact rod actuation and affect the flight of the rod. Angular operating ranges were recorded at two actuation voltages (12; 15 V), for which each handpiece could fire 16 times at a rate of 4 Hz (Table 5.2). The 10 g impactor operating at 12 V had the smallest maximum deviation in degrees, while the 30 g impactor operating at 15 V had the largest. Generally, maximum positive deviation from level proved to be the limiting end of the angular spectrum, and the 30 g impactor performed better on this front overall. Should the 30 g impactor be deployed, the operator would have to hold the handpiece relatively level, if not slightly downward, but would be able to rely on consistent firing.

Table 5.2: Handpiece angular operating ranges

| Firing Angle | 12 V | | 15 V | |
|-------------------|-------|------|-------|------|
| | 10 g | 30 g | 10 g | 30 g |
| Maximum (degrees) | 2.5 | 7.5 | 17.5 | 22.5 |
| Minimum (degrees) | -42.5 | -30 | -47.5 | -40 |

The prototype was accepted as generally reliable with some need for future development (Research Integrity 1, App. Table D.2). Ultimately, the device worked within a narrow range of strike distances and orientations but was reliable enough to obtain results in a clinical setting with adequate training and experience.

5.3.3 Impact Force

The second clinical protocol standard (Clinical Protocol 2, App. Table D.2) specified that impact force should not exceed 50 N , which was the maximum initial prescribed load in the clinical post-operative protocol. An impact load cell (ICP® Force Sensor Model 208C02, PCB Piezotronics Inc, USA) was used to record the impact force of the two handpieces. First, the handpieces were deconstructed and placed in a similar setup used in Chapter 4. All components were mounted in 3D-printed supports that could interface with the previously commissioned T-slot bar structure. This would offer a controlled starting point for testing. The initial results for the T-slot bar setup can be viewed in Figure 5.12. Here, the ensemble average of 15 consecutive strikes was plotted (first strike used as trigger). A rectangular window was used crop the profile once the curve either crossed the x-axis or reached a local minimum (first occurrence). From the loading profiles, the 30 g impactor struck harder and had a longer contact time than the 10 g impactor in all configurations. The PEEK tip configuration served to greatly reduce peak impact force and extend contact time. All curves except for the 30 g steel tip impactor remained below the 50 N impact force threshold; though, at 12 V , the average peak impact force was 52.31 N .

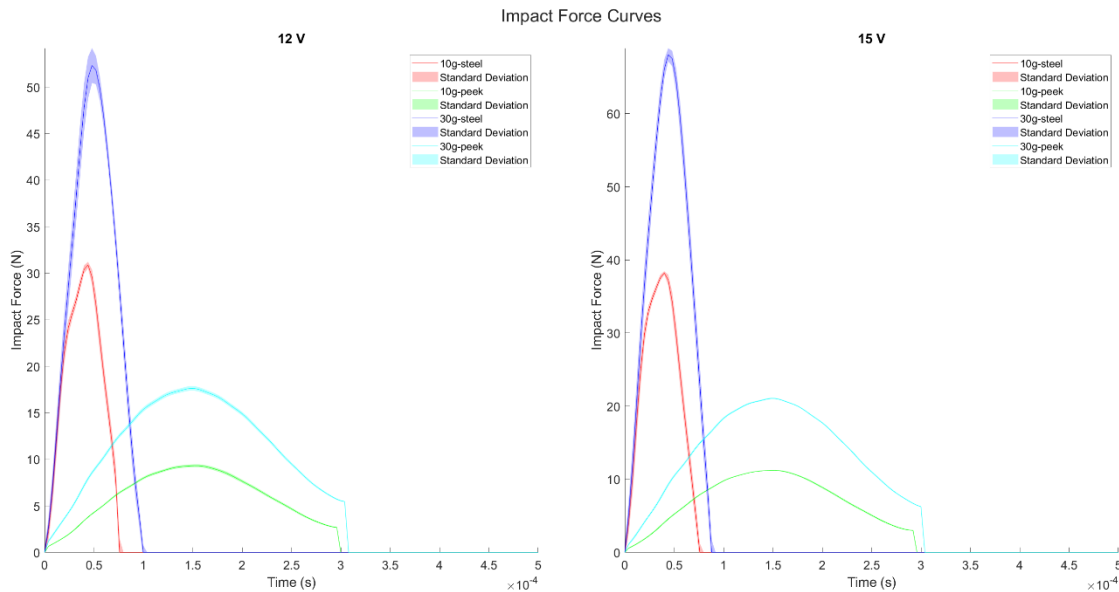


Figure 5.12: Loading profiles – T-slot stand impactors

The same test was executed again with the impactors assembled in their handheld configurations. With the handpieces, five sets of strikes were recorded. A sample set of loading profiles can be

viewed in Figure 5.13. Here, the loading profiles were observed to have lower peak impact force and greater variability. The same patterns were generally observed, with less distance in peak impact force between the steel tip 10 *g* and 30 *g* impactors.

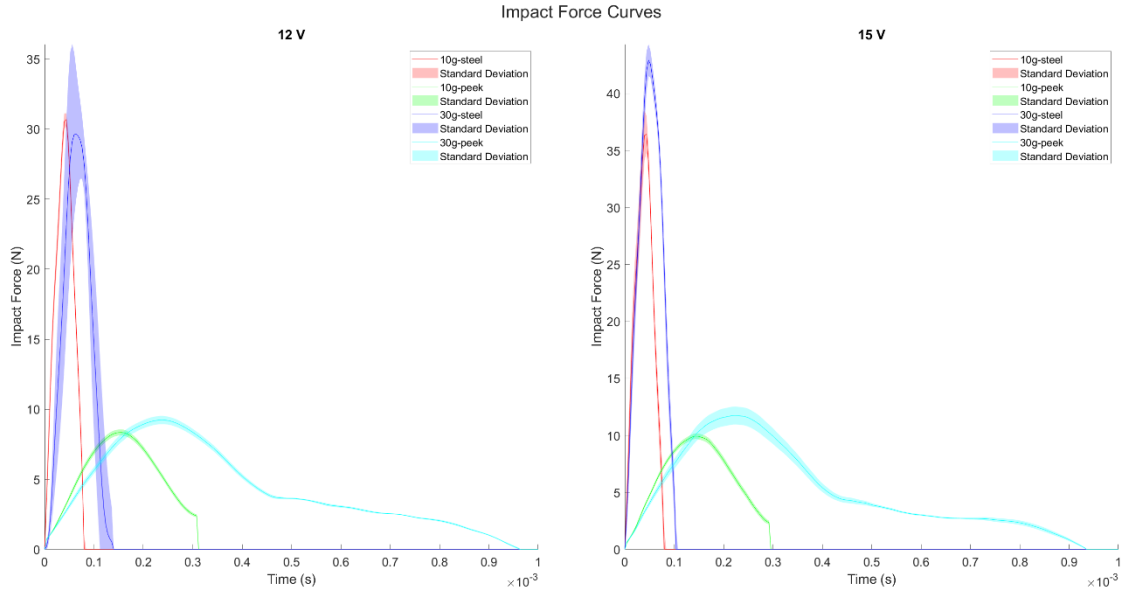


Figure 5.13: Loading profiles – handheld impactors

Plotting the average peak impact force recorded in each trial vs. actuation voltage, the graph in Figure 5.14 was generated. Increasing the actuation voltage tended to increase peak force, and none of the configurations exceeded 50 *N* of peak impact force.

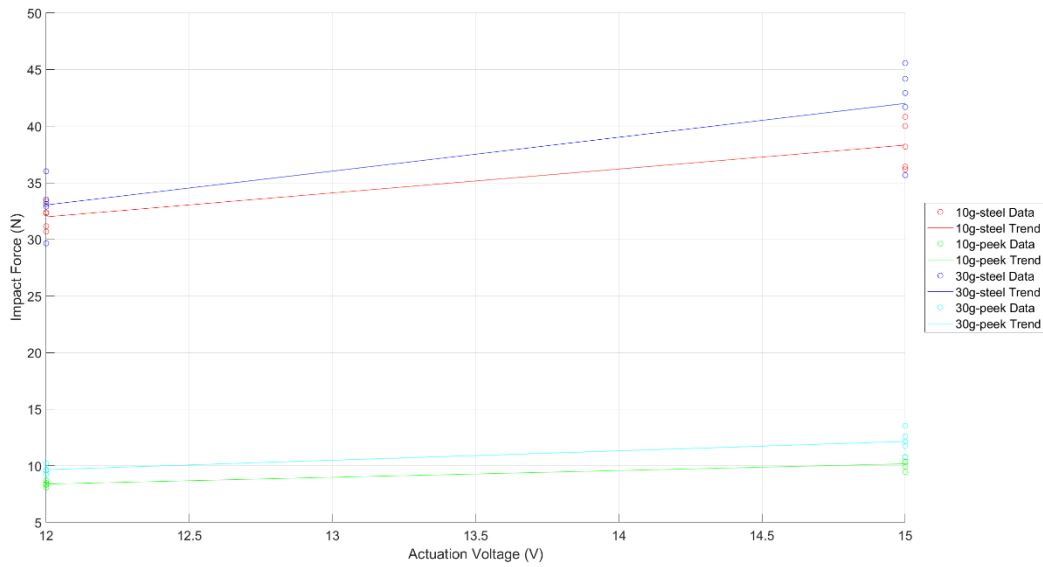


Figure 5.14: Peak impact force vs. actuation voltage – handheld impactors

Furthermore, looking at average contact time vs. actuation voltage (Figure 5.15), heavier impactors tended to increase contact time along with softer impact interfaces. For the PEEK tip, results were quite variable and there were large discrepancies between the 10 g and 30 g impactors.

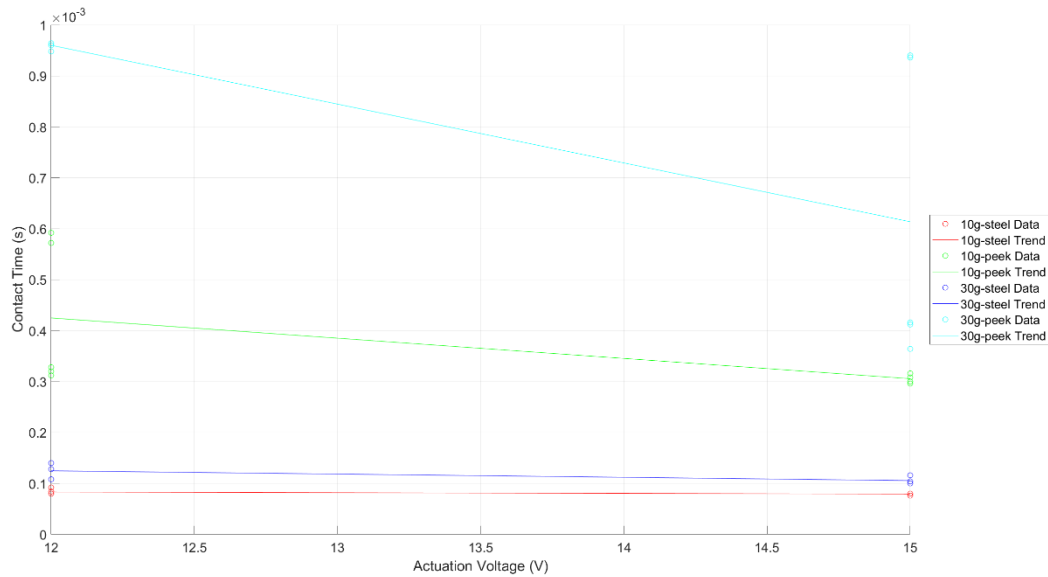


Figure 5.15: Contact time vs. actuation voltage – handheld impactors

The impact load cell data confirmed the safety and general functionality of the handheld impactors. In the form of their handpiece configurations, the impactors did not exceed 50 N of impact force

in any trial, complying with the second clinical standard (Clinical Protocol 2, App. Table D.2). Heavier impactors and softer impact interfaces were also confirmed to increase contact time in the handheld tests, providing some evidence that they could aid in improving the sensitivity and accuracy of the vibration approach in a clinical setting compared to use of the Periotest handpiece alone.

5.3.4 Velocity

Impact rod velocities of the impactors in the T-slot bar structure configuration were measured according to the protocol discussed in Section 4.3.9.1. These measurements did not have high relevance to any particular standard but were helpful in finite element model safety tests and for general characterization of handpiece performance. Figure 5.16 shows the raw velocity profiles of the handpieces. The 10 g and 30 g impact rods had similar velocity profiles over a 3 mm distance. The peak velocities ranged from 167 – 205 mm/s, with increased actuation voltage serving to raise maximum velocity. Periotest handpiece velocities also fall within this range [28, 59], lending some confirmation that the handpieces were operating within reasonable velocity bounds.

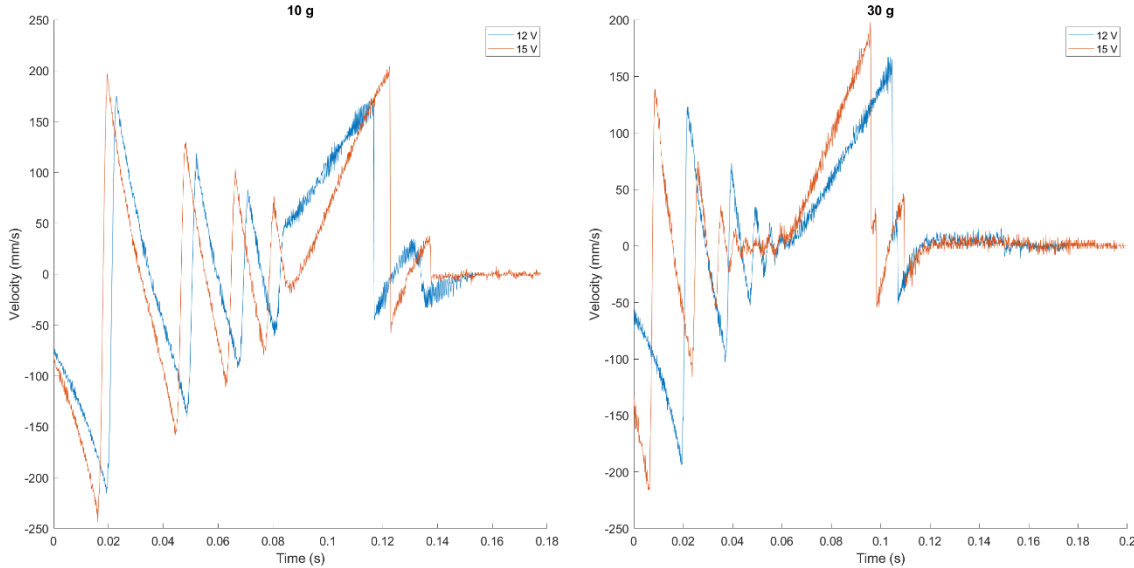


Figure 5.16: Raw velocity profiles – T-slot stand impactors

5.3.5 Temperature

CSA standards 60601-1 11.1.1 and 60601-1 11.1.2.2 specified the maximum temperature limits for various parts of the handpieces. Accordingly, temperature readings from thermistors placed at

the electromagnet, casing, steel tip, and driver were recorded for continuous operation of the 10 g impactor. The impactor was allowed adjust to the ambient conditions of the test environment (thermostat 19.5°C) before commencing the test. After starting the test, the impactor was fired freely into air in continuous 16 strike bursts (4 Hz). Every 4 s, or after each set of strikes, temperature readings were recorded. The test was terminated after 60 min. The setup was designed to mimic worst-case normal use as specified by the stated standards. Worst-case normal use was synthesized as a malfunction that would cause the handpiece to continuously run unattended for a period of one hour under standard temperature and pressure conditions. The data was used to plot the transient temperature profiles of various handpiece components in Figure 5.17.

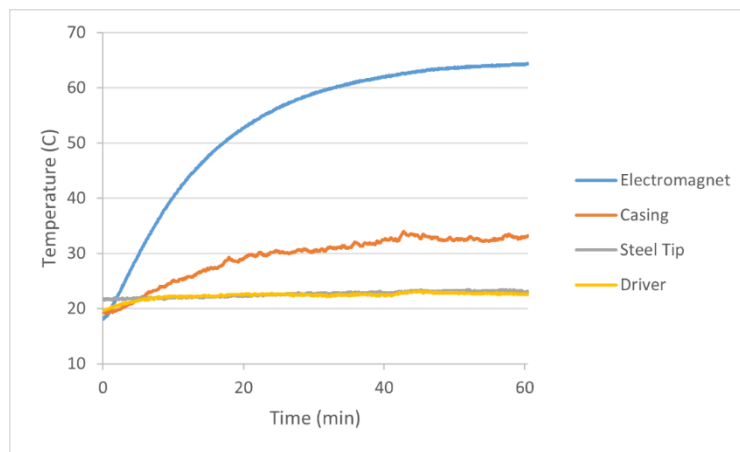


Figure 5.17: Transient temperature profiles of various components of 10 g handpiece under worst-case normal use

From Figure 5.17, the electromagnet was the biggest temperature risk, reaching a maximum temperature 64.40°C . Table 5.3 contains a summary of component maximum temperatures and the associated specified CSA standard limits (details in App. Table D.2). All temperatures stayed well within the guidelines.

Table 5.3: Maximum temperatures of various components of 10 g handpiece under continuous operation

| Component | Maximum Temperature (C) | CSA Standard Limit (C) |
|---------------|-------------------------|------------------------|
| Electromagnet | 64.40 | 90 |
| Casing | 33.98 | 48 |
| Steel Tip | 23.41 | 51 |
| Driver | 23.19 | 90 |

5.3.6 Functionality

5.3.6.1 Overview

Intra-team prescribed standards Research Integrity 1 and 2 (App. Table D.2) specified two of the main conditions for hypothesis testability. Namely, that the deployed handpiece should provide a reliably different frequency excitation bandwidth than the ASIST and better sensitivity and accuracy in the ASIST's worst performing case. It was demonstrated by Mostafa et al. that the ASIST performed poorly in low interface conditions (silicone) [27]. The development study also demonstrated that a 10 g impact rod performed similarly to the ASIST, and impact rods weighing more than 20 g could provide some advantage in visualizing the first mode frequency of low stiffness interfaces. If similar conclusions could be drawn with handheld impactors, then at least one would provide a benefit to clinical testing. Like the impact force tests, five measurement trials were conducted with each handpiece configuration on a silicone interface setup with and without the GV connector installed. The Experimental setup, data acquisition system, and signal processing procedure were identical to those discussed in Section 4.2.

5.3.6.2 Time Domain

Sample ensemble average time domain signals for strikes collected without the GV installed can be viewed in Figure 5.18. PEEK tip strikes clearly revealed a low-lying frequency within the system. Additionally, the 30 g steel tip impactor appeared to have some effect in attenuating the high frequency mode compared to the 10 g steel tip impactor, although it was less pronounced than when manipulating impact interface stiffness.

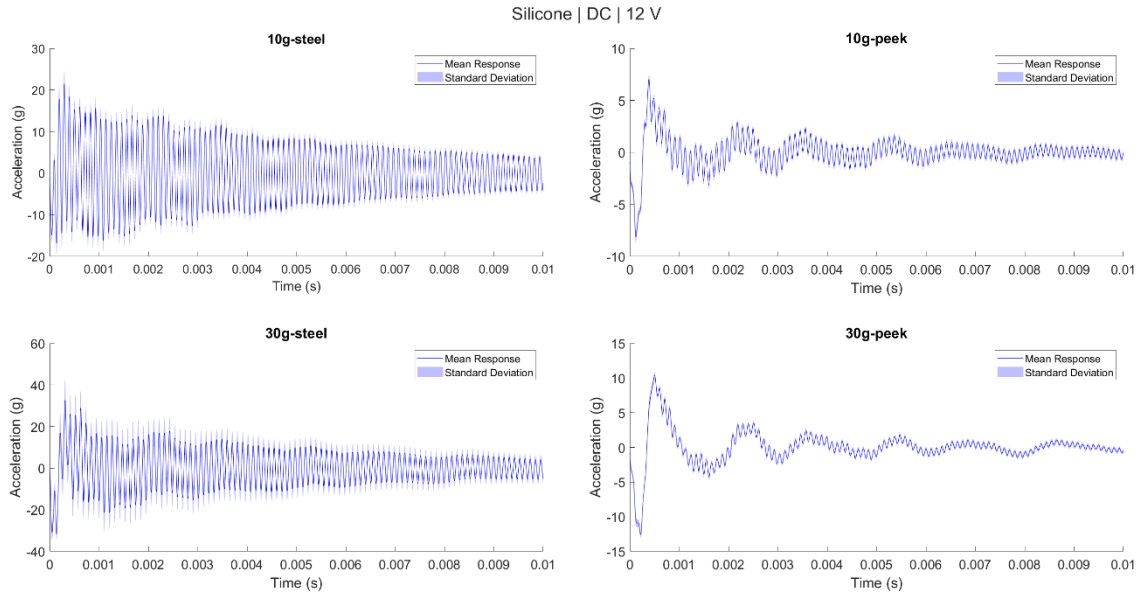


Figure 5.18: Time domain signals – silicone; DC; 12 V; handheld

Sample time domain signals with the GV connector installed can be viewed in Figure 5.19. Here, the signals generally contained more noise, and the effects of increasing impactor mass were less pronounced. Decreasing impact interface stiffness by installation of the PEEK tip served to attenuate high-frequency components of the signals.

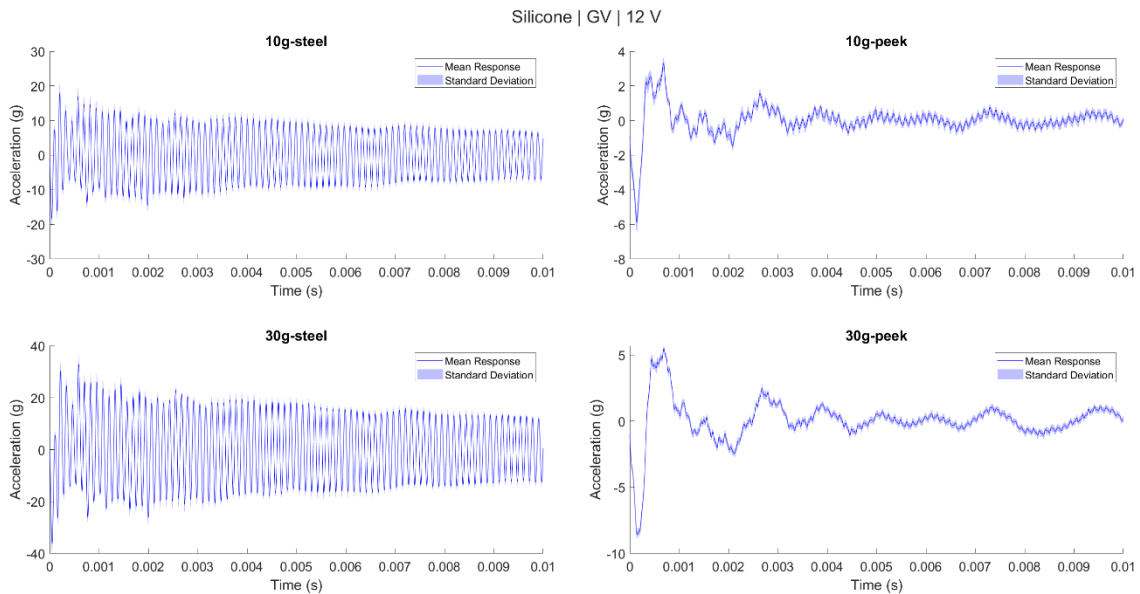


Figure 5.19: Time domain signals – silicone; GV; 12 V; handheld

5.3.6.3 Frequency Domain

The frequency domain results largely told the same story as the time domain results. For measurements conducted on the silicone setup without the GV connector installed, very little power could be visualized in the low frequency domain with the 10 *g* steel tip impactor. A small low frequency peak became apparent with the 30 *g* steel tip impactor, and both PEEK tip measurements excited a low frequency mode around 671 *Hz*.

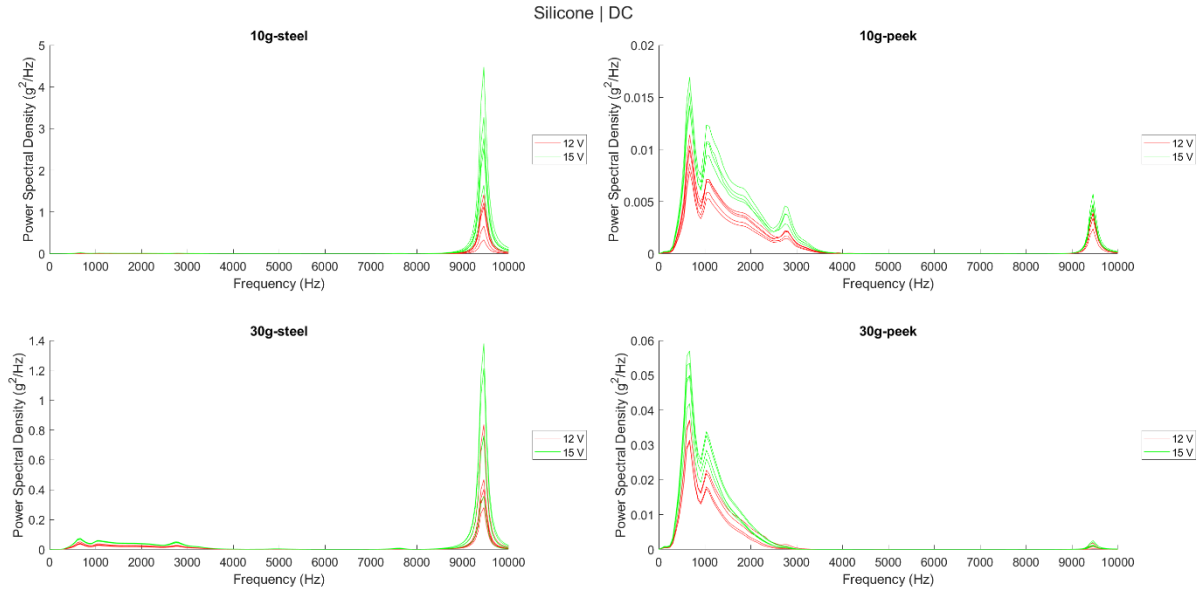


Figure 5.20: Frequency domain signals – silicone; DC; handheld

Similar results were obtained with the GV connector installed (Figure 5.21); however, there was clearer influence of noise within the system.

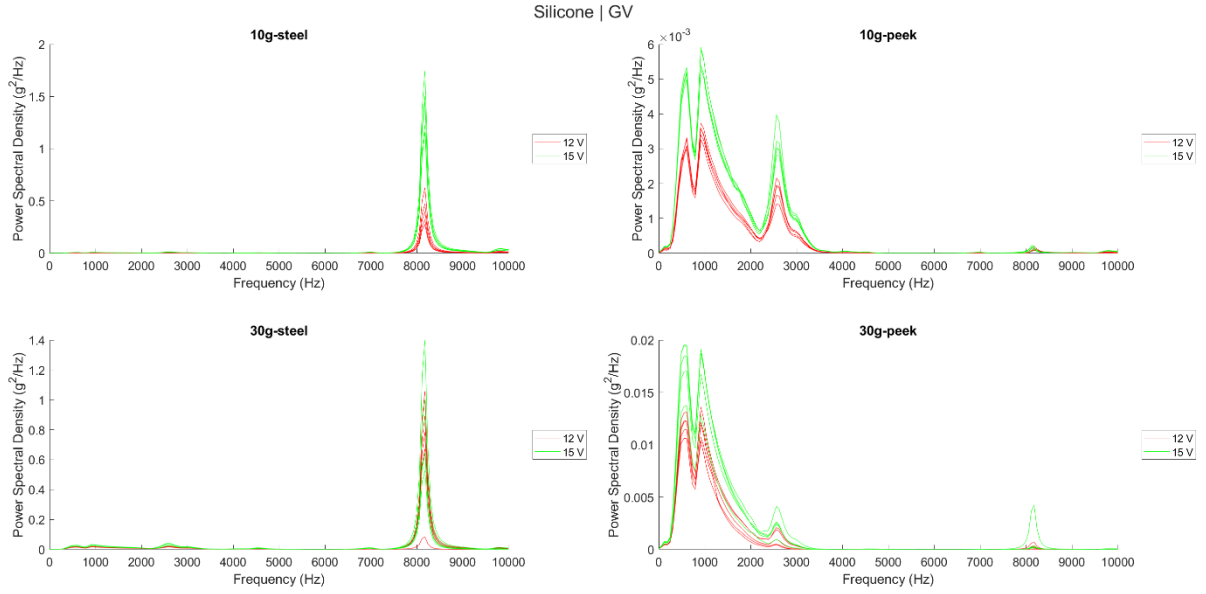


Figure 5.21: Frequency domain signals – silicone; GV; handheld

5.3.6.4 Amplitude Ratio

Using the frequency domain data, amplitude ratios, calculated in a similar fashion to Section 0, were plotted against actuation voltage for each impactor and implant configuration (Figure 5.22). For a given impactor configuration, amplitude ratios remained relatively constant over two actuation voltages (12; 15 V). The 30 g steel tip impactor lowered the amplitude ratio compared to the 10 g steel tip impactor, but only the PEEK tip impactors balanced the signals in favour of the first mode frequency.

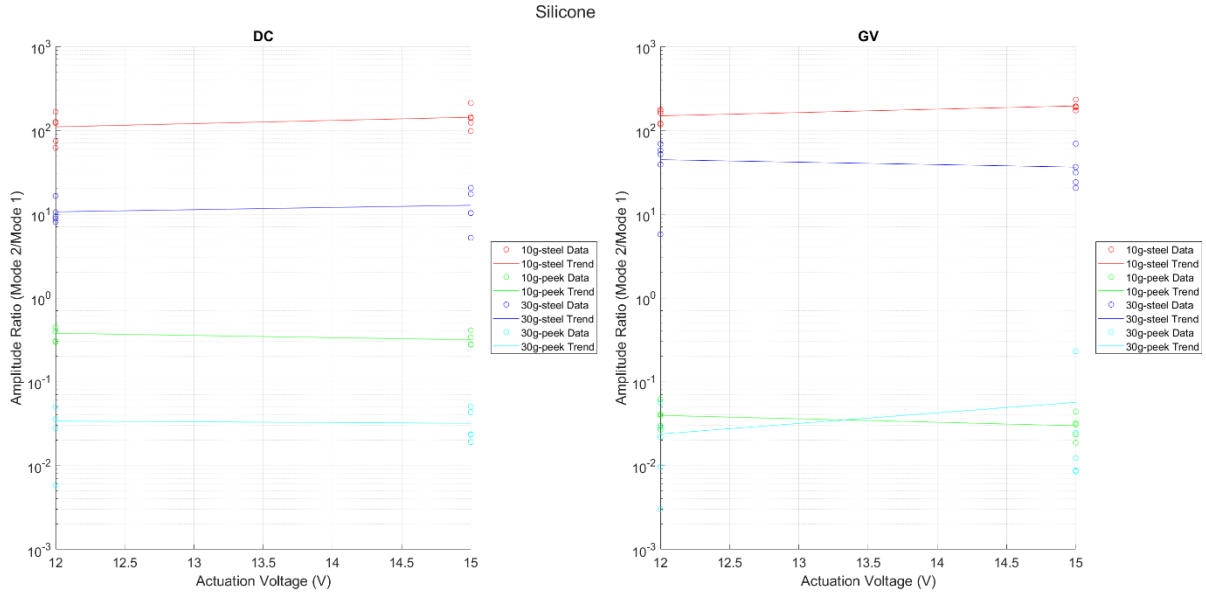


Figure 5.22: Amplitude ratio – silicone interface; handheld impactors

5.3.6.5 Mode 1 Amplitude

First mode power spectral density estimates were plotted against actuation voltage in Figure 5.23. Like the results of Chapter 4, the 30 *g* impactor (steel and PEEK tip) ended up maximizing the amplitude of the first mode frequency in all cases.

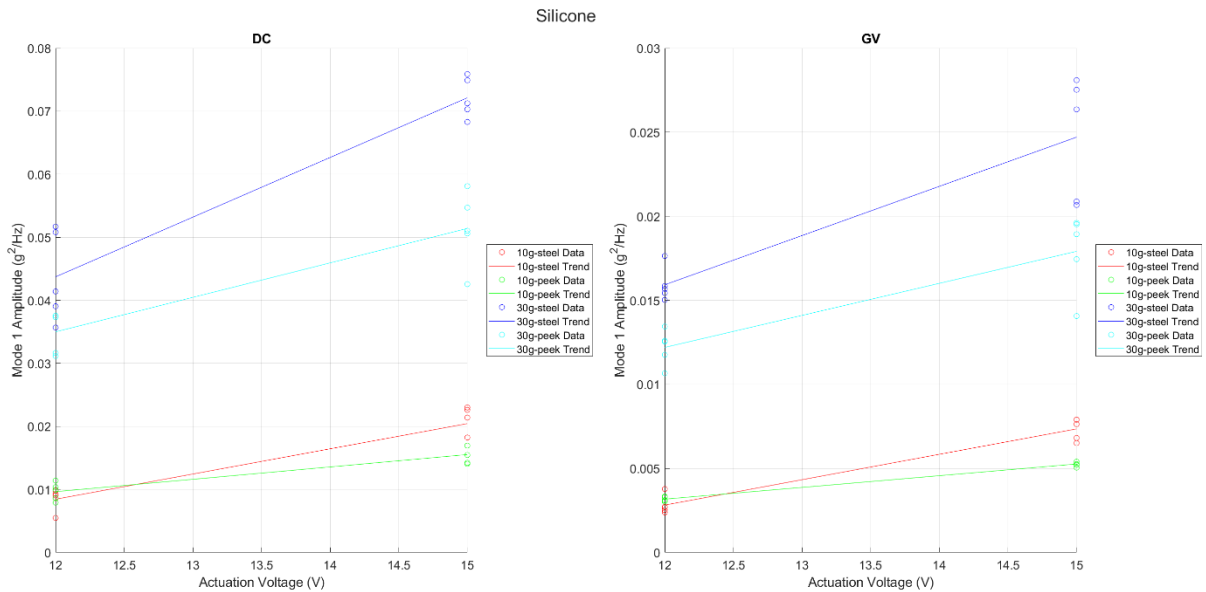


Figure 5.23: Mode 1 amplitude – silicone interface; handheld impactors

5.3.6.6 Band Power

Finally, band power was plotted (Figure 5.24). The 10 *g* steel tip impactor seemed to maximize band power in most cases; however, results were mixed, and the 30 *g* impactor elicited similar power when the GV connector was installed on the implant.

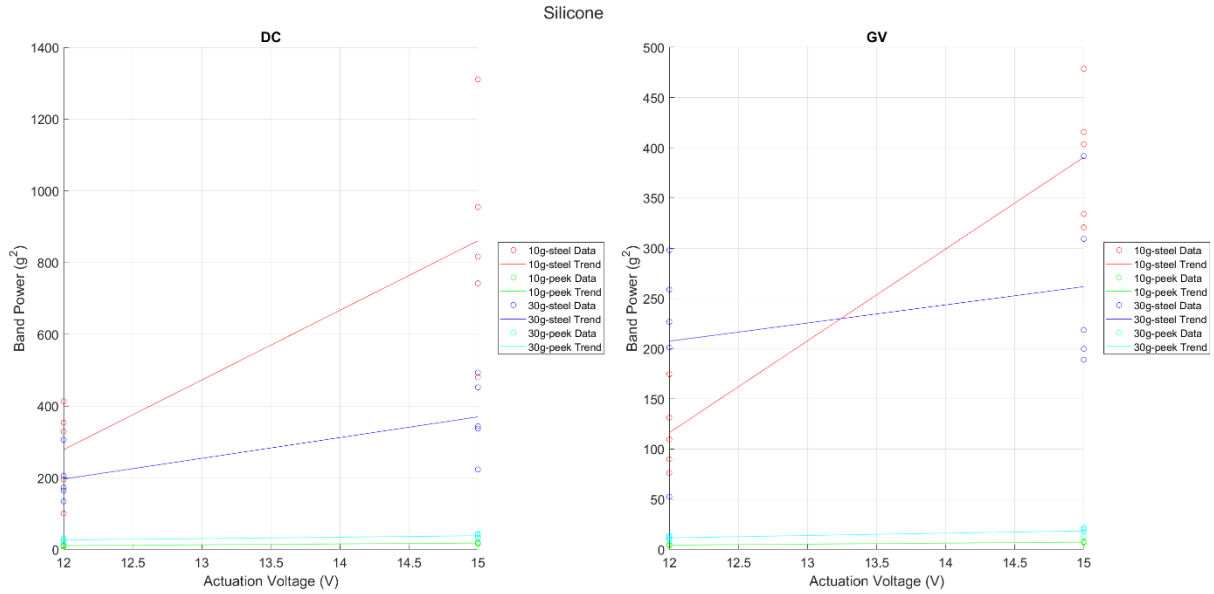


Figure 5.24: Band power – silicone interface; handheld impactors

5.3.6.7 Conclusion

This brief test provided evidence to support that handheld impactors performed similarly to the benchtop impactors of Chapter 4. The 30 *g* impactor maximized first mode power spectral density in all cases and greatly reduced signal amplitude ratio compared to the 10 *g* impactor. Use of the PEEK impact tip also caused the first mode to become the dominant frequency in all cases (amplitude ratio less than 10^0). It has been shown that the ASIST was unable to adequately excite the first mode of a silicone interface setup [27], and the 10 *g* impactor generally performed comparably to the ASIST (Section 0). With the 30 *g* impactor in combination with both the stainless steel and PEEK impact tips clearly changing frequency excitation bandwidth and improving first mode sensitivity relative the 10 *g* impactor and ASIST, it was the clear choice for clinical deployment. This decision was also made amidst other clinical testing changes, in which the measurement routine execution time was reduced through hardware and software improvements as well as elimination of transverse ASIST measurements. Considering all

information, it was advantageous to deploy the 30 *g* impactor with both stainless steel and PEEK impact tips along continued testing with the ASIST. All measurements would be recorded axially under the new protocol.

5.3.7 Conclusion

Both impactors in all configurations passed the major safety checks and hazard assessments put together by the clinical research team. Major considerations included general reliability, impact force, and maximum temperature in worst case normal use. The impactors complied with the associated self-prescribed and CSA standards and obtained or exceeded the minimum adherence level in all rows of the master standards table (App. Table D.2). Since both impactors would be safe to use, the choice for deployment of the 30 *g* impactor came down to functionality. The 30 *g* impactor generally offered better sensitivity in the low interface condition and would be paired with the ASIST handpiece in the clinic to cover a large frequency domain. Consensus to both questions outlined in Section 5.3.1 was ‘yes’ for the 30 *g* impactor.

5.4 Design of Experiments

5.4.1 Overview

With both impactors proving reasonably reliable and safe after an extensive design and manufacture process, the final stage of development would involve a benchtop validation experiment. The goal of the experiment was to validate the use of either handpiece through the entire data acquisition and model matching process. The responding variable would be bone-implant interface stiffness as defined by Mohamed [28], which was similar overall to the ASIST Stability Coefficient (ASC) developed by Westover et al. [16]. The experimental structure was strongly influenced by the work of Westover et al. in comparing the ASIST and Osstell systems on osseointegrated implants for bone anchored hearing aids [55]. In the experiment, the systems were used to assess the stability of implants in several configurations with varying interface stiffnesses. Five repeated measures were recorded by one operator at each intersection of factors. The goal of the experiment was to evaluate the sensitivity of the devices to changes in interface stiffness and implant geometry. The hypothesis being that the ASIST would be more sensitive to changes in interface stiffness and less sensitive to changes in abutment length (implant component) than the Osstell. The results of the experiment are well summarized by Figure 5.25, which shows a

comparison of the average measurements taken at each intersection of factors. The graphic presents a smart framework for comparison of osseointegrated implant stability measurement systems, encompassing fundamental objectives of evaluating sensitivity to interface stiffness and insensitivity to implant geometry.

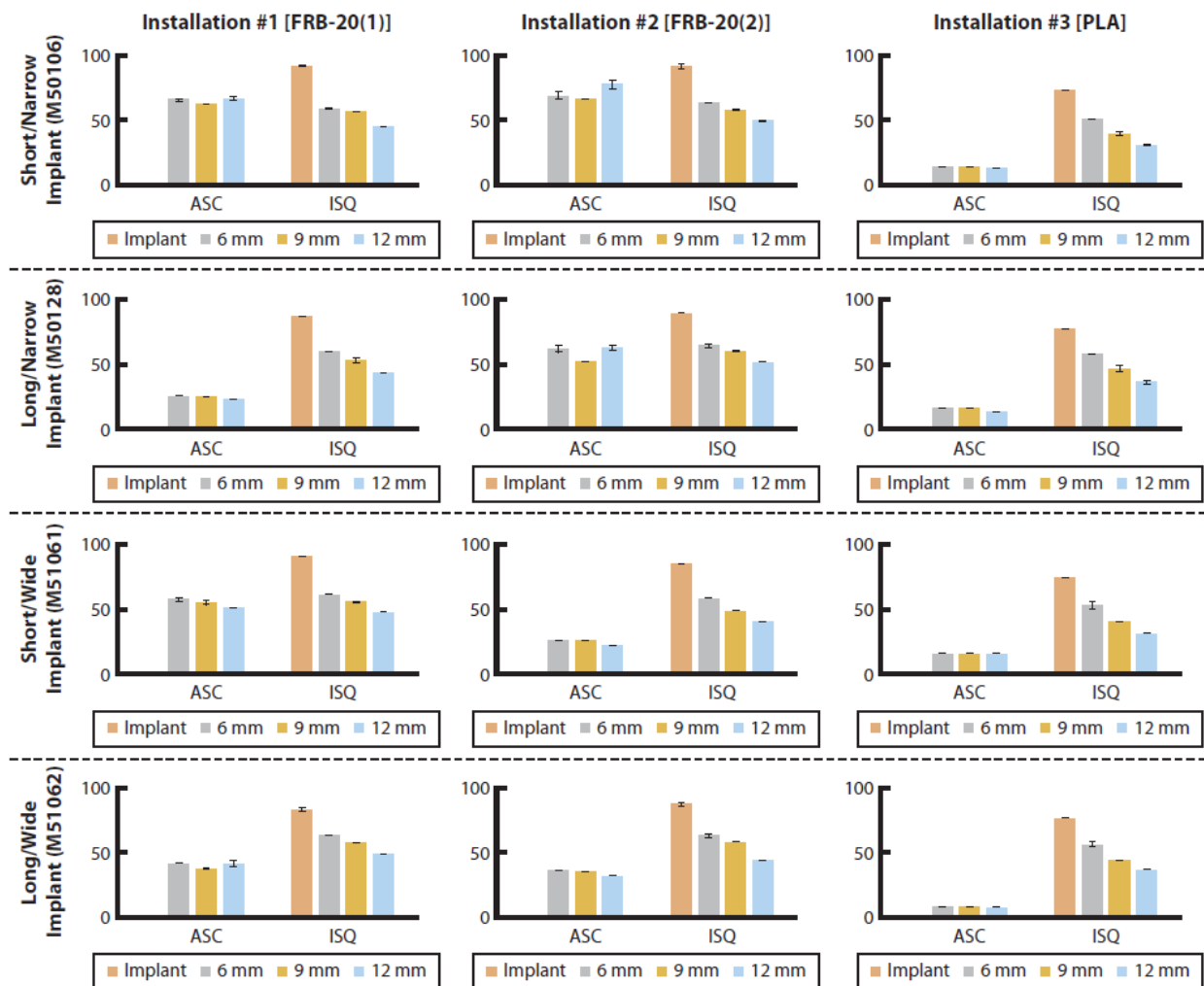


Figure 5.25: ASIST and Osstell Comparison – Journal of Prosthetic Dentistry [55]. Different installations represent different interface stiffnesses; abutment length shown in legend

The present experiment aimed to modify this framework to compare the 10 g and 30 g impactors. Additionally, validation would be bolstered through the introduction of a random effect in the form of multiple operators. The objectives were threefold:

1. Evaluate the sensitivity of each handpiece to interface stiffness.
2. Evaluate the sensitivity of each handpiece to implant geometry.

3. Compare the performance of the impactors to make an informed selection for further development.

5.4.2 Pilot Test

The signals collected from the silicone setup for standards compliance were matched to a 1D finite element model developed in a parallel study by Mohamed [28]. Matching was conducted through a custom MATLAB application in which signals were imported, initial guesses were set by the user, and an optimization routine was run, resulting in outputs for interface stiffness in N/m , frequency values and damping ratios for each mode of vibration, and other any variable parameter. A screenshot of the guided user interface can be viewed in Figure 5.26.

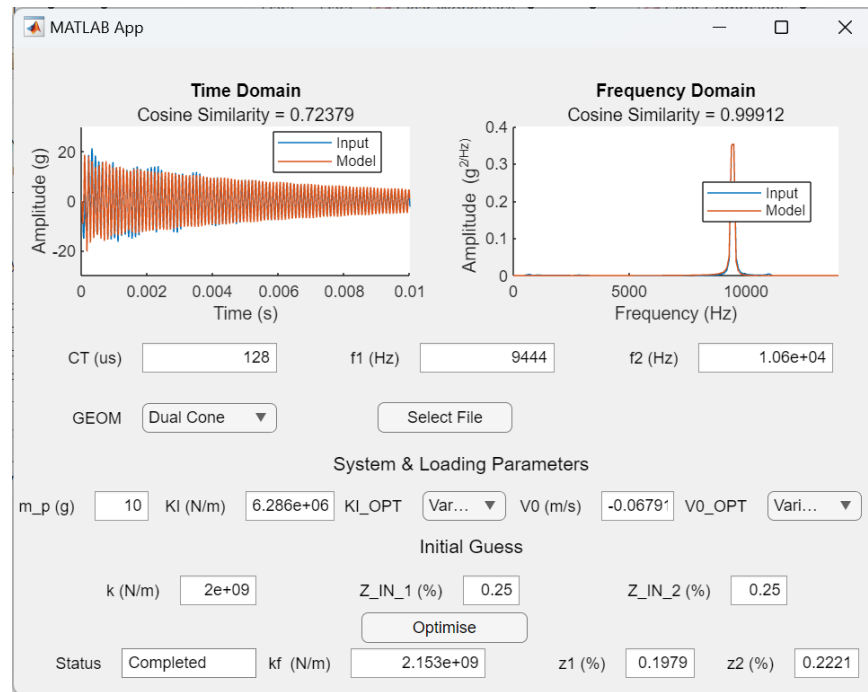


Figure 5.26: 1D finite element model GUI

Interface stiffness estimates were extracted and averaged for each impactor configuration. A boxplot of these measurements for the silicone interface setup can be viewed in Figure 5.27. In the full range, vastly different estimates were obtained for the 10 g steel tip impactor from all other impactor configurations.

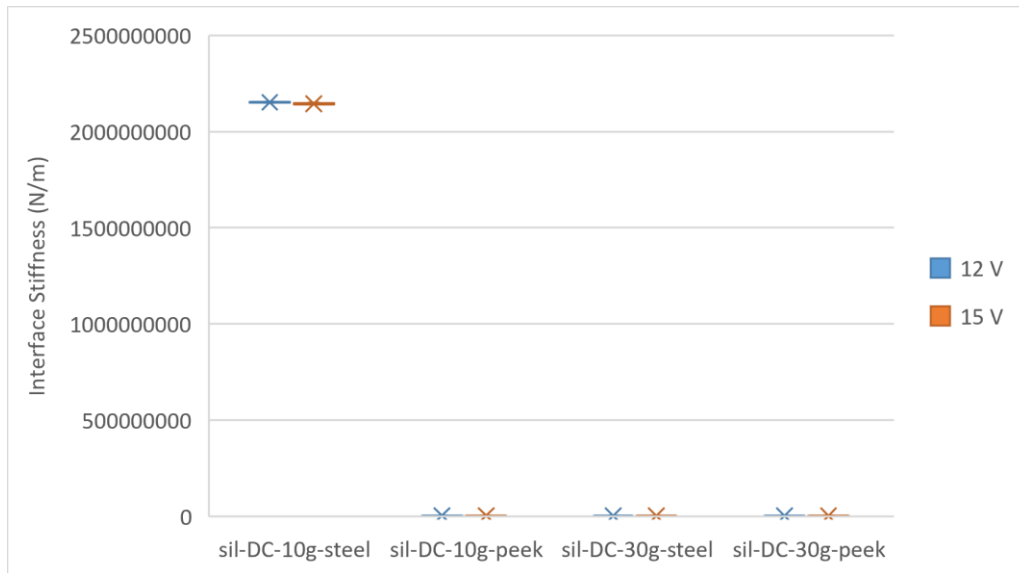


Figure 5.27: Full range boxplot of silicone interface stiffness estimates

In the reduced range (Figure 5.28), the measurements generally took on similar values, especially relative to full scale; however, there appeared to be some differences in variance. Heavier rods with softer impact interfaces resulted in slightly lower interface scores, and the 30 g steel tip impactor had the greatest variance.

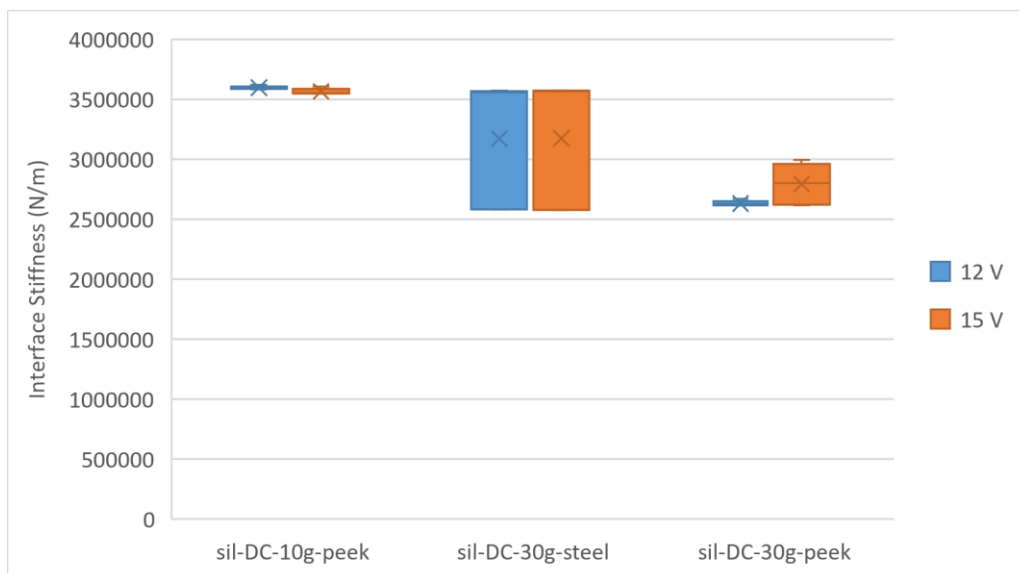


Figure 5.28: Reduced range boxplot of silicone interface stiffness estimates

5.4.3 Design

A mixed effects model framework was selected to include a variety of fixed and random effects. The boxplot demonstrated that for a given interface a wide range of estimates could be obtained, with some estimates landing extraordinarily close to each other. The matching process appeared to be extremely sensitive to signal composition. The highest measurement was obtained by an impactor configuration that tended to elicit large amplitude ratio signals; however, within a certain compositional threshold, measurements appeared to be accurate and repeatable. Considering the bias of measurements toward large numerical values, a transformation such as a log link was not out of the question but would have to be verified during statistical analysis. In the Westover experiment [55], five repeated measures provided adequate power to the study. Judging by the behaviour of the present scale, a similar order of replicates would be appropriate. The present experiment was designed to have seven factors to satisfy all objectives of the study. Like the development study, interface stiffness would be the primary independent variable and three adhesives would represent low, intermediate, and high stiffness interface conditions (silicone, paraffin wax, and superglue, respectively). This factor would help satisfy the first objective, and the associated null hypothesis would be that both handpieces are not sensitive to interface stiffness. Introducing dual cone adapter length and GV connector presence as factors would help satisfy the second objective of the experiment. These factors would both have two levels: 68.5 *mm* or 88.5 *mm* for dual cone adapter and uninstalled or installed for GV connector. The null hypothesis for both factors would be that both handpieces are not sensitive to dual cone adapter length or presence of the GV connector. For study speed and practicality, interface stiffness, dual cone adapter length, and presence of the GV connector would be blocked factors. That is, all runs of a given interface stiffness would be executed on a single day, and all remaining factors would be tested in random order for a given implant configuration (interface; dual cone adapter; GV connector). This was because of limited access to implants for creating simultaneous setups and extensive component installation times along with repeated installations posing risk to interface integrity. The third and final objective would be satisfied by the introduction of impact rod (impactor) mass as a factor. Here, the levels would be 10 *g* or 30 *g*. Impact tip, operator, and trial were also considered factors; however, they each represented a different component of the prospective mixed effects model. Impact tip (stainless steel; PEEK) would be represented as a fixed covariate, three operators would be treated as subjects, and three trials would be treated as

repeated measures. The null hypothesis for impact rod would be that there are no differences in the response variable (interface stiffness) between the handpieces. Ultimately, the study aimed to discern any performance differences in sensitivity, accuracy, or reliability. The null hypothesis for impact tip would be that there are no differences in the response variable, with failure to reject the hypothesis leading to elimination of the covariate from analysis. Since operators would be treated as subjects, there was no associated hypothesis. And lastly, the null hypothesis for trial would be that there is no difference in the response variable, failure to reject the hypothesis also leading to potential collapse of the factor. With trial having decent potential to be an insignificant effect, there was potential for up to nine replicates in statistical analysis. In the less optimal scenario, where trial was significant, three subjects was deemed to be sufficient considering the Westover experiment and observed high sensitivity and limited variability of the approach. A summary of the factors, levels, and design can be viewed in Table 5.4.

Table 5.4: Prospective validation study design

| Factor | Levels | -1 | 0 | 1 | Effect | Hypothesis | Design |
|-------------------|---------------|-----------|----------|----------|-----------------|-------------------|---------------------|
| Interface | 3 | Low | Int | High | Fixed | Sensitive | Blocked Factors |
| Dual Cone Adapter | 2 | Short | | Long | Fixed | Insensitive | |
| GV Connector | 2 | Off | | On | Fixed | Insensitive | |
| Impact Rod | 2 | Small | | Large | Fixed | Evaluate | Randomized Factors |
| Impact Tip | 2 | Soft | | Stiff | Fixed Covariate | Insensitive | |
| Operator | 3 | 1 | 2 | 3 | Random | N/A | Randomized Subjects |
| Trial | 3 | 1 | 2 | 3 | Fixed | Insensitive | Repeated Measures |

5.5 Conclusion

Two handheld impactors were designed and manufactured for clinical and experimental use. The impactors were evaluated for safety, functionality, and reliability. Both impactors were deemed to be safe and make the general hypothesis testable in clinical and experimental settings. With room for only one handpiece to be deployed to the clinic, the 30 g impactor was selected for its

uniqueness in mass and frequency input from the ASIST (Periotest handpiece). Finally, a benchtop experiment was designed to further evaluate and discriminate the performance of the handpieces across multiple operators, with the ultimate objective of providing a recommendation for a single, reliable impactor.

Chapter 6 Experimental Validation of Handheld Impactors

6.1 Introduction

6.1.1 Background

A thorough development process led to the design and manufacture of two impactors for transfemoral implant stability assessment. After rigorous testing, the 30 *g* impactor complied with all safety and performance standards and was cleared for clinical deployment. Still, the optimal impactor for the proposed percussion approach was in question. A study conducted by Mohamed et al. demonstrated that the Periotest handpiece was insufficient to excite the first axial mode of the OPL system across all interface conditions [27]. The development and evaluation study detailed in Chapter 4 advanced two promising courses of action:

1. Select the 10 *g* impact rod, performing similarly to the Periotest, and provide a soft impact interface for low frequency excitation along with the regular 316 stainless steel tip.
2. Select the 30 *g* impact rod, causing mid-range noise in the high stiffness condition, and again, provide two levels of impact interface stiffness.

The hope of both options was that some future framework would allow for trust/distrust decisions to be made between interchangeable tip measurements. The aim of this study was to make a final decision between the two manufactured handpieces. To do so, an experimental procedure like that outlined by Westover et al. was adopted [55]. In the Westover investigation, the Osstell and ASIST devices we compared in a benchtop implant stability experiment. The ability of the devices to isolate interface stiffness and judge implant stability was evaluated over a range of interface stiffnesses and implant configurations. Here, a similar framework will be implemented with the addition of a random operator effect.

6.1.2 Objectives

The success of the present study relied on the simultaneous development and execution of several processes. For sound impactor validation, an objective framework for signal model matching had to be developed. The development process relied on the qualitative assessment of acquired signal characteristics and mathematical model behaviour. The performance of the impactors had to be

evaluated against each other in the entire measurement protocol, and the superior impactor had to be fully validated across multiple operators, implant configurations, and interface stiffness conditions. The objectives of the study are summarized below:

1. Develop an objective framework for signal model matching and implant stability assessment.
2. Evaluate the performance of both impactors and make a final design recommendation.
3. Validate the function of the selected impactor across multiple operators, implant configurations, and interface stiffness conditions.

6.2 Materials and Methods

6.2.1 Overview

A full factorial design of experiments framework was executed in accordance with the design presented in Section 5.4 and specific factors and levels contained in Table 5.4. Three participants were recruited and trained to operate both impactors. The experiment was blocked into three days; in each block, an entire set of factors were tested for a given interface stiffness level. E.g., on day one, all measurements associated with the silicone interface were completed. The blocking scheme was hierarchically organized by BII stiffness experimental model on a given day, two dual cone adapter levels, then two GV connector levels. I.e., both GV connector levels were tested for a given dual cone adapter before moving to the next dual cone adapter level. Within the blocks, each level of impact rod, impact tip, and operator were randomized. Finally, three repeated measures were taken by each operator for the unique combination of factors. Within this design, interface stiffness, dual cone adapter length, and presence of GV connector were organized as blocked factors representing fixed effects; impact rod and impact stiffness were organized as randomized factors representing fixed effects (with impact stiffness later treated as a fixed covariate effect); operators were organized as randomized subjects representing a random effect; and three consecutive measurements were organized as repeated measures representing a fixed effect. In this design, participants were assumed to come from a larger population of operators and added the principal random effect to the experiment.

6.2.2 Experimental Setup

In a similar fashion to the process outlined in Section 4.2, OPL Type A implant stems were installed in Sawbones composite femurs. The femurs were altered in accordance with the steps outlined in Figure 4.4, where the distal end of the femur was removed, and the intramedullary cavity was drilled to allow for a uniform 0.1 *mm* thick interface between the implant and bone. For the silicone and superglue interfaces, the adhesives were thickly coated on to the entire bonding region of the implant (Figure 4.3) before the implant was inserted into the altered femur. The bone-implant systems were allowed to cure upright for 72 hours. Double-sided tape was used as a stopper to ensure an approximate 16 *mm* gap was maintained between the start of the bonding region of the implant stem and cut face of the composite femur. Large portions of excess adhesive were removed before extensive curing, and after the curing period, any remnants on the exposed bonding region and around the cut-face were carefully removed. For the paraffin wax interface setup, granular paraffin wax was melted into a homogenous liquid on a hot plate at approximately 250°C. The implant and bone were placed in a temperature chamber at 65°C and allowed to reach equilibrium for approximately 20 *min*. After the elapsed time, the components were removed, the bone was mounted upright in a clamp, and the implant was inserted with a piece of supporting cardboard (double-sided tape failed to adhere to the hot implant) to ensure a ~16 *mm* bonding region gap. Molten wax was slowly dripped into the interface gap between the implant and bone with an eyedropper until wax began to spill over the cut face. The temperature of the bone and implant was deliberately set close to the melting point of the paraffin wax to ensure that solidification would occur soon after dripping the molten wax. This would allow the wax to penetrate down the interface as much as possible before partially solidifying and forming a plug, allowing more wax to fill the bonding region. In this state, the system was allowed cool for 24 hours. Excess wax was then removed from the exposed bonding region and cut face as well as from a small proximal hole in the composite femur. Finally, the assembly was put back into the temperature chamber at 55°C (below paraffin wax melting point) for one hour to allow potential interface faults caused by the cooling process or excess material removal to heal. The assembly was removed and allowed to cool for 24 hours before any testing was conducted. For each setup, the same operator assembled the implant system according to the experimental block being tested. I.e., a particular dual cone adapter and GV connector (if present) were installed. The composite bone was then fixed in a

clamp with a damping liner. Further experimental model and acquisition system technical details can be found in Table 6.1, and a photo of the experimental setup can be viewed in Figure 6.1.

Table 6.1: Experimental model and acquisition system components

| Experimental Model | |
|-----------------------------|--|
| <i>Component</i> | <i>Description</i> |
| Composite Femur | Sawbones SKU 3403 composite femur (Pacific Research Group, USA). Drilled to allow for 0.1 mm uniform interface between composite bone and implant. |
| Implant Stem | OPL Type A implant stem (Permedica, Italy). \varnothing 14 mm \times 160 mm. |
| Silicone Interface | DOWSIL 7091 silicone rubber adhesive (DOW, USA). |
| Paraffin Wax Interface | Raw paraffin wax. Melted and solidified to form interface. |
| Superglue Interface | LePage Ultra Gel superglue (LePage, Canada). |
| Short Dual Cone Adapter | OPL Type A dual cone adapter (Permedica, Italy). 68.5 mm length. |
| Long Dual Cone Adapter | OPL Type A dual cone adapter (Permedica, Italy). 88.5 mm length. |
| Internal Locking Screw | OPL internal locking screw (Permedica, Italy). Tighten to 10 Nm. |
| GV Connector | OPL GV connector (Permedica, Italy). |
| Distal Screw | OPL distal screw (Permedica, Italy). Tighten to 2 Nm without GV connector installed or 10 Nm with GV connector installed. |
| Damping Liner | Silicone rubber liner for mechanical isolation. |
| Bone Clamp | Fully fixed clamp with squeezing force controlled by exposed threaded shaft length (37 mm). |
| Acquisition System | |
| <i>Component</i> | <i>Description</i> |
| Accelerometer | Analog Devices ADXL1004 MEMS Accelerometer (Analog Devices, USA). |
| Accelerometer Casing | 3D-printed casing for accelerometer protection. |
| Double-Sided Tape | Double-sided Gorilla tape for adhesion between accelerometer and implant. |
| Analog-to-Digital Converter | National Instruments NI-9205 DAQ (National Instruments, USA). |
| Host PC | Host PC for signal processing through LabVIEW GUI (National Instruments, USA). |

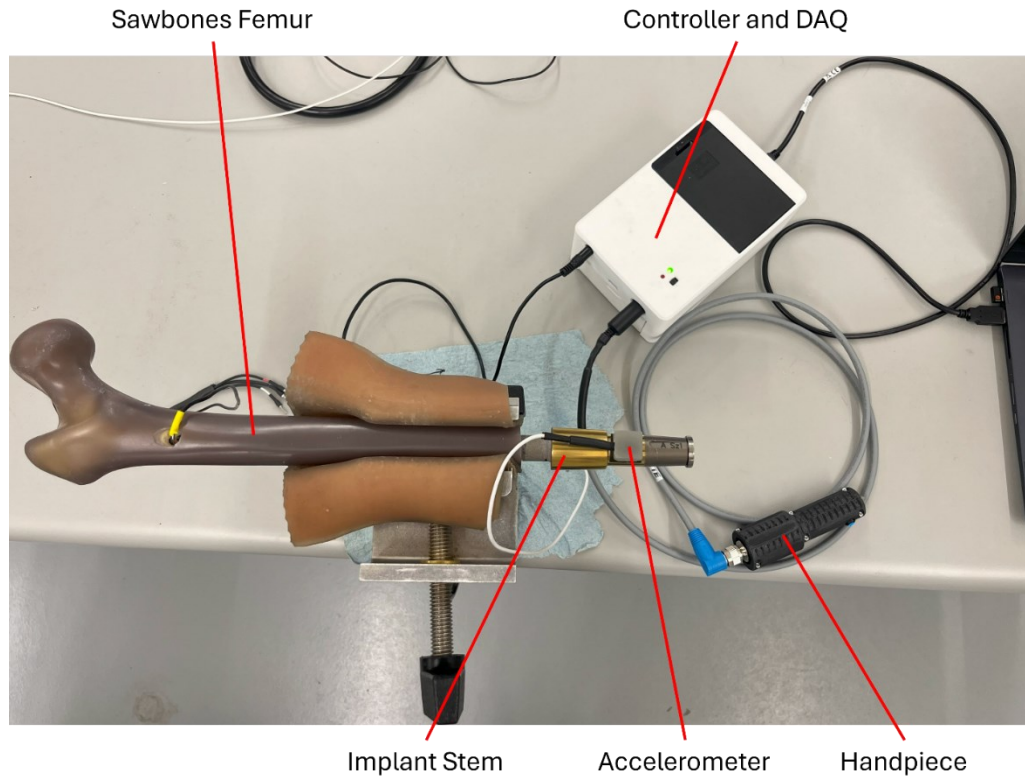


Figure 6.1: Benchtop validation experiment setup

6.2.3 Experimental Procedure

As detailed in Chapter 5 two handpieces were developed for testing by multiple operators. The handpieces were characterized by different impact rod masses. One had a mass of 10 *g*, while the other had a mass of 30 *g*. Additionally, each handpiece came with two different impact tips: one machined from 316 stainless steel and the other from PEEK. Two configurations of the 10 *g* handpiece can be viewed in Figure 6.2.

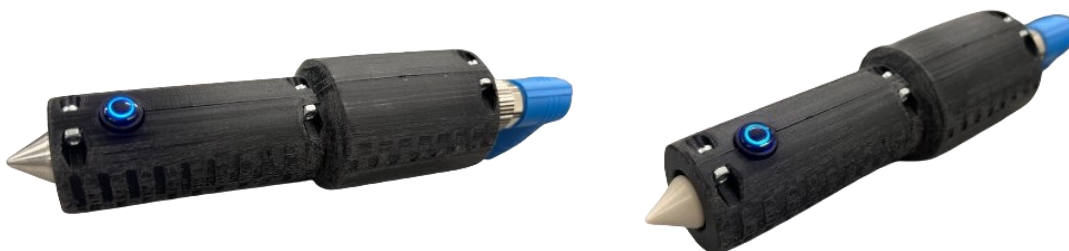


Figure 6.2: 10 g handpiece. Left, steel tip configuration; right, PEEK tip configuration

Participants were trained on an existing experimental TFA implant model, including accelerometer installation and handpiece operation. The accelerometer was installed on the implant by cutting a small piece of doubled-sided Gorilla tape (approximately $1.5\text{ cm} \times 1.5\text{ cm}$), sticking the side with exposed adhesive to either the approximate middle of the uniform cylindrical portion of the dual cone adapter or approximate middle of the top, anterior face of the GV connector (if installed), peeling the plastic covering off the other face, and gently pressing the accelerometer down on the exposed adhesive with the signal line extending towards the proximal end of the implant to ensure orientation in the axial direction. Once the accelerometer was installed, an assisting operator would activate the acquisition system through a custom LabVIEW GUI. The impactors were operated by positioning the impact tip approximately $1 - 3\text{ mm}$ from the distal screw in the 3:00 position (medial side) and holding the handpiece as level as possible. Correct handpiece position is demonstrated in Figure 6.3.



Figure 6.3: Medial (3:00) strike position on distal screw

Once the operator was comfortable with the position and orientation of the handpiece, the actuation button could be pressed to initiate striking. The handpiece would fire 16 times (first strike used as an acquisition trigger); throughout the strikes, the operator would concentrate on holding the handpiece as steady as possible. It should be noted that an untrivial amount of practice and skill was needed to execute the striking portion of measurement, given that moving the handpiece too far away from the distal screw would result in missed strikes and exceeding the upwards operating

angle of the handpiece would result in inadequate impact velocity to meet certain strike threshold parameters. A photo of an active operator can be viewed in Figure 6.4.



Figure 6.4: Participant operating handpiece

Within an experimental block and quasi-random operation order, three repeated measures were taken by the same operator. The operator would install the accelerometer on the implant once and actuate the handpiece to strike the implant at least three consecutive times. If less than 12 strikes were recorded according to the LabVIEW GUI or another complication occurred during acquisition, the operator was allowed to discard and redo the measurements in error at their discretion. Accelerometer signals were recorded at a sampling frequency of 250 kHz , which was magnitude orders above the most conservative Nyquist frequency estimate. The Nyquist frequency was assumed to be twice the accelerometer bandwidth ($24\text{ kHz} * 2 = 48\text{ kHz}$), which was also well above the largest anticipated implant frequencies. After completion of the experiment, the accelerometer signals were digitally processed by applying a lowpass Butterworth filter with cutoff frequency of 20 kHz . The ensemble average of time domain signals belonging to the same measurement (batch of strikes) was taken before passing the final signal to a 1D finite element model for interface stiffness extraction. A signal processing parameter summary can be viewed in Table 6.2.

Table 6.2: Signal processing parameters for benchtop validation experiment

| Signal Processing | | |
|-------------------|------------------------|-------------------|
| | Parameter | Value |
| Samples | Frequency (kHz) | 250 |
| | Length | 2000 |
| Filter | Design | Butterworth (IIR) |
| | Order | 8 |
| | Cutoff Frequency (kHz) | 20 |
| | Type | Lowpass |
| | Phase Shift | Regular |
| Strikes | Recorded | 15 |
| | Ensemble Average | Time Domain |

6.3 Results

6.3.1 Overview

All processed signals were fed to a 1D finite element model to extract system parameters and interface stiffness estimates. The decision-making protocol used in the matching process is outlined in Figure 6.5. In the protocol, both steel and PEEK tip measurements were matched to the model. The decision-making tree assisted in setting up initial conditions for the model as well as deciding on which impact interface stiffness measurement to trust. To set up the model, decisions had to be made about which present frequencies were important. The domain of interest ($0 \text{ Hz} \leq f < 10000 \text{ Hz}$) was subdivided into three regions according to the flowchart (Figure 6.5). The third region was always of interest because it guaranteed the presence of either the first (relative shearing) or the second (compression and expansion) axial mode of vibration. The first and second regions were defined on the basis that significant power spectral density in the first region would be indicative of a low interface stiffness case and be key in making a trust-distrust decision on the

impact tips used. It was observed within the data that relatively little power spectral density was distributed in the band from 0 – 750 *Hz* unless a first mode was present in the case of the silicone interface setup. This was indicative that significant power spectral density in the first region was not likely to be attributed to mechanical noise in any case. I.e., mechanical noise or internal modes of implant vibration were likely greater than or equal to 750 *Hz* in all cases. In the second region, there was potential for the occurrence of the first axial mode as well as multiple sources of noise. Using this information, criteria and thresholds were developed that would optimize matching of the first axial mode in as many cases as possible while maintaining an objective and robust framework. Thresholds were created relative to the largest peaks in the second and third regions. A peak in the first region would be included in the model if it reached at least 50% the height of both Peak 2 and 3 according to the flowchart (Figure 6.5). Peak 2 would be included if Peak 1 was less than 50% of its height, and in all other cases, only Peak 3 would be considered in the model. Once decisions were made about which frequencies to include in the model, initial guesses were set, and model optimizations were run. Finally, if the PEEK tip measurement elucidated a mode in Region 1 while the steel tip did not, the PEEK tip measurement was to be trusted. Otherwise, the steel tip measurement was to be trusted. Additionally, match correctness for the trusted measurement was evaluated by whether the interface stiffness result fell into a particular range. This range was $10^6 - 10^7$ *N/m* for the silicone (low) interface, $10^7 - 10^9$ *N/m* for the paraffin wax (intermediate) interface, and $10^9 - 10^{10}$ *N/m* for the superglue (high) interface. These ranges were established by observing the general distribution of interface stiffness data, known to be correctly or incorrectly matched.

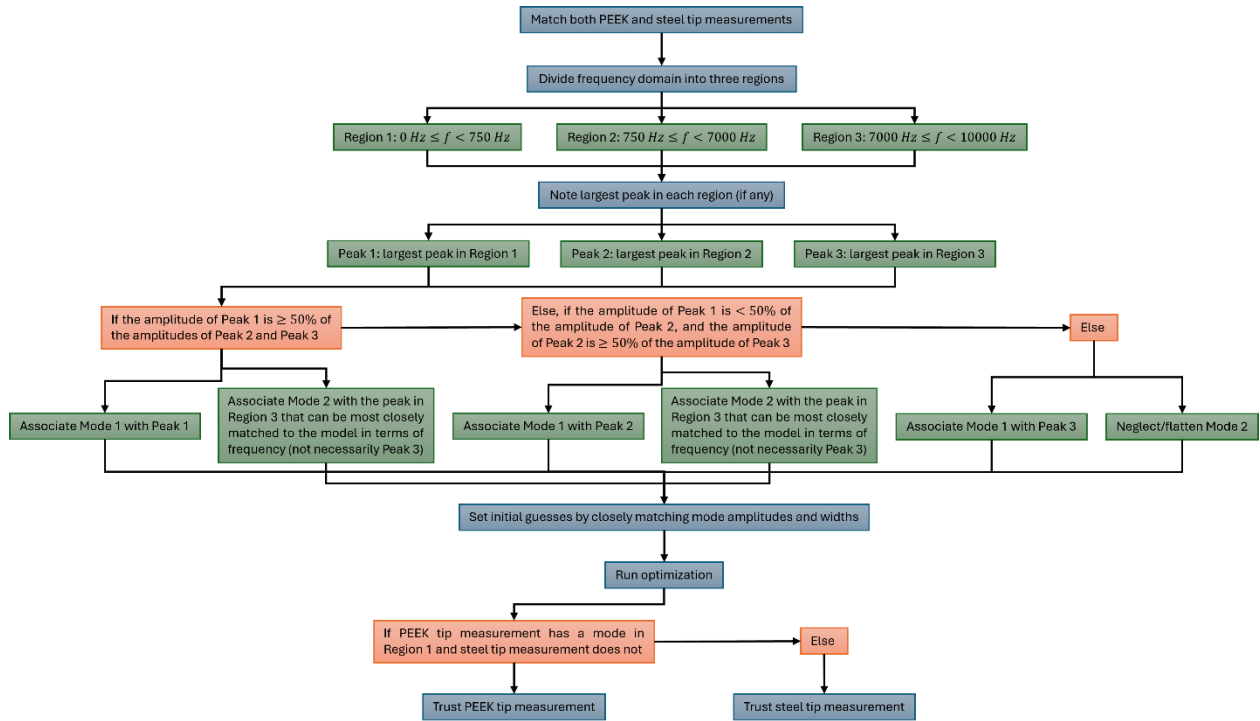


Figure 6.5: Matching protocol flow chart. Blue text, sequential step; green text, classification step; orange text, 'if' statement with true outcome leading down flow chart and not true outcome leading to next horizontal statement

6.3.2 Matching

Matching was conducted through two custom MATLAB applications: one for setups without the GV connector installed, and one for setups with the GV connector installed. Within each application, the dual cone adapter length and impact rod mass were specified. Initial estimates of impact stiffness (peak contribution), initial velocity (peak height), interface stiffness (peak location), and damping ratio (peak width) were input to their respective fields. In all cases, impact stiffness and initial velocity were allowed to freely vary. Once optimization was complete, outputs included model-signal time and frequency domain cosine similarity, impact stiffness, initial velocity, interface stiffness, and frequencies and damping ratios for each mode. For all interfaces, the principal challenge was to correctly match the first mode frequency. For silicone interface signals, steep tip measurements, 10 or 30 *g* impactor implemented, rarely resulted in first mode matching. The 30 *g* impactor clearly improved first mode resolution for steel tip measurements; however, its amplification was rarely enough to meet thresholds set by the matching protocol. An example of this situation can be seen in Figure 6.6, in which, despite the presence of a mode in Region 1, the peak in Region 3 was the only one which met the matching criteria. The resulting optimization led to the conclusion of a high stiffness interface for the steel tip measurement.

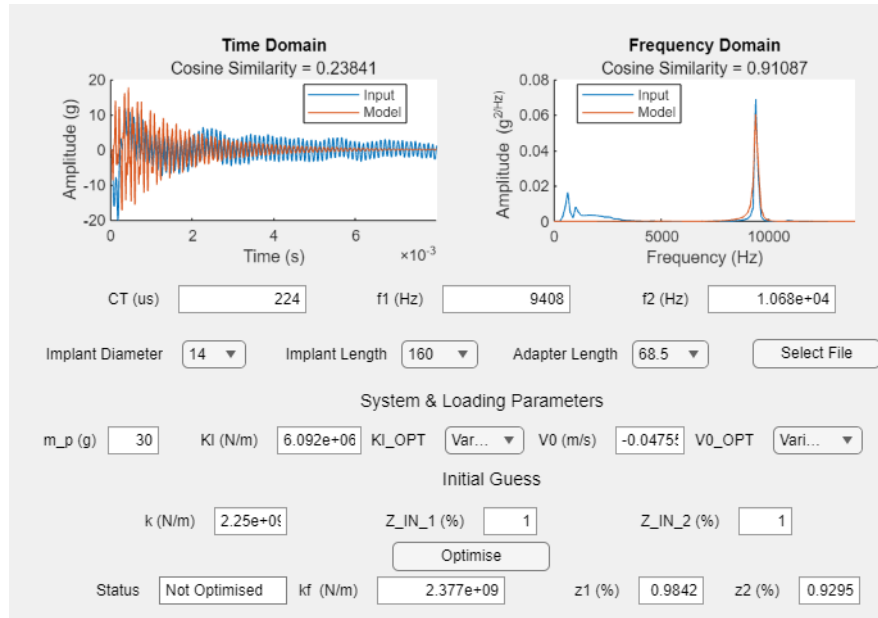


Figure 6.6: Matching window – silicone; 68.5 mm DC; GV off; 30 g rod; steel tip

The first axial mode of the silicone setups became much easier to visualize with PEEK tip measurements. Even the 10 g impactor was able to match the Region 1 frequency and conclude the correct interface stiffness in all cases. PEEK tip measurements greatly attenuated higher frequency components and revealed high levels of band power in Region 1 for silicone interface setups. A sample 10 g – PEEK measurement on a silicone interface setup can be viewed in Figure 6.7.

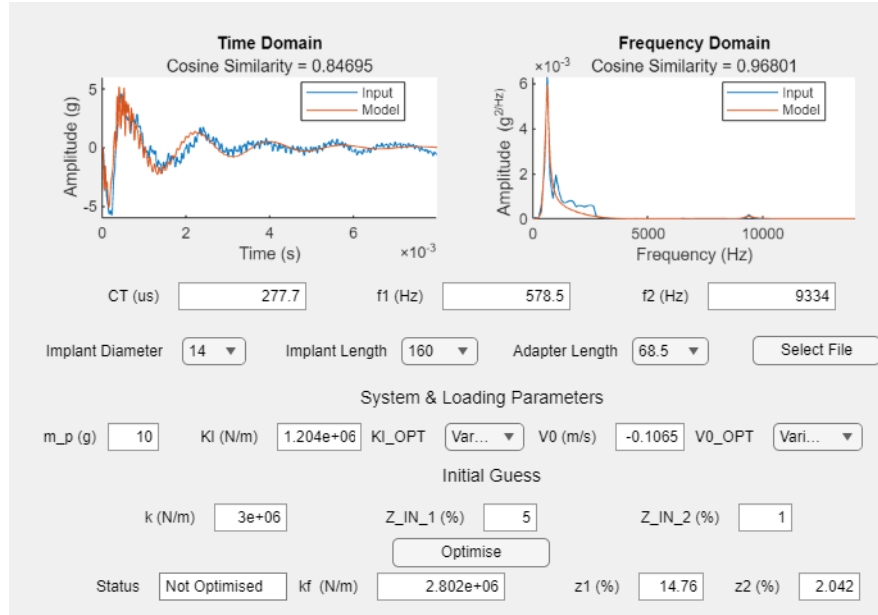


Figure 6.7: Matching window – silicone; 68.5 mm DC; GV off; 10 g rod; PEEK tip

Alternatively, the 30 g steel tip impactor would occasionally result in a false conclusion where the 10 g impactor would have otherwise provided the correct outcome. This would most often occur for superglue interface setups. The 30 g impactor tended to excite a frequency in the range of 3000 Hz, which would subsequently be included in the model and cause an intermediate stiffness interface conclusion. This phenomenon was similarly observed in Chapter 4, where heavier impact rods would cause higher levels of intermediate bandwidth noise. A sample matching window of this issue can be viewed in Figure 6.8.

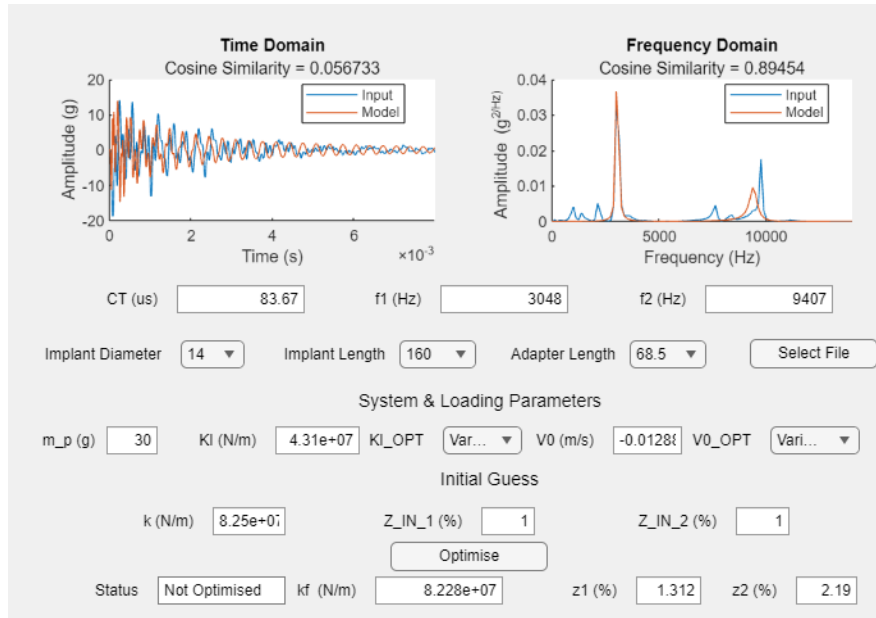


Figure 6.8: Matching window – superglue; 68.5 mm DC; GV off; 30 g rod; steel tip

In this case, the 10 g impactor (steel tip) correctly matched all superglue interface setups by providing elevated resolution in the high frequency bandwidth of Region 3. A correctly matched superglue signal can be viewed in Figure 6.9.

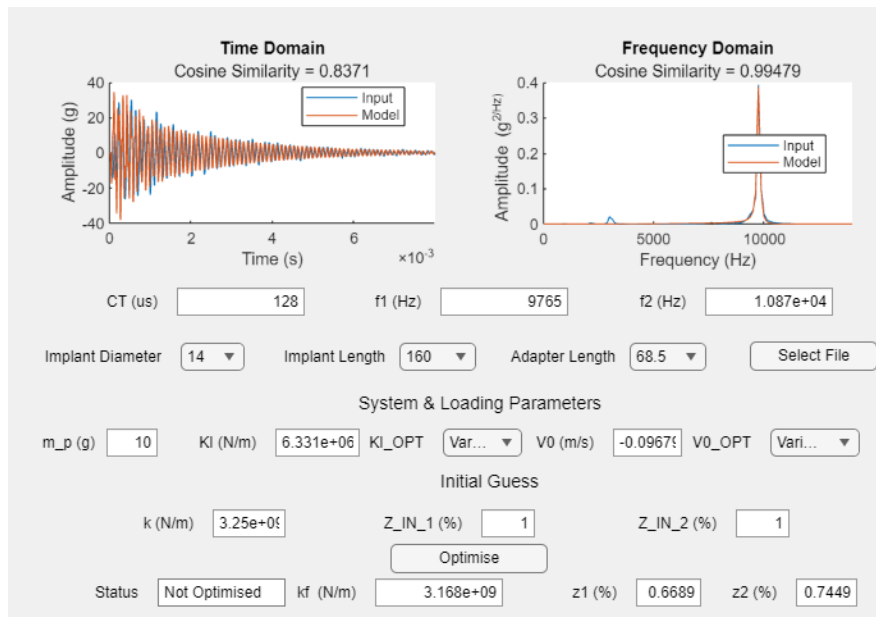


Figure 6.9: Matching window – superglue; 68.5 mm DC; GV off; 10 g rod; steel tip

Paraffin wax interface setups presented the most challenging case for correct matching. For setups without a GV connector installed and with a 68.5 mm dual cone adapter, the signals were always

matched correctly by both impactors. However, significant noise was still seen in the signals, particularly around 8250 Hz, just below the second mode of vibration. This noise can be seen in the correctly matched signal in Figure 6.10.

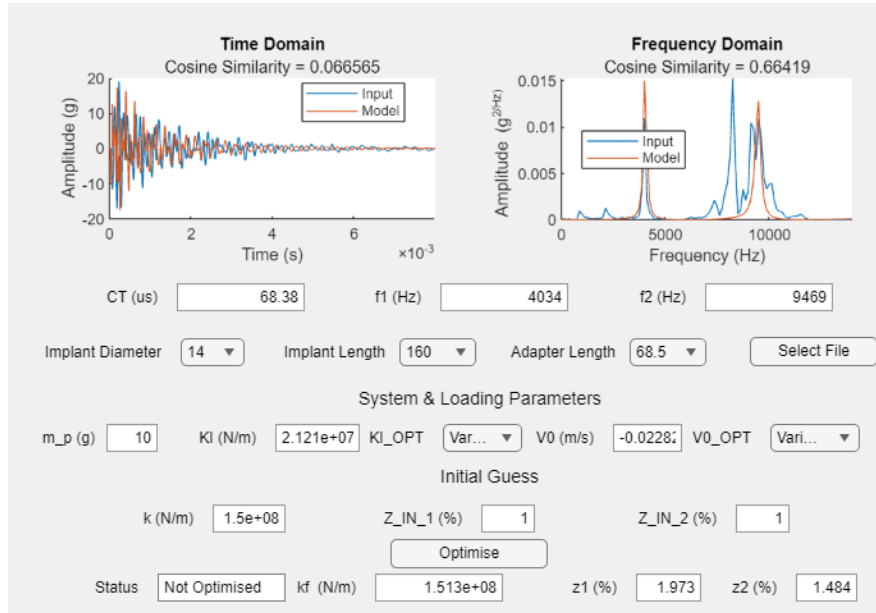


Figure 6.10: Matching window – paraffin wax; 68.5 mm DC; GV off; 10 g rod; steel tip

The relative contribution of this noise was amplified by both the longer dual cone adapter and presence of the GV connector. With the GV connector installed and for a 68.5 mm dual cone adapter, this noise was centered at approximately 7500 Hz. In most complex configurations of the implant system, noise from this unknown source overwhelmed desirable information in the acquired signals and often led to high stiffness interface conclusions for wax setups (incorrect). A wax setup being incorrectly matched to this high frequency noise can be viewed in Figure 6.11.

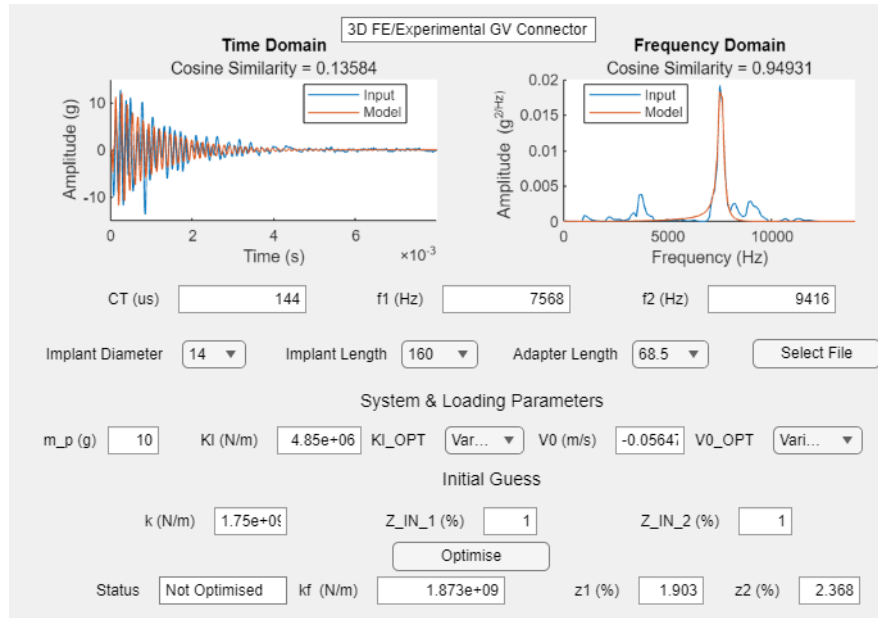


Figure 6.11: Matching window – paraffin wax; 68.5 mm DC; GV on; 10 g rod; steel tip; raw signal

Overall, the 10 g impactor performed extremely well for low and high interface setups, but tremendously underperformed for complex intermediate setups (long dual cone adapter or presence of GV connector). On the other hand, the 30 g impactor performed equally well in low interface conditions, marginally better in intermediate conditions, and poorly in high interface conditions, generally attenuating a greater range of high frequency information. A summary table showing the accuracy of each impactor in each situation can be viewed in Table 6.3.

Table 6.3: Handpiece measurement accuracy summary – raw signals

| 10 g Impactor | | | | | | | | | | | | |
|----------------------|-----------------|------|------|------|---------------------|------|------|------|------------------|------|------|------|
| <i>Interface</i> | <i>Silicone</i> | | | | <i>Paraffin Wax</i> | | | | <i>Superglue</i> | | | |
| GV | Off | | On | | Off | | On | | Off | | On | |
| DC (mm) | 68.5 | 88.5 | 68.5 | 88.5 | 68.5 | 88.5 | 68.5 | 88.5 | 68.5 | 88.5 | 68.5 | 88.5 |
| Accuracy (%) | 100 | 100 | 100 | 100 | 100 | 0 | 0 | 0 | 100 | 100 | 100 | 100 |
| 30 g Impactor | | | | | | | | | | | | |
| <i>Interface</i> | <i>Silicone</i> | | | | <i>Paraffin Wax</i> | | | | <i>Superglue</i> | | | |
| GV | Off | | On | | Off | | On | | Off | | On | |
| DC (mm) | 68.5 | 88.5 | 68.5 | 88.5 | 68.5 | 88.5 | 68.5 | 88.5 | 68.5 | 88.5 | 68.5 | 88.5 |
| Accuracy (%) | 100 | 100 | 100 | 100 | 100 | 100 | 33 | 78 | 22 | 0 | 22 | 11 |

The question became whether introducing a noise filtering protocol would improve the outcomes for a particular impact rod. It seemed likely that the 10 g impactor would be able cover the whole range of interface stiffnesses with minimal intervention compared to what would be needed for the 30 g impactor. The 10 g impactor could identify pertinent signal information in the extremes and would need a noise filtering protocol to be successful in the intermediate, where the 30 g impactor may have needed treatments throughout the range of its operation. With this in mind, a subset of experimental model configurations were run through a notch filtering protocol. A 4th order Butterworth band stop filter was implemented in the signal preprocessing code at the largest peak identified as a source of noise in the first round of matching. That is, in signals that were correctly matched, the largest unmatched peak was attenuated, and in signals that were incorrectly matched, the matched peak was attenuated. In general, these peaks ranged from 7250 Hz for the most massive implant configuration to 8250 Hz in the lightest implant configuration and fell directly below the true second mode of the system. The signal in Figure 6.11 was treated, and its post-treatment matching window (correct) can be viewed in Figure 6.12.

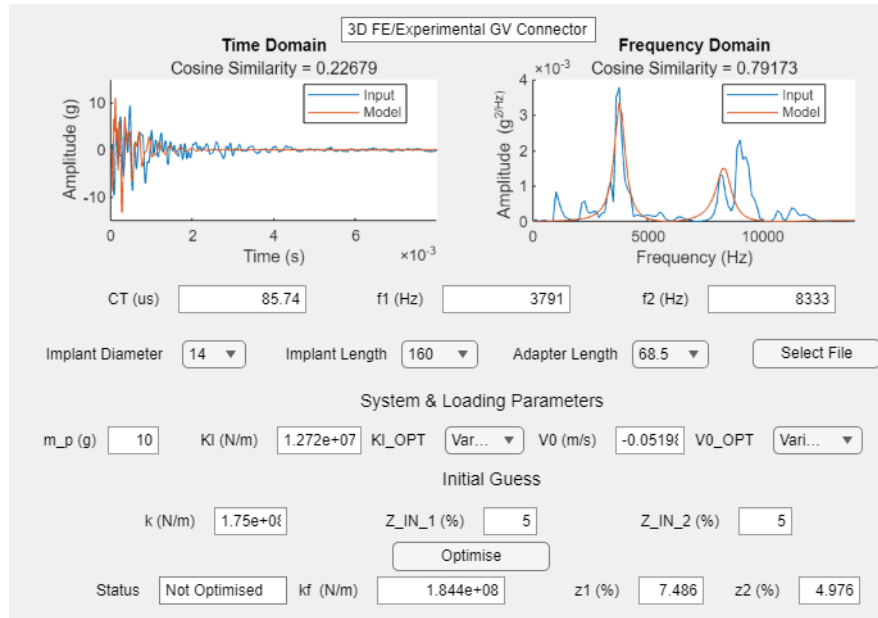


Figure 6.12: Matching window – paraffin wax; 68.5 mm DC; GV on; 10 g rod; steel tip; notch filter

Notch filter treatment drastically improved the accuracy of matching outcomes with application in only a small subset of signals. The 10 g impactor had 100% accuracy except for one implant configuration (88.5 mm dual cone adapter without GV connector installed), while the 30 g impactor had 100% accuracy for all low and intermediate interface stiffness cases (same outcomes for high cases). The accuracy results can be viewed in Table 6.4. Prospective methods for objective implementation of a noise attenuation protocol will be explored later in the chapter.

Table 6.4: Handpiece measurement accuracy summary – notch filter

| 10 g Impactor | | | | | | | | | | | | |
|----------------------|-----------------|------|------|------|---------------------|------|------|------|------------------|------|------|------|
| <i>Interface</i> | <i>Silicone</i> | | | | <i>Paraffin Wax</i> | | | | <i>Superglue</i> | | | |
| GV | Off | On | Off | On | Off | On | Off | On | Off | On | Off | On |
| DC (mm) | 68.5 | 88.5 | 68.5 | 88.5 | 68.5 | 88.5 | 68.5 | 88.5 | 68.5 | 88.5 | 68.5 | 88.5 |
| Accuracy (%) | 100 | 100 | 100 | 100 | 100 | 0 | 100 | 100 | 100 | 100 | 100 | 100 |
| 30 g Impactor | | | | | | | | | | | | |
| <i>Interface</i> | <i>Silicone</i> | | | | <i>Paraffin Wax</i> | | | | <i>Superglue</i> | | | |
| GV | Off | On | Off | On | Off | On | Off | On | Off | On | Off | On |
| DC (mm) | 68.5 | 88.5 | 68.5 | 88.5 | 68.5 | 88.5 | 68.5 | 88.5 | 68.5 | 88.5 | 68.5 | 88.5 |
| Accuracy (%) | 100 | 100 | 100 | 100 | 100 | 100 | 100 | 100 | 22 | 0 | 22 | 11 |

6.4 Discussion

6.4.1 Overview

The data outcomes for both the matching procedure conducted on raw signals and signals run through the notch filter protocol were tabulated and imported to SPSS Statistics (IBM, USA). Statistical analysis was only run on measurements deemed to be true relative to their alternative impact stiffness counterpart. Attempts were made to run the datasets through a linear mixed effects model analysis, but results were typically ill-fitting and difficult to generate. Upon further exploration into the spread of the data and its distribution, it was discovered that interface stiffness outcomes were better visualized on a logscale and may not have followed a normal distribution. Additionally, it became desirable to analyze the binary outcome metric of match correctness (whether interface stiffness results accurately matched true interface stiffness levels). Interface stiffness level ranges were previously defined in Section 6.3.1. It was decided that a generalized linear mixed effects model could better represent the complex nature of the data. True to the design of the experiment, operators were treated as subjects, and trials were treated as repeated measures

under the respective hierarchical organization of interface stiffness, dual cone adapter, GV connector, and impact rod. Furthermore, interface stiffness, dual cone adapter, GV connector, impact rod, and trials were treated as fixed effect factors. Impact tip was also treated as a fixed effect factor (covariate) until probable cause for elimination from the model was found. Due to difficulty in model generation, various covariance and regression structures were tested in tandem. Complex covariance structures generally failed to produce positive-definite Hessian matrices or encountered run-time errors. A variety of regression structures generally succumbed to the same issues or resulted in an insignificant corrected model. For interface stiffness (N/m) data, a gamma regression structure worked well. The structured used a Gamma probability distribution with a log link function and was recommended by the program for target data containing all positive values and skewed towards larger values. Similarly, a normal distribution with log link was tried, but failed to produce a result. For the binary outcome ‘match correctness’ data, two regression structures produced results. The structures that were tried were a binary logistic regression (binomial distribution with logit link, recommended when target is a binary response predicted by a logistic regression model) and a binary probit regression (binomial distribution with probit link, recommended when target is a binary response with an underlying normal distribution). Between the two structures, only the binary probit regression yielded a significant corrected model in all cases. Finally, two covariance structures were tried: compound symmetry and scaled identity. Only the scaled identity structure produced results in all cases in conjunction with the selected regression structures. Additionally, between compound symmetry and scaled identity, the scaled identity covariance structure produced smaller Akaike corrected and Bayesian information criterion values ($-2 \log \text{likelihood}$) in all cases where a result could be obtained for both structures. Considering the minimized information criterion values of the scaled identity covariance structure and significant corrected model p-values of the Gamma regression and binary probit regression fits to their respective datasets, these structures were selected for generating generalized linear mixed effects models for interface stiffness and match correctness data. Once models were generated within this framework, impact stiffness was observed to be an insignificant covariate in all cases and was subsequently removed from statistical analysis.

6.4.2 Generalized Linear Mixed Effects Models

6.4.2.1 Gamma Regression – Raw Signals

A gamma regression model was first run for the model matching data generated from raw input signals. The predicted by observed plot in Figure 6.13 showed evidence of a significant relationship between the model and data and generally good model fit.

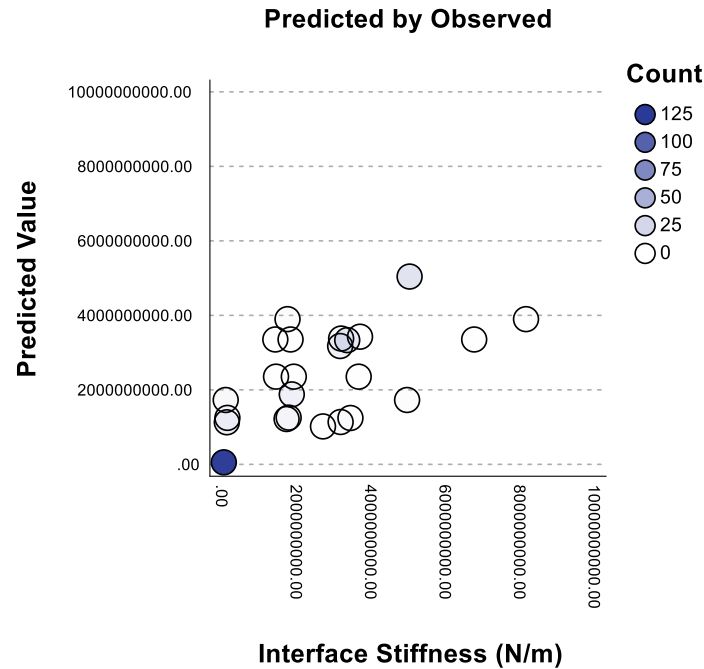


Figure 6.13: Predicted by observed plot for gamma regression on data from raw signals

Furthermore, the corrected model fixed effect was significant ($p - value < 0.001$). Generally, the hypothesized outcome for the experiment was that at least one of the measurement systems would be sensitive to different interfaces and insensitive to all other implant system component levels. The performance of each impact rod was to be evaluated with the respect to this assertion. In accordance with two of the hypotheses, interface stiffness represented a significant fixed effect and dual cone adapter represented an insignificant fixed effect (measurement system insensitive to this component). However, the GV connector fixed effect was significant, along with a host of multi-factor interaction terms. This result was congruent with high-level findings, in that the performance of the impactors was observed to be highly dependent on implant configurations within specific interface levels. Moreover, significant differences were observed between the

impactors, suggesting that performance differences would be distinguishable. A summary of the fixed effects can be viewed in Table 6.5.

Table 6.5: Fixed effects for gamma regression on data from raw signals

| Fixed Effects^a | | | | |
|----------------------------------|----------|-----|-----|-------|
| Source | F | df1 | df2 | Sig. |
| Corrected Model | 89.827 | 71 | 144 | <.001 |
| Interface | 2635.086 | 2 | 144 | <.001 |
| DC | .024 | 1 | 144 | .877 |
| GV | 96.769 | 1 | 144 | <.001 |
| Rod | 329.520 | 1 | 144 | <.001 |
| Trial | 1.050 | 2 | 144 | .353 |
| Interface * DC | 30.778 | 2 | 144 | <.001 |
| Interface * GV | 31.783 | 2 | 144 | <.001 |
| Interface * Rod | 106.878 | 2 | 144 | <.001 |
| Interface * Trial | 2.105 | 4 | 144 | .083 |
| DC * GV | 14.511 | 1 | 144 | <.001 |
| DC * Rod | 68.420 | 1 | 144 | <.001 |
| DC * Trial | .987 | 2 | 144 | .375 |
| GV * Rod | 6.690 | 1 | 144 | .011 |
| GV * Trial | 3.968 | 2 | 144 | .021 |
| Rod * Trial | .576 | 2 | 144 | .563 |
| Interface * DC * GV | 12.312 | 2 | 144 | <.001 |
| Interface * DC * Rod | 18.920 | 2 | 144 | <.001 |
| Interface * DC * Trial | 4.801 | 4 | 144 | .001 |
| Interface * GV * Rod | 2.150 | 2 | 144 | .120 |
| Interface * GV * Trial | 8.576 | 4 | 144 | <.001 |
| Interface * Rod * Trial | 1.646 | 4 | 144 | .166 |
| DC * GV * Rod | 13.523 | 1 | 144 | <.001 |
| DC * GV * Trial | 2.322 | 2 | 144 | .102 |

| | | | | |
|-----------------------------------|----------------------------|----|--------------|-------|
| DC * Rod * Trial | 1.563 | 2 | 144 | .213 |
| GV * Rod * Trial | 3.227 | 2 | 144 | .043 |
| Interface * DC * GV * Rod * Trial | 3.828 | 20 | 144 | <.001 |
| Probability Link a | distribution: function: | | Gamma Log | |

a. Target: Interface Stiffness (N/m)

Weighted fixed effects can be viewed in Figure 6.14, where thicker lines represent greater effects. Here, it can be seen that at the highest level, interface stiffness, GV connector, and impact rod were significant, while dual cone adapter and trial were insignificant. This is at least a partially encouraging result in that four of five of the main effects hypotheses were correct. On the other hand, lots of the interaction terms had large effects, suggesting that underperforming areas of impactor operation could be narrowed down to specific circumstances.

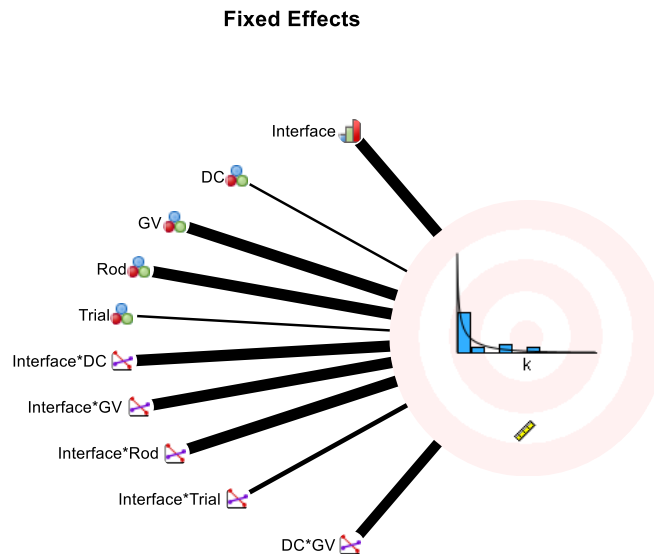


Figure 6.14: Weighted fixed effects for gamma regression on data from raw signals (thicker line represents greater effect)

Overall interface stiffness mean estimates were generated in Table 6.6 and plotted in Figure 6.15. The ascending levels of the nominal interface stiffness fixed effect corresponded with clearly increasing interface stiffness measurement estimates. Additionally, these estimates fell magnitudes apart on the N/m scale.

Table 6.6: Interface stiffness estimates for gamma regression on data from raw signals

Estimates

| Interface Stiffness | Mean | Std. Error | 95% Confidence Interval | |
|---------------------|------------|------------|-------------------------|------------|
| | | | Lower | Upper |
| Silicone | 3.0750E+06 | 1.9508E+05 | 2.7126E+06 | 3.4858E+06 |
| Paraffin Wax | 6.7813E+08 | 4.3021E+07 | 5.9821E+08 | 7.6873E+08 |
| Superglue | 1.0752E+09 | 6.8209E+07 | 9.4845E+08 | 1.2188E+09 |

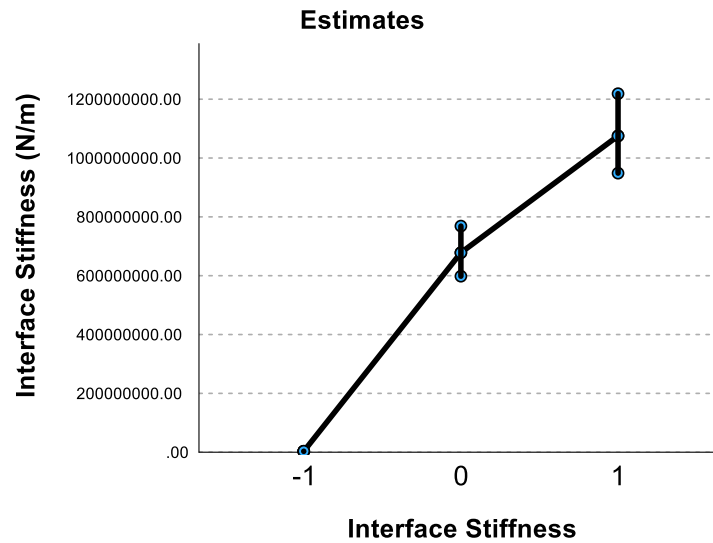


Figure 6.15: Interface stiffness estimates for gamma regression on data from raw signals

For interface stiffness estimates by impact rod fixed effect levels (Figure 6.16), higher impact rod mass corresponded to generally lower interface stiffness estimates. This made sense considering heavier rods amplified contributions from lower frequency modes. Between the handpieces, the 30 g impactor generally resulted in lower interface stiffness estimates. This held some bearing on impact rod selection, as clinical evaluation should err on the side of caution when attempting to make conclusions about the state of post-operative healing. I.e., it would be safer to conclude a lower interface stiffness with all ramifications, than a higher interface stiffness. Although, overall accuracy would likely outweigh this consideration in the final decision-making process.

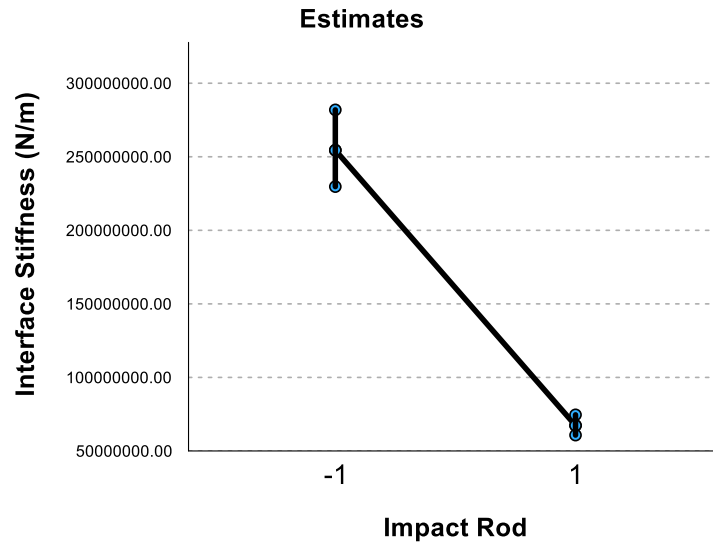


Figure 6.16: Interface stiffness by impact rod for gamma regression on data from raw signals

Looking at the interaction between impact rod and interface stiffness (Figure 6.17), the 10 *g* impactor generally showed greater measurement resolution across a range of interface stiffnesses. Unsurprisingly, the 30 *g* impactor showed similar estimates for intermediate and high interface conditions, and the 10 *g* impactor overestimated wax interface stiffness with reference to the 30 *g* measurements. From the accuracy results, it was known that the 30 *g* impactor performed marginally better in this situation.

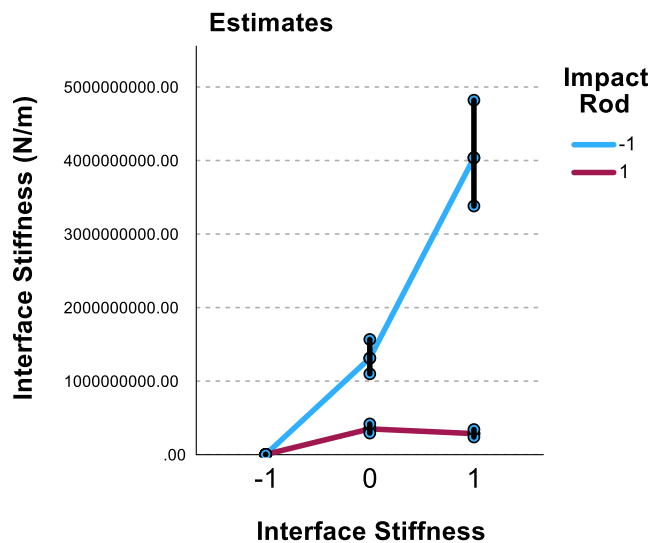


Figure 6.17: Interface stiffness and impact rod interaction estimates for gamma regression on data from raw signals

All results considered, without any treatment of signals, the combined measurement approaches showed good sensitivity to interface stiffness across a range of implant configurations and for multiple operators. However, the 10 g impactor showed greater resolution across the range of interface stiffnesses and generally more promise in producing accurate results.

6.4.2.2 Binary Probit Regression – Raw Signals

The first binary probit regression showed an overall high classification correctness (Table 6.7), indicating a good fit between the model and data.

Table 6.7: Classification for binary probit regression on data from raw signals

| Classification | | | |
|----------------|-------------------|-----------|-----------|
| Overall | Percent | Correct | = 95.4% |
| a | | | |
| | | Predicted | |
| Observed | | | |
| | | Correct | Incorrect |
| Correct | Count | 142 | 8 |
| | % within Observed | 94.7% | 5.3% |
| Incorrect | Count | 2 | 64 |
| | % within Observed | 3.0% | 97.0% |

a. Target: Match Correctness

The corrected model fixed effect was also significant ($p - value < 0.001$). Interface stiffness had a significant effect on match correctness, but the rest of the main effects did not. Interface stiffness by impact rod was the only significant interaction. Additionally, trial was not a significant fixed effect and had no significant interactions, so was dropped from analysis. All p-values can be viewed in Table 6.8.

Table 6.8: Fixed effects for binary probit regression on data from raw signals

Fixed Effects^a

| Source | F | df1 | df2 | Sig. |
|---------------------------|----------------------------|-----|--------------------|-------|
| Corrected Model | 3.713 | 23 | 192 | <.001 |
| Interface | 4.705 | 2 | 192 | .010 |
| DC | .694 | 1 | 192 | .406 |
| GV | 1.129 | 1 | 192 | .289 |
| Rod | .311 | 1 | 192 | .578 |
| Interface * DC | .196 | 2 | 192 | .822 |
| Interface * GV | 2.080 | 2 | 192 | .128 |
| Interface * Rod | 9.143 | 2 | 192 | <.001 |
| DC * GV | .951 | 1 | 192 | .331 |
| DC * Rod | .221 | 1 | 192 | .639 |
| GV * Rod | .058 | 1 | 192 | .810 |
| Interface * DC * GV | .458 | 2 | 192 | .633 |
| Interface * DC * Rod | 1.005 | 2 | 192 | .368 |
| Interface * GV * Rod | .041 | 2 | 192 | .959 |
| DC * GV * Rod | .108 | 1 | 192 | .743 |
| Interface * DC * GV * Rod | .495 | 2 | 192 | .611 |
| Probability Link a | distribution: function: | | Binomial Probit | |

a. Target: Match Correctness

Weighted fixed effects can be viewed in Figure 6.18. It can be seen that the interface and impact rod interaction had greater weight than interface stiffness alone. All other effects were insignificant. Given this information, it would be possible to deduce which impactor was more accurate across the various interface stiffness scenarios.

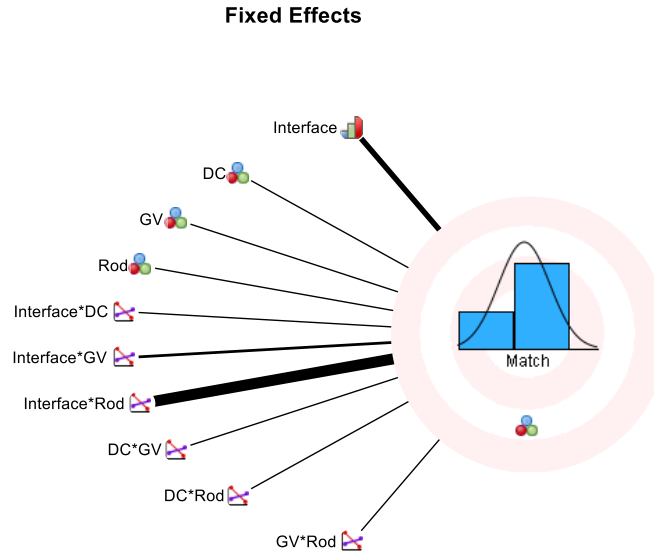


Figure 6.18: Weighted fixed effects for binary probit regression on data from raw signals (thicker line represents greater effect)

The grand mean for match correctness was promisingly high at 92.7%, with the standard error and confidence interval given in Table 6.9.

Table 6.9: Estimated grand mean for binary probit regression on data from raw signals

Estimated Means: Grand Mean Estimates^a

| 95% Confidence Interval | | | |
|-------------------------|------------|-------|-------|
| Mean | Std. Error | Lower | Upper |
| .927 | .060 | .725 | .990 |

a. Target: Match Correctness

Addressing match correctness estimates for each interface (.

Table 6.10 and Figure 6.19), it was observed that the wax interface experienced the worst classification rate at just 51.7% match correctness. Silicone experienced perfect matching, while superglue had decent matching at 82.4% correct. Considering under performance in the paraffin wax case, implementing a notch filter protocol for a subset of the wax interface signals was deemed the most efficient proof of concept intervention that would provide evidence for enhancement of the worst outcome, while minimizing the amount of digital intervention and bias that would be introduced to analysis.

Table 6.10: Estimated interface means for binary probit regression on data from raw signals

Estimates

| Interface Stiffness | Mean | Std. Error | 95% Confidence Interval | |
|---------------------|-------|------------|-------------------------|-------|
| | | | Lower | Upper |
| Silicone | 1.000 | .001 | .958 | 1.000 |
| Paraffin Wax | .517 | .292 | .080 | .931 |
| Superglue | .824 | .173 | .348 | .988 |

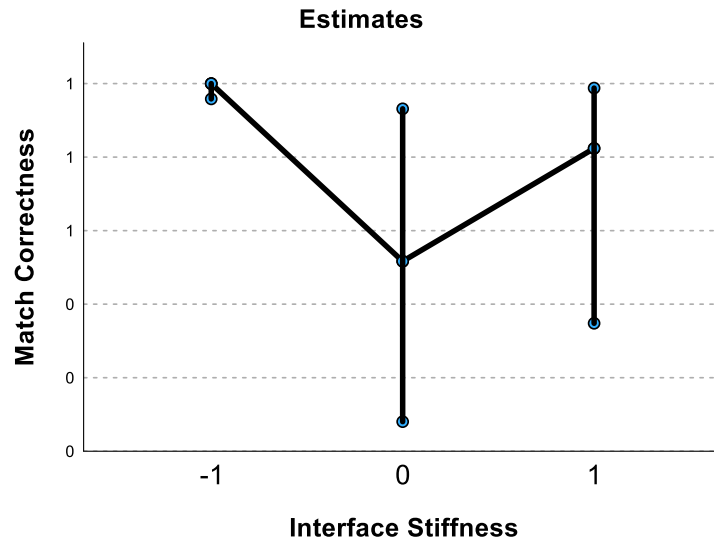


Figure 6.19: Match correctness estimates for binary probit regression on data from raw signals

Additionally, looking at match correctness estimates by impact rod plot (Figure 6.20), the 10 *g* impactor performed better overall on raw signals. This provided further evidence for attempting an intervention to provide proof-of-concept improvement to the impactor with the most promise.

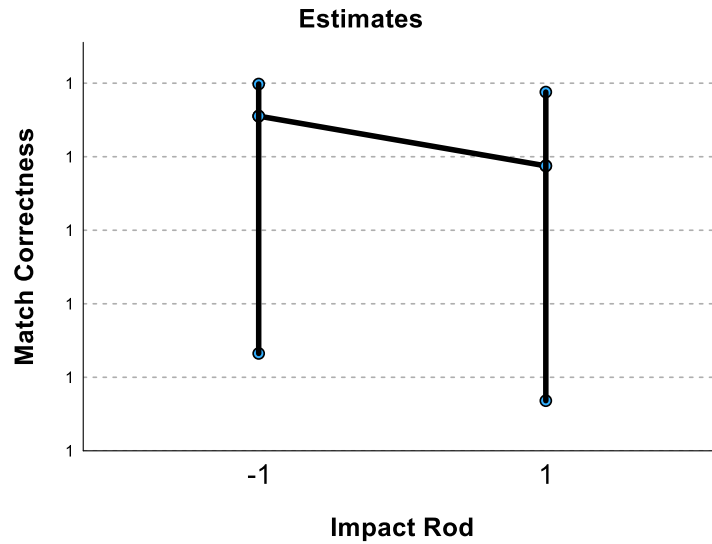


Figure 6.20: Match correctness by impact rod for binary probit regression on data from raw signals

Finally, from the interface stiffness and impact rod interaction plot (Figure 6.21), the 10 *g* impactor performed well in the extremes but lost considerable classification strength for the paraffin wax interface, lending further credence to noise treatment in this region. The 30 *g* impactor showed equal performance for the low interface, much better performance in the intermediate, and poor performance for the high interface compared to the 10 *g* impactor.

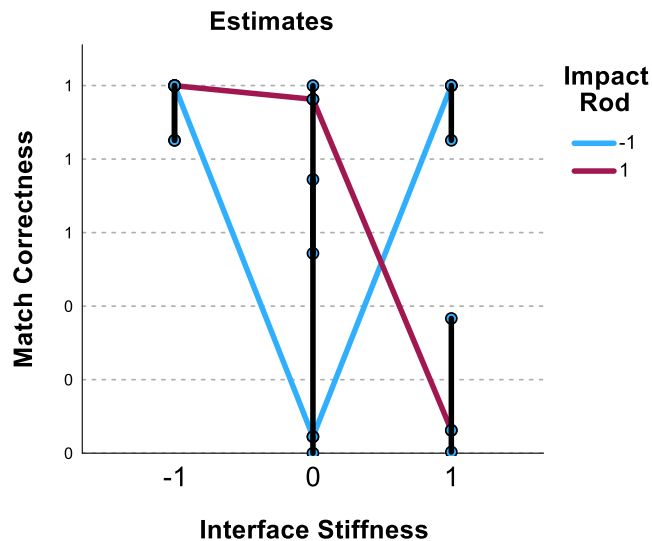


Figure 6.21: Interface stiffness and impact rod interaction estimates for binary probit regression on data from raw signals

6.4.2.3 Gamma Regression – Notch Filter

Upon implementation of the notch filter protocol, the gamma regression model fit improved. The predicted by observed plot (Figure 6.22) displayed a greater linear relationship between the variables.

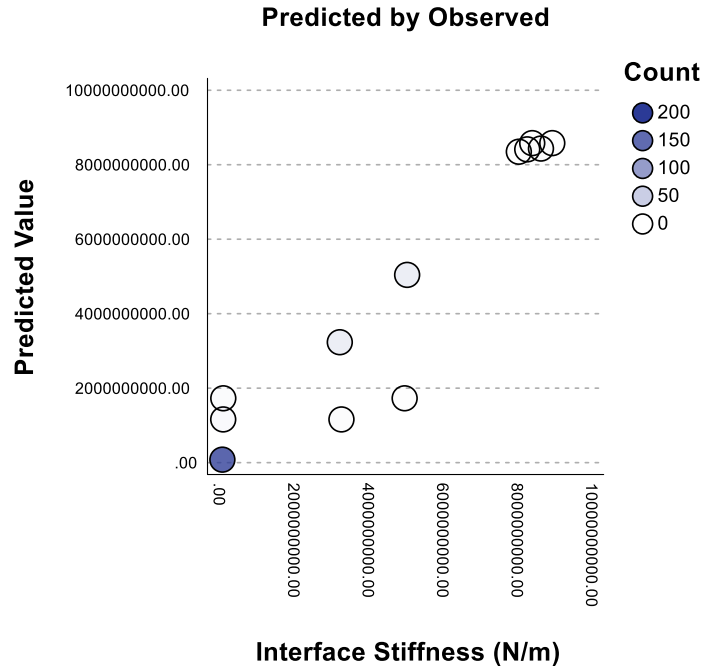


Figure 6.22: Predicted by observed plot for gamma regression on data from notch filter signals

The corrected model fixed effect was still significant ($p - value < 0.001$) along with interface and impact rod. GV connector flipped to insignificant, joining dual cone adapter and trial among the insignificant main effects. However, the number of significant interaction terms increased from 14 to 17. This was not necessarily a negative result, as it indicated that there was increased specificity to the cases that were underperforming. A gained insignificant main effect (outside of interface stiffness) may be viewed favourably, even considering an increase in significant interactions. All fixed effects can be viewed in Table 6.11.

Table 6.11: Fixed effects for gamma regression on data from notch filter signals

Fixed Effects^a

| Source | F | df1 | df2 | Sig. |
|-------------------------|----------|-----|-----|-------|
| Corrected Model | 129.703 | 71 | 144 | <.001 |
| Interface | 3729.523 | 2 | 144 | <.001 |
| DC | 3.244 | 1 | 144 | .074 |
| GV | 1.341 | 1 | 144 | .249 |
| Rod | 455.819 | 1 | 144 | <.001 |
| Trial | 1.327 | 2 | 144 | .269 |
| Interface * DC | 71.633 | 2 | 144 | <.001 |
| Interface * GV | 42.692 | 2 | 144 | <.001 |
| Interface * Rod | 174.374 | 2 | 144 | <.001 |
| Interface * Trial | 1.724 | 4 | 144 | .148 |
| DC * GV | 37.841 | 1 | 144 | <.001 |
| DC * Rod | 100.185 | 1 | 144 | <.001 |
| DC * Trial | 4.251 | 2 | 144 | .016 |
| GV * Rod | 59.591 | 1 | 144 | <.001 |
| GV * Trial | 9.943 | 2 | 144 | <.001 |
| Rod * Trial | 1.588 | 2 | 144 | .208 |
| Interface * DC * GV | 33.264 | 2 | 144 | <.001 |
| Interface * DC * Rod | 26.546 | 2 | 144 | <.001 |
| Interface * DC * Trial | 4.567 | 4 | 144 | .002 |
| Interface * GV * Rod | 26.317 | 2 | 144 | <.001 |
| Interface * GV * Trial | 11.252 | 4 | 144 | <.001 |
| Interface * Rod * Trial | 1.588 | 4 | 144 | .181 |
| DC * GV * Rod | 64.126 | 1 | 144 | <.001 |
| DC * GV * Trial | 2.056 | 2 | 144 | .132 |
| DC * Rod * Trial | 4.040 | 2 | 144 | .020 |
| GV * Rod * Trial | 11.117 | 2 | 144 | <.001 |

| | | | | |
|-----------------------------------|-------|----------------------------|-----|--------------|
| Interface * DC * GV * Rod * Trial | 6.646 | 20 | 144 | <.001 |
| Probability Link a | | distribution: function: | | Gamma Log |

a. Target: Interface Stiffness (N/m)

Weighted fixed effects can be viewed in Figure 6.23. Although both were insignificant main effects, it is worth noting that dual cone adapter length held greater weight than presence of the GV connector.

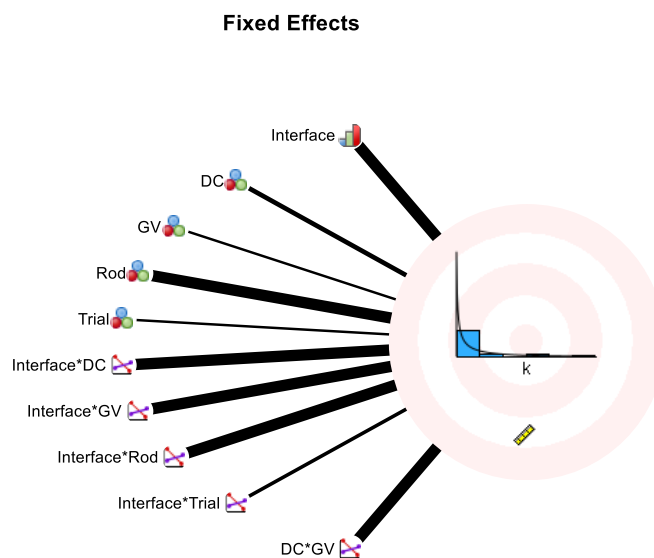


Figure 6.23: Weighted fixed effects for gamma regression on data from notch filter signals (thicker line represents greater effect)

The treated interface stiffness estimates can be viewed in Table 6.12. The only difference between notch filter signals and raw signals was a notable drop in the paraffin wax interface stiffness estimate. The curvature in the interface stiffness estimates by interface level plot (Figure 6.24) was also inverted, more accurately representing assumptions about the scale and distribution of interface stiffness estimates across the range of actual interface stiffness levels. That is, across the range of interface stiffness levels, estimates should be exponentially distributed with increasing variance.

Table 6.12: Interface stiffness estimates for gamma regression on data from notch filter signals

Estimates

| Interface Stiffness | Mean | Std. Error | 95% Confidence Interval | |
|---------------------|----------------|--------------|-------------------------|----------------|
| | | | Lower | Upper |
| Silicone | 3074974.042 | 154035.081 | 2785099.567 | 3395018.790 |
| Paraffin Wax | 266157954.451 | 13332685.588 | 241067532.064 | 293859799.827 |
| Superglue | 1075157714.659 | 53858017.493 | 973803760.206 | 1187060636.473 |

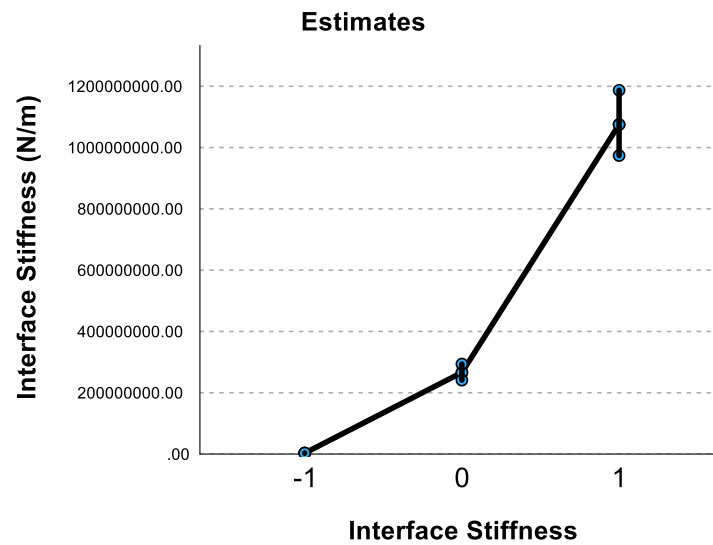


Figure 6.24: Interface stiffness estimates for gamma regression on data from notch filter signals

From the interface stiffness by impact rod plot (Figure 6.25), it was still the case that the 10 *g* impactor, whether the matches were correct or incorrect, estimated higher interface stiffnesses than the 30 *g* impactor. This discrepancy was reduced because of lower estimates for wax interface cases, particularly for the 10 *g* impactor.

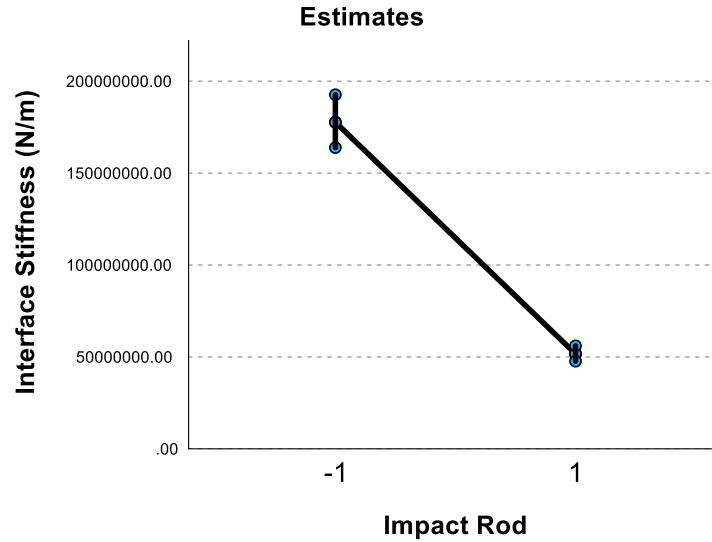


Figure 6.25: Interface stiffness by impact rod for gamma regression on data from notch filter signals

Finally, it can be seen in Figure 6.26 that the 10 *g* impactor had much larger sensitivity to changes in interface stiffness levels than the 30 *g* impactor. The 10 *g* impactor also maintained the expected exponential distribution of measurement values.

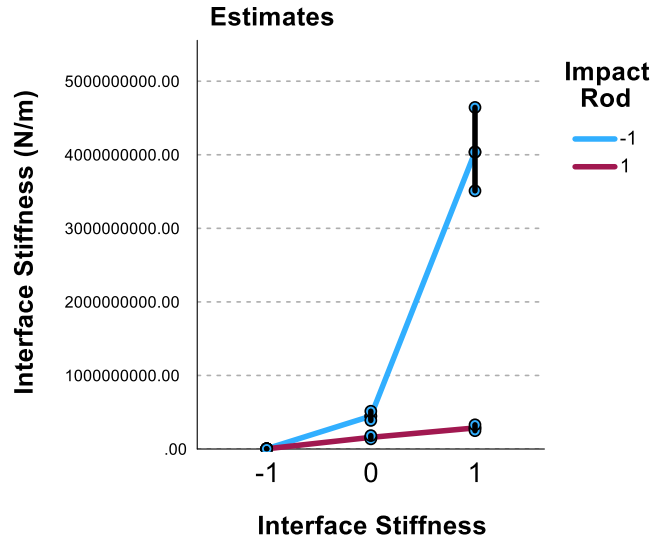


Figure 6.26: Interface stiffness and impact rod interaction estimates for gamma regression on data from notch filter signals

6.4.2.4 Binary Probit Regression – Notch Filter

The binary probit regression model improved its classification rate from 95.4% to 97.7% with application of the notch filter protocol. A classification summary can be viewed in Table 6.13.

Table 6.13: Classification for binary probit regression on data from notch filter signals

Classification
Overall Percent Correct = 97.7%
a

| Observed | | Predicted | |
|-----------|-------------------|-----------|-----------|
| | | Correct | Incorrect |
| Correct | Count | 171 | 5 |
| | % within Observed | 97.2% | 2.8% |
| Incorrect | Count | 0 | 40 |
| | % within Observed | 0.0% | 100.0% |

a. Target: Match Correctness

For the main effects, corrected model and interface stiffness remained significant, while dual cone adapter, GV connector, and impact rod remained insignificant. Furthermore, all interaction effects maintained the same significance status, with interface by impact rod being the only significant interaction. All fixed effects can be viewed in Table 6.14.

Table 6.14: Fixed effects for binary probit regression on data from notch filter signals

Fixed Effects^a

| Source | F | df1 | df2 | Sig. |
|---------------------------|----------------------------|-----|--------------------|-------|
| Corrected Model | 4.510 | 23 | 192 | <.001 |
| Interface | 4.738 | 2 | 192 | .010 |
| DC | 1.356 | 1 | 192 | .246 |
| GV | 1.117 | 1 | 192 | .292 |
| Rod | 2.326 | 1 | 192 | .129 |
| Interface * DC | .423 | 2 | 192 | .656 |
| Interface * GV | .445 | 2 | 192 | .641 |
| Interface * Rod | 9.075 | 2 | 192 | <.001 |
| DC * GV | 1.117 | 1 | 192 | .292 |
| DC * Rod | .191 | 1 | 192 | .663 |
| GV * Rod | .296 | 1 | 192 | .587 |
| Interface * DC * GV | .445 | 2 | 192 | .641 |
| Interface * DC * Rod | 1.101 | 2 | 192 | .335 |
| Interface * GV * Rod | .923 | 2 | 192 | .399 |
| DC * GV * Rod | .296 | 1 | 192 | .587 |
| Interface * DC * GV * Rod | .923 | 2 | 192 | .399 |
| Probability Link a | distribution: function: | | Binomial Probit | |

a. Target: Match Correctness

Weighted fixed effects can be viewed in Figure 6.27. For the main effects, interface had the greatest weight and was the only significant factor; impact rod followed as the strongest insignificant factor. Interface by impact rod was clearly the most significant interaction term.

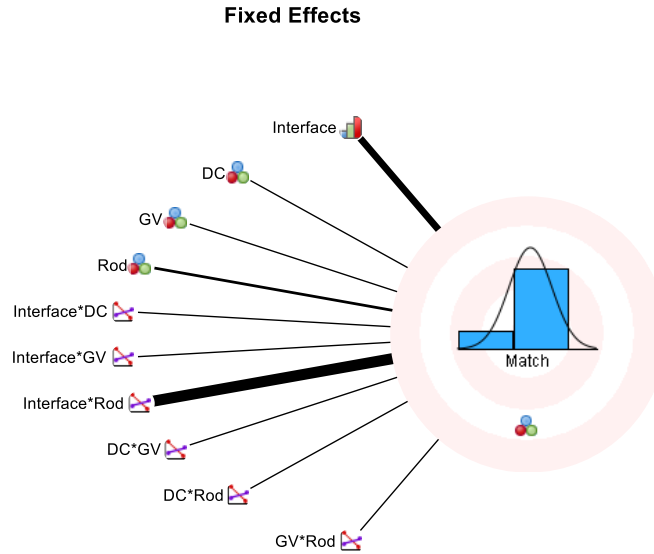


Figure 6.27: Weighted fixed effects for binary probit regression on data from notch filter signals (thicker lines represent greater effects)

The grand estimated mean in Table 6.15 increased from 92.7% to 98.9% match correctness.

Table 6.15: Estimated grand mean for binary probit regression on data from notch filter signals

Estimated Means: Grand Mean Estimates^a

| 95% Confidence Interval | | | |
|-------------------------|------------|-------|-------|
| Mean | Std. Error | Lower | Upper |
| .989 | .010 | .944 | .999 |

a. Target: Match Correctness

The estimates for each interface stiffness level (Table 6.16 and Figure 6.28) remained the same except for paraffin wax (interface that received treatment), which increased from 51.7% to 99.5% match correctness across all implant configurations. Superglue continued to experience misclassification issues for measurements initiated by the 30 *g* impactor.

Table 6.16: Estimated interface means for binary probit regression on data from notch filter signals

Estimates

| Interface Stiffness | Mean | Std. Error | 95% Confidence Interval | |
|---------------------|-------|------------|-------------------------|-------|
| | | | Lower | Upper |
| Silicone | 1.000 | .001 | .982 | 1.000 |
| Paraffin Wax | .995 | .010 | .896 | 1.000 |
| Superglue | .824 | .134 | .463 | .975 |

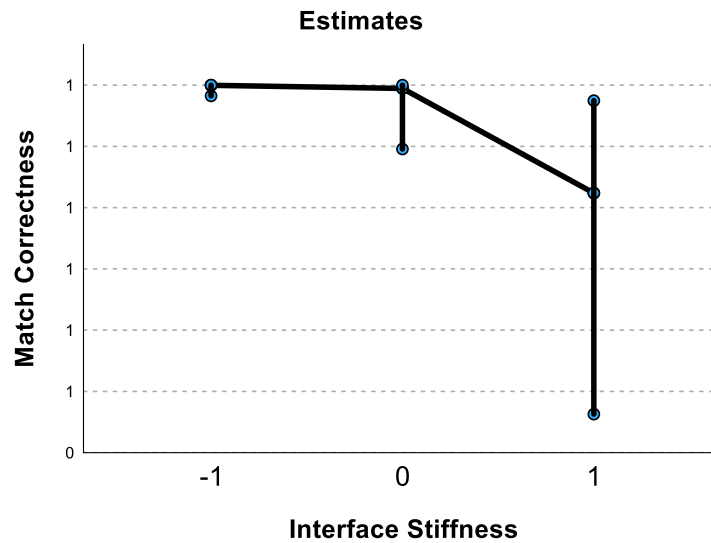


Figure 6.28: Match correctness estimates for binary probit regression on data from notch filter signals

According to Figure 6.29, the 10 *g* impactor continued to be the most accurate of the two tested, with a 95.5% overall classification rate against the 30 *g* impactor's 88.8%.

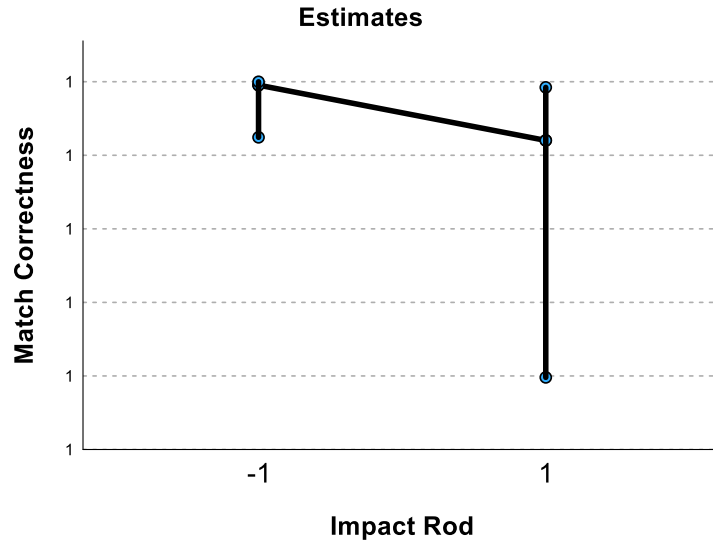


Figure 6.29: Match correctness by impact rod for binary probit regression on data from notch filter signals

Finally, Figure 6.30 shows match correctness estimates for interface stiffness and impact rod interaction. Across a range of interface stiffness levels, the 10 *g* impactor generally maintained a comparable or greater classification strength compared to the 30 *g* impactor. Only for the intermediate interface did the 10 *g* impactor continue to slightly underperform; although, the gap between the impactors was greatly reduced.

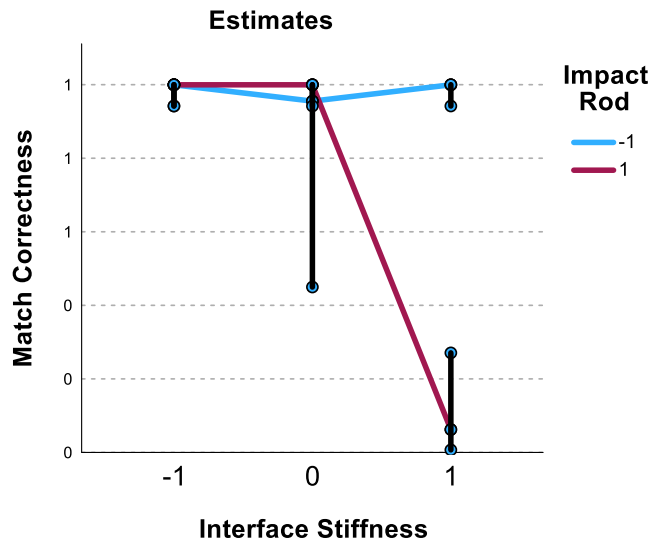


Figure 6.30: Interface stiffness and impact rod interaction estimates for binary probit regression on data from notch filter signals

6.4.2.5 Summary

Figure 6.31 shows a summary of the analysis results across all raw signals acquired in the benchtop validation experiment. The bars represent the average measurement, with error bars indicating one standard deviation. The shaded regions on the plots represented ranges for low interface stiffness (red), intermediate stiffness (yellow), and high stiffness (green). The 10 *g* impactor perfectly classified interface stiffness measurements for the low and high interface stiffness levels (columns) across all implant configurations (rows). The impactor also performed perfectly for the intermediate stiffness level in conjunction with the simplest implant configuration. However, for other implant configurations, the 10 *g* impactor often misclassified the intermediate stiffness level as a high stiffness measurement. The 30 *g* impactor performed perfectly for the silicone interface but had varying levels of accuracy for the other interfaces. It perfectly classified the wax interface under the simplest implant configuration and had mixed success under more complex implant configurations. For the superglue interface, the 30 *g* impactor frequently misclassified the measurements as intermediate stiffness cases. Operator (subject) effects appeared to be relatively negligible, especially if the impactor generally performed consistently under a given combination of factors. Operator also appeared to have a random rather than systematic (fixed) effect under conditions where the measurements were highly variable. In these cases, the measurement systems were primarily battling noise within the bone-implant system to properly classify the interface stiffness level. The 10 *g* rod was relatively immune to noise in extreme interface conditions but struggled with revealing high frequency noise for complexly configured implants in the intermediate stiffness condition. Conversely, the 30 *g* impact rod was immune to noise in the low condition and performed better in the intermediate condition than the 10 *g* rod by attenuating high frequency noise. In the high condition, the 30 *g* impactor was extremely susceptible to intermediate frequency noise, subsequently classifying acquired signals as belonging to an intermediate stiffness condition. Pervasive noise at multiple interface stiffness conditions presented a difficult problem for system optimization. Statistical analysis suggested that the 10 *g* impactor generally held more promise for measurement accuracy than the 30 *g* impactor. Subsequently, the decision was made to implement a simple notch filter to test the effectiveness of implementing a noise mitigation protocol with the least subjective intervention possible.

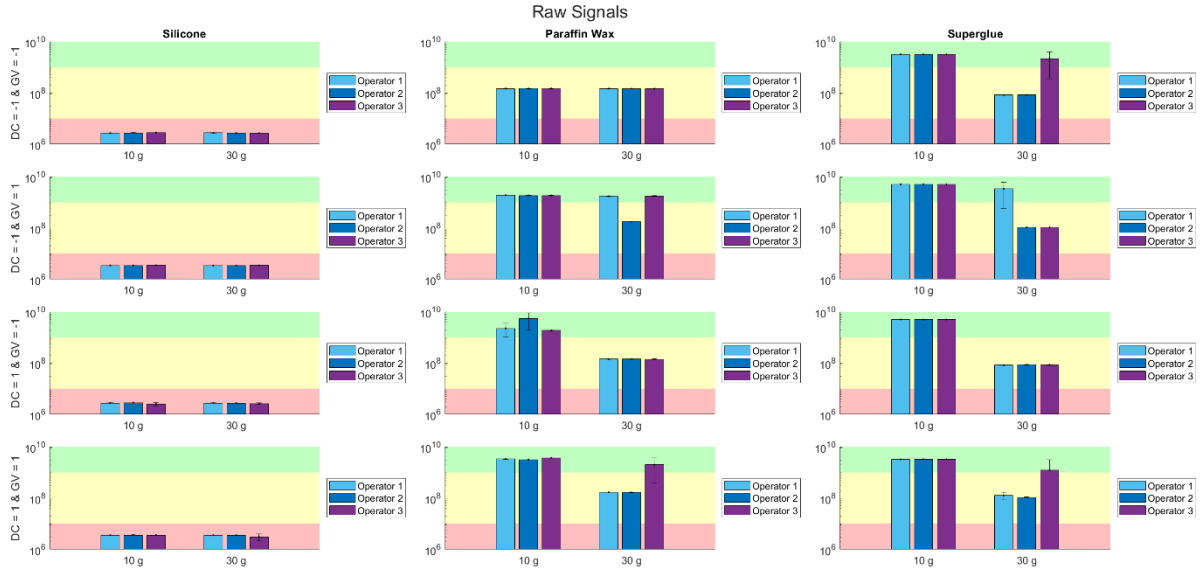


Figure 6.31: Results summary for raw signals

Upon implementing a noise mitigation protocol for the paraffin wax interface signals (condition for which the 10 g impactor underperformed), the 10 g impactor began to perform correctly and consistently across more complex implant configurations. Only for the 88.5 mm dual cone adapter without the GV connector installed did the impactor continued to grossly underperform, even measuring greater interface stiffness values than before the notch filter treatment was implemented. After treatment, the 30 g impactor performed perfectly for the paraffin wax interface.

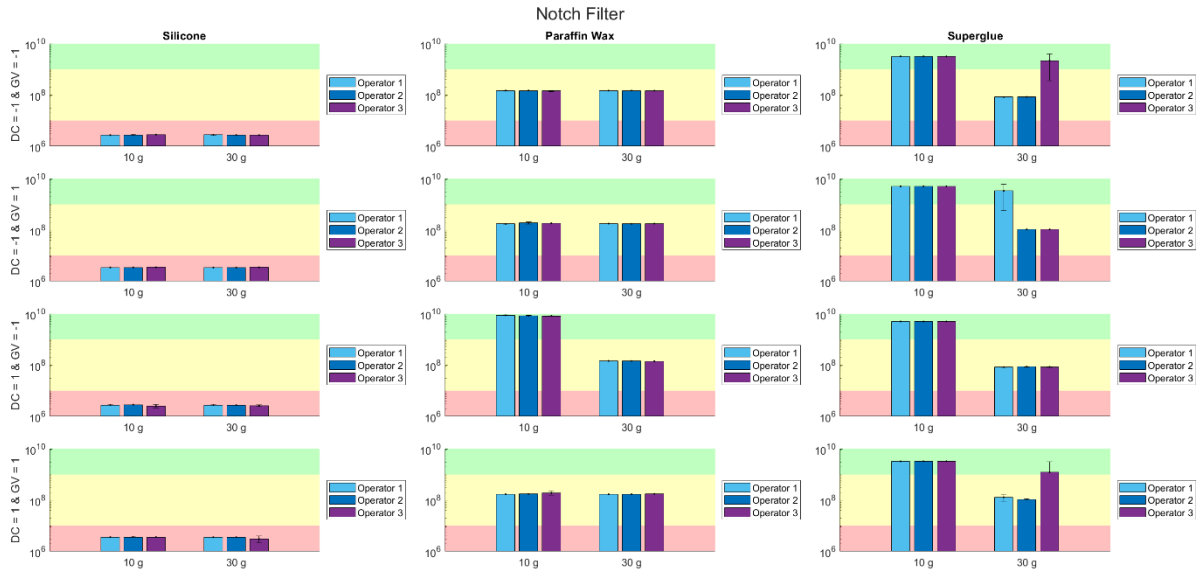


Figure 6.32: Results summary for notch filter signals

For the long dual cone adapter, applying a notch filter to the signals acquired from 10 *g* impactor strikes revealed large high frequency contributions, most likely from the second wax interface mode. However, these contributions greatly outweighed any first mode contributions, causing the measurements to be incorrectly matched. Such a case can be seen in Figure 6.33.

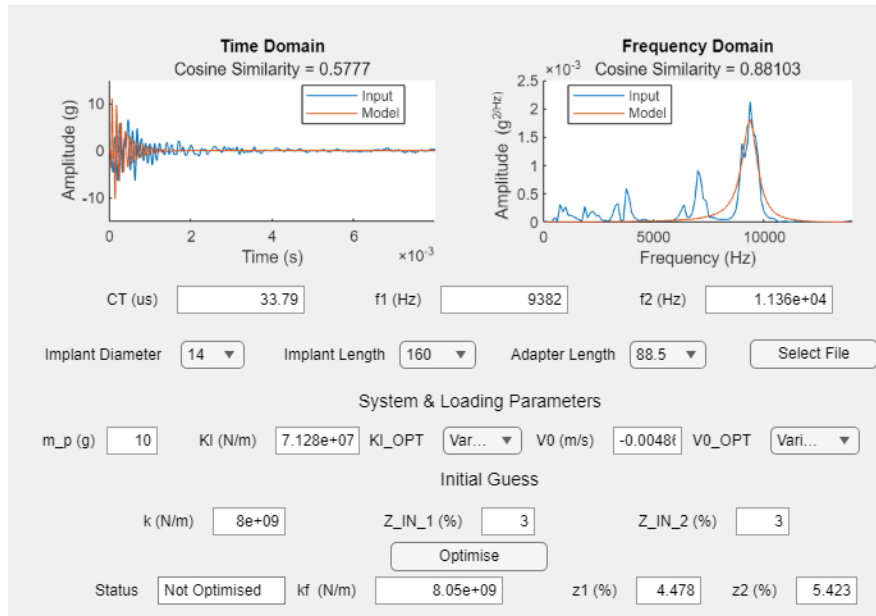


Figure 6.33: Matching window – paraffin wax; 88.5 mm DC; GV off; 10 *g* rod; steel tip; notch filter

Under the simplest implant configuration, the measurement system proved to work perfectly with actuation from the 10 *g* impactor. Under more complex implant configurations, the impactor faced greater classification challenges. In specific cases, the 10 *g* impactor excelled in classification, while in others, the 30 *g* impactor performed better. Non-uniformity in noise distribution throughout the bone-implant systems presented a significant hurdle for perfect classification in all interface conditions and implant configurations. Implementation of a noise attenuation protocol significantly improved the results; however, the success of current implementation was somewhat akin to a self-fulfilling prophecy. The ideal system would be designed to objectively filter noisy contributions. If robust, such a system would also negate the need for a complex matching protocol. Instead, an analyst could potentially trust all frequency contributions in each signal, making the peak selection process during matching much simpler and more objective.

6.4.3 Modal Tests

6.4.3.1 Overview

A series of tests were conducted to look at sources of noise within two bone-implant systems and potential strategies for mitigation or attenuation of the sources. First, a crude impact hammer was created by mounting an impact load cell (ICP® Force Sensor Model 208C02, PCB Piezotronics Inc, USA) to a custom 3D-printed handle. The hammer was used in a variety of ways to strike the bone-implant systems, and acceleration responses were recorded. Due to hardware limitations, impact force and acceleration signals were recorded simultaneously but not synchronously. That is, both the input and output signals of the impact event were recorded, but the data acquisition clocks could not be synchronized. This meant that formal modal analysis could not be executed; however, output signals were normalized with respect to their input counterparts. In a second set of tests, a strategy revolving around exploiting shape and phase characteristics of the modes of interest was implemented to screen out noise through analog intervention. In this approach, two accelerometers were introduced to the bone-implant systems, and their acceleration signals were recorded synchronously for system responses elicited by the impactors under scrutiny.

6.4.3.2 Impact Hammer

A simple impact hammer was created by mounting an impact load cell to a 3D-printed handle. The hammer was used to strike bone-implant interface setups in various ways to test for sources of noise within the system. A picture of the impact hammer can be viewed in Figure 6.34.



Figure 6.34: Impact hammer used in modal tests

An alternative boundary condition was tested in a variety of configurations, considering possible noise leakage caused by or conducted through the bone clamp used in all previous tests and experiments. The setup consisted of a Sawbones thigh with an embedded bone-implant system (previously described). The thigh was modified by cutting the distal end to envelope the implant stem head and rest nearly flush with the start of the dual cone adapter. Any bone-implant system was securely embedded by first wrapping the composite bone with silicone liners (like the damping liner used in previous tests and experiments). The liners were wrapped in such a way to fill any gaps in the system (e.g., the exposed bonding region between cut end of femur and implant stem head) and create a uniform interface between the bone, implant, and thigh. The thigh modification and liners were implemented to simulate stoma formation and soft tissue damping seen in the clinic. Additionally, clinical bandages were added (potential source of damping), and the whole system was gently constricted with two large diameter hose clamps. Finally, the system was ratcheted down to a sturdy table surface. A photo of the setup can be viewed in Figure 6.35.

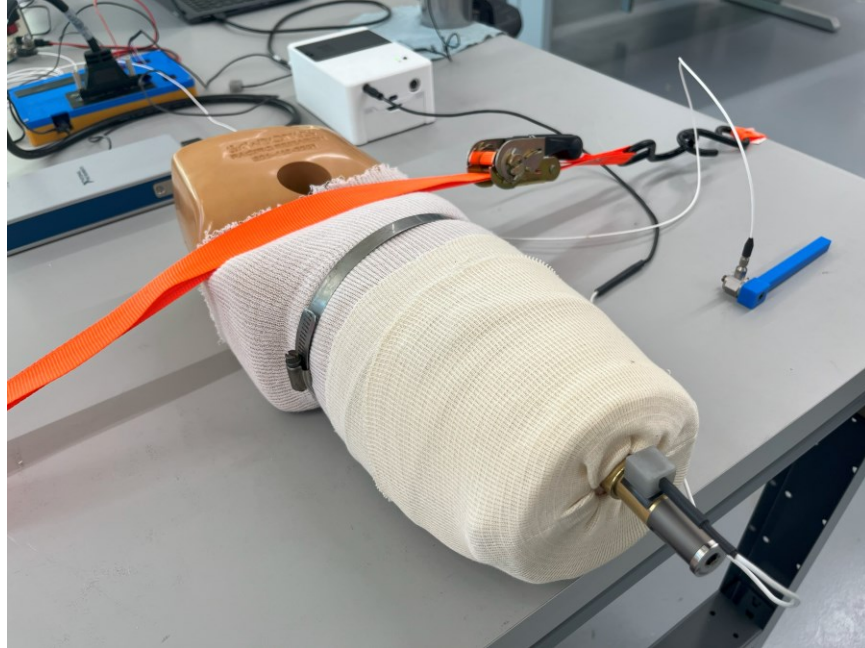


Figure 6.35: Sawbones thigh setup

The first test was conducted to see if the $\sim 3000\text{ Hz}$ noise frequently revealed in the superglue setup by the 30 g impactor could be traced to any source. Various positions were tested to see if the normalized contribution from the frequency bin was exceptionally strong for a specific location. The positions tested are described in Table 6.17.

Table 6.17: Position test legend

| Position | Description |
|----------|--|
| 1 | Dual cone adapter |
| 2 | Implant stem |
| 3 | Mid-femur |
| 4 | Proximal femur |
| 5 | Distal-lateral clamp |
| 6 | Proximal-lateral clamp |
| 7 | Distal-medial clamp |
| 8 | Proximal-medial clamp |
| Thigh | Dual cone adapter (Sawbones thigh setup) |

Two bone-implant systems (silicone; superglue), identical to the systems tested in the main procedure of the validation experiment, were struck five times at the distal screw in the 3:00 position and axial direction. Accelerometer and impact load cell signals were recorded simultaneously. For analysis, both signals were treated with a 4th order lowpass Butterworth filter with cut off frequency of 24 *kHz* for the accelerometer and 36 *kHz* for the impact load cell. The signals were then transformed into the frequency domain using a periodogram function. Plots for the signals collected at Position 4 can be viewed in Figure 6.36.

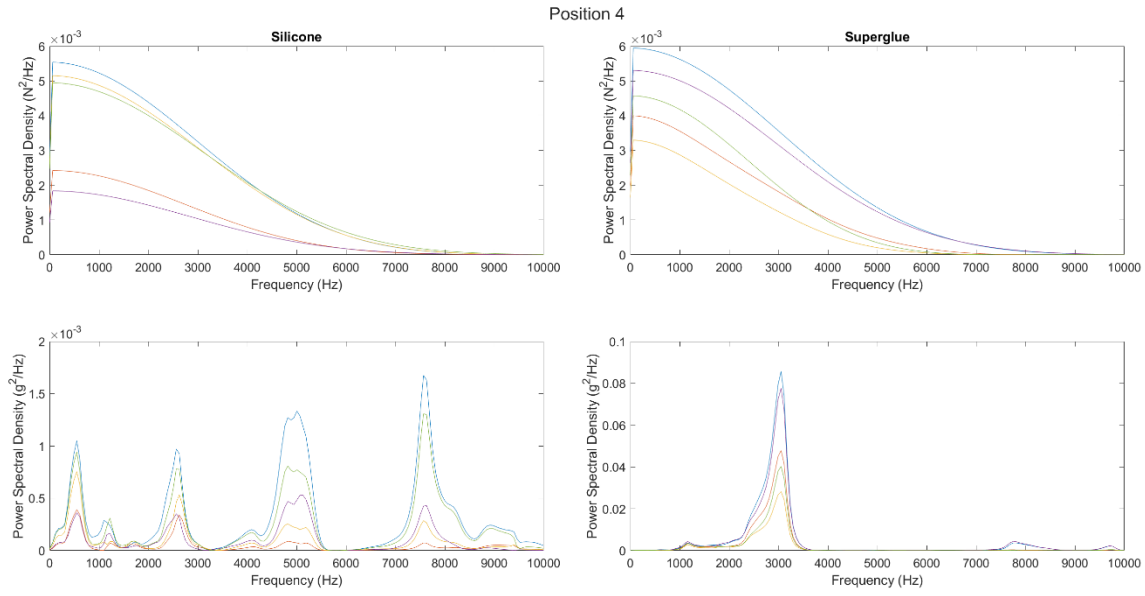


Figure 6.36: Position 4 modal measurements

Acceleration power spectral density curves were then normalized by the maximum value of their associated impact force power spectral density curve. For each position, the ensemble average of the normalized curves was taken. The curves were plotted together in Figure 6.37, including eight positions in various locations on the implant, composite bone, and bone clamp and one position on the Sawbones thigh setup. It should be noted that the mass of the impact rod was approximately 40 g. As evidenced in previous tests, this level of mass shifted signal contributions significantly to the intermediate and, to lesser extent, low frequency domains. In Figure 6.37, the impact hammer strikes elicited responses that were roughly akin to those of a 30 g or heavier impact rod. For the superglue setup, nontrivial noise was excited around 3000 Hz; for the silicone setup, some contribution of the first axial mode of the system could be seen. Interestingly, for the superglue setup, the peak with the highest force normalized power spectral density belonged to the average of measurements taken at Position 4. In this position, the accelerometer was placed in the axial direction on a proximal portion of the bone. The peak belonged to a frequency at 3051.76 Hz and had a similar height to peaks with roughly similar frequencies belonging to Positions 1 and 2 (dual cone and implant stem respectively). For Position 3 (accelerometer placed mid-bone within the bone clamp grips), the ~3000 Hz peak contribution was significantly less than the highest three curves. The normalized measurement represented the sensitivity of modes or frequencies to a force input. It was difficult to tell which direction sources of vibration within the system were propagated

from, but it is possible that axial modes from the composite bone itself leaked into measurements taken at the dual cone adapter. In light of the high sensitivity of the ~ 3000 Hz peak at the proximal femur and low sensitivity mid-femur, where the bone was tightly gripped, it could be possible that this set of conditions was at least semi-optimal for bone vibration. Additionally, the peak was still prominent for the Sawbones thigh boundary condition, suggesting that this mode likely belonged to a source internal to the bone-implant system. For the Sawbones thigh setup, the peak also appeared damped, lending some validation to the idea that the frequency leaked from a bone source, as movement of the bone would intuitively be highly susceptible to the imposed boundary condition. Within finite element models, the composite femur was modelled as fully fixed, preventing simulation of any bone vibrational mode. For the silicone setup, there appeared to be some mid-range noise between 2000 – 3000 Hz. It would not be unreasonable to conjecture that this noise could be from the same source (i.e., a bone vibrational mode). However, the low interface condition generally appeared to be less susceptible to noise in the mid-range.

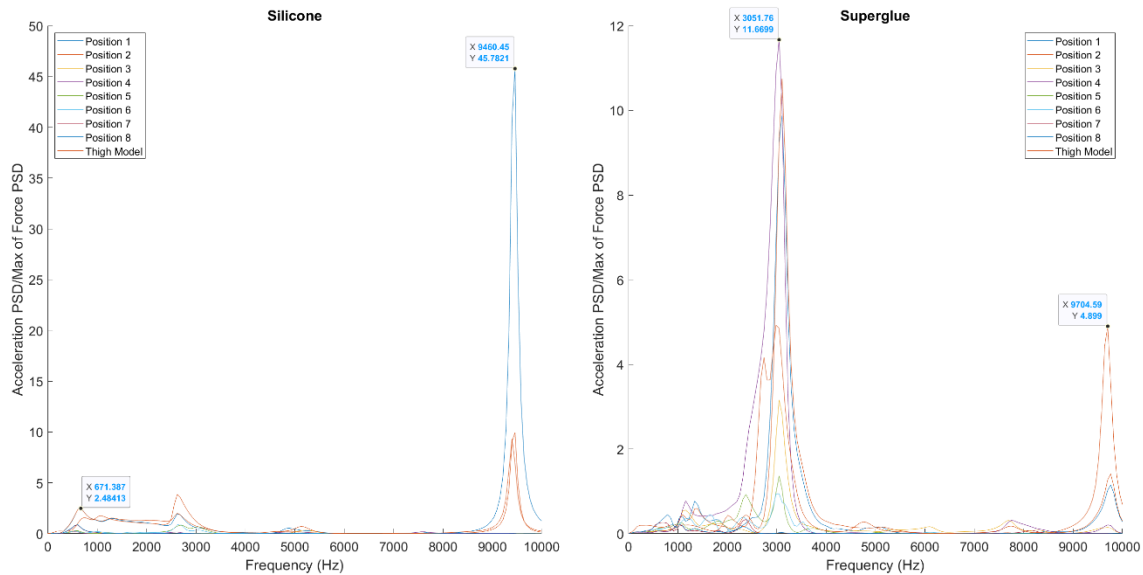


Figure 6.37: Signals from accelerometer placed in various positions on implant and composite femur

In the main procedure of the validation study and for the intermediate interface condition, high-range noise was an extreme detriment to classification accuracy and frequently skewed outcomes to high interface condition conclusions. Noise was often seen around 7500 Hz depending on the implant configuration and could be greatly amplified by the presence of the GV connector. For this noisy source, it was conjectured that it was likely different from the noise at 3000 Hz and possibly

attributed to transverse or out-of-plane motion of the implant. It was observed in the superglue interface impact simulation that leakage from transverse or mixed modes was certainly possible, especially in the high range. A series of tests were conducted to gather evidence for noise leakage from a transverse source. A variety of accelerometer and strike orientations were tested as given by Table 6.18.

Table 6.18: Transverse noise test legend

| Code | Description |
|-------------|---|
| AA-AS | Axial accelerometer; axial strike |
| AA-TS | Axial accelerometer; transverse strike |
| TA-AS | Transverse accelerometer; axial strike |
| TA-TS | Transverse accelerometer; transverse strike |

For implant configurations without the GV connector installed, relatively little noise appeared in the high range for axial accelerometer signals elicited by an axial strike. For the other configurations, noise was seen in varying degrees around 7500 *Hz*. When the accelerometer was oriented transversely and the implant was struck axially, the largest contributions of this noise were observed. This would suggest that axial strikes were capable, even effective, at exciting transverse or out-of-plane modes, or at least some out-of-plane noise. Transverse frequencies found in the silicone and superglue setups closely matched obscuring frequencies in the wax interface condition of the validation experiment. This lent some credence to the noise-filtering approach and warranted further investigation into the noise sources. The results can be viewed in Figure 6.38.

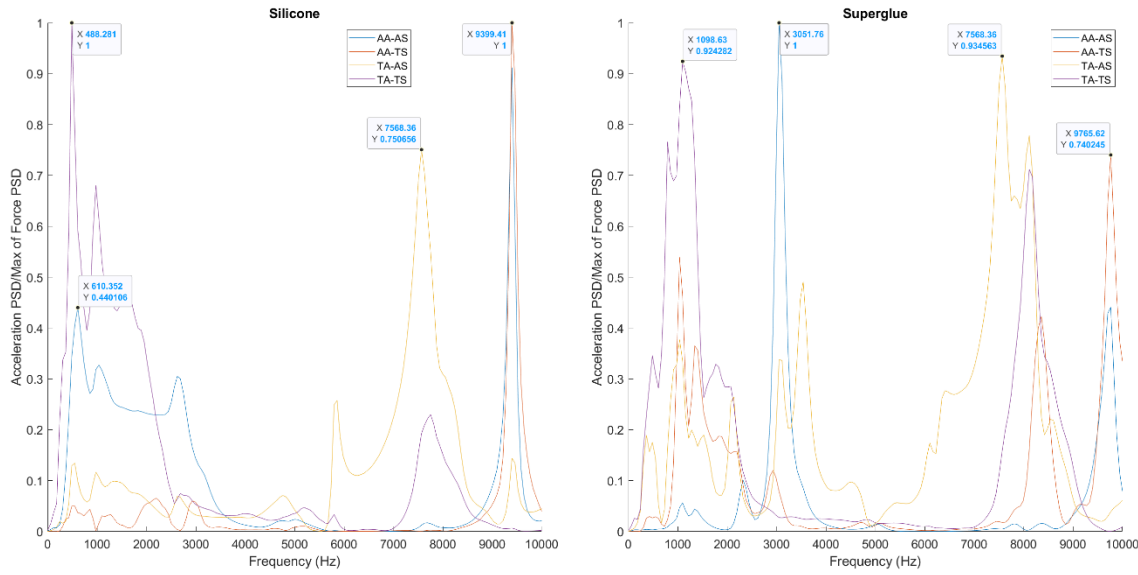


Figure 6.38: Signals acquired to test presence of transverse noise without GV connector installed

The next step was to test how transverse noise would change in response to the installation of the GV connector, especially considering the amplifying effect it had in the main procedure of the validation experiment. The GV connector was installed on both setups, and acceleration responses to impact hammer strikes were recorded at various locations. Codes for the presently described test can be viewed in Table 6.19.

Table 6.19: Transverse GV connector noise test legend

| Code | Description |
|-------|---|
| DC-AA | GV connector installed; DC location; axial accelerometer; axial strike |
| DC-TA | GV connector installed; DC location; transverse accelerometer; axial strike |
| GV-AA | GV connector installed; GV location; axial accelerometer; axial strike |
| GV-TA | GV connector installed; GV location; transverse accelerometer; axial strike |

With the GV connector installed on the superglue setup and for both axial locations, high-contributing frequencies (relative to the first mode) between 7000 – 8000 *Hz* could be seen (Figure 6.39). This same noise was not apparent in the silicone setup. For both setups and both

transverse locations, high-contributing noise was seen in the same band. The transverse measurements also contained frequency information that closely matched the second mode in the silicone case and first mode in the superglue case. Given the crossover in signal composition between axial and transverse measurements, it was not unreasonable to think that transverse modes or noise could leak into axially recorded signals. This phenomenon was previously explored in Section 4.3.10.2 with transverse contamination observed in the superglue interface impact finite element model. In the present test, transverse noise was seen in the same band for both silicone and superglue interface setups. This noise appeared to be completely transverse for silicone, as corresponding axial frequencies were not observed. It is possible that this noise leaked through in the superglue case, as matching frequencies were observed; however, it is currently difficult to conclude how modes crossover between measurements taken in different orientations. In any case, it is reasonable to conclude that stiffer interfaces may be more susceptible to this issue.

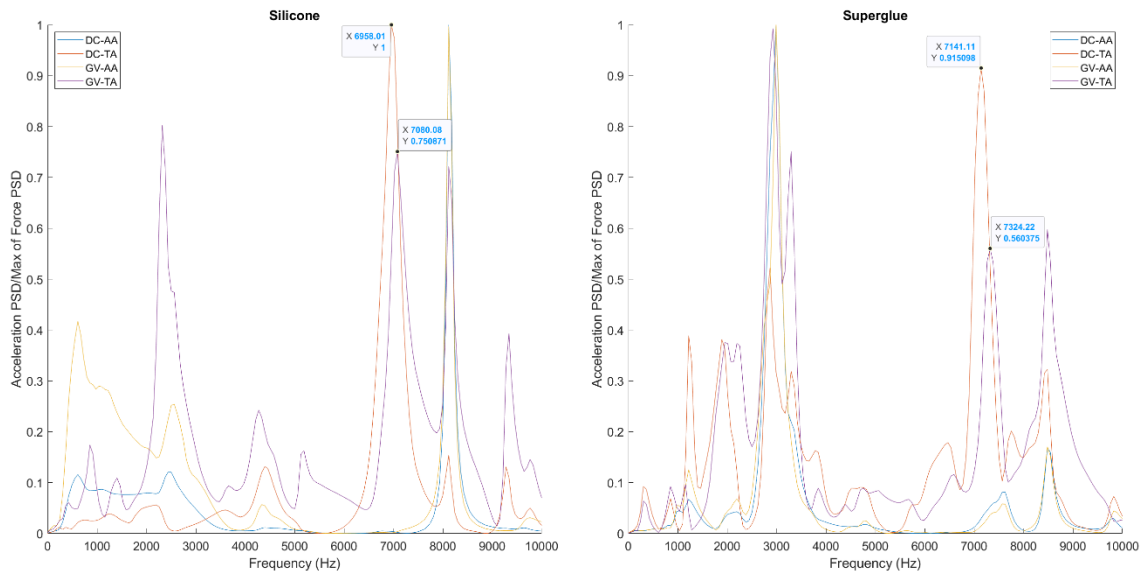


Figure 6.39: Signals acquired to test presence of transverse noise with GV connector installed – bone clamp setup

The same measurements were taken with the Sawbones thigh setup instead of the bone clamp to see if the noise could be at all attributed to boundary condition. The results can be viewed in Figure 6.40. It was immediately apparent that the same transverse noise existed; however, greater damping (width of the peaks) appeared in the system. This indicated that the boundary condition had some effect, particularly when it came to introducing greater damping to the system, but did not altogether stop transverse or other sources of noise.

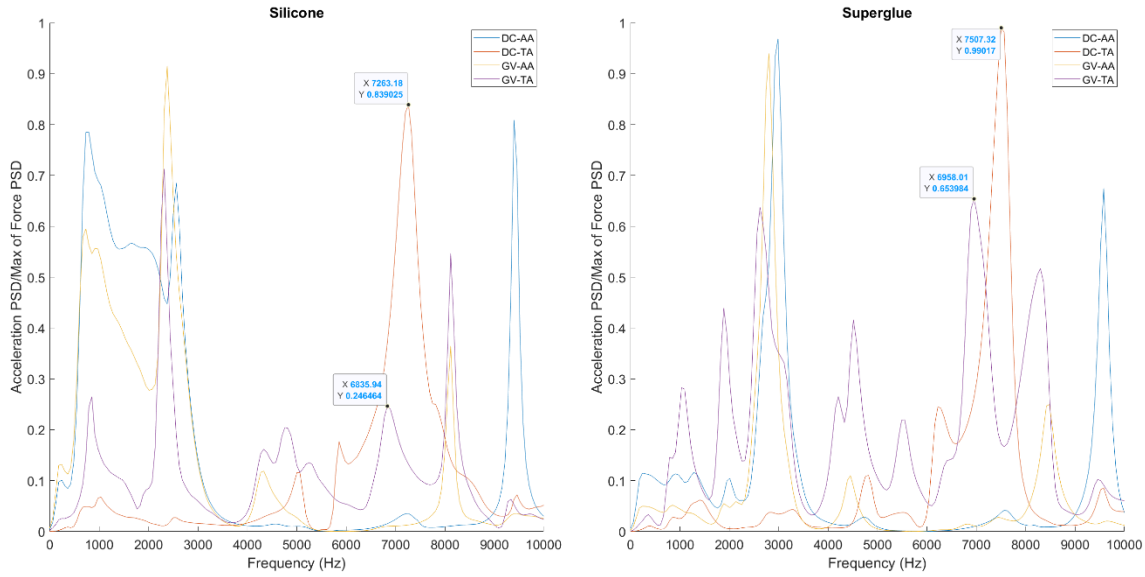


Figure 6.40: Signals acquired to test presence of transverse noise with GV connector installed – Sawbones thigh setup

Finally, to perform a general assessment of the noise presented by the boundary condition and GV connector, axial measurements with codes given in Table 6.19 were plotted together.

Table 6.20: Summary plot legend

| Code | Description |
|----------|--|
| DC-clamp | DC only; bone clamp boundary condition; axial accelerometer; axial strike |
| DC-thigh | DC only; Sawbones thigh boundary condition; axial accelerometer; axial strike |
| GV-clamp | GV connector installed; bone clamp boundary condition; axial accelerometer; axial strike |
| GV-thigh | GV connector installed; Sawbones thigh boundary condition; axial accelerometer; axial strike |

In general, the same sources of noise were present in both systems. The ~ 3000 Hz noise was consistently high across superglue interface configurations; however, it had greater damping when the GV connector was introduced and for the thigh boundary condition. The ~ 7500 Hz noise was high for the superglue interface setup with the GV connector installed and clamp boundary condition. The thigh boundary condition seemed to quell this source of noise; although, some contribution was still observed. The thigh boundary condition also improved first mode

contribution for both interface conditions and implant configurations; however, it also amplified noise between 2000 – 3000 *Hz* for the silicone setup.

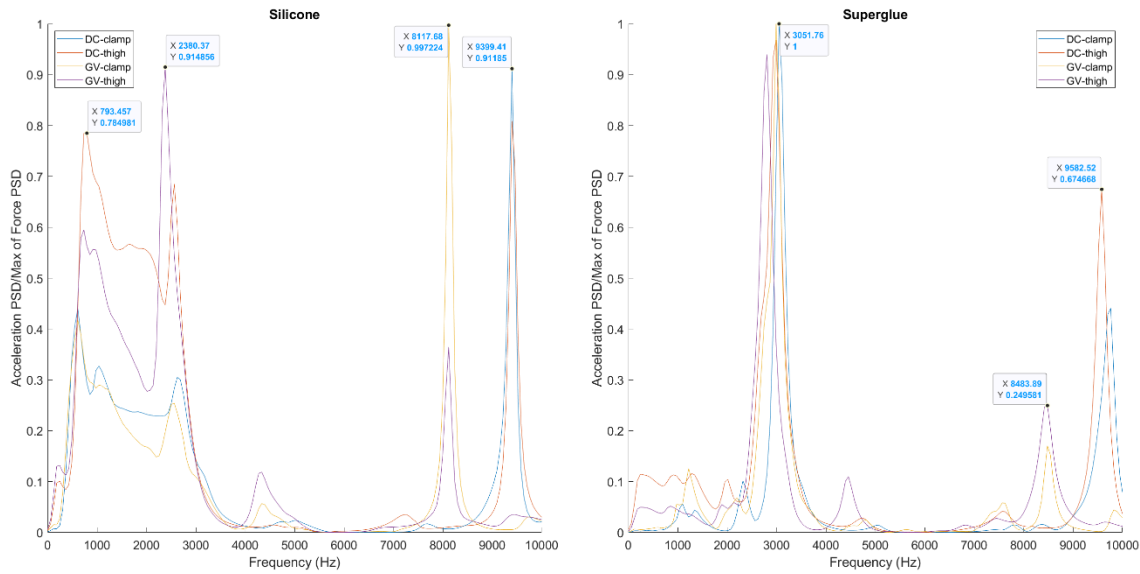


Figure 6.41: Summary plot of modal tests

The modal tests revealed a variety of noisy peaks across various interface conditions, implant configurations, and boundary conditions. Introducing the Sawbones thigh boundary condition presented some interesting results, such as increased damping, but no clearcut benefit over the bone clamp boundary condition. Results suggested possible noise sources from both axial and transverse sources, including axial bone vibration, mixed modes, and to lesser extent, boundary condition influence. The wax interface in the main procedure of the benchtop validation experiment was plagued by result-altering noise in the 7000 – 8000 *Hz* bandwidth. The modal results showed that noise in this band was present in axial superglue measurements; however, it was not present in axial silicone measurements. Furthermore, when only the accelerometer orientation was changed to the transverse direction, there were significant (often the highest) contributions in this bandwidth for both tested interface conditions. This provided some evidence to suggest that intermediate to high stiffness interface conditions may be susceptible to transverse noise contamination, further validating the decision to implement a notch filter for a portion of the analysis in the validation experiment.

6.4.3.3 Phase Analysis

In view of the abundant of noise within the bone-implant systems and lack of definitive answers for sources of said noise, it was deemed necessary to ideate ways in which future experiments and vibration approaches could isolate peaks containing information exclusively pertaining to the bone-implant interface or axial modes of vibration of the implant (i.e., the compressive mode). It was hypothesized that characteristics of the modes of interest were not being fully exploited. There was still useable information regarding mode shapes that could possibly be used to distinguish modes from mechanical noise within the system. Originally, it was thought that by placing a second accelerometer in a different axial location than the first, modes could be distinguished by phase matching. The signals obtained by the accelerometers should be guaranteed to be in phase for any first and second mode of the system, while noise from bending or other local sources would have a strong chance of being out of phase. It should be noted that the second mode would only be in phase if both accelerometers were placed on the same side of the implant relative to its node. If they would be placed on opposite sides of the node, they would be 180° out of phase. For the setups tested, they would always be on the same side. Tests were conducted on the general setup pictured in Figure 6.42. The general setup was not considerably different from the main validation experiment setup, except that the top accelerometer was placed as close as possible to the distal end of the GV connector, while the side accelerometer was placed as close as possible to the proximal end of the GV connector. When the implant was struck in the 3:00 position on the distal screw, signals from the accelerometers were recorded simultaneously and synchronously by multiplexing the data acquisition system. This meant that the samples would be recorded at 125 kHz (half the normal sampling rate) for each accelerometer and be staggered by 4 μ s. The offset between the signals was dealt with post-acquisition by resampling the proximal accelerometer signal (channel AI1) to match the distal accelerometer signal (channel AI0).

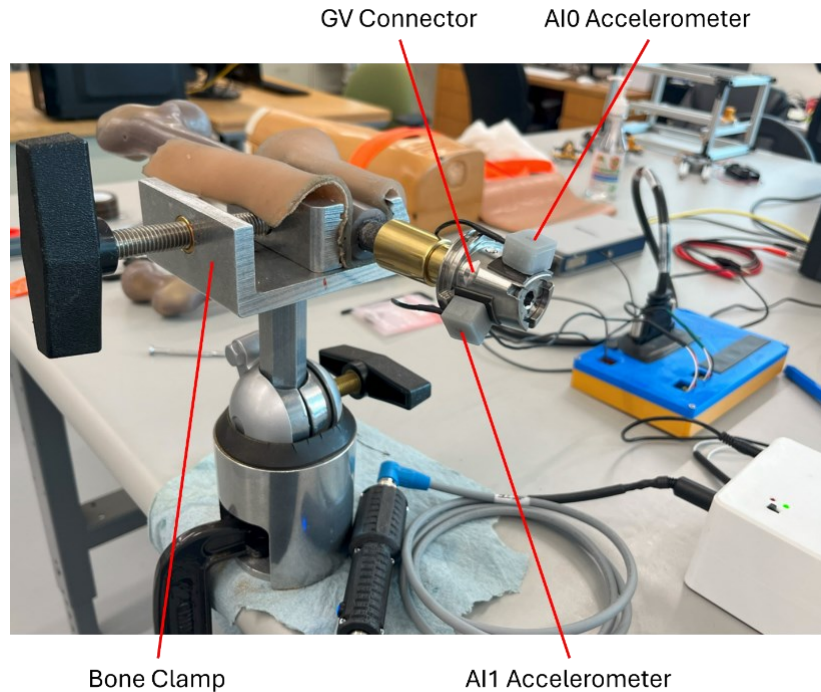


Figure 6.42: Phase analysis setup

Tests were performed with the implant configured with the 68.5 mm dual cone connector and GV connector installed. Both handpieces and impact stiffnesses were tested on the silicone and superglue interface setups. The results produced interesting and partially successful findings. For the 10 g impactor with steel impact tip (Figure 6.43), the phase plots generally showed poor similarity in the mid-range, which matched expectations. Qualitatively, the silicone setup had tight phase matching in the low-range around the first mode, broad dissimilarity in the mid-range, and some matching in the high-range around the second mode. The superglue setup signals were broadly dissimilar in phase until the high range, which showed reasonably good matching. At a bird's eye view, this was a promising result; however, there was no advantageous difference in phase matching between noise around 7500 Hz and the first mode of the superglue setup. Although relatively small compared to the mid-range, differences in phase between the signals were too similar at both peaks to make any meaningful conclusions about their legitimacy in conveying information about the bone-implant interface. However, other characteristics of the observed frequencies could be potentially valuable in noise distinction. For both the silicone and superglue interfaces, the peaks of interest were observed to match tightly in damping, dominant frequency, and to some extent, amplitude value. The other peaks were much more dissimilar,

including the $\sim 7500\text{ Hz}$ peak, which shifted in local dominant frequency value. Moreover, the $\sim 3000\text{ Hz}$ peak exhibited similar behaviour. Qualitatively, the accelerometer signals had some frequency domain differences at the known noisy peaks. It should be noted that the signals were normalized by their peak time domain acceleration value post-acquisition to help control for differences in sensitivity between the sensors. With this in mind, differences in amplitudes between the signals were taken with a grain of salt.

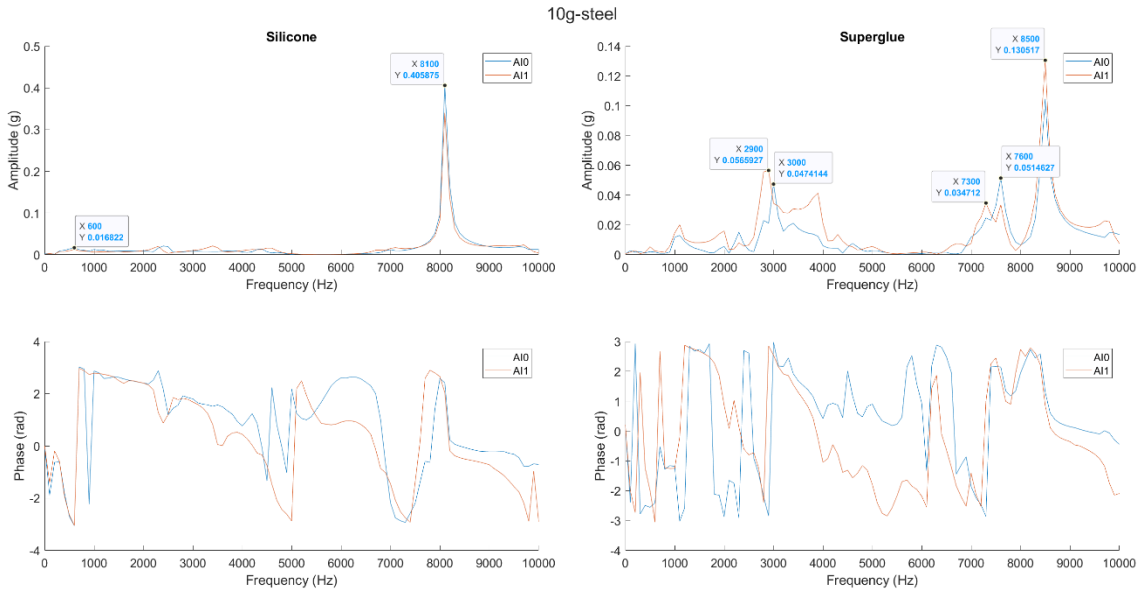


Figure 6.43: Phase analysis – 10 g impact rod with steel tip

For the 10 g handpiece with PEEK tip (Figure 6.44), similar themes were found. Signal phase curves were similar at the modes of interest but were also similar at certain noisy peaks, making the use of this information in isolation hazardous at best. Tight matching was seen in phase, damping, dominant frequency, and amplitude at the first and second modes of the silicone setup. Any other peaks in the setup were mismatched in numerous ways. The first mode of the superglue setup showed decent matching in phase, damping, frequency, and amplitude; however, another peak at 1100 Hz (no known relevance to interface) displayed similar matching.

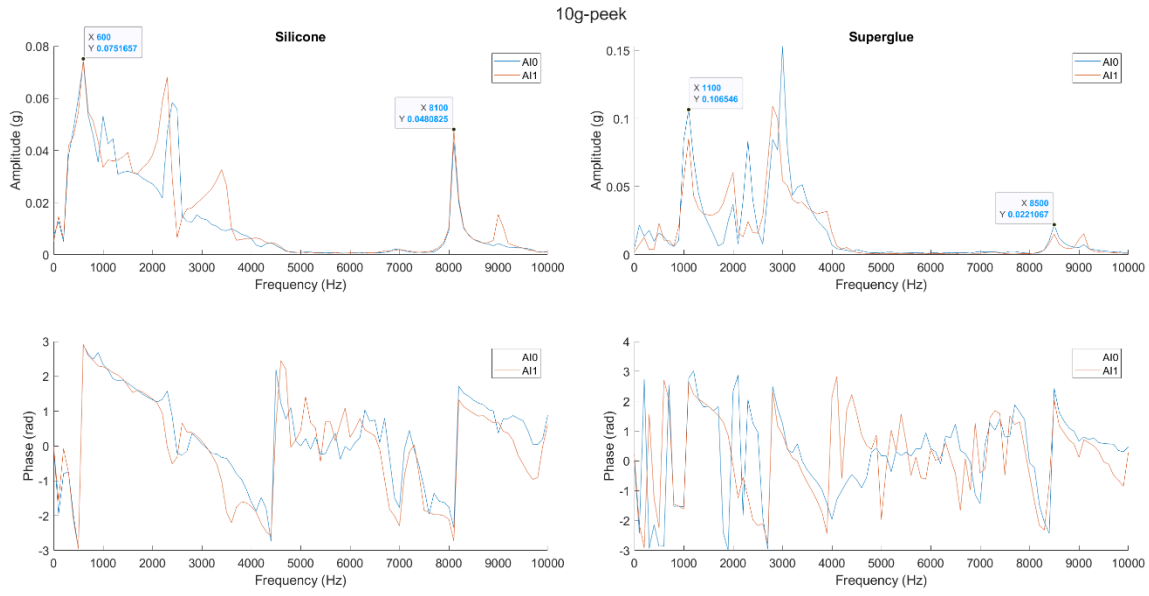


Figure 6.44: Phase analysis – 10 g impact rod with PEEK tip

The steel tip 30 g impactor (Figure 6.45) produced similar findings to the 10 g steel tip case, with slightly better resolution at the first mode in the silicone setup. Again, good matching could be seen at the first and second modes of the silicone setup and first mode of the superglue setup. The ~ 7500 Hz source that produced problems in previous sections appeared mismatched in the frequency domain in terms of peak shape and local dominant frequency ($7600 \rightarrow 7300$ Hz). The ~ 3000 Hz peak was also mismatched and showed a dominant frequency shift from $3000 \rightarrow 2900$ Hz.

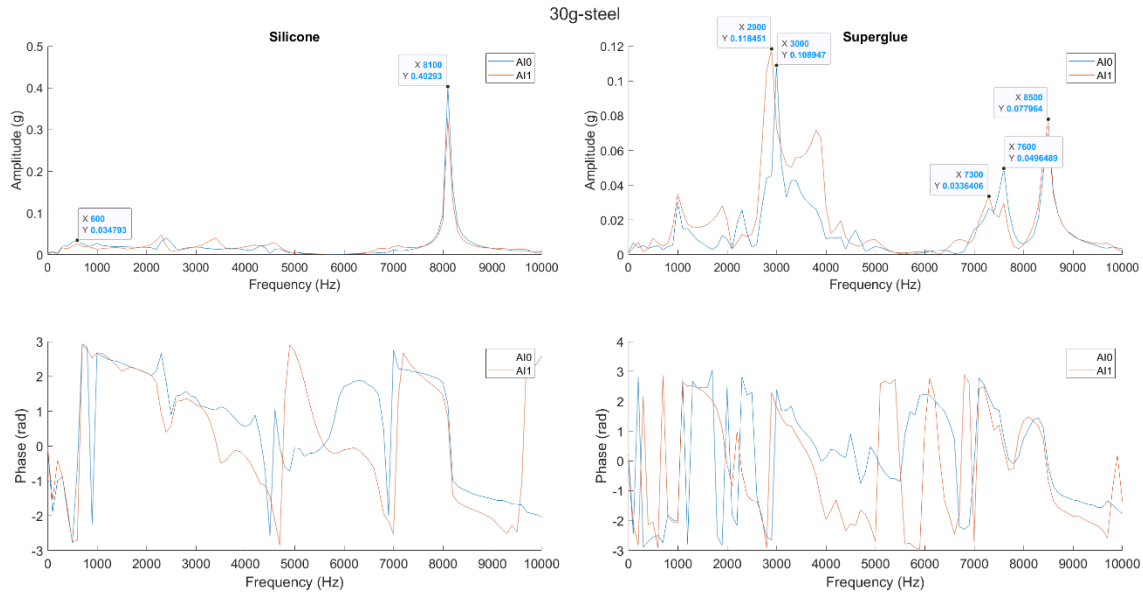


Figure 6.45: Phase analysis – 30 g impact rod with steel tip

Finally, there were similar findings between the 30 g PEEK and 10 g PEEK results. Overall, tight matching was found between the signals at the modes of the interest. There was poor resolution in the high range of the superglue setup, and tight matching was found at one noisy peak (1000 Hz).

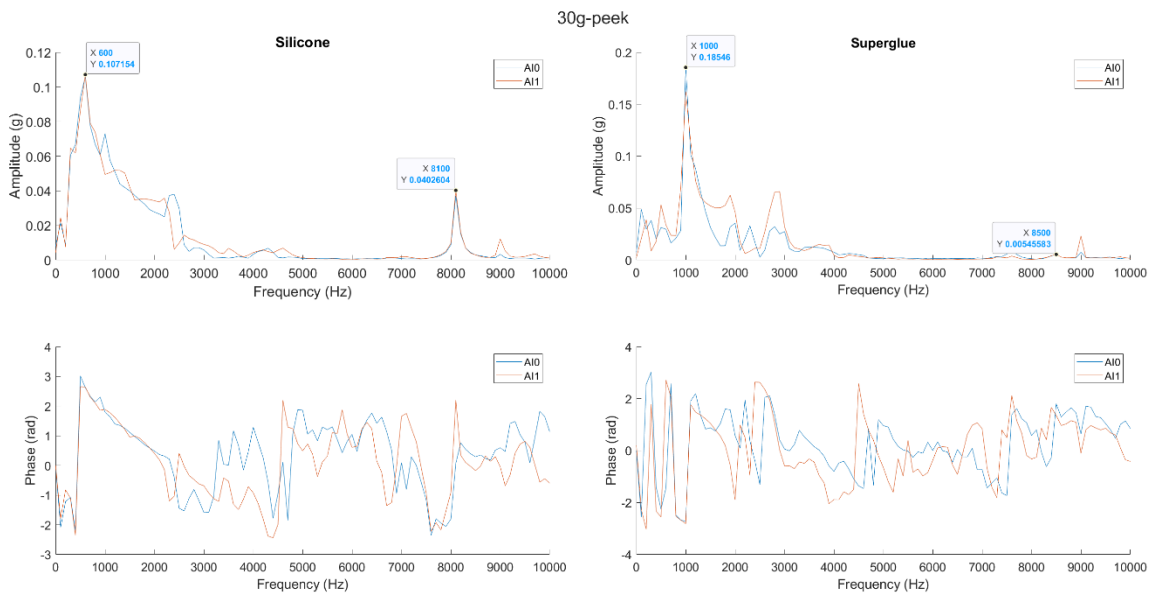


Figure 6.46: Phase analysis – 30 g impact rod with PEEK tip

Phase analysis presented a semi-promising approach to noise detection within multiple bone-implant interface conditions. Unexpectedly, phase data by itself did not provide adequate

information, but other frequency domain characteristics showed qualitative (for now) differences between suspected noisy peaks and modes of interest within the systems. In particular, the suspected noise peaks showed mismatching in the frequency domain in one or more ways: general shape, local dominant frequency, or amplitude, while the modes of interest generally showed good matching in terms of phase, damping, dominant frequency, and amplitude. There was a single peak in the superglue interface setup that demonstrated good matching by the metrics outlined, despite likely being attributed to noise. This set of tests provided further evidence for distinguishing modes of interest from noise peaks and the notch filter approach used in the main procedure of the benchtop validation experiment as well as the possibility for an objective approach to noise detection and attenuation. The presented method provided an additional analog intervention that injected another layer of unique information into the analysis. With more information so far making it qualitatively possible to detect noise, it is conceivable that a numerical routine could be implemented to detect and attenuate noise by using frequency domain characteristics of synchronously recorded acceleration signals at different locations on an implant within a TFA model.

6.5 Conclusion

In this investigation, an objective framework for response signal matching to a 1D finite element model was developed and implemented on data collected from multiple operators. Operators collected measurements with two handpieces for three bone-implant interface stiffness conditions. The approach demonstrated excellent sensitivity to BII stiffness, and the 10 *g* impactor correctly classified all conditions for the simplest implant configuration (68.5 *mm* DC; no GV connector). However, there was significant noise in the system, especially for the wax interface, which caused misclassification in a handful of cases. The 10 *g* impactor had difficulty classifying intermediate interface configurations, while the 30 *g* had difficulty classifying high interface configurations. Implementation of a notch filter protocol greatly improve the 10 *g* impactor results, and the handpiece was recommended for future development. Sources of noise and the potential of a phase analysis noise attenuation protocol were explored. Results were largely inclusive; however, implementation of coherence and cross-correlation techniques on response-only data seem to be an overall promising approach. Future work should address the functionality of the handpiece by

developing a robust actuation mechanism and analog methods for noise identification and attenuation.

Chapter 7 Conclusion

7.1 Contribution

The author of this thesis designed, prototyped, and manufactured an impactor for transfemoral implant stability assessment. Two full experimental studies were executed, including pre-experimental design, protocol generation, physical model and data acquisition set up, experimental runs with prototype impactors, signal processing, analysis and 1D finite element model matching (model developed and validated by Mohamed [28]), and statistical analysis. Simple impact models were developed in the lead up to the development and evaluation study. In the benchtop validation study, the author set up and extracted results from two 3D finite element models, originally developed and validated by Mohamed [28]. All members of the research team contributed to the generation of clinical standards and handpiece deployment criteria. The author and fellow engineering team members conducted preliminary testing and analysis on handheld prototype impactors to ensure standards compliance and prepare for benchtop validation. In the benchtop validation experiment, the author served as one of three participants, two other team members serving as the remaining participants. In the last stages of the thesis, conclusions were drawn through statistical analysis and a final handpiece was presented as an impactor to join the novel ASIST system for osseointegrated transfemoral implant stability assessment.

7.2 Significance

Considering the novelty of the undertaking and multi-modality approach of development and validation, substantial headway has been made towards accurate and reliable mechanical stability assessment of transfemoral implants. Currently, there is no mechanical assessment approach that provides a quantitative measure of bone-implant interface stiffness on an absolute scale. There are also no clinically deployed research or commercial devices for mechanical stability assessment of transfemoral implants. This research has successfully extended the ASIST approach for dental and craniofacial implant stability assessment to the largest orthopaedic devices: transfemoral implants. This work has provided a comprehensive, benchtop validated, non-invasive approach to osseointegrated transfemoral implant stability assessment. From some of the smallest osseointegrated implants to the large OPL system, an impactor with a ram mass of only $\sim 10\text{ g}$ in conjunction with impact tips of vary stiffness can provide tailorable frequency input, ensuring

sensitivity of the ASIST approach. Now, there is a development process for all manner of intermediary implants: transtibial, transhumeral, and many more. The work conducted by Mohamed [26, 27, 28] and continued in this project are landmark accomplishments in the field. Together, they map a way forward for early detection of transfemoral implant loosening and failure, adaption of the ASIST approach to other orthopaedic implants, and the study of osseointegration at large.

7.3 Limitations

At the end of this project, there are a few limitations to the work; however, they will be not insurmountable for future researchers. The device does not have significant problems with repeatability, as the approach it adopts is unique from the interactions of the Periotest with smaller implants. Transitory strike conditions such as distance from the implant and angle of attack may primarily affect response band power and have limited influence on signal composition. This is good news; however, perhaps a poorly conceived actuation mechanism made operation difficult. The handpieces had to be positioned within a narrow range of strike distances and inclinations, necessitating skilled operation. The most glaring limitation is the presence of unidentified mechanical noise within the bone-implant systems. This is unsurprising considering the complexity of the distal implant assembly. The assembly had up to five separate interfacing components, with two screws pre-tensioning the system. Any number of individual component vibrations, out-plane modes, or sources of mechanical leakage could complicate axial responses. Presumably, this would be an issue for any mechanical approach. For example, in a quantitative ultrasound study, the transfemoral implant was modelled as a solid cylinder [48]; there is not even a comparative framework to this end, but numerous ‘boundary conditions’ of component interfaces may confound wave reflections from the bone-implant interface. Another limitation to the present study is the lack of coherence and cross-spectrum analysis performed on response data. The study used one accelerometer to record axial response signals. A stronger study would have recorded strike loading profiles or two response signals as in [25]. If this was done, there is a possibility that some of the problematic noise could have been objectively attenuated by assigning a coherence or ‘quality factor’ minimum to each peak [25].

7.4 Future Work

There are innumerate paths that the research field could follow. Certainly, mechanical noise is one of the primary limitations of the present approach. To this end, at least two remedies have potential. The first would be to build off the work of Lu et al. [24, 25] and establish an analog intervention for noise control. This option was partially explored in Section 6.4.3.3, where the phase responses of signals from two accelerometers were compared. Regardless of the success of phase comparison, there were certainly qualitative frequency domain differences between accelerometer measurements that could have been exploited. Implementing formal coherence, quality factor [25], or response-only cross-correlation [80] techniques could provide a framework for accurate and objective noise attenuation. Alternatively, since the system at hand is in a part a classification tool, a machine learning instrument, such as a denoising autoencoder, could be implemented to ‘learn’ what a noisy signal looks like and attenuate the problematic peaks. However, there is currently no precedent for this approach within the field. Other future work includes improving the functionality of the device, especially through a novel actuation system. It was particularly difficult to synthesize a compact actuator that could ‘throw, pull, and catch’ an inertial body at a distance, and even more difficult to make it reliable. A mechanism with more control may implement a stepper or servo motor in some fashion.

Future studies should investigate different TFA models. On the experimental side, curing epoxy resin models are interesting and provide a large, continuous range of interface stiffnesses to analyze [24, 25, 47, 48]. Animal models also provide the highest level of validation possible, as stability measurements can be directly compared to gold standard histologic analysis; however, they require a high degree of coordination and potential harm to animals when benchtop models may suffice for development and validation before clinical deployment. Longitudinal clinical studies may illuminate the practical potential of stability assessment approaches, but validation in this setting remains a challenge. Radiostereometric analysis (RSA) seems to be one of the most promising radiographic assessment approaches [42, 43] and may pair strongly with the present approach in a clinical study. Advances in micro-CT will continue to make waves in the study of bone structure and osseointegration, and it also seems inevitable that quantitative ultrasound will emerge as a competitor to vibration assessment approaches. Very little work has been conducted on guided

waves, so there is immense room in the field for technological leaps. It will not be long before there is a reliable, non-invasive device for instantaneous transfemoral implant stability assessment.

References

- [1] M. Myers, "Above-the-Knee Amputations," StatPearls Publishing, 2023.
- [2] B. Imam, "Incidence of lower limb amputation in Canada," *Canadian Journal of Public Health*, vol. 108, no. 4, pp. 374-380, 2017.
- [3] J. S. Hoellwarth, "Osseointegration for Amputees: Current Implants, Techniques, and Future Directions," *Journal of Bone and Joint Surgery*, vol. 8, no. 3, 2020.
- [4] A. Esquenazi, "Lower Limb Amputations: Epidemiology and Assessment," PM&R Knowledge NOW, 29 6 2021. [Online]. Available: <https://now.aapmr.org/lower-limb-amputations-epidemiology-and-assessment/>. [Accessed 31 7 2024].
- [5] M. D. Muller, "Transfemoral Amputation: Prosthetic Management," in *Atlas of Amputations and Limb Deficiencies, Fourth Edition*, American Academy of Orthopaedic Surgeons, 2016, pp. 537-554.
- [6] G. M. Berke, "Transfemoral Amputation: The Basics and Beyond," Prosthetics Research Study, 2008.
- [7] R. A. Leijendekkers, "Comparison of bone-anchored prostheses and socket prostheses for patients with a lower extremity amputation: a systematic review," *Disability and Rehabilitation*, vol. 39, no. 11, pp. 1045-1058, 2017.
- [8] A. Maryniak, "Technical Overview of Osseointegrated Transfemoral Prostheses: Orthopedic Surgery and Implant Design Centered," *Journal of Engineering and Science in Medical Diagnostics and Therapy*, vol. 1, no. 2, 2018.
- [9] J. S. Hebert, "Osseointegration for Lower-Limb Amputation: A Systematic Review of Clinical Outcomes," *Journal of Bone and Joint Surgery*, vol. 5, no. 10, 2017.

- [10] M. Rehani, "Bone-anchored prostheses for transfemoral amputation: a systematic review of outcomes, complications, patient experiences, and cost-effectiveness," *Frontiers in Rehabilitation Sciences*, vol. 5, 2024.
- [11] R. Brånemark, "Osseointegration in skeletal reconstruction and rehabilitation: A review," *Journal of Rehabilitation Research and Development*, vol. 38, no. 2, pp. 175-181, 2001.
- [12] K. Hagberg, "One hundred patients treated with osseointegrated transfemoral amputation prostheses - Rehabilitation perspective," *Journal of Rehabilitation Research & Development*, vol. 46, no. 3, pp. 331-344, 2009.
- [13] R. Atallah, "Complications of bone-anchored prostheses for individuals with an extremity amputation: A systematic review," *PLOS One*, vol. 13, no. 8, 2018.
- [14] X. Gao, "Biomechanical behaviours of the bone-implant interface: a review," *Journal of the Royal Society, Interface*, vol. 16, no. 156, 2019.
- [15] E. M. Zanetti, "Clinical Assessment of Dental Implant Stability During Follow-Up: What Is Actually Measured, and Perspectives," *Biosensors*, vol. 8, no. 3, 2018.
- [16] L. Westover, "Advanced System for Implant Stability Testing (ASIST)," *Journal of Biomechanics*, vol. 49, no. 15, pp. 3651-3659, 2016.
- [17] L. Westover, "Application of the advanced system for implant stability testing (ASIST) to natural teeth for noninvasive evaluation of the tooth root interface," *Journal of Biomechanics*, vol. 69, pp. 129-137, 2018.
- [18] C. Jar, "An analytical model to measure dental implant stability with the Advanced System for Implant Stability Testing (ASIST)," *Journal of the Mechanical Behavior of Biomedical Materials*, vol. 150, 2024.
- [19] W. Xu, "A Resonant Frequency Measurement System for Osseointegration Trans-Femoral Implant," *Key Engineering Materials*, Vols. 295-296, pp. 139-144, 2005.

- [20] F. Shao, "Natural Frequency Analysis of Osseointegration for Trans-femoral Implant," *Annals of Biomedical Engineering*, vol. 35, no. 5, pp. 817-824, 2007.
- [21] N. J. Cairns, "Evaluation of Modal Analysis Techniques using Physical Models to Detect Osseointegration of Implants in Transfemoral Amputees," in *33rd Annual International Conference of the IEEE EMBS*, Boston, Massachusetts, USA, 2011.
- [22] N. J. Cairns, "Simulating the Bone-Titanium Interfacial Changes Around Transfemoral Osseointegrated Implants Using Physical Models and Modal Analysis," in *Proceedings of the International Workshop on Innovative Simulation for Health Care*, 2012.
- [23] N. J. Cairns, "Ability of modal analysis to detect osseointegration of implants in transfemoral amputees: a physical model study," *Medical & Biological Engineering & Computing*, vol. 51, no. 1-2, pp. 39-47, 2013.
- [24] S. Lu, "Experimental Investigation of Vibration Analysis on Implant Stability for a Novel Implant Design," *Sensors*, vol. 22, no. 4, 2022.
- [25] S. Lu, "Monitoring Osseointegration Process Using Vibration Analysis," *Sensors*, vol. 22, no. 18, 2022.
- [26] M. Mohamed, "Stability Assessment of Osseointegrated Transfemoral Bone-Implant Systems using Finite Element Modal Analysis," in *Proceedings of the Canadian Society for Mechanical Engineering International Congress 2022*, Edmonton, AB, Canada, 2022.
- [27] M. Mohamed, "Evaluation of the Transfemoral Bone–Implant Interface Properties Using Vibration Analysis," *Annals of Biomedical Engineering*, 2024.
- [28] M. Mohamed, "Mathematical and Experimental Modelling of the Dynamic Response of the Transfemoral Bone Implant System and Bone Anchored Hearing Aids and its Potential Application to the Non-invasive Evaluation of Implant Stability," University of Alberta, 2023.

- [29] P. Sugarbaker, "Above-knee Amputation," in *Musculoskeletal Cancer Surgery*, Kluwer Academic Publishers, 2001, pp. 349-360.
- [30] A. Meffen, "Understanding variations in reported epidemiology of major lower extremity amputation in the UK: a systematic review," *BMJ Open*, vol. 11, no. 10, pp. 3562-3568, 2021.
- [31] M. Spoden, "Amputation rates of the lower limb by amputation level - observational study using German national hospital discharge data from 2005 to 2015," *BMC Health Services Research*, vol. 19, no. 1, 2019.
- [32] J. S. Hoellwarth, "Bone density changes after five or more years of unilateral lower extremity osseointegration: Observational cohort study," *Bone Reports*, vol. 18, 2023.
- [33] M. A. Muderis, "The Osseointegration Group of Australia Accelerated Protocol (OGAAP-1) for two-stage osseointegrated reconstruction of amputated limbs," *The Bone & Joint Journal*, Vols. 98-B, no. 7, pp. 952-960, 2016.
- [34] M. A. Muderis, "Single-stage osseointegrated reconstruction and rehabilitation of lower limb amputees: the Osseointegration Group of Australia Accelerated Protocol-2 (OGAAP-2) for a prospective cohort study," *BMJ Open*, vol. 7, no. 3, 2017.
- [35] J. S. Hoellwarth, "The Clinical History and Basic Science Origins of Transcutaneous Osseointegration for Amputees," *Advances in Orthopedics*, vol. 2022, 2022.
- [36] J. S. Hoellwarth, "Transcutaneous Osseointegration for Amputees: What Is It, How Did It Evolve, and What May Develop?," *Current Physical Medicine and Rehabilitation Reports*, vol. 11, pp. 6-15, 2023.
- [37] M. Ramakrishna, "A brief history of osseointegration: A review," *IP Annals of Prosthodontics and Restorative Dentistry*, vol. 7, no. 1, pp. 29-36, 2021.
- [38] B. M. Isaacson, "Osseointegration: a review of the fundamentals for assuring cementless skeletal fixation," *Orthopedic Research and Reviews*, vol. 6, pp. 55-65, 2014.

- [39] R. M. Grzeskowiak, "Bone and Cartilage Interfaces With Orthopedic Implants: A Literature Review," *Frontiers in Surgery*, vol. 7, 2020.
- [40] J. G. Tropf, "Osseointegration for amputees: Current state of direct skeletal attachment," *Orthoplastic Surgery*, vol. 12, pp. 20-28, 2023.
- [41] V. Swami, "Current trends to measure implant stability," *Journal of Indian Prosthodontic Society*, vol. 16, no. 2, pp. 124-130, 2016.
- [42] R. L. Hansen, "Does migration of osseointegrated implants for transfemoral amputees predict later revision? A prospective 2-year radiostereometric analysis with 5-years clinical follow-up," *Orthopaedics & Traumatology, Surgery & Research*, vol. 105, no. 5, pp. 1013-1020, 2019.
- [43] A. Nebergall, "Stable fixation of an osseointegrated implant system for above-the-knee amputees," *Acta Orthopaedica*, vol. 83, no. 2, pp. 121-128, 2012.
- [44] R. Vayron, "Assessment of the biomechanical stability of a dental implant with quantitative ultrasound: A three-dimensional finite element study," *Journal of the Acoustical Society of America*, vol. 139, no. 2, pp. 773-780, 2016.
- [45] R. Vayron, "Ultrasonic evaluation of dental implant osseointegration," *Journal of Biomechanics*, vol. 47, no. 14, pp. 3562-3568, 2014.
- [46] R. Vayron, "Comparison of Resonance Frequency Analysis and of Quantitative Ultrasound to Assess Dental Implant Osseointegration," *Sensors*, vol. 18, no. 5, 2018.
- [47] B. S. Vien, "A Quantitative Approach for the Bone-implant Osseointegration Assessment Based on Ultrasonic Elastic Guided Waves," *Sensors*, vol. 19, no. 3, 2019.
- [48] W. Wang, "Application of guided wave methods to quantitatively assess healing in osseointegrated prostheses," *Structural Health Monitoring*, vol. 17, no. 6, 2018.

- [49] Y. Liu, "Challenges of Using Resonance Frequency Analysis to Identify Stability of a Dental Implant Placed in the Mandible," *International Journal of Oral & Maxillofacial Implants*, vol. 36, no. 2, pp. 7-21, 2021.
- [50] N. Meredith, "A Review of Nondestructive Test Methods and Their Application to Measure the Stability and Osseointegration of Bone Anchored Endosseous Implants," *Critical Reviews in Biomedical Engineering*, vol. 26, no. 4, pp. 275-291, 1998.
- [51] S. Winkler, "Stability of Implants and Natural Teeth as Determined by the Periotest over 60 Months of Function," *Journal of Oral Implantology*, vol. 27, no. 4, pp. 198-203, 2001.
- [52] M. G. Faulkner, "Measuring Abutment/Implant Joint Integrity with the Periotest Instrument," *International Journal of Oral & Maxillofacial Implants*, vol. 14, no. 5, pp. 681-688, 1999.
- [53] D. Lukas, "Periotest - a dynamic procedure for the diagnosis of the human periodontium," *Clinical Physics and Physiological Measurement*, vol. 11, no. 1, pp. 65-75, 1990.
- [54] L. J. Dario, "Electronic monitoring of dental implant osseointegration," *Journal of the American Dental Association*, vol. 133, no. 4, pp. 483-490, 2002.
- [55] L. Westover, "Comparison of implant stability measurement devices for bone-anchored hearing aid systems," *Journal of Prosthetic Dentistry*, vol. 119, no. 1, pp. 178-184, 2018.
- [56] L. Westover, "Longitudinal Evaluation of Bone-Anchored Hearing Aid Implant Stability Using the Advanced System for Implant Stability Testing (ASIST)," *Otology & Neurotology*, vol. 39, no. 6, pp. 489-495, 2018.
- [57] G. Galteri, "Reliable in vitro method for the evaluation of the primary stability and load transfer of transfemoral prostheses for osseointegrated implantation," *Frontiers in Bioengineering and Biotechnology*, vol. 12, 2024.

- [58] G. Faulkner, "Apparatus and Method for Assessing Percutaneous Implant Stability". World Intellectual Property Organization International Bureau Patent WO 2008/019489 A1, 21 2 2008.
- [59] R. G. Robertson, "Multiple Impulse Method of Tooth Mobility Assessment," University of London, 1995.
- [60] J. Wohlgemuth, "Dental Percussion Instrument". United States Patent Patent 4689011, 25 8 1987.
- [61] R. C. Swain, "Development and Modeling of an Impact Test to Determine the Bone-Implant Interface Properties of Osseointegrated Implants," University of Alberta, 2006.
- [62] "Piezoelectric Accelerometers," Hottinger Brüel & Kjær, 2024. [Online]. Available: <https://www.hbkworld.com/en/knowledge/resource-center/articles/vibration/piezoelectric-accelerometers#accelerometer-characteristics>. [Accessed 31 7 2024].
- [63] *Periotest Classic Operating Instructions English*, Medizintechnik Gulden Manufacturer of the Periotest, 2015.
- [64] P. Avitable, "Modal Testing," The Society for Experimental Mechanics/John Wiley & Sons Ltd, 2018.
- [65] G. Gilardi, "Literature survey of contact dynamics modelling," *Mechanism and Machine Theory*, vol. 37, no. 10, pp. 1213-1239, 2002.
- [66] "Overview of materials for Cyanoacrylate Adhesive," MatWeb, 2024. [Online]. Available: <https://www.matweb.com/search/datasheettext.aspx?matguid=d0d7dbec7666421caf8aa08724b634c5>. [Accessed 31 7 2024].
- [67] M. E. Hossain, "Experimental Study of Physical and Mechanical Properties of Natural and Synthetic Waxes using Uniaxial Compressive Strength Test," in *Proceedings of the Third International Conference on Modeling, Simulation and Applied Optimization*, Sharjah, U.A.E, 2009.

- [68] J. Mathews, "Guide to Adhesively Mounting Accelerometers," Endevco an Amphenol Company, 2022.
- [69] B. Fladung, "Windows used for Impact Testing," University of Cincinnati, 1997.
- [70] M. Gasior, "Improving FFT Frequency Measurement Resolution by Parabolic and Gaussian Spectrum Interpolation," in *European Organization for Nuclear Research*, Knoxville, TE, USA, 2004.
- [71] K. O. McGraw, "Forming Inferences about some Intraclass Correlation Coefficients," *Psychological Methods*, vol. 1, no. 1, pp. 30-46, 1996.
- [72] T. K. Koo, "A Guideline of Selecting and Reporting Intraclass Correlation Coefficients for Reliability Research," *Journal of Chiropractic Medicine*, vol. 15, no. 2, pp. 155-163, 2016.
- [73] A. Salarian, "Intraclass Correlation Coefficient (ICC)," MATLAB Central File Exchange, 2024. [Online]. Available: <https://www.mathworks.com/matlabcentral/fileexchange/22099-intraclass-correlation-coefficient-icc>. [Accessed 31 7 2024].
- [74] D. Tirelli, "Modal Analysis of Small & Medium Structures by Fast Impact Hammer Testing Method," European Union, 2011.
- [75] "Biomechanical Materials for Testing & Validation," Sawbones, 2023. [Online]. Available: <https://www.sawbones.com/biomechanical-product-info>. [Accessed 31 7 2024].
- [76] "Metals and Alloys - Densities," The Engineering ToolBox, 2004. [Online]. Available: https://www.engineeringtoolbox.com/metal-alloys-densities-d_50.html. [Accessed 31 7 2024].
- [77] "316 Stainless Steel, annealed bar," MatWeb, 2024. [Online]. Available: <https://www.matweb.com/search/DataSheet.aspx?MatGUID=dfced4f11d63459e8ef8733d1c7c1ad2&ckck=1>. [Accessed 31 7 2024].
- [78] "iglide J, sleeve bearing, mm," igus motion plastics, 2024. [Online]. Available: <https://www.igus.ca/product?artNr=JSM-0507-05>. [Accessed 31 7 2024].

- [79] *CAN/CSA-C22.2 No. 60601-1:14 (Medical electrical equipment - Part 1: General requirements for basic safety and essential performance)*, CSA Group, 2022.
- [80] F. Shen, "Using the Cross-Correlation Technique to Extract Modal Parameters on Response-Only Data," *Journal of Sound and Vibration*, vol. 259, no. 5, pp. 1163-1179, 2003.
- [81] "PEEK Chemical Compatibility," CP Lab Safety, 2024. [Online]. Available: <https://www.calpaclab.com/polyetherether-ketone-peek-chemical-compatibility-chart/>. [Accessed 31 7 2024].
- [82] I. T. Heikkinen, "Chemical compatibility of fused filament fabrication-based 3-D printed components with solutions commonly used in semiconductor wet processing," *Additive Manufacturing*, vol. 23, pp. 99-107, 2018.
- [83] Al-Mamun, "Corrosion behavior and biocompatibility of additively manufactured 316L stainless steel in a physiological environment: the effect of citrate ions," *Additive Manufacturing*, vol. 34, 2020.
- [84] J. M. Toth, "Biocompatibility of PEEK Polymers," in *PEEK Biomaterials Handbook (Second Edition)*, Plastics Design Library, 2019, pp. 107-119.

Appendix A Magnetic Flux Density Estimates of Periotest Handpiece Coils

A.1 Overview

This appendix contains the calculations for magnetic flux density estimates of the Periotest handpiece solenoid and electromagnet. The dimensions of the solenoid and electromagnet coils were measured with a caliper during a dissection of a Periotest handpiece.

A.2 Periotest Solenoid

The number of turns was calculated in Equation A.1 from the solenoid dimensions, where n is number of turns, L is bobbin length in mm , D_{gauge} is wire diameter in mm , D_{out} is outer diameter of the bobbin in mm , and D_{in} is inner diameter of the bobbin in mm .

$$n = \frac{L}{D_{gauge}} * \frac{D_{out} - D_{in}}{2D_{gauge}} = \frac{5}{0.18} * \frac{9 - 6}{2(0.18)} = 216 \quad A.1$$

The current used in following calculation was specified by an electrical engineer team member who was involved in the design of the ASIST motherboard. Magnetic flux density was calculated in Equation A.2, where B is magnetic flux density in Gs , k is material permeability (1 for air), μ_0 is vacuum permeability in N/A^2 , n is number of turns, L is bobbin length in m , and I is current in A .

$$B = k\mu_0 \frac{n}{W} I = 1(4\pi * 10^{-7}) \frac{216}{0.005} 0.350 = 190.0 Gs \quad A.2$$

A.3 Periotest Electromagnet

The number of turns was calculated in Equation A.3 from the solenoid dimensions, where n is number of turns, L is bobbin length in mm , D_{gauge} is wire diameter in mm , D_{out} is outer diameter of the bobbin in mm , and D_{in} is inner diameter of the bobbin in mm .

$$n = \frac{L}{D_{gauge}} * \frac{D_{out} - D_{in}}{2D_{gauge}} = \frac{18.5}{0.18} * \frac{9 - 3.85}{2(0.18)} = 1428 \quad A.3$$

The current used in following calculation was specified by an electrical engineer team member who was involved in the design of the ASIST motherboard. Magnetic flux density was calculated in Equation A.4, where B is magnetic flux density in Gs , k is material permeability (1 for air), μ_0 is vacuum permeability in N/A^2 , n is number of turns, L is bobbin length in m , and I is current in A .

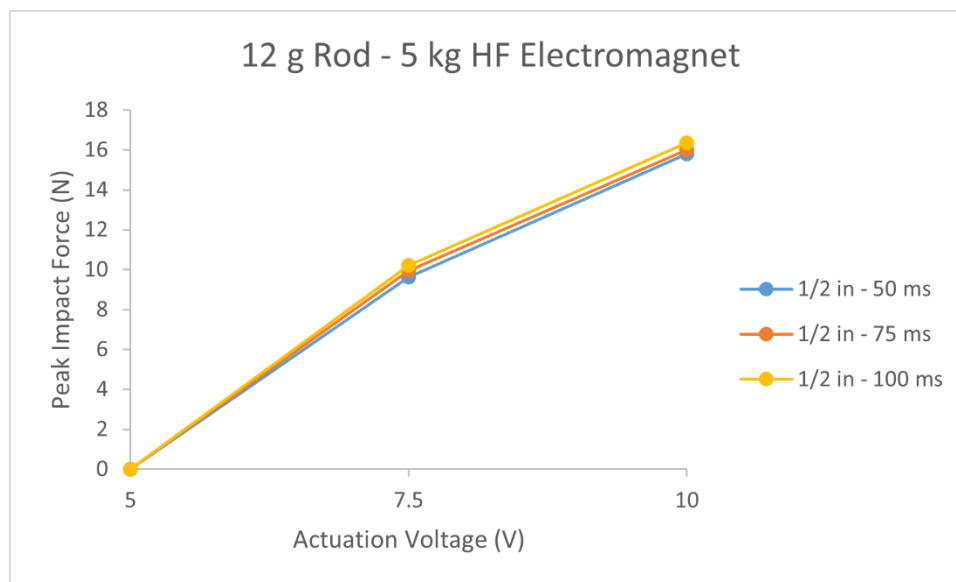
$$B = k\mu_0 \frac{n}{L} I = 1(4\pi * 10^{-7}) \frac{1428}{0.0185} 0.350 = 339.5 \text{ } Gs \quad A.4$$

Appendix B Benchtop Prototype Impact Force vs. Actuation Voltage Plots

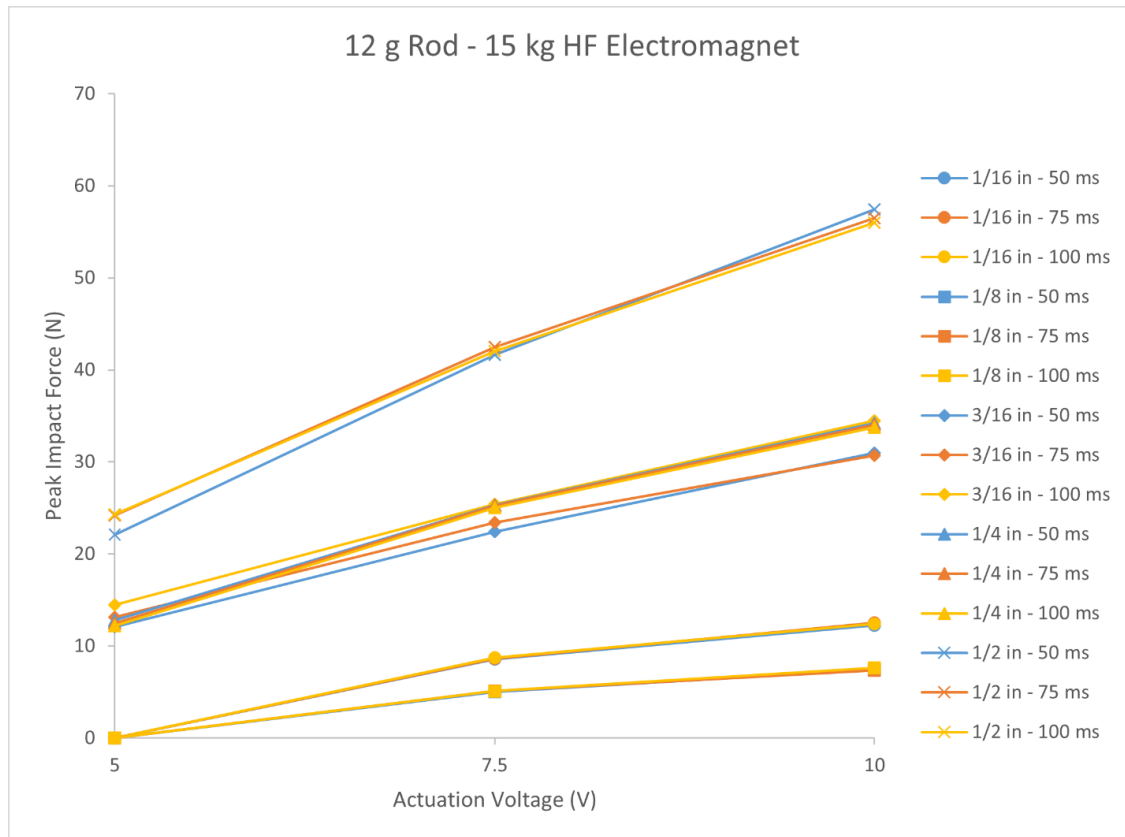
B.1 Overview

Impact force tests were conducted for various configurations of the first modular benchtop prototype impactor. Peak impact force was recorded for various combinations of magnets at multiple electromagnet actuation voltages. The tests are detailed in Section 3.5.2.1; associated plots can be viewed in Section B.2 below.

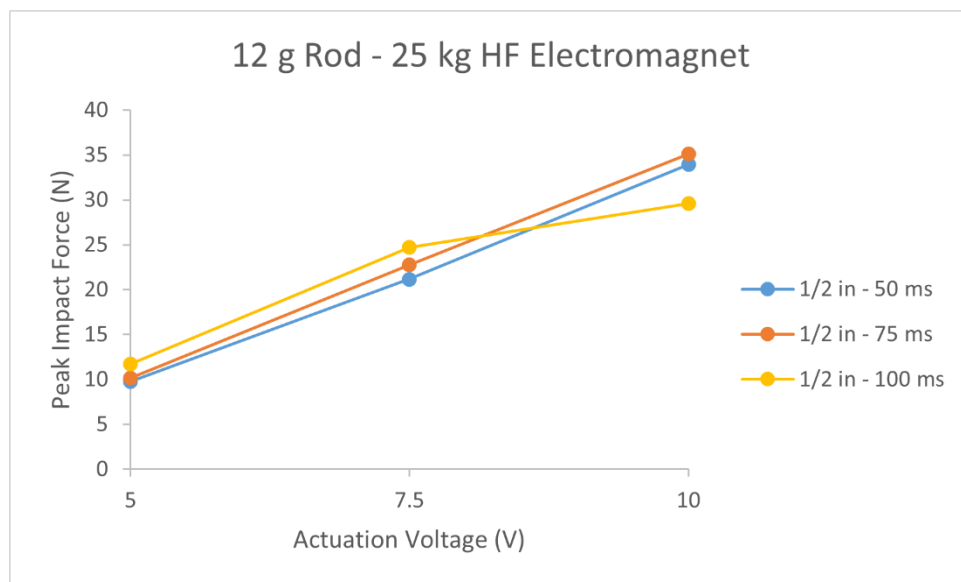
B.2 Plots



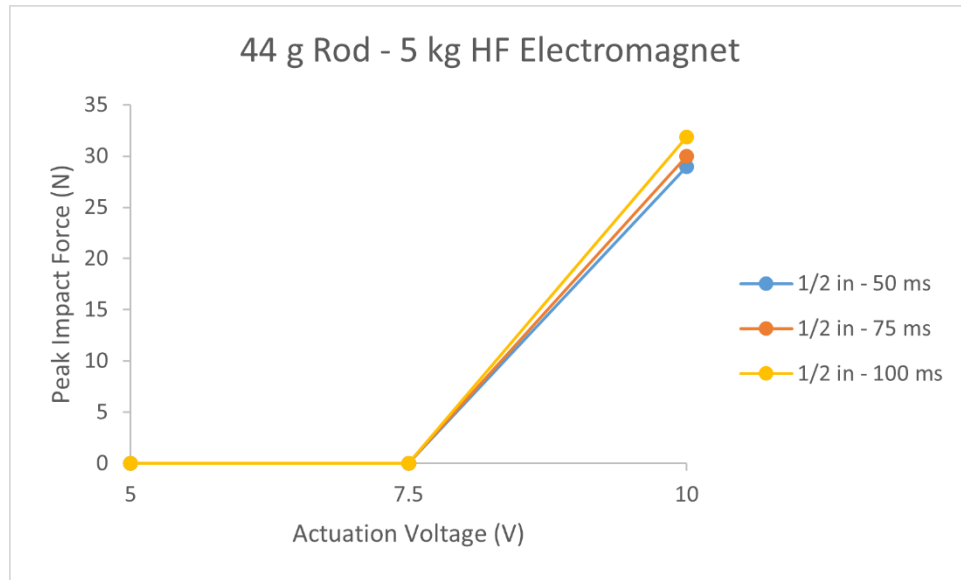
App. Figure B.1: Impact force of 12 g rod with 5 kg HF electromagnet (neodymium magnet length – actuation time in legend)



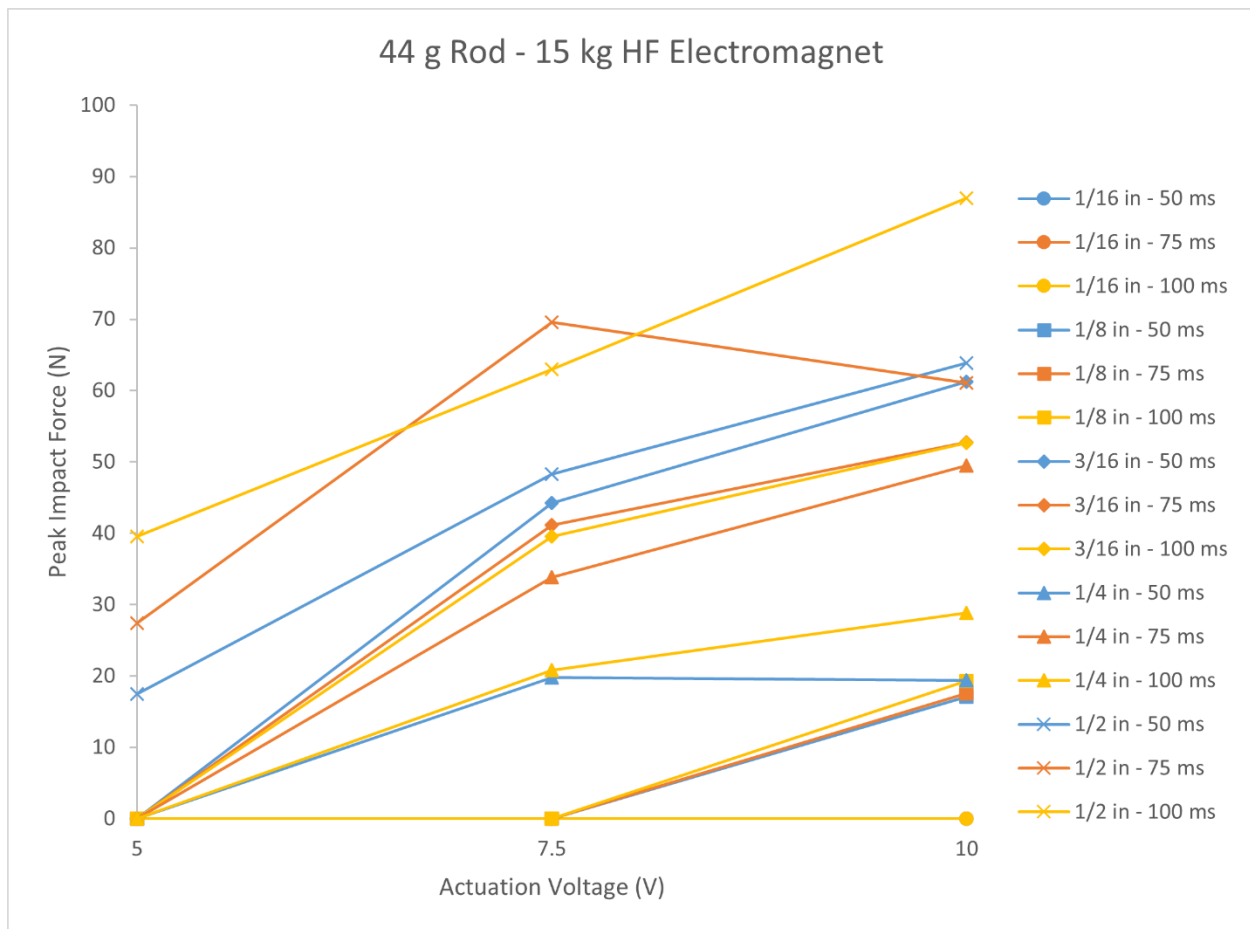
App. Figure B.2: Impact force of 12 g rod with 15 kg HF electromagnet (neodymium magnet length – actuation time in legend)



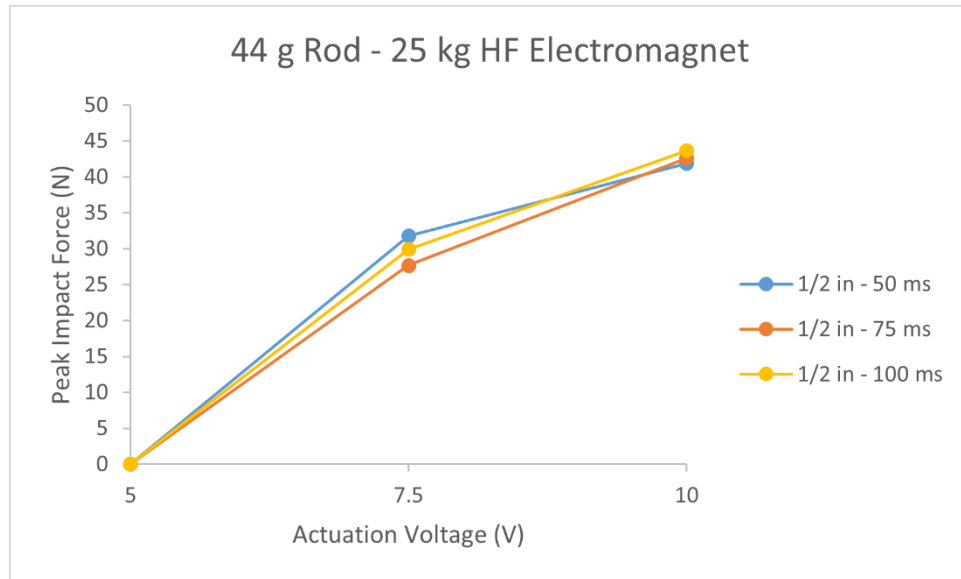
App. Figure B.3: Impact force of 12 g rod with 25 kg HF electromagnet (neodymium magnet length – actuation time in legend)



App. Figure B.4: Impact force of 44 g rod with 5 kg HF electromagnet (neodymium magnet length – actuation time in legend)



App. Figure B.5: Impact force of 44 g rod with 15 kg HF electromagnet (neodymium magnet length – actuation time in legend)



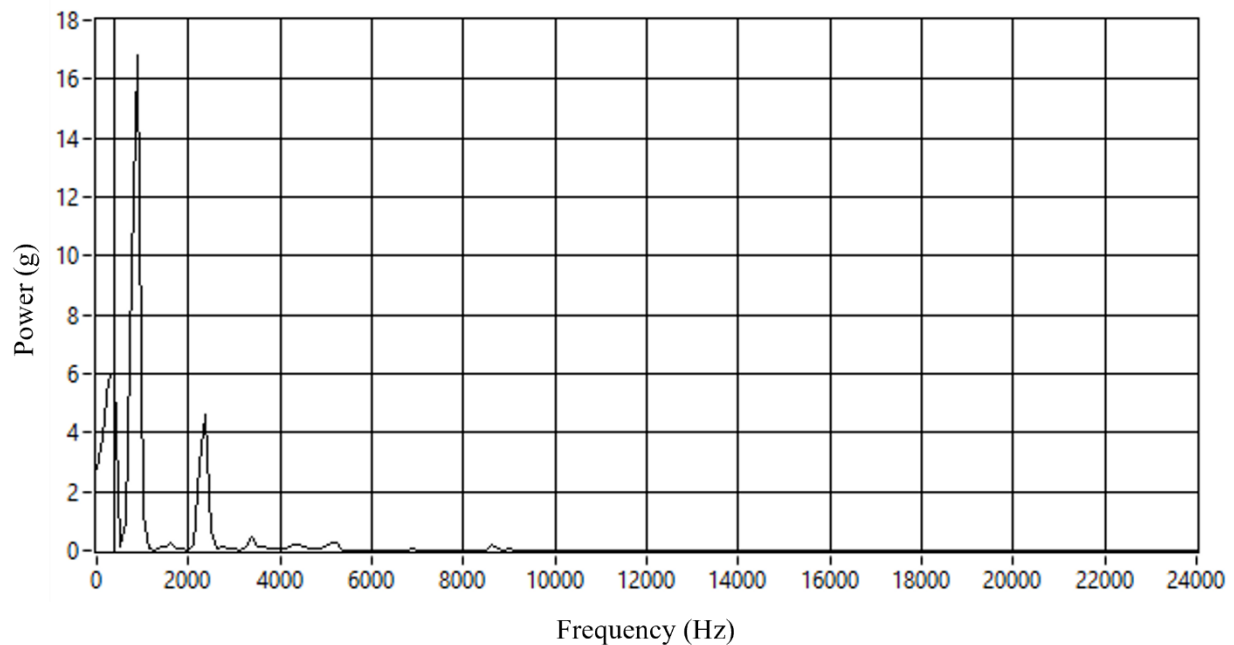
App. Figure B.6: Impact force of 44 g rod with 25 kg HF electromagnet (neodymium magnet length – actuation time in legend)

Appendix C Ascending Mass Power Spectrum Plots

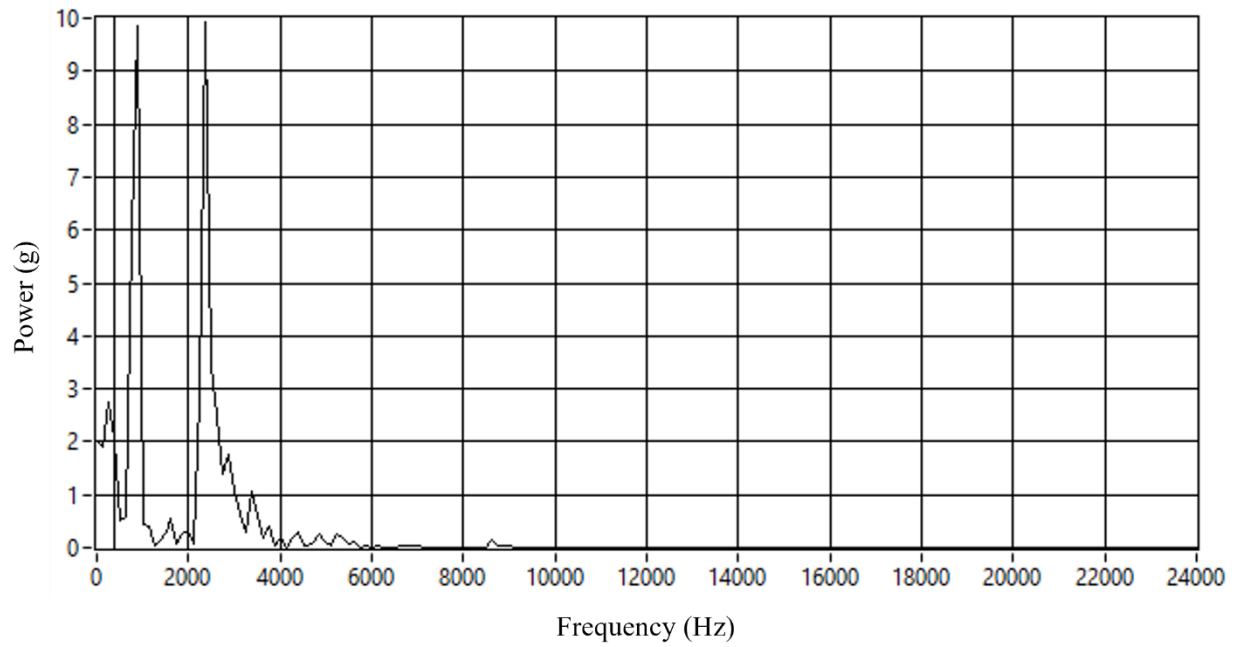
C.1 Overview

This appendix contains power spectrum plots for the replica implant superglue interface setup discussed in Section 3.6.3.2. The GV connector was installed on the setup and signals elicited by impact rods of increasing mass were recorded in the transverse direction. The resulting ascending mass power spectrum plots can be viewed in Section C.2 below. The noisiest signal represented the limiting case for large-mass excitation.

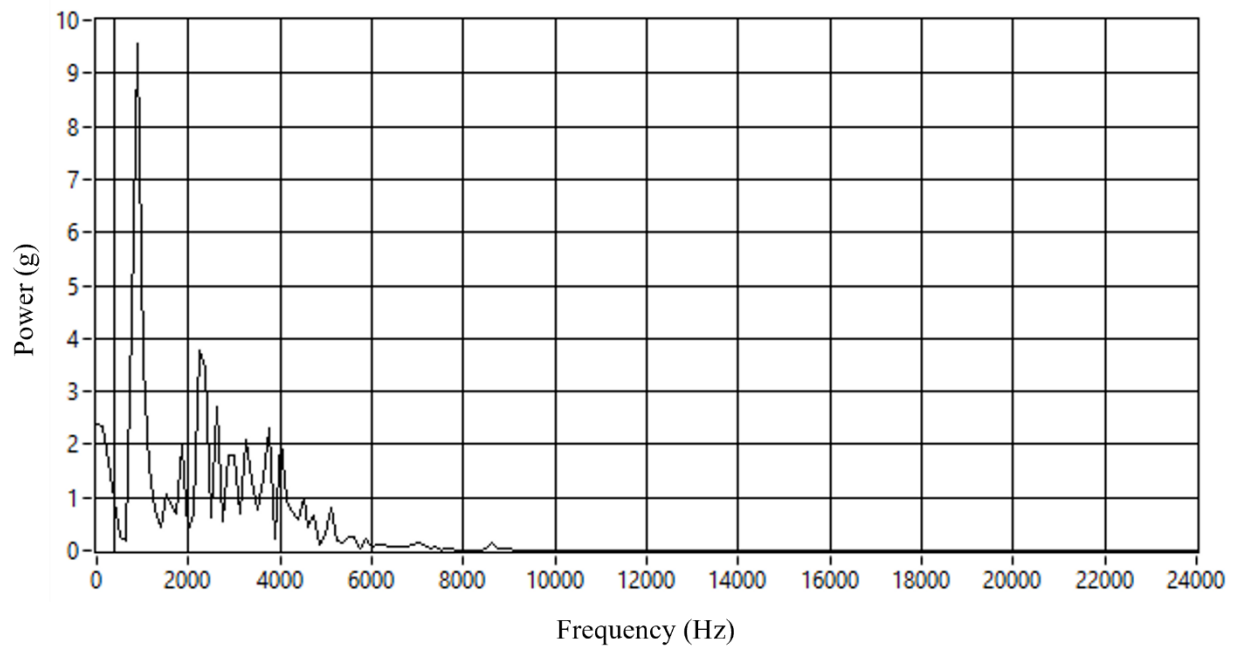
C.2 Plots



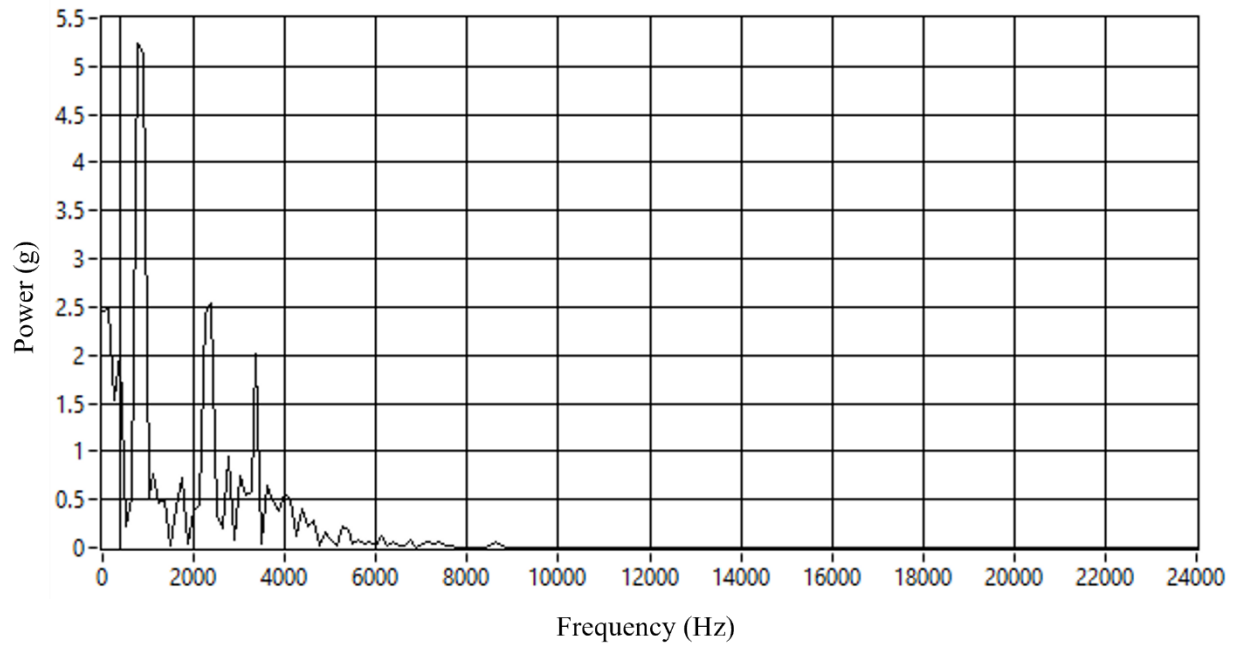
App. Figure C.1: Power spectrum of superglue interface setup. GV connector struck transversely with 50 g impact rod



App. Figure C.2: Power spectrum of superglue interface setup. GV connector struck transversely with 60 g impact rod



App. Figure C.3: Power spectrum of superglue interface setup. GV connector struck transversely with 70 g impact rod



App. Figure C.4: Power spectrum of superglue interface setup. GV connector struck transversely with 90 g impact rod

Appendix D Clinical and CSA Standards

D.1 Overview

Clinical, research, and CSA standards were collaboratively developed and compiled by the research team. A comprehensive overview of the development and compliance process can be reviewed in Section 5.3. Definitions necessary for comprehension of the master standards table in Section D.3 are outlined in Section D.2.

D.2 Definitions

D.2.1 Worst Reasonably Foreseeable Misuse

The prototype should continue to meet general and patient safety standards as well as any other applicable standard under the worst reasonably foreseeable misuse case. This case was defined as continuous use for twice the expected duration of a clinical test at 110% the maximum rated voltage for normal operation. An ambient temperature of 25°C applied.

D.2.2 Single Fault Condition

The prototype should continue to meet general and patient safety standards as well as any other applicable standard with exposure to a single fault condition. Specific conditions are defined in App. Table D.2.

D.2.3 Standard Colour Codes

Standards were colour coded according to their minimum adherence level. The colour of a cell in the Type/Minimum Level column of App. Table D.2 indicated its minimum adherence level according to the legend in App. Table D.1. The colour of the rest of the cells in each row indicated the level of adherence met. Contextual standards were labelled blue and had no associated minimum level of adherence.

App. Table D.1: Standards legend

| Minimum Level Colour Code |
|---|
| Contextual standard |
| Acceptable risk with acknowledgement of need for future development |
| Standard met |

D.3 Standards Summary

App. Table D.2: Standards summary

| Standard | Type/Minimum Level | Description | Summary/Excerpt from [79] | Notes |
|----------------------|-------------------------|---|--|--|
| Clinical Protocol 1 | Risk Management | Cleaning and disinfection compatibility | All external parts and surfaces are compatible with isopropyl alcohol (70%). | 316 stainless steel [77], PEEK [81], and PLA [82] compatible. |
| Clinical Protocol 2 | Patient Safety | Applied force limit | Handheld impact force does not exceed 50 N (prescribed initial static load limit). | See Section 5.3.3. |
| Research Integrity 1 | Operational Performance | General reliability | Handheld operation results in 16 strikes in 4 s and reliable data acquisition. | Generally reliable with adequate training and experience. Device works within a narrow margin of strike distances and orientations. Future development needed. |
| Research Integrity 2 | Operational Performance | Device independence | Handheld frequency excitation bandwidth is reliably different than the ASIST. | See Sections 5.3.6.3 and 5.3.6.4. |
| Research Integrity 3 | Operational Performance | Device functionality | Handheld first axial mode power spectral density is greater than or amplitude ratio (mode 2 PSD/mode 1 PSD) is less than the ASIST in its worst performing case (low interface condition). | See Sections 5.3.6.4 and 5.3.6.5. |

| | | | | |
|-------------------------|-----------------|--|--|--------------------------------------|
| CSA 60601-1 4.1 | Context | * Conditions for application to ME EQUIPMENT or ME SYSTEMS | Unless otherwise specified, the requirements of this standard shall apply in NORMAL USE and reasonably foreseeable misuse. When applying this standard to ME EQUIPMENT or ME SYSTEMS intended for the compensation or alleviation of disease, injury or disability, the definitions and requirements that use the term PATIENT shall be considered as applying to the person for whom the ME EQUIPMENT or ME SYSTEM is intended. | |
| CSA 60601-1 4.3 | Context | * ESSENTIAL PERFORMANCE | The MANUFACTURER shall identify which functions of the ME EQUIPMENT and ME SYSTEMS are ESSENTIAL PERFORMANCE. Where this standard specifies that ESSENTIAL PERFORMANCE is to be maintained following a particular test, these functions shall be used and compliance shall be checked by inspection, and if necessary, by functional test. | |
| CSA 60601-1 4.7 | Context | * SINGLE FAULT CONDITION for ME EQUIPMENT | ME EQUIPMENT shall be so designed and manufactured that it remains SINGLE FAULT SAFE, or the RISK remains acceptable as determined through application of 4.2. | |
| CSA 60601-1 4.8 | Risk Management | Components of ME EQUIPMENT | All components, including wiring, the failure of which could result in a HAZARDOUS SITUATION shall be used in accordance with their specified ratings unless a specific exception is made in this standard or through the RISK MANAGEMENT PROCESS. | Met at an actuation voltage of 12 V. |
| CSA 60601-1 9.2.1 | Risk Management | * General | ME EQUIPMENT with moving parts shall be designed, built and laid out so that, when PROPERLY INSTALLED and used as indicated in the ACCOMPANYING DOCUMENTS or under reasonably foreseeable misuse, the RISKS associated with those moving parts are reduced to an acceptable level. | |

| | | | | |
|--------------------|-----------------|--|---|---|
| CSA 60601-1 9.3 | Risk Management | * HAZARD associated with surfaces, corners and edges | Rough surfaces, sharp corners and edges of ME EQUIPMENT that could result in an unacceptable RISK shall be avoided or covered. | Fillets incorporated in design and burrs removed during construction. |
| CSA 60601-1 9.6.1 | General Safety | * General | ME EQUIPMENT shall be designed so that human exposure to acoustic energy and vibration shall not result in an unacceptable RISK. | |
| CSA 60601-1 9.6.3 | Patient Safety | * Hand-transmitted vibration | Except for vibrations directly required to carry out the INTENDED USE of the ME EQUIPMENT, means shall be provided to protect the PATIENT, OPERATOR and other persons if in NORMAL USE the hand-transmitted frequency-weighted r.m.s. acceleration generated by the ME EQUIPMENT exceeds the value below: - 2.5 m/s^2 for a cumulative time of 8 h during a 24 h period. - Allowable accelerations for different times are inversely proportional to the square root of the time (e.g. the allowable acceleration for 2 h would be 5.0 m/s^2). | Maximum allowable r.m.s acceleration over a 4.8 s period: 19.74 g. Worst case r.m.s acceleration for silicone setup: 17.49 g. Future development needed for other setups. |
| CSA 60601-1 11.1.1 | General Safety | * Maximum temperature during NORMAL USE | When ME EQUIPMENT is operated in worst-case NORMAL USE including the maximum ambient operating temperature specified in the technical description (see 7.9.3.1): - ME EQUIPMENT parts shall not reach temperatures exceeding the values given in Table 22 and Table 23; - the ME EQUIPMENT shall not cause the surfaces of the test corner to exceed 90°C ; and - THERMAL CUT-OUTS shall not operate in NORMAL CONDITION. | Casing maximum: 48°C . Tip maximum: 51°C . See Table 5.3. |

| | | | | |
|----------------------------|-----------------|---|---|--|
| CSA 60601-1 11.1.2.2 | Patient Safety | * APPLIED PARTS not intended to supply heat to a PATIENT | The limits of Table 24 shall apply. If the surface temperature of an APPLIED PART exceeds 41°C, the maximum temperature shall be disclosed in the instructions for use and the clinical effects with respect to characteristics such as body surface, maturity of PATIENTS, medications being taken or surface pressure shall be determined and documented in the RISK MANAGEMENT FILE. Where 41°C is not exceeded, no justification is required. | See Table 5.3. |
| CSA 60601-1 11.6.1 | Risk Management | General | The construction of ME EQUIPMENT and ME SYSTEMS shall ensure a sufficient degree of protection against overflow, spillage, leakage, ingress of water or particulate matter, cleaning, disinfection and sterilization as well as compatibility with substances used with the ME EQUIPMENT. | Generally true but needs to be vetted in future development. |
| CSA 60601-1 11.6.6 | Risk Management | Cleaning and disinfection of ME EQUIPMENT and ME SYSTEMS | ME EQUIPMENT, ME SYSTEMS and their parts, including APPLIED PARTS and ACCESSORIES, shall be capable of withstanding, without damage or deterioration of safety provisions, the cleaning or disinfection PROCESSES specified in the instructions for use. | See Clinical Protocol 1. |
| CSA 60601-1 11.7 | Patient Safety | Biocompatibility of ME EQUIPMENT and ME SYSTEMS | ME EQUIPMENT, ME SYSTEM and their parts or ACCESSORIES intended to come into direct or indirect contact with biological tissues, cells or body fluids shall be assessed and documented according to the guidance and principles given in the ISO 10993 series of standards. | 316 stainless steel [83] and PEEK [84] compatible. |
| CSA 60601-1 11.8 | Single Fault | * Interruption of the power supply / SUPPLY MAINS to ME EQUIPMENT | ME EQUIPMENT shall be so designed that an interruption and restoration of the power supply shall not result in a HAZARDOUS SITUATION other than interruption of its intended function. | |
| CSA 60601-1 13.2.8 | Single Fault | Locking of moving parts | ME EQUIPMENT shall be so designed that it remains SINGLE FAULT SAFE when moving parts become jammed. | |

| | | | | |
|----------------------------|-----------------|----------------------------|---|---|
| CSA 60601-1 15.2 | Risk Management | * Serviceability | Parts of ME EQUIPMENT subject to mechanical wear, electrical and environmental degradation or aging that could result in an unacceptable RISK if allowed to continue unchecked for too long a period shall be accessible for inspection, replacement and maintenance. | Met by clam shell design. |
| CSA 60601-1 15.3.1 | Risk Management | General | ME EQUIPMENT or its parts shall have adequate mechanical strength and shall not result in an unacceptable RISK due to moulding stress or when subjected to mechanical stress caused by pushing, impact, dropping, and rough handling. | Generally true but needs to be vetted in future development. |
| CSA 60601-1 15.3.2 | Risk Management | * Push test | ENCLOSURES of ME EQUIPMENT shall have sufficient rigidity to protect against unacceptable RISK. | Future development needed. |
| CSA 60601-1 15.3.4.1 | Risk Management | HAND-HELD ME EQUIPMENT | HAND-HELD ME EQUIPMENT and ME EQUIPMENT parts that are HAND-HELD shall not result in an unacceptable RISK as a result of a free fall. | Future development needed. |
| CSA 60601-1 15.3.5 | Risk Management | * Rough handling test | MOBILE ME EQUIPMENT and ME EQUIPMENT parts that are MOBILE shall withstand the stress caused by rough handling and movement and shall not result in an unacceptable RISK. | Future development needed. |
| CSA 60601-1 15.3.7 | Risk Management | * Environmental influences | The selection and treatment of materials used in the construction of ME EQUIPMENT shall take account of the INTENDED USE, the EXPECTED SERVICE LIFE and the conditions for transport and storage. The ME EQUIPMENT shall be so designed and constructed that during its EXPECTED SERVICE LIFE any corrosion, aging, mechanical wear, or degradation of biological materials due to the influence of bacteria, plants, animals and the like, shall not reduce its mechanical properties in a way that results in an unacceptable RISK. | Generally true but more durable casing materials should be implemented in future development. |

| | | | | |
|-----------------------------------|-----------------|--------------------------------------|--|---|
| CSA 60601-1 15.4.1 (a) | Risk Management | Construction of connectors | Plugs for connection of PATIENT leads shall be so designed that they cannot be connected to other outlets on the same ME EQUIPMENT intended for other functions, unless it can be proven that no unacceptable RISK can result. | Handpiece and accelerometer connectors are structurally different. |
| CSA 60601-1 15.4.4 | Risk Management | * Indicators | Unless it is otherwise apparent to the OPERATOR from the normal operating position, indicator lights shall be provided to indicate that ME EQUIPMENT is ready for NORMAL USE. | Actuation button illuminated when power is supplied to the handpiece. |
| CSA 60601-1 15.4.6.1 (a) | Risk Management | Fixing, prevention of maladjustment | All actuating parts of ME EQUIPMENT shall be so secured that they cannot be pulled off or work loose during NORMAL USE. | |
| CSA 60601-1 15.4.7.2 | Single Fault | Accidental operation of ME EQUIPMENT | HAND-HELD and foot-operated control devices shall not result in an unacceptable RISK by changing their control setting when accidentally placed in an abnormal position. | |
| CSA 60601-1 15.4.8 | Risk Management | Internal wiring of ME EQUIPMENT | Aluminum wires of less than 16 mm^2 cross-section shall not be used in ME EQUIPMENT. | |